UNIVERSITY OF CALIFORNIA
SANTA CRUZ

TERRESTRIAL EXOPLANET ATMOSPHERES: FROM PRIMORDIAL COMPOSITIONS TO LIKELY OBSERVABLE BIOSIGNATURES

A dissertation submitted in partial satisfaction of the requirements for the degree of

Doctor of Philosophy

in

ASTRONOMY AND ASTROPHYSICS

by

Margaret A. Thompson

March 2023

The Dissertation of Margaret A. Thompson is approved:

Jonathan J. Fortney, Chair

Myriam Telus

Laura K. Schaefer

Joshua Krissansen-Totton

Andrew J. Skemer

Peter Biehl
Vice Provost and Dean of Graduate Studies

Table of Contents

List of Figures **vi**

List of Tables **xviii**

Abstract **xxiv**

Acknowledgments **xxvi**

Dedication **xxx**

1 Introduction **1**
1.1 Terrestrial Planet Formation 3
1.2 The Meteorite Record 5
1.3 Origins of Rocky Planet Atmospheres 11
1.4 Searching for Signs of Life on Rocky Exoplanets 15

2 Composition of Terrestrial Exoplanet Atmospheres from Meteorite Outgassing Experiments **21**
2.1 Introduction 21
2.2 Results 26
2.3 Discussion 36
2.4 Extended Data Figures 38
2.5 Methods 44
2.5.1 Sample Preparation & Experimental Procedure 44
2.5.2 Data Calibration: Ion Fragmentation, Terrestrial Atmospheric Adsorption & Background Subtraction Corrections 45
2.5.3 Calculations to Determine Gas Species' Partial Pressures 48
2.5.4 Reproducibility of Experimental Results 51
2.5.5 Calculating Oxygen Fugacity 52
2.5.6 Comparison with Model Assumptions 54
2.5.7 Least Squares Regression Technique for Ion Fragments and Species Degeneracies 55
2.5.8 Degeneracies between Gas Species and Mass Numbers 56

2.5.9 Solid Phases . . . 61
2.5.10 Outgassed Gas Species' Masses . . . 62
2.5.11 Comparison with Prior Studies . . . 64
2.6 Supplementary Information . . . 68

3 Outgassing composition of the Murchison meteorite: Implications for volatile depletion of planetesimals and interior-atmosphere connections for terrestrial exoplanets 74
3.1 Introduction . . . 75
3.2 Methods . . . 81
3.2.1 Heating Experiments . . . 81
3.2.2 Sample Digestion and ICP-MS Analysis . . . 84
3.3 Results . . . 88
3.4 Discussion . . . 97
3.4.1 Effects of Experimental Variables on the Degree of Vaporization 97
3.4.2 Comparison with Prior Experimental Studies . . . 100
3.4.3 Comparison with Our Outgassing Experiments and Thermochemical Equilibrium Models . . . 103
3.5 Implications for Volatile Depletion of Planetesimals and Terrestrial Exoplanet Atmospheres . . . 112
3.6 Supplementary Information . . . 119
3.6.1 Chemical Equilibrium Models . . . 119
3.6.2 Data Calibration for Elemental Concentrations . . . 120
3.6.3 Analysis of the Calibration to Derive Elemental Concentrations . 121
3.6.4 Elemental Concentrations and Outgassing Analysis . . . 122
3.6.5 Alternative Data Calibrations . . . 123
3.6.6 Additional Elements Measured by ICP-MS . . . 123

4 The Case and Context for Atmospheric Methane as an Exoplanet Biosignature 139
4.1 Introduction . . . 139
4.1.1 Biological Methane Production on Earth . . . 142
4.2 Results . . . 144
4.2.1 The Case for Methane as a Biosignature . . . 144
4.2.2 Abiotic Sources of Methane . . . 149
4.2.3 Methane Beyond Earth: Mars and Temperate Exo-Titans . . . 158
4.3 Discussion . . . 167
4.3.1 Towards Procedures to Identify Methane Biosignatures . . . 167
4.3.2 Detectability Prospects . . . 169
4.4 Conclusions . . . 170
4.5 Supplementary Information . . . 173
4.5.1 Atmospheres with Abundant CH_4 and CO_2 in Chemical Equilibrium– Discussion of Woitke et al. 2021 . . . 173
4.5.2 Additional Water-Rock and Metamorphic Reactions and Key Unknowns . . . 174

4.5.3 Photochemical Destruction and Recombination Pathways for Methane 176
4.5.4 Gas Giant Planets . . . 179
4.5.5 Super-Earths and Sub-Neptune Planets . . . 180
4.6 Materials and Methods . . . 181
4.6.1 Photochemical Model: PhotochemPy . . . 181
4.6.2 Carbon Partitioning and Magmatic Outgassing Calculations . . . 181
4.6.3 Calculations of Global CH_4 Flux Estimates from Abiotic Sources 186
4.6.4 Calculations of Atmospheric Methane Lifetime for Volatile-Rich Bodies . . . 192

5 Summary and Future Directions **206**
5.1 Summary . . . 206
5.2 Future Directions . . . 209
5.2.1 Experimental Constraints on Volatile Partitioning in Magma Exoplanets . . . 209
5.2.2 Modeling the Compositional Diversity of Rocky Exoplanets . . . 214

Bibliography **218**

List of Figures

2.1 **Mole fractions of the measured species outgassed as a function of temperature for each chondrite sample**. The results are for 3 mg samples of (a) Murchison, (b) and (c) Jbilet Winselwan, and (d) Aguas Zarcas. We analyzed two 3 mg samples of Jbilet Winselwan under identical conditions to test reproducibility and show the results in (b) and (c). H_2 has the largest variation between the two experiments with Jbilet Winselwan. Across the three samples, some species exhibit major variations in their relative abundances over specific temperature intervals. For instance, CO and CO_2's abundances increase around 650 - 750 °C. Although the mole fraction of H_2S varies considerably over the entire heating range, it peaks near ∼900-1000 °C and then decreases at higher temperatures for all three chondrites. For most samples, there is a prominent increase in H_2's abundance near ∼1100 °C. 29

2.2 **Ratios of mole fractions of outgassed bulk elements hydrogen, carbon, oxygen, and sulfur as a function of temperature for the three chondrite samples.** From top to bottom the ratios are: carbon/oxygen, hydrogen/carbon, sulfur/oxygen and hydrogen/oxygen. Blue, purple and orange curves represent elements outgassed from Murchison, Winselwan, and Aguas Zarcas, respectively. 30

2.3 **Comparison between equilibrium calculations (left) and experimental results (right) under the same pressure and temperature conditions.** Figures (a) and (b) illustrate outgassing abundances calculated assuming chemical equilibrium for an average CM chondrite bulk composition at 1E-3 Pa (a) and experimental outgassing results for the average of the three CM chondrite samples measured at 1E-3 Pa (b). In (b), each species' curve is dominated by the sample that has the most abundant amount of that species at a given temperature. Figures (c) and (d) show the results for outgassing from a Murchison composition using chemical equilibrium calculations (c) and experimental outgassing results from the Murchison sample (d). The dashed curves in (b) and (d) show 'equilibrium-adjusted' experimental abundances in which the equilibrium model was used to recalculate gas speciation using the experimental abundances at intervals of 50 °C. The mass (in amu) of each species is in parentheses. See Figure 2.9 for other volatile species that theoretically degas with mole fractions above 1×10^{-4} according to chemical equilibrium calculations but are not measured in the experiments. . . . 32

2.4 **Oxygen fugacities relative to the quartz-fayalite-magnetite (QFM) buffer from theory and experiments.** Oxygen fugacity of an average bulk CM chondrite composition as a function of temperature from chemical equilibrium calculations (black curve, labeled Theory) and the oxygen fugacity of the average of the three CM chondrites measured experimentally (blue and orange curves, labeled Experiment). Two abundance ratios were used to calculate f_{O_2}: H_2O/H_2 (blue curve) and CO_2/CO (orange curve). We cannot determine f_{O_2} directly from the O_2 abundance because after correcting for terrestrial atmospheric adsorption its abundance goes to zero (see Methods). 36

2.5 **Data Calibration Steps**. Each figure illustrates the partial pressures (bars) for the molecular species measured from 200 °C to 1200 °C. Each sample's data is calibrated by first correcting for ion fragments and atmospheric adsorption and then background subtracting. 39

2.6 **Results of analyzing ion fragments using a non-linear least squares regression**. The outgassing abundances in (a) are for the Murchison sample with the panel on the right side showing the average standard deviation determined from the Monte Carlo simulation for each of the species measured. The abundances in (b) are the average of the three CM chondrites. 40

2.7 **Comparison between the yields of major volatiles released from Jbilet Winselwan samples during two identical experiments.** The mole fraction summed over temperature for each volatile species is normalized to the total mole fraction of released gases summed over temperature and expressed as a percentage. The uncertainty on the mean relative abundance for each volatile species is the 95% confidence interval of the mean. The volatile yields are fairly reproducible between the two experiments, especially for the most dominant outgassed species (H_2O, CO, CO_2). 41

2.8 **Comparison between the yields of major volatiles released from the samples.** The mole fraction summed over temperature for each volatile species is normalized to the total mole fraction of released gases summed over temperature and expressed as a percentage. The data for Winselwan is the mean of the two individual experiments conducted with the uncertainty reported as the 95% confidence interval of the mean (see Methods and Figure 2.7). The mean relative abundance of all three samples for each volatile species is also shown with the uncertainty reported as the 95% confidence interval of the mean. All three samples have similar outgassing abundances for the most dominant outgassing species (H_2O, CO, and CO_2). While H_2 and H_2S have larger variations up to an order of magnitude, the relative abundances for each species across the three samples are within 2σ of each other. 42

2.9 **Additional Outgassing Species from Chemical Equilibrium Calculations** Outgassing abundances for additional species not measured in the experiments calculated assuming chemical equilibrium for Murchison (a) and an average CM chondrite bulk composition (b) at 1E-3 Pa. The outgassing of H_2O is also shown as a reference. 43

2.10 **Schematic of Instrument Set-Up.** Each powdered sample is placed inside a small alumina crucible which itself is placed inside a alumina mini combustion boat. The boat is inserted into an alumina tube to the center of the furnace that can reach temperatures up to 1200 °C. The furnace is connected to a turbomolecular pump which maintains the entire system at a high-level vacuum, and to a residual gas analyzer which measures the partial pressures of up to 10 species continuously throughout the experiment. A thermocouple inside the tube measures the temperature as a function of time. The thermocouple is placed within 50 mm of the sample containers and both are within the furnace's 13 cm hotspot to ensure accurate temperature measurements. 68

2.11 **Total pressure of measured volatiles released from the samples as a function of temperature.** Variations in total pressure with temperature suggest that the amount of outgassing varies throughout the experiment. The average difference between the maximum and minimum total pressure is 6E-9 bars. Most samples show an increase in total pressure near 400 °C. 69

2.12 **Comparison between original results and results of separating the 32 amu signal into sulfur and O_2 components**. Figure (a) shows the outgassing abundances in which the signal at 32 amu is not separated into the sulfur and O_2 components (i.e., Figure 2.3 (b)). Figure (b) shows the results of separating the signal at 32 amu into its sulfur and O_2 abundances. 70

2.13 **Cumulative Outgassing Abundances**. The cumulative outgassing trends for samples of (a) Murchison, (b) Jbilet Winselwan, (c) Aguas Zarcas, and (d) the average of the three CM chondrite samples. 73

3.1 **The experimental heating procedures used for the two furnaces (temperature vs. time) to analyze the outgassing composition of Murchison.** (a) Heating schemes used for experiments performed with the furnace at atmospheric pressure (Furnace A). (b) Heating schemes used for experiments performed with the furnace operating in a high vacuum environment (Furnace B). Each set of experiments heated Murchison samples to 400, 600, 800 and 1000 °C. 84

3.2 **Average intensities from the unheated Murchison samples and the residues from the sets of stepped-heating experiments performed at atmospheric pressure (10^5 Pa/1 bar).** (a) Intensities normalized to V, (b) Intensities normalized to V and the average of the two unheated Murchison samples. The analytical uncertainties in (a) and (b) are the 1σ standard deviations for the normalized data propagated from the RSD uncertainties of Table 3.4. In (a) the uncertainties are smaller than the datapoints. In (b), the red vertical line represents the reproducibility between the V-normalized intensities of the two unheated Murchison samples, expressed as the maximum relative difference calculated using Equation 3.1. The x-axis refers to the temperature to which the residues were heated with "unheated" corresponding to the average of the two unheated Murchison samples and "400 C" corresponding to the average of the two residues heated to 400 °C, etc. 90

3.3 **Average intensities from the unheated Murchison samples and the set of stepped-heating experiments performed in a high vacuum environment ($\sim 10^{-4}$ Pa/10^{-9} bar).** (a) Intensities normalized to V, (b) Intensities normalized to V and the average of the two unheated Murchison samples. The analytical uncertainties in (a) and (b) are the 1σ standard deviations for the normalized data propagated from the RSD uncertainties of Table 3.4. In (a) the uncertainties are smaller than the datapoints. In (b), the red vertical line represents the reproducibility between the V-normalized intensities of the two unheated Murchison samples, expressed as the maximum relative difference calculated using Equation 3.1. The x-axis refers to the temperature to which the residues were heated with "unheated" corresponding to the average of the two unheated Murchison samples and "400 C" corresponding to the residue heated to 400 °C, etc. 91

3.4 **Experimentally-measured outgassing composition of a 3 mg powdered Murchison sample from 200-1200 °C under a high-vacuum environment ($\sim 10^{-4}$ Pa at lower temperatures and $\sim 10^{-3}$ Pa at higher temperatures) (lower panel) compared with the outgassing trends of S and Zn under the same vacuum conditions from this study (upper panel).** In the lower panel, the outgassing composition is shown as mole fractions of different outgassed species on a log scale as a function of temperature. The outgassing composition of Murchison was determined using a residual gas analyzer mass spectrometer that monitored the abundances (i.e., mole fractions) of the highly volatile outgassing species H_2O, H_2, CO, CO_2 and H_2S (see Thompson et al. (2021) for further details). Each species is labeled and its mass number is in parentheses. The dashed curves show 'equilibrium-adjusted' experimental outgassing compositions which are the result of taking Thompson et al. (2021)'s experimental elemental outgassing results at intervals of 50 °C and inputting those into the chemical equilibrium model of Figure 3.5 (see Schaefer & Fegley (2007, 2010) for details on the equilibrium model) to recompute how the gas composition would speciate under equilibrium conditions. The upper panel shows the S and Zn outgassing trends from this study, expressed as these elements' intensities, normalized to V and the average of the two unheated Murchison samples, for the residues heated under vacuum. 105

3.5 **Chemical equilibrium model results for the outgassing composition of Murchison from 200-1200 °C under a high-vacuum environment (∼10^{-4} Pa).** (a) The calculated mole fractions of the gas species that were also measured in the outgassing experiments of Thompson et al. (2021) (Figure 3.4) assuming chemical equilibrium under the same temperature and pressure conditions as the laboratory experiments of Thompson et al. (2021) and the vacuum experiments in this study. (b) Calculated mole fractions of the additional gas species containing the elements measured in this bulk element study (e.g., S, Fe, Mg, Zn) according to chemical equilibrium calculations under the same temperature and high-vacuum pressure conditions. 106

3.6 **Chemical equilibrium model results for the outgassing composition of Murchison from 400-1200 °C under atmospheric pressure.** Each figure shows outgassing of the species that contain the elements we measured in this bulk element study (i.e., S, Zn, Cr, etc.), and H_2O for reference. "50 air" (a) shows the results of the outgassing model for 100 g of Murchison, 50 g of air and the total gas pressure is fixed to 1 bar. "100 air" (b) shows the outgassing model results for 100 g of Murchison, 100 g of air and the total gas pressure is fixed to 1 bar. . . . 107

3.7 **Calibration curves for determining sample concentrations.** We used the In-normalized measurements for the procedural blank (blue circle) and four geological reference standards, BCR-2 (yellow star), BHVO-2 (green square), WMS-1a (orange X), WPR-1a (red circle), along with their published concentrations (ppm) from GeoReM to create five-point calibration curves using a linear regression (gray line). The tan box shows the slope, intercept, and r^2 values for the linear regression line. We treated BIR-1 (pink triangle) as an "unknown" standard to test the robustness of our calibration (Figure 3.8). 126

3.8 **Comparison of calculated BIR-1 elemental concentrations to the published concentrations from GeoReM.** The points show BIR-1's calculated concentrations (ppm) normalized to its published concentrations (ppm) from the GeoReM database (Jochum et al. 2007). The uncertainties of the published GeoReM concentrations are propagated and expressed as the 95% confidence intervals, all of which are within the datapoints. For most elements, the calculated concentrations reproduce the published concentrations within ∼20% error. Our calculated concentrations of S, Ni and P are near or below the quantification limit, which is why their ratios are at or near zero. However, the S, Ni and P concentrations for our unheated Murchison samples reproduce the unheated Murchison concentrations of Braukmüller et al. (2018) (B18) within 20% error (see Figure 3.9). Elements are arranged on the x-axis from left to right in order of decreasing 50% condensation temperature (Lodders 2003).127

3.9 **Comparison of calculated elemental concentrations (in ppm) of the two unheated Murchison samples analyzed to the Murchison concentrations determined by Braukmüller et al. (2018) (B18).** The points show the average concentrations of the two unheated Murchison samples measured in this study normalized to the average elemental concentrations of the two Murchison samples measured by B18. The uncertainties are the propagated 95% confidence intervals of means from both our unheated Murchison samples and the two Murchison samples from B18. Elements are arranged on the x-axis from left to right in order of decreasing 50% condensation temperature (Lodders 2003). 128

3.10 **Average elemental concentrations from the unheated Murchison samples and the residues from the sets of stepped-heating experiments performed at atmospheric pressure (10^5 Pa/1 bar).** (a) Elemental concentrations (ppm), (b) Elemental concentrations normalized to the CI chondrite Ivuna (Braukmüller et al. 2018) and Co. The x-axis refers to the temperature to which the residues were heated to with "unheated" corresponding to the average of the two unheated Murchison samples and "400 C" corresponding to the average of the two residues heated to 400 °C, etc. 129

3.11 **Average elemental concentrations from the unheated Murchison samples and the set of stepped-heating experiments performed in a high vacuum environment ($\sim 10^{-4}$Pa/10^{-9} bar).** (a) Elemental concentrations (ppm), (b) Elemental concentrations normalized to the CI chondrite Ivuna (Braukmüller et al. 2018) and Co. The x-axis refers to the temperature to which the residues were heated to with "unheated" corresponding to the average of the two unheated Murchison samples and "400 C" corresponding to the residue heated to 400 °C, etc. 130

4.1 **Atmospheric CO to CH_4 ratio may help distinguish biogenic and abiotic methane.** Ratio of atmospheric CO to CH_4 for abiotic worlds and those with biospheres as a function of volcanic H_2 flux. The curves show the calculated atmospheric CO/CH_4 as a function of volcanic H_2 flux for abiotic worlds (blue circles), H_2-based biospheres (includes H_2-consuming anoxygenic photosynthesis, CO-consuming acetogenesis, organic matter fermentation and acetotrophic methanogenesis) (pink diamonds), H_2-based and Fe-based photosynthesis biospheres (i.e., "hybrid," orange triangles) from Schwieterman et al. (2019), and the methanogen-acetogen ecosystem and anoxygenic phototroph-acetogen ecosystem from Kharecha et al. (2005) (i.e., their cases 2 and 3) (red squares). The horizontal shaded regions correspond to the distributions of atmospheric CO/CH_4 for abiotic worlds (blue) and those with methanogenic biospheres (pink, yellow and orange) as a function of volcanic H_2 flux calculated by Sauterey et al. (2020). The atmospheric CO/CH_4 for abiotic worlds is predicted to be several orders of magnitude greater than that for inhabited worlds. Schwieterman et al. (2019), Kharecha et al. (2005) and Sauterey et al. (2020) found that low CO/CH_4 atmospheric ratios ($\sim$0.1) are a strong sign of methane-cycling biospheres for reducing planets orbiting Sun-like stars like Archean Earth, suggesting that atmospheric CO/CH_4 is a good observable diagnostic tool to distinguish abiotic planets from those with anoxic biospheres. The light pink '+'-hatched region corresponds to an ecosystem with CO-based autotrophic acetogens (AG) and methanogenic acetotrophs (AT); the light orange 'X'-hatched region corresponds to an ecosystem with H_2-based methanogens (MG), AG, and AT; the orange '.'-hatched region corresponds to the most complex ecosystem consisting of MG, AG, AT and anaerobic methanotrophy (MT) (Sauterey et al. 2020). All calculations assume a CO_2-CH_4-N_2 bulk atmosphere. 162

4.2 **Summary of known abiotic sources of methane on Earth (©2022 Elena Hartley (elabarts.com)).** In general, the abiotic sources of methane can be divided into three categories: high-temperature magmatic outgassing (volcanism); low-temperature water-rock and metamorphic reactions; and impacts. Currently, subaerial (submarine) volcanoes on Earth only generate $\leq 10^{-3}$ ($\sim 10^{-2}$) Tmol/year of methane (see main text). Low-temperature water-rock reactions that generate methane occur at mid-ocean ridges, deep-sea hydrothermal vents, subduction zones, and continental settings. Methane can also be generated by metamorphic reactions, particularly in subduction zones and continental settings such as ophiolites, orogenic massifs, and Precambrian shields. Both water-rock and metamorphic reactions can generate variable quantities of methane depending on the geochemical conditions, but, on Earth, methane fluxes are orders of magnitude smaller than biological sources. Finally, impacts or other exogeneous sources can generate methane. The impact flux was larger during earlier periods in Earth's history, and such large impact fluxes are necessary to generate significant methane. A critical factor that influences the amount of methane that can be generated via all of these processes is the source of reducing power; in comparatively oxidizing surface environments with abundant CO_2, a reductant is needed to reduce carbon to CH_4. For magmatic outgassing, the reducing power ultimately comes from the mantle, with more reduced mantles outgassing more methane relative to CO_2 and CO. For low-temperature water-rock and metamorphic reactions, the key source of reducing power is ferrous iron (Fe^{2+}) in the crust, and in some cases the redox state of the mantle can also influence methane generation. For impact events, the metallic or ferrous iron that is delivered by the impactor serves as the source of reducing power 163

4.3 **Most carbon partitions into graphite under reducing conditions and so cannot degas as CH_4.** The ratio of the amount of remaining graphite to the original carbon content as a function of oxygen fugacity. We used a batch-melting model to determine how volatiles would partition between the rock and melt over a ∼10 km deep column of newly produced crust with pressures from ∼0-0.5 GPa and temperatures from 1400-1445 K (Section 4.6.2 in SI). For each oxygen fugacity, we ran a Monte Carlo simulation varying the input parameters including CO_2 and H_2O mass fractions in the mantle source rock, the fraction of source material that is melted during emplacement, and the planetary melt production rate. The average ratio of remaining graphite to initial carbon content from the Monte Carlo simulation is shown with the uncertainty reported as the 95% confidence interval. The horizontal dashed line (y = 1) illustrates the original amount of carbon, and ratios that fall on this line have all of the original carbon stable as graphite. The shaded vertical regions show the estimated oxygen fugacities of Mercury's lavas (Namur et al. 2016), the Martian mantle (Hirschmann & Withers 2008), terrestrial basalts (Doyle et al. 2019), Earth's upper mantle (Cottrell & Kelley 2011), and Archean Earth's mantle (Kadoya et al. 2020) for reference. . 164

4.4 **Summary of known abiotic CH_4 sources with their estimated global CH_4 flux values compared to Earth's current biogenic CH_4 flux.** As in Table S1, for each abiotic source considered, we present those sources for which we can estimate global CH_4 flux values from a given reference. In the cases where there are multiple global CH_4 flux estimates for a given reference of an abiotic source, we show the maximum and minimum CH_4 flux estimates by the vertical lines. The transparent purple probability distribution for the maximum abiotic CH_4 flux from serpentinization is from Krissansen-Totton et al. (2018b), and the right-hand y-axis shows the probability density of this distribution. None of the abiotic sources considered have estimated global CH_4 fluxes that are similar to or exceed Earth's modern biogenic CH_4 flux. In fact, most of the abiotic sources have predicted global CH_4 fluxes that are at least an order of magnitude less than Earth's biogenic CH_4 flux. We do not show the flux estimates that exceed the iron supply because such extremely large fluxes are based on experimental results for which there are issues with organic contamination (see main text). 165

4.5 **The photochemical lifetime of methane biosignature false positives produced by melting volatile-rich Titan-analogs is short.** Estimated lifetime of atmospheric methane as a function of planet's water mass and initial methane volatile inventory. Assuming methane's escape rate is diffusion-limited and that its steady-state mixing ratio is 10%, we varied the initial methane volatile inventory (drawing values from a uniform distribution from 0.01% to 1.0% relative to weight % water, represented by the color bar) and the mass fraction of the planet's water (exploring values from 0.01% to 10% of the mass of the planet, assuming an Earth-mass planet) and calculated the estimated lifetime for methane in the atmosphere (see SI Section 4.6.4). The red curve represents Titan's methane inventory (∼0.35 %, Tobie et al. (2012)). For planets with Titan-like methane inventories and water mass fractions that are 1% (10%) of the planet's mass, the lifetime of atmospheric methane will be ∼10 Myrs (∼100 Myrs). 166

4.6 **Methane surface flux required to sustain CH_4- and CO_2-rich atmospheres in photochemical steady state.** Using PhotochemPy, we ran a series of models with an initial atmospheric composition that is Archean Earth-like (orbiting the Sun at 2.7 Ga) exploring a range of CH_4 and CO_2 surface mixing ratios from 10^{-5} to 0.1 and 0.1 to 0.5, respectively. The contour colors correspond to the CH_4 surface flux required to sustain the atmospheric mixing ratios. While the model accounts for haze formation, we found that at higher CH_4 mixing ratios, the model had trouble converging to a steady-state solution. For those cases corresponding to the hatched region of the figure, we ran models that used the same Archean Earth-like initial atmospheric composition but removed the haze component in order to ensure model convergence. Ultimately, for abundant atmospheric CH_4 (i.e., surface mixing ratios above $\sim 10^{-3}$) to be stable against photochemistry in terrestrial planet atmospheres requires a significant replenishment source that results in large CH_4 surface fluxes that are likely much larger than Earth's current biological flux. 196

4.7 **Simultaneous outgassing of CH_4 and CO_2 with negligible CO is highly unlikely unless large quantities of graphite are efficiently converted to CH_4 via metamorphism.** Outgassing fluxes as a function of oxygen fugacity. We used the same batch-melting model as described in Figure 4.3 and solved for speciation of gases produced by magmatic outgassing. The results are the average outgassing fluxes (in Tmol/year) of CH_4, CO_2 and CO from the Monte Carlo simulation with uncertainties reported as the 95% confidence intervals. The graphite results assume that either 100% or 1% of the remaining graphite can be converted into outgassed CH_4. The horizontal dashed lines show current outgassing fluxes on Earth for reference (e.g., biological CH_4 flux). For a planet with a very reduced melt composition, outgassing of any carbon species (i.e., CH_4, CO_2, and CO) will be negligible. In addition, for all oxygen fugacities considered from extremely reduced ($IW - 11$) to highly oxidized ($IW + 5$), the magmatic outgassing fluxes of CH_4 are still orders of magnitude lower than Earth's modern biological CH_4 flux of 30 Tmol/year. 197

4.8 **Possible procedure to search for methane biosignatures on terrestrial exoplanets that takes into account the planetary context.** Once an exoplanet has been detected, it is important to characterize its bulk properties (e.g., mass, radius, orbital properties, presence of a surface, host star properties). In addition, constraining its atmospheric composition, particularly the abundances CH_4, CO_2, CO, H_2, H_2O and confirming that the atmosphere is anoxic, is essential for determining the presence of a methanogenic biosphere. Using this data with a photochemical model can determine the surface fluxes of the different atmospheric constituents that are necessary to sustain the observed atmospheric abundances. If the inferred CH_4 surface fluxes are consistent with plausible biogenic levels, then all possible false positive scenarios must be evaluated. If all false positives can be definitively ruled out then a methane biosignature has been identified at a high level of confidence that must be statistically determined. However, if all false positives cannot be ruled out, then it is necessary to look for corroborating evidence like additional gas species (e.g., methyl chloride, and organosulfur compounds) and the presence of surface pigments. Credits (images): Don Dixon, Wikimedia Commons; Donald Hobern; kuhnmi; NASA/JPL-Caltech/Lizbeth B. De La Torre; Doc Searls. 199

List of Tables

2.1 **Total mass of volatile species released (in g) and relative abundances (in %) of outgassed species summed over temperature for the three CM chondrite samples.** Abundances are in partial pressures normalized to the total pressure of all released gases measured summed over temperature and are reported as percentages. The species corresponding to each mass number is in parentheses. The uncertainties reported for Jbilet Winselwan are the 95% confidence intervals of the means. Since some species have overlapping mass numbers (e.g., S and O_2), we provide a detailed description of the calculations made in determining these relative abundances in Methods. 27

2.2 **Relative outgassed atomic abundances (in %) summed over temperature of hydrogen, carbon, oxygen, nitrogen and sulfur for the three samples.** As in Table 2.1, abundances are in partial pressure normalized to the total pressure of all released gases measured and are reported as percentages. The uncertainties reported for Jbilet Winselwan are the 95% confidence intervals on the means. Comparison between the initial (pre-degassing) normalized atomic abundances for average CM chondrites and the outgassed normalized atomic abundances are shown, both reported as percentages (bottom two rows). These atomic abundances are normalized to the sum of the elements measured in the experiments, i.e., H, C, O, N, S. The uncertainties for the pre-degassing normalized atomic abundances are (1σ) standard deviations. The uncertainties for the outgassed quantities are expressed as the 95% confidence intervals of the means. The initial bulk atomic abundances of CM chondrites come from the literature (Nittler et al. 2004; Alexander et al. 2012). 28

2.3 **Table of the mass spectrum for each gas species in our experiments.** For the ten masses measured during the experiments, several could correspond to gas molecules that, when ionized by the RGA, produce fragments that contribute to the signal of other masses measured. For each of the gas species that correspond to one of the ten measured masses, we used the mass spectrum from National Institute of Standards and Technology (NIST)'s Mass Spectrometry Data Center to determine the possible ion fragments (NIST & Wallace 2018). We also include an additional ion fragment for water at 2 amu from MKS (MKS 2005). For each species in the table, we list the mass numbers of its known ion fragments and their signal intensities relative to the major peak due to the gas species itself (i.e., the signal percentage of the gas species is 100%). In the last column, we provide the normalized signal intensities (i.e., all of the signals sum to 100%). We only list ion fragments whose mass numbers correspond to those measured in our outgassing experiments. For atoms and species that either do not suffer from ion fragments or whose fragments correspond to masses that we do not measure, we assume all of its signal is concentrated at its mass number. 71

2.4 **Previously determined average bulk composition of CM chondrites and Murchison from literature** [a](Alexander et al. 2012), [b](Nittler et al. 2004), [c](Fuchs et al. 1973). The uncertainties are the 1σ standard deviations. 72

2.5 **Comparison of primary algebraic data analysis and Monte Carlo non-linear least squares (MC) data analysis for Murchison.** The second and third columns show the average partial pressure (in bars) for each species. The fourth column shows the standard deviation of the average partial pressure for each species analyzed using the Monte Carlo technique. These partial pressures are corrected for ion fragments and atmospheric adsorption but have not been background subtracted. . . . 72

3.1 **Summary of the bake-out scheme prior to the heating experiments (top) and the steps for the heating experiments performed with Furnace A (middle) and B (bottom).** We performed two complete sets of heating experiments with Furnace A (i.e., eight Murchison samples were heated in total), and we performed one set of heating experiments with Furnace B (i.e., four Murchison samples heated). 87

3.2 **Intensities in counts per second (cps) for the two sets of Murchison samples heated under atmospheric pressure following the procedures outlined in Figure 3.1(a) determined by ICP-MS analysis.** The M-400 (1) and M-400 (2) columns show the intensities for the samples heated to 400 °C, and so on for the samples heated to 600, 800, and 1000 °C. The elements are listed in order of increasing atomic mass. 94

3.3 **Intensities in counts per second (cps) for the set of Murchison samples heated under a high-vacuum environment ($\sim 10^{-4}$ Pa) following the procedures outlined in Figure 3.1(b) and the two unheated Murchison samples (M-UH) determined by ICP-MS analysis.** For the unheated Murchison samples, the average of the two samples is used in Figures 3.2 and 3.3. The elements are listed in order of increasing atomic mass. 95

3.4 **ICP-MS analytical uncertainties (i.e., relative standard deviations (RSD)) for all Murchison samples analyzed.** Each value shows the RSD of the intensity (expressed as a %) measured by the ICP-MS. UH (1) and UH (2) refer to the two unheated samples of Murchison. Columns 400 (1), 600 (1), 800 (1), and 1000 (1) show the RSDs for the first set of samples heated under atmospheric pressure. Columns 400 (2), 600 (2), 800 (2), and 1000 (2) show the RSDs for the second set of samples heated under atmospheric pressure. Lastly, columns 400 (3), 600 (3), 800 (3), and 1000 (3) show the RSDs for the set of samples heated under vacuum. 96

3.5 **Masses of the samples before and after the heating experiments and the masses digested for ICP-MS analysis**. For the mass of the samples heated to specific temperatures, the first column indicates the temperature to which the sample was heated. For example, for the first set of heating experiments performed under atmospheric pressure, 400 refers to the sample heated to 400 °C. All masses are shown in mg. . . 131

3.6 **Instrumental Settings, Performance and Acquisition Parameters for ICP-MS**. The instrument set-up for the ICP-MS consisted of a Peltier cooled (2 °C) cyclonic spray chamber. MR refers to medium resolution. 132

3.7 **ICP-MS intensities and analytical uncertainties for all rock standards analyzed along with the procedural blank measurement.** Each value shows the average intensity (in cps) measured by the ICP-MS and the value in parentheses is the analytical uncertainty for that average intensity measurement expressed as the relative standard deviation (RSD) in %. 133

3.8 **Percent differences (%) between the V-normalized intensities of the two sets of Murchison samples heated under atmospheric pressure.** UH refers to the percent difference between the two unheated Murchison samples. 400, 600, 800 and 1000 refer to the percent differences between the two Murchison samples heated to those respective temperatures under atmospheric pressure. 134

3.9 **Elemental concentrations in ppm for the two sets of Murchison samples heated under atmospheric pressure following the procedures outlined in Figure 3.1(a) determined by ICP-MS analysis.** For each element, the uncertainty is expressed as the % error between the calculated elemental concentration for BIR-1 and the published concentration following Equation 3.9 in Supplementary Information. The elements are listed in order of increasing atomic mass. *For S, Ni and P, because their calculated concentrations for BIR-1 are at or below the quantification limit, we instead use the % error between the calculated elemental concentrations for the unheated Murchison samples and those determined by Braukmüller et al. (2018) (B18). 135

3.10 **Elemental concentrations in ppm for the set of Murchison samples heated under a high-vacuum environment ($\sim 10^{-4}$ Pa) following the procedures outlined in Figure 3.1(b) and the two unheated Murchison samples (M-UH) determined by ICP-MS analysis.** For each element, the uncertainty is expressed as the % error between the calculated elemental concentration for BIR-1 and the published concentration following Equation 3.9 in Supplementary Information. For the unheated Murchison samples, the average of the two samples is used in Figures 3.9-3.11. The elements are listed in order of increasing atomic mass. *For S, Ni and P, because their calculated concentrations for BIR-1 are at or below the quantification limit, we instead use the % error between the calculated elemental concentrations for the unheated Murchison samples and those determined by Braukmüller et al. (2018) (B18). 136

3.11 **Concentrations of the BIR-1 standard measured by ICP-MS compared to the published values from GeoReM (Jochum et al. 2007).** Each value in the first two columns shows the concentration (in ppm). The third column shows the uncertainty of the published BIR-1 uncertainties from GeoReM reported as the 95% confidence intervals of the means. The last column shows the uncertainty between our measured BIR-1 concentrations and those from GeoReM, expressed as the % error between the calculated elemental concentration for BIR-1 and the published concentration following Equation 3.9 in Supplementary Information. 136

3.12 **Comparison of the elemental concentrations (in ppm) of our two unheated Murchison samples and those of the two unheated Murchison samples from Braukmüller et al. (2018) (B18).** The second and third columns correspond to the elemental concentrations determined for our two unheated Murchison samples, with the fourth column showing their uncertainties. The fifth and sixth columns correspond to the elemental concentrations for two Murchison samples measured in B18, with the seventh column giving their uncertainties. The concentrations are reported in ppm and the uncertainties are the calculated 95% confidence intervals of the means. 137

3.13 **Summary of data calibration methods tested.** The calibration methods can be divided into two types: 1) the left column shows the different calibration methods tested using data that has been In-normalized and blank-subtracted (i.e., the In-normalized data was subtracted from the total procedural blank's (TPB) In-normalized data); 2) the right column shows the different calibration methods tested using data that has been In-normalized and the TPB was used as a point in the calibration curves. The major outgassing trends are consistent regardless of which calibration method is used. The method highlighted by * is the method that we used to derive elemental concentrations because it resulted in the most robust calibrations for the largest set of elements. 138

4.1 Monte Carlo sampling distributions for carbon partitioning and gas speciation calculations. 198

4.2 Summary of abiotic CH_4 sources and their estimated global CH_4 flux values (Part 1). *Indicates that the experimental measurements may have over-estimated the amount of methane generated due to the presence of background sources. 200

4.3 Summary of abiotic CH_4 sources and their estimated global CH_4 flux values (Part 2). *Indicates that the experimental measurements may have over-estimated the amount of methane generated due to the presence of background sources. 201

4.4 Summary of abiotic CH_4 sources and their estimated global CH_4 flux values (Part 3). *Indicates that the experimental measurements may have over-estimated the amount of methane generated due to the presence of background sources. 202

4.5 Summary of abiotic CH_4 sources and their estimated global CH_4 flux values (Part 4). *Indicates that the experimental measurements may have over-estimated the amount of methane generated due to the presence of background sources. 203

4.6 Summary of abiotic CH_4 sources and their estimated global CH_4 flux values (Part 5). *Indicates that the experimental measurements may have over-estimated the amount of methane generated due to the presence of background sources. 204

4.7 Estimated lifetime of atmospheric CH_4 for Earth-mass terrestrial planets with Titan-like initial volatile inventory and different size water mass fractions. 205

Abstract

Terrestrial Exoplanet Atmospheres:

From Primordial Compositions to Likely Observable Biosignatures

by

Margaret A. Thompson

Exoplanet science is now focusing on characterizing the physics and chemistry of exoplanet atmospheres, including those of terrestrial-class, potentially habitable planets. In this thesis, I use a combination of laboratory experiments and theoretical modeling to understand two themes related to these atmospheres: (1) their primordial outgassing compositions from an experimental cosmochemistry approach, and (2) the planetary context for observable biosignature gases using modeling tools.

There is no first-principles understanding of how to connect a planet's bulk composition to its initial atmospheric properties. Since terrestrial exoplanets likely form their atmospheres through outgassing, an important step towards establishing this connection is to assay meteorites, remnants of planetary building blocks, by heating and measuring their outgassed volatiles. In the first theme, I use multiple experimental techniques to determine meteorites' outgassing compositions over a range of temperatures and pressures. I describe the results of heating carbonaceous chondrite samples and measuring their abundances of released volatiles as a function of temperature in a high-vacuum environment. I find that these meteorites outgas significant amounts of H_2O, CO, CO_2 and smaller quantities of H_2 and H_2S. I also discuss a complementary

bulk element analysis to monitor outgassing of heavier elements (e.g., sulfur, iron, zinc). I compare these experimental results to thermochemical equilibrium models of chondrite outgassing and determine how these experiments can improve atmospheric models and inform the connection between bulk composition and early atmospheres.

For the second theme, I perform a comprehensive analysis of the necessary planetary conditions for atmospheric methane to be a compelling biosignature gas. Methane is one of the only biosignatures that JWST can readily detect in terrestrial atmospheres. Therefore, it is essential to understand methane biosignatures to contextualize these imminent observations. Using a combination of multiphase thermodynamic and atmospheric chemistry models, I investigate abiotic sources of methane and determine the planetary conditions for which these sources could be enhanced on terrestrial planets so as to result in false positives. I determine that known abiotic processes cannot easily generate atmospheres rich in CH_4 and CO_2 with limited CO due to the strong redox disequilibrium between CH_4 and CO_2, providing the first tentative framework for assessing methane biosignatures.

Acknowledgments

First and foremost, I thank my PhD advisors, Profs. Myriam Telus and Jonathan Fortney, for their unwavering support and guidance throughout the last six years. Myriam, thank you for taking a chance with me, as a student who, before working with you, had never done any experimental cosmochemistry research. Learning from you has been the most wonderful experience of my academic career. I am so grateful for your mentorship and training that gave me the skills to be a confident and diligent laboratory cosmochemist. Thank you for being an incredible role model as a scientist, teacher, leader and friend. Jonathan, thank you for your constant advise and for creating a wonderful exoplanet community that reinforced my passion for the field and gave me a true sense of belonging. Thank you also for giving me the flexibility to take on projects outside of the astronomy norm and for your constant enthusiasm and support of my work.

In addition to my advisors, I would like to thank my mentors, Prof. Joshua Krissansen-Totton, Prof. Laura Schaefer, and Dr. Davy Kirkpatrick. To Josh, thank you for approaching me about our methane biosignatures project and for your constant guidance from that day forward. Prior to working with you, I lacked confidence in my skills as a modeler, and your patience and support throughout our project truly gave me that confidence. To Laura, thank you for your support throughout my experimental projects and for your insight into the world of planetary outgassing and magma oceans. My conversations with you sparked my curiosity in the topics that I will focus on as a postdoc. Lastly, to Davy, thank you for being the absolute best first academic mentor

anyone could ask for. Without you, I know that I would not have pursued a PhD in astronomy. My passion for this field was sparked during our first summer working together, and I am so grateful for your constant mentorship over the last 12+ years.

Even with my inspiring advisors and mentors, my time in graduate school would not have been nearly as special without my fellow graduate students at UCSC. To those in my cohort, including Rosa, Kevin, Callie, Amanda, and Enia thank you for always being there for me and for making the tough days bearable. To my predecessors, especially Diana, Jamie, Brenna, Graham, Molly, Sara, and Brittany, thank you for being so inspiring and taking me under your wings. To the later cohorts, thank you for your dedication to keeping our astronomy community, and the UCSC community at large, strong and just. It has been a privilege to have had the opportunity to work with several outstanding undergraduate students including Kyle, Matraca, and Taylor. Thank you all for your dedication to our research and for being wonderful scientists. Lastly, to the postdocs, especially Xinting, Emily, Jasmeet, Josh and Emilie, thank you for your support and mentorship.

Special thanks to my magical Santa Cruz friends Diana, Jamie, Rosa, Mike, Dave, Monine, Kevin, Avesta, and Emily. You all have made my time in Santa Cruz one of the most treasured periods of my life. Thank you for sharing some of your magic with me, taking me on the most wonderful adventures, and for being there through the thick and thin. I love you all dearly and am eternally grateful that this experience gave me incredible life-long friends.

To Jeremy, thank you for being my best friend, strongest supporter, and con-

stant champion in the truest sense of each. From the moment we met, you have always uplifted me and pushed me to believe in myself, especially when I was scared to do so. Thank you for making our time in Santa Cruz so truly wonderful. You are my home and I love you.

I can say with absolute certainty that I would not be where I am today without the immense love and unwavering support of my parents, Catherine and Dave. Thank you both for showing me the true meaning of love, hard work, and dedication. Dad, thank you for the countless hours of homework help and for inspiring my curiosity and passion for space that has given my life so much meaning. Mom, thank you for always being my rock and support system, for holding me through many spells of tears, and for reminding me that YOLO is truly a state of mind. I am me because of you two.

Published Material

The text of this dissertation includes reprints of the following published material led by Thompson, with the permission of the listed coauthors.

Chapter 2 was published in the literature as Thompson et al. (2021). I was responsible for performing the laboratory experiments and subsequent analysis, writing the text, and creating the figures. I wish to thank my coauthors Myriam Telus, Laura Schaefer, Jonathan J. Fortney, Toyanath Joshi, and David Lederman for their immense support throughout this research project.

Chapter 3 is currently under review at *The Planetary Science Journal* and is expected to be published later this year.

Chapter 4 was published in the literature as Thompson et al. (2022). I was

responsible for performing the analysis, creating the figures and writing the text. I wish to thank my coauthors Joshua Krissansen-Totton, Nicholas Wogan, Myriam Telus and Jonathan J. Fortney for their generous support and feedback throughout this research.

Scientific Acknowledgments

I gratefully acknowledge research support from the Achievement Rewards for College Scientists Foundation scholarship and NASA under award 19-ICAR192-0041. This research was also supported by the NASA Emerging Worlds grant no. 80NSSC18K0498 and NASA Planetary Science Early Career Award grant no. 80NSSC20K1078 to Myriam Telus. In addition, my research with Joshua Krissansen-Totton was supported by the NASA Sagan Fellowship and through the NASA Hubble Fellowship Grant HF2-51437 awarded by the Space Telescope Science Institute, which is operated by the Association of Universities for Research in Astronomy, Inc., for NASA, under Contract NAS5-26555.

I also thank the UCSC Plasma Analytical Facility and the Lederman Lab in the UCSC's Physics Department for use of their experimental equipment and analytical instruments. I acknowledge support from Toyanath Joshi, David Lederman and Dyke Andreasen when using their instruments. I am very grateful for insightful conversations with Andy Skemer, Xinting Yu, David Catling, Edward Schwieterman, Kevin Zahnle and Stephanie Olson throughout my research projects. Lastly, I am thankful to Paolo Sossi, James Kasting, Aaron Wolf and other anonymous reviewers who provided constructive referee reports that improved the manuscripts described in this thesis.

For Dave, Catherine and Jeremy

Chapter 1

Introduction

The detection and characterization of terrestrial exoplanets, particularly those that are potentially habitable, is one of the key scientific challenges of the next several decades. With the advanced capabilities of NASA's James Webb Space Telescope (JWST) and upcoming 25-40-meter-class ground-based telescopes like the Giant Magellan Telescope (GMT), the Thirty Meter Telescope (TMT), and the European Extremely Large Telescope (ELT), we will soon begin to characterize the physics and chemistry of low-mass, terrestrial exoplanets (Wordsworth & Kreidberg 2022). Such observations will provide the unique opportunity to place Earth and the other terrestrial planets in our Solar System in the wider context of planet formation and evolution in the universe (Lapôtre et al. 2020). In preparation for these upcoming observations, which will consist largely of spectroscopic measurements of planetary atmospheres, we need suitable theoretical tools, informed by experimental data, to model the diversity of these planets and their atmospheres and to ensure that observations are properly interpreted. Devel-

oping these models requires interdisciplinary expertise across multiple fields including astrophysics, planetary science, Earth science and chemistry. Some of the major open questions about terrestrial-class exoplanets include: How do these planets and their atmospheres form and evolve? What is the connection between a rocky planet's interior (i.e., bulk) composition and its atmospheric properties? What are the best near-term observable biosignatures and their necessary planetary context? These outstanding questions motivate a comprehensive theoretical understanding of rocky exoplanet (and atmosphere) formation and evolution that is driven both by our detailed knowledge of the terrestrial planets in our Solar System and grounded by experimental data.

This thesis is concerned with two central themes related to terrestrial-class exoplanets. The first aims to understand the origins of terrestrial exoplanet atmospheres and their primordial chemical compositions using an experimental cosmochemistry approach. This work also provides important insights into the depletion of volatile elements on planetesimals during planet formation. The second theme uses a combination of thermodynamics and atmospheric chemistry models to evaluate the planetary context for observable biosignature gases, with a particular focus on methane. The work described here was completed at an opportune time as the field of exoplanet science is entering an observational revolution, with the culmination of NASA's Kepler mission that discovered over 2000 exoplanets and the launch of JWST that will provide the first opportunity to characterize the atmospheres of rocky, potentially habitable worlds. For example, in the coming years, JWST will observe and characterize the atmospheres of multiple rocky exoplanets including the planets in the Trappist-1 system, LHS 3844b,

55 Cancri e, and K2-141b (Lim et al. 2022; Kreidberg et al. 2021; Hu et al. 2021; Dang et al. 2021).

Looking ahead to the next decade, this work is particularly timely since the 2020 Decadal Survey on Astronomy and Astrophysics recommended the Habitable Worlds Observatory (a ∼6 meter infrared/optical/UV space telescope) for NASA's next flagship mission, with its primary goal being to characterize Earth-like exoplanets and search for signs of life in their atmospheres (Clery 2023). Accordingly, this thesis aims to take important steps forward in our understanding of the origins of terrestrial exoplanet atmospheres and the planetary conditions necessary for signs of life to be detected in them. This work requires coupling experimental data to comprehensive theoretical models to properly simulate the chemical and physical processes that occur in and interact between rocky planets' interiors and atmospheres. To begin, I will provide some background on terrestrial planet and atmosphere formation and evolution and the importance of meteorites for uncovering these processes in the Solar System.

1.1 Terrestrial Planet Formation

Terrestrial planets are mostly composed of refractory materials (e.g., silicates, metal, sulfides). Unlike giant planets with their significant, extended atmospheres, terrestrial planets have a solid surface and a thin (or no) atmosphere. Current knowledge of terrestrial planet formation is based on our understanding of the formation of rocky planetary bodies in the Solar System. In the conventional model of planet formation, hereafter referred to as the planetesimal model, planets form via many collisions between

small objects that form larger ones. This process occurs in stages starting with μm-sized dust grains in the protoplanetary disk. Larger dust particles tend to settle toward the disk midplane while smaller particles are more tightly coupled to the gas in the disk. The dust grains collide and readily stick together to form mm- to cm-sized aggregates. However, growing these aggregates via sticking beyond meter-size is challenging (i.e., the "meter-size barrier") due to faster collision speeds and lower sticking-area-to-mass ratios that are more likely to lead to erosion than growth. Instead, turbulent concentration and instabilities in the gas disk can cause the formation of gravitationally bound clumps that collapse and form 10-1000 km-sized bodies called planetesimals. Planetesimals interact dynamically which causes the largest objects to have the most probable conditions for additional growth. This is believed to lead to runaway and oligarchic growth that results in Moon- to Mars-sized planetary embryos. Once planetesimals are depleted, oligarchic growth ceases and embryos can occasionally collide, resulting in the Solar System's architecture of four terrestrial planets orbiting coplanar on widely-separated orbits (Chambers 2010, 2023).

Recently, another theory of rocky planet formation has emerged, called the pebble accretion model. This model is initially similar to the planetesimal model with dust grains adhesively sticking together to form pebble aggregates (mm to cm in size or possibly slightly larger). However, once the protoplanetary disk is dominated by these pebbles with only a few large objects and nebular gas still present, the pebbles are readily captured gravitationally by larger objects. The nebular gas exerts a drag force on the pebbles which causes them to lose energy when they encounter a larger object

and thereby prevents them from escaping the larger object's gravity. This process results in the formation of a few isolated planetesimals or planetary embryos which can grow quickly via efficient capture of pebbles (Cormier et al. 2022). A recent study by Chambers simulated both planetesimal and pebble accretion planet formation processes in an evolving protoplanetary disk driven by disk wind. They find that planetesimal accretion is the dominant method for planetary growth in the inner regions of the Solar System, particularly inside the ice line, the region in the disk where water condenses (Chambers 2023). It is still an active area of study to determine which of these two models of terrestrial planet formation dominated in the Solar System and which one tends to dominate in exoplanetary systems. In any case, understanding terrestrial planet formation is an essential ingredient to comprehensively place our Solar System in the wider context of planetary system formation and evolution in the universe.

1.2 The Meteorite Record

Throughout various planet formation processes in the Solar System, the chemistry of the protoplanetary disk and that of growing planetary bodies evolved both spatially and temporally. In order to understand this chemical evolution and how the terrestrial planets ended up with the their current compositions, a key tool that is used is detailed chemical analysis of meteorites, a central component in the field of cosmochemistry. Meteorites are rocky objects that come from different regions in the Solar System and eventually land on Earth. Most meteorites originate in the asteroid belt, although some come from the Moon, Mars and possibly comets from farther regions in

the Solar System. Meteorites can be broadly divided into two types. The first type are chondrites which come from undifferentiated parent bodies in the asteroid belt, meaning that they did not experience significant heating to cause the body to melt and separate into a core and mantle, and are similar to sedimentary rocks, composed of physical mixtures of accreted components. Chondrites are the most common type of meteorite, comprising ∼85% of the samples in our collections. The second type of meteorites derive from differentiated (or at least partially differentiated) parent bodies with compositions affected by prior melting and crystallization, and they can be further divided into achondritic meteorites, irons and stony irons. This second type of meteorites encompass ∼15% of the meteorites in our collection and come from the asteroid belt, the Moon and Mars (McSween & Huss 2010).

This thesis largely focuses on chondritic meteorites as they are the most abundant primitive rock samples that preserve the composition of aggregate material in the protoplanetary disk during planet formation. However, in the Conclusion, we discuss promising future avenues of study with achondritic meteorites.

Chondrites consist of the following components: chondrules, refractory inclusions, metals and sulfides, and matrix material. Chondrules, the main component of most chondrites, are mm-sized spherical inclusions that formed via flash heating at temperatures between 1770-2120 K and subsequently experienced rapid cooling and solidification (at rates from seconds to hours). Most chondrules are primarily made of olivine and/or pyroxene with some glass, and they come in two compositional types: Type I are FeO-poor and Type II are FeO-rich. Refractory inclusions in chondrites

encompass two types: calcium-aluminum-rich inclusions (CAIs) and amoeboid olivine aggregates (AOAs). CAIs are both the oldest components in chondrites and the oldest known objects that formed in the Solar System. They are composed of a variety of minerals (e.g., hibonite, perovskite, spinel) whose phases either condensed directly from the cooling gas of the solar nebula or crystallized from melts. AOAs are made of mostly forsterite and smaller amounts of Fe-Ni metal, are fine-grained and porous, and likely formed after CAIs. Metals and sulfides are another component of chondrites consisting of highly refractory siderophile elements (e.g., Ir, Os, Ru, Mo, W), metallic iron, and iron sulfide and are often found within CAIs, within or as rims on chondrules, and as metal grains. Lastly, matrix is an optically opaque mixture of fine-grained ($\sim$ 50-100 nm) minerals that fill the spaces between the other chondrite components and contain mixtures of silicates, oxides, sulfides, metal, phyllosilicates and carbonates (McSween & Huss 2010).

Chondrites are classified into clans that are further divided into groups based on their bulk chemical compositions and relative abundances of the different chondrite components. Each of the chondrite groups are further classified based on the degree to which the samples have been altered by processes that occurred after their formation (i.e., petrologic types). Based on chondrites' chemical compositions, they can be broadly divided into three clans: ordinary, enstatite, and carbonaceous chondrites. As the name suggests, ordinary chondrites are the most abundant type of chondrite and consist of three groups: H (high Fe), L (low Fe), and LL (even lower Fe). Enstatite chondrites are strongly chemically reducing (i.e., less oxygen), and therefore most of the iron in

these chondrites occurs as metal. Enstatite chondrites can be divided into two groups: EH (high iron metal) and EL (low iron metal). Lastly, carbonaceous chondrites, the focus of the meteorite samples studied in this thesis, consist of many different chemical groups: CI, CM, CR, CB, CO, CV, CK, CH. In general, carbonaceous chondrites contain more volatiles than the other chondrite clans, exhibiting a variety of chemical compositions, oxidation states and abundances of chondrite components. For example, CI chondrites have the closest chemical compositions to that of the solar photosphere, meaning that their compositions are relatively unmodified from the original composition of the solar nebula. CI chondrites contain no chondrules and have essentially unfractionated elemental abundances whereas CV and CO chondrites are more depleted in volatile elements, enriched in refractory elements, and contain a moderate proportion of chondrules (Weisberg et al. 2006).

In addition to classifying chondrites based on their chemistry, they are also identified according to their petrologic type which describes the degree to which chondrites have been modified by thermal metamorphism (i.e., heating) or aqueous alteration (i.e., reactions with water) processes on their parent bodies. The petrologic types range from 1 to 6, with 3 representing the least altered, any type lower than 3 indicating increasing degrees of aqueous alteration with decreasing petrologic type, and any type greater than 3 representing increasing degrees of thermal metamorphism with increasing petrologic type. Therefore, chondrites with petrologic type 1 are the most aqueously altered, and those with petrologic type 6 are the most thermally metamorphosed (Weisberg et al. 2006; McSween & Huss 2010).

Isotopes provide key insights into the formation reservoirs of the different chondrite clans. Based on isotopic measurements of the three chondrite types, we observe differences between the carbonaceous chondrites and the other two types (ordinary and enstatite chondrites). These differences are often referred to as the isotopic dichotomy, with ordinary and enstatite chondrites encompassing the non-carbonaceous (NC) chondrite group and the carbonaceous chondrites (CC) representing the other group. This dichotomy suggests that these two groups of meteorites derive from two genetically distinct reservoirs, with the NC reservoir located inside the orbit of Jupiter and the CC reservoir forming outside of the orbit of Jupiter (Kleine et al. 2020). Mixing between the NC and CC reservoirs due to Jupiter's migration can explain how we currently have both NC and CC materials in the asteroid belt and how both groups are found as meteorites on Earth.

One of the main ways to constrain the timescales and processes associated with planet formation in the early Solar System is through isotopic measurements of meteorites. Some of the main isotopic systems that are analyzed for meteorites to inform planet formation include long-lived radioactive decay systems (e.g., $^{238/235}$U-$^{207/206}$Pb) which provide absolute ages; short-lived nuclide systems (e.g., ^{26}Al-^{26}Mg) which constrain the relative timing of events in the early Solar System such as initial silicate melting on planetesimals; isotopic heterogeneity in noble gases that informs the timing of volatile accretion and loss during planet formation; and mass-dependent stable isotopic fractionation of light elements (e.g., H, C, O, S) to constrain the conditions and processes of planetary accretion (Halliday & Kleine 2006). In fact, the main way to

determine the age of the Solar System (∼4.567 Gyrs) is based on long-lived radioactive decay measurements of CAIs, the first formed solids in the solar nebula (Scott & Krot 2014; Connelly et al. 2012). Based on the short-lived nuclide ^{26}Al chronometer, chondrules also formed early in the Solar System (Nagashima et al. 2018).

In addition to isotopic systems, the bulk chemistry and elemental fractionation patterns of meteorites are also essential for understanding the various nebular and planetary processes that led to the current compositions of the terrestrial planets in the Solar System. Elemental fractionation provides insight into key processes such as evaporation and condensation, melting and crystallization, physical mixing, and changes in redox (i.e., electron distribution) conditions. Traditionally, meteorites have been assumed to be leftover planet building block materials and therefore used to understand the bulk compositions of the terrestrial planets. For example, by comparing chemical and isotopic properties (e.g., oxygen isotopes) of mantle rocks on Earth to those of various chondritic meteorites, prior studies have claimed that Earth accreted from predominantly enstatite chondrite material with smaller contributions of carbonaceous chondrite-like matter (Javoy 1995; Javoy et al. 2010; Lodders 2000). While Mars and asteroid 4 Vesta can be reproduced by mixtures of different meteorites, when considering a comprehensive set of chemical and isotopic properties (e.g., Mg, Si, Al abundances, oxygen isotopes), recent studies find that it is challenging to explain Earth's composition by combinations of known meteorite types alone (Mezger et al. 2020; Righter et al. 2006). As evidence, these studies cite the fact that the bulk silicate Earth is more depleted in moderately and highly volatile elements compared to chondritic meteorites,

and therefore there must be a major component that is not represented in our meteorite collections that contributed to Earth's accretion. A recent study by Sossi et al. 2022 suggests that Earth, and possibly Earth-like exoplanets, formed by stochastic accretion of many different bodies with variable compositions (Sossi et al. 2022). Despite the fact that the extent to which specific meteorite types, and chondrites in particular, contributed to Earth's accretion is still under debate, chondrites remain the only samples that preserve the composition of aggregate material in the protoplanetary disk and can be rigorously studied in the laboratory, so it is essential to understand their chemistry to inform the formation and evolution of rocky planets.

1.3 Origins of Rocky Planet Atmospheres

For the foreseeable future, atmospheres will be the main feature of rocky exoplanets that ground- and space-based telescopes can observe and study in depth via spectroscopy. Therefore, determining how rocky planets form their atmospheres is essential to understand their current compositions and what the compositions tell us about other features of these worlds. There are two main mechanisms by which planets obtain an atmosphere. The first type of atmospheres are primary atmospheres that form by capturing H_2-rich gases from the stellar nebula. This nebular ingassing process is the predominant way that gas giant planets, such as Jupiter and Saturn, acquire their atmospheres. The other kind of atmospheres are commonly referred to as secondary atmospheres which form via outgassing of volatile species during and after planetary accretion. While atmosphere formation for the gas giant planets is dominated by the

first mechanism, the process is more complicated for smaller worlds. If a rocky protoplanet can accrete enough mass before the gas in the protoplanetary disk dissipates, then nebular ingassing can contribute to the early atmosphere formation for such a planet. However, multiple factors can cause a rocky planet to lose those nebular ingassed volatiles early in its history. For example, a terrestrial planet may not be able to retain significant primary atmospheres due to its low planetary gravity, large impact events, and high levels of extreme-ultraviolet and X-ray radiation from the young host star (Lammer et al. 2018; Schlichting & Mukhopadhyay 2018). As a result, terrestrial planets likely form their atmospheres predominantly via the second mechanism, outgassing of volatiles during and after planetary accretion (Elkins-Tanton & Seager 2008).

Volatile elements (e.g., H, C, O, N, S) are the dominant constituents of the terrestrial planet atmospheres in the Solar System and are the main elements considered in this thesis. Understanding the sources of volatiles and their distribution during planet formation is currently a key area of study both in Solar System science and exoplanet science, especially with burgeoning observational studies of protoplanetary disks over the last several decades (Andrews 2020). As with the other elements and isotopic compositions discussed in the prior section, chondritic meteorites have been assumed to compositionally represent the source material that delivered volatile elements to the Solar System's terrestrial planets. However, there is currently a debate as to whether or not the Solar System's terrestrial planets could have acquired their volatiles through materials with compositions like those of known chondritic meteorites alone, and if so,

what types of chondrites played the most important role. While some studies have claimed that the Solar System's terrestrial planets accreted their volatiles from various mixtures of chondrites (e.g., Lodders (2000); Piani et al. (2020)), others find that the terrestrial planets must have, to some degree, formed out of material that is unsampled by meteorites (e.g., Burkhardt et al. (2021); Sossi et al. (2022)). Therefore, there is still more theoretical and experimental work to be done to determine what materials supplied volatile elements to Earth and other terrestrial planets in the Solar System. Nevertheless, chondritic meteorites are still important samples to study as they are the only samples that provide a chemical record of the nebular and planetary processes that took place during planet formation, contain volatile elements, and are available for rigorous laboratory study.

The fact that outgassing is a central process controlling terrestrial planet atmosphere formation and evolution indicates that the atmospheres of these worlds are strongly connected to their interiors (Elkins-Tanton & Seager 2008). Planetary outgassing has been modelled for the Solar System's terrestrial planets and also for some rocky exoplanets. For example, there has been extensive work on simulating outgassing during Earth's and other terrestrial planets' early histories, particularly during the magma ocean phase, which occurs when a rocky planet's surface is completely or partially molten (Lammer et al. 2018; Zahnle et al. 1988; Gaillard & Scaillet 2014; Schaefer & Fegley 2010; Herbort et al. 2020). Based on geochemical studies of Earth and other rocky bodies in the Solar System and models of planetary accretion, many rocky planets likely had a partially or completely molten magma ocean phase in their early evolution

due to the high degree of heating experienced during planet formation (Elkins-Tanton 2012; Schaefer & Elkins-Tanton 2018). Magma ocean models have been able to reproduce the observable properties of Earth, Moon and Mars (e.g., mantle composition and oxidation state) (Schaefer & Elkins-Tanton 2018). Prior to a planet's magma ocean phase, outgassing is also an important mechanism by which planetesimals can lose volatiles, influencing their final volatile inventories and those of the rocky planets into which they form. Similarly, once a planet's magma ocean has solidified, outgassing can continue to be a dominant mechanism throughout the planet's evolution, replenishing the atmosphere through various tectonic activities (e.g., volcanism).

Despite the great progress in simulating outgassing for the terrestrial planets in the Solar System, we still lack a first-principles understanding of how to connect a rocky planet's bulk composition to its early atmospheric properties. An important step towards establishing this connection is by studying the outgassing compositions of a compositionally diverse set of materials over a range of temperatures, pressures and redox states. A key aspect of this thesis is to provide new ground-truth measurements of the outgassing compositions of chondritic meteorite samples to inform this connection between rocky planet interiors and atmospheres and to provide constraints on the parameter space of plausible initial atmospheric compositions for these worlds. This work is described in Chapters 2 and 3, which are published as "Composition of terrestrial exoplanet atmospheres from meteorite outgassing experiments," Thompson et al. (2021) in *Nature Astronomy* and "Outgassing composition of the Murchison meteorite: Implications for volatile depletion of planetesimals and interior-atmosphere connections for

terrestrial exoplanets," Thompson et al. 2023 currently under review at *The Planetary Science Journal*, respectively.

1.4 Searching for Signs of Life on Rocky Exoplanets

In the coming decades, one of the main scientific endeavors will be to search for signs of life on rocky, potentially habitable exoplanets (Harrison et al. 2021). The first step towards this goal is to assess a planet's habitability, a measure of its potential to support life. At present, a defining feature of a habitable planet is that it is capable of supporting stable liquid water on its surface (Schwieterman et al. 2018; Kopparapu et al. 2020). With this criterion, a common first-order means of identifying plausibly habitable worlds is to search for planets in the Habitable Zone (HZ), the range of distances around a star that permit a planet with an atmosphere to maintain surface liquid water (Schwieterman et al. 2018). Planets in the HZ can be quickly identified if the semimajor axis of its orbit and the luminosity of its host star are known. However, a complete assessment of planetary habitability involves understanding the interplay among many other factors, both stellar and planetary, such as instellation of the host star, orbital architecture and dynamics of the planetary system, atmospheric composition and properties (e.g., greenhouse gases, atmospheric escape, volatile inventory), planetary tectonic regime, and surface-atmosphere and surface-interior feedback effects (Kopparapu et al. 2020). It is essential to utilize as complete a set of these factors affecting planetary habitability that are observable with current and upcoming instruments to ensure that potential signs of life on rocky exoplanets are properly interpreted.

Multiple studies have determined initial estimates for the occurrence rate of potentially habitable planets (i.e., likely rocky worlds in the HZ of their host stars) (e.g., Petigura et al. (2013a); Mulders et al. (2018); Foreman-Mackey et al. (2014); Stark et al. (2019)). For example, a recent study that compiled estimated occurrence rates determined that the fraction of F, G, K stars that have at least one planet in the HZ (i.e., $\eta_{\rm Earth}$) is ∼0.24 (Stark et al. 2019). For M dwarf stars, Dressing & Charbonneau calculated that $\eta_{\rm Earth}$ could be between ∼0.16 - 0.24 depending on the assumptions about the width of the HZ (Dressing & Charbonneau 2015). As more exoplanet systems are discovered and characterized over the next several decades with missions like NASA's Transiting Exoplanet Survey Satellite and the James Webb Space Telescope, we will have a larger statistical sample from which to make more robust $\eta_{\rm Earth}$ estimates.

One of the biggest challenges to searching for life on rocky exoplanets is that our present knowledge of the possible diversity of biochemistries that may exist on these worlds is severely limited to a sample size of 1. As a result, our understanding of life's requirements is confined only to our knowledge of life on Earth. Based on this, essential components for life include an energy source, a supply of elements that can form molecules with a diversity of shapes and properties, a solvent to support the synthesis and interaction of these molecules, and the physical and chemical conditions to support the molecules and interactions that biochemistry needs (Hoehler et al. 2020). For Earth, light and redox chemical energy provide the energy source, the necessary elements include carbon, hydrogen, nitrogen, oxygen, phosphorus and sulfur (i.e., the biogenic elements) and metals, liquid water is the solvent, and a variety of environmental

parameters provide the required conditions for biochemical interactions. As evolution is a central aspect of life on Earth, another useful definition comes from Schrödinger, stating that life is a non-equilibrium system that utilizes free energy and contains instructions for its own self-replication which, in turn, is a prior for Darwinian evolution (Schrödinger 1944; Krissansen-Totton et al. 2022). As we seek to identify signs of life on exoplanets, it is important to generalize our understanding of life's requirements and the ways in which life can modify a planet's environment.

Since atmospheres will be the primary observable features of these worlds for the foreseeable future, one of the main ways to detect signs of life is to search for "biosignatures," chemical and/or physical indications of present or past forms of life, in planetary atmospheres. It is important to note that, at present, all proposed biosignatures are only *potential* biosignatures. Therefore, it is necessary to evaluate the planetary context for which such potential biosignatures are the most compelling signs of present or past biological activity and to identify the cases in which such potential biosignatures are instead false positives and generated by abiotic processes. The focus of this thesis is on gaseous biosignatures that are either direct or indirect products of metabolism in a planet's atmosphere, although there are also surficial and temporal biosignatures (Schwieterman et al. 2018).

The most commonly discussed biosignature gas for exoplanet studies is O_2 and its photochemical by-product O_3 (Meadows et al. 2018). The case for O_2 as a biosignature stems from the fact that on Earth it is produced predominantly from oxygenic photosynthesis, and O_3 is subsequently created via photochemical reactions

involving O_2 in Earth's stratosphere (Schwieterman et al. 2018). Due to the prevalence of its energy source (i.e., light) and basic substrates (i.e., CO_2 and H_2O), oxygenic photosynthesis may be one of the most productive metabolisms on exoplanets. O_2 and O_3 are also promising biosignatures due to their detectability, having strong absorption features in the visible and near-infrared, and ultraviolet, visible, near- and mid-infrared parts of the spectrum, respectively (Schwieterman et al. 2018). However, in order for O_2 to accumulate in an atmosphere, some of the organic matter that is produced via photosynthesis must be sequestered from the atmosphere (e.g., through various burial mechanisms). In addition, recent studies have investigated the potential for abiotic processes to generate significant levels of atmospheric O_2 on simulated exoplanets around different types of host stars and under various planetary evolution scenarios (e.g., Luger & Barnes (2015); Wordsworth & Pierrehumbert (2014); Hu et al. (2020); Krissansen-Totton et al. (2021)). These studies illustrate the importance of accounting for a planet's entire planetary and astrophysical context when evaluating biosignatures. Other biosignature gases that have been proposed include N_2O, CH_4, CH_3Cl, C_2H_6, and NH_3 (Schwieterman et al. 2018).

In addition to evaluating individual biosignature gases, it is important to consider the coexistence of multiple gases as biosignature pairs or groups. Atmospheric chemical disequilibrium is a more generalized framework for detecting biosignature groups. The argument for chemical disequilibrium as a biosignature comes from Earth, which has the largest thermodynamic chemical disequilibrium of all Solar System rocky planets that have significant atmospheres due to the presence of life (Lovelock 1975;

Krissansen-Totton et al. 2016, 2018b). Based on modern Earth's atmosphere, two proposed disequilibrium biosignature groups include the simultaneous presence of O_2 and CH_4 and the coexistence of N_2, O_2 and liquid H_2O as opposed to the more thermodynamically stable nitrate. Another promising disequilibrium biosignature pair is CO_2 and CH_4, as these two species are at the opposite ends of the redox spectrum for carbon which has implications for how both species can be generated simultaneously via abiotic processes alone (Krissansen-Totton et al. 2018b). This biosignature pair will be discussed in more detail in Chapter 4.

Understanding the planetary context for biosignature gases often requires investigating how life and the atmosphere coevolved throughout Earth's history. Although there is currently only one planet known to host life, each of Earth's geological periods encompasses a particular set of atmospheric oxidation states and compositions along with biosphere properties. Each of these eons provides an analog for a potential biogeochemical state of a terrestrial, habitable exoplanet and can inform the planetary context for biosignatures and their potential false positive/negative scenarios. For example, the Earth during the Archean eon (4.0-2.5 Ga) prior to the rise of oxygenic photosynthesis contained detectable levels of the disequilibrium biosignature pair, CO_2 and CH_4, in the atmosphere and serves as an anoxic biosphere template for oxygen-poor, habitable-zone planets (Krissansen-Totton et al. 2018a,b). In addition, for O_2, the delay between the start of oxygenic photosynthesis on Earth at $\sim$3.0 Ga and the rise of atmospheric O_2 to detectable, modern levels during the late Proterozoic ($\sim$800 Ma) demonstrates a false negative scenario in which life was present but this biosignature gas was not detectable

yet due to various factors of the planetary environment that are still being determined (Planavsky et al. 2014; Reinhard et al. 2016; Schwieterman et al. 2018). The evolution of Earth's biogeochemical state through time provides an invaluable window to uncover the complex interplay between geological and biological processes which must be understood to create realistic models of terrestrial planet evolution and interpret observations of potentially habitable worlds.

In order to comprehensively evaluate potential biosignatures in the atmosphere of a terrestrial exoplanet, its entire planetary and astrophysical context must be considered. This thesis focuses on the planetary context for atmospheric CH_4 to be a compelling biosignature gas in the era of JWST. This work is described in Chapter 4 and is published in *The Proceedings of the National Academy of Sciences* as "The case and context for atmospheric methane as an exoplanet biosignature," Thompson et al. (2022).

Chapter 2

Composition of Terrestrial Exoplanet Atmospheres from Meteorite Outgassing Experiments

2.1 Introduction

We are at the dawn of an exciting technological era in astronomy with new large-aperture telescopes and advanced instrumentation, both in space and on the ground, leading to major advances in exoplanet characterization. To optimize the use of these new facilities, we need suitable theoretical models to obtain a better understanding of the diversity of exoplanet atmospheres. Statistical studies using NASA's *Kepler*

mission data suggest that terrestrial and other low-mass planets are common around G, K and M stars (Petigura et al. 2013b,a; Dressing & Charbonneau 2015). Given the large number of current and anticipated low-mass exoplanet discoveries, the next phase in exoplanet science is to characterize the physics and chemistry of their atmospheres. For the foreseeable future, Solar System meteorites provide the only direct samples that can be rigorously studied in the laboratory to gain insight into the initial atmospheric compositions of these planets.

Although gas giant planets, like Jupiter and Saturn, form primary atmospheres by capturing gases from the stellar nebula, atmosphere formation for low-mass planets is more complicated. While nebular ingassing can contribute to early atmosphere formation if a protoplanet accretes enough mass before the gas disk dissipates, several factors can result in loss of nebular volatiles early in the planet's history (Sharp 2017; Schlichting & Mukhopadhyay 2018; Wu et al. 2018). For instance, terrestrial planets' inability to retain significant primary atmospheres can be due to low planetary mass, large impactors and high EUV and X-ray flux from young host stars (Lammer et al. 2018). Instead, low-mass planets likely have secondary atmospheres which form via outgassing of volatiles during and after planetary accretion (Elkins-Tanton & Seager 2008). The Solar System's terrestrial planets are believed to have formed by accretion of planetesimals that have compositions similar to chondritic meteorites, which are a likely source of atmospheric volatiles for such planets (Ahrens et al. 1989; Lammer et al. 2018). As a result, an important step towards establishing the connection between terrestrial planets' bulk compositions and their atmospheres is to directly measure the

outgassed volatiles from meteorites.

While meteorites come in a wide variety with a range of volatile contents, they can be classified into three main types: chondrites, achondrites and irons. Chondrites are stony meteorites that come from undifferentiated planetesimals composed of aggregate material from the protoplanetary disk, while achondrites and iron meteorites have melted and derive from partially or fully differentiated planetesimals. Both chondrites and achondrites likely contributed to forming the Sun's terrestrial planets (Lammer et al. 2018). Our study focuses on CM-type carbonaceous chondrites because their compositions provide a strong match to that of the solar photosphere, second only to CI-type chondrites, so they serve as representative samples of the bulk composition of material in the solar nebula during planet formation. While planet formation alters planetesimals through various thermal and differentiation processes, carbonaceous chondrite-like material was a likely source of volatiles for the terrestrial planets, and CM chondrites are among the most volatile-rich of remnant materials, making these samples well-suited for studying initial outgassed atmospheres (Lodders & Fegley 1998; Wasson & Kallemeyn 1988).

Planetary outgassing has been modeled both for the Solar System's terrestrial planets and for some low-mass exoplanets. Many prior studies have focused on outgassing during a planet's magma ocean phase and Earth's early degassing history, with several models investigating the outgassing composition from meteorites (e.g., (Zahnle et al. 1988; Lammer et al. 2018; Gaillard & Scaillet 2014; Schaefer & Fegley 2010; Herbort et al. 2020)). Currently, however, there is limited experimental data to constrain

these models and, in particular, none to inform meteorite outgassing studies. Prior experiments that heated meteorites were limited in several key ways due to restrictions in the number and type of samples used, the temperatures to which the samples where heated, and the number of gas species that were accurately measured (e.g., Court & Sephton (2009); Gooding & Muenow (1977); Lange & Ahrens (1982); Burgess et al. (1991); Springmann et al. (2019)), while this study measures many of the dominant outgassing species across a temperature range relevant for terrestrial planet atmospheres for multiple meteorite samples. In addition, some studies shocked samples prior to analyzing their volatile species so they do not properly simulate outgassing conditions from bulk chondritic material (e.g., Tyburczy et al. (1986)), while other studies focused on either a small subset of volatiles or trace metals and other volatile elements that are not major constituents of rocky planet atmospheres (e.g., Ikramuddin et al. (1977); Court & Sephton (2009); Springmann et al. (2019), see "Comparison with Prior Studies" in Methods). As a result, these studies are unsuitable for validating outgassing models for terrestrial planets. Therefore, to inform the initial composition of terrestrial planet atmospheres, we have designed an experimental procedure to directly measure by mass spectrometry a large set of the major outgassed species (e.g., H_2O, CO_2) from diverse meteorites over a wide temperature range.

For this study, three chondrites are analyzed: Murchison, Jbilet Winselwan and Aguas Zarcas. Murchison was observed to fall in Australia in 1969 (Krinov 1969); Jbilet Winselwan was collected in Western Sahara in 2013 (Ruzicka et al. 2015); and Aguas Zarcas fell in Costa Rica in 2019 (Soto et al. 2019). We minimized terrestrial

contamination and weathering effects by ensuring that none of our samples have fusion crust, which is altered during atmospheric entry; by using two fall samples which are minimally altered by terrestrial contamination; and by significantly reducing the majority of adsorbed species on the samples (see Methods).

Our experimental set-up consists of a furnace connected to a residual gas analyzer (RGA) mass spectrometer and a vacuum system. This system heats samples at controlled rates (up to 1200 °C) in a high-vacuum environment ($\sim 10^{-4}$ Pa (10^{-9} bar) at lower temperatures and $\sim 10^{-3}$ Pa (10^{-8} bar) at higher temperatures) and measures the partial pressures of up to 10 volatile species made up of hydrogen, carbon, nitrogen, oxygen and sulfur. For each of our experiments, a sample was heated in an open crucible (and thereby open to mass loss) from 200 to 1200 °C (475-1475 K) at a rate of 3.3 °C/minute and the partial pressures of the outgassing molecular species were continuously monitored using the RGA. The results from these experiments are expressed in three major forms. The first two are the instantaneous partial pressures (p_i, for species i) and mole fractions ($\chi_i = \frac{p_i}{p_{\text{Total}}}$, for species i where $p_{\text{Total}} = \sum_i p_i$, and see Methods (e.g., Equation 3) for elemental mole fractions) of outgassed volatiles as a function of temperature. The third is relative abundances of outgassed volatiles from each sample, reported as partial pressures normalized to the total pressure of released gases summed over temperature, $P_{i,\text{Total}} = \frac{\sum_T p_i}{\sum_T p_{\text{Total}}}$, for species i, and for elemental abundances $P_{j,\text{Total}} = \frac{\sum_T p_j}{\sum_j (\sum_T p_j)}$, for element j (i.e., H, C, O, N, and S).

The RGA measures the partial pressures of 10 selected species according to their molecular masses, assuming species are singly ionized (i.e., the mass-to-charge

ratio equals the molecular mass): 2 amu (H_2), 12 amu (carbon), 14 amu (nitrogen), etc. The signals for each of the species tracked during the outgassing experiments have been corrected for ion fragments and the possibility of terrestrial atmospheric adsorption and contamination using a set of linear equations. This approach also accounts for the background signal (Figure 2.5) In addition, since the masses of several molecules overlap, we developed a method to address these degeneracies (see Methods). An alternative approach to correct for ion fragments using a least squares regression produces generally similar results (see Methods, Table 2.5 and Figure 2.6).

2.2 Results

Tables 2.1 and 2.2 report the relative abundances of outgassed volatile species and elements from the three chondrites. We analyzed samples of Jbilet Winselwan twice under identical conditions to test the reproducibility of our experimental procedure, so its final reported relative abundances are given by the mean and 95% confidence interval of the mean of the two analyses (see Methods and Figure 2.7). As shown in Table 2.1, we find that H_2O has the largest relative abundance ($\sim$66$\pm$11 %) for all the meteorite samples followed by CO ($\sim$18$\pm$8 %), CO_2 ($\sim$15$\pm$5 %), and H_2 ($\sim$1$\pm$1 %) (see Figure 2.8). The signal at 34 amu has a lower relative abundance while the signals at 12, 14, 16, 32, and 40 amu along with N_2 have relative abundances that are effectively 0 (see Methods). In terms of the elemental abundances in Table 2.2, hydrogen has the highest concentration ($\sim$48$\pm$5 %) followed by oxygen ($\sim$41$\pm$2 %), carbon ($\sim$12$\pm$4 %), and sulfur ($\sim$0.03$\pm$0.02 %), averaged across all three samples (uncertainties reported as

the 95% confidence interval).

Table 2.1: **Total mass of volatile species released (in g) and relative abundances (in %) of outgassed species summed over temperature for the three CM chondrite samples.** Abundances are in partial pressures normalized to the total pressure of all released gases measured summed over temperature and are reported as percentages. The species corresponding to each mass number is in parentheses. The uncertainties reported for Jbilet Winselwan are the 95% confidence intervals of the means. Since some species have overlapping mass numbers (e.g., S and O_2), we provide a detailed description of the calculations made in determining these relative abundances in Methods.

	Murchison	Jbilet Winselwan	Aguas Zarcas
Total Gas Mass	5.00×10^{-4} g	$5.50\pm1.50 \times 10^{-4}$ g	8.00×10^{-4} g
2 amu (H_2)	0.20	1.27±15.64	1.38
12 amu (C)	0.0	0.0	0.0
14 amu (N)	0.0	0.0	0.0
16 amu (CH_4/O)	0.0	0.0	0.0
18 amu (H_2O)	71.62	61.30±33.73	65.02
28 amu (CO)	13.45	19.90±15.74	20.50
28 amu (N_2)	0.0	0.0	0.0
32 amu (S/O_2)	0.0	0.0	0.0
34 amu (H_2S)	0.05	0.11±0.40	0.11
40 amu (Ar)	0.0	0.0	0.0
44 amu (CO_2)	14.67	17.43±34.03	12.98

We expect the three CM chondrite samples to have similar outgassed abundances given their similar bulk compositions which are within 20 mg/g for most volatile elements (Table 2.4). Our experimental results confirm this prediction with the relative abundances for each species across the three samples being within 3σ of each other. Figure 2.1 shows the mole fractions of the measured volatile species as a function of temperature from each of the three meteorite samples. Several differences to note between the three meteorites are that Murchison has larger water but smaller CO outgassed abundances compared to Winselwan and Aguas Zarcas. In addition, Aguas Zarcas has a larger CO abundance but smaller CO_2 abundance than Murchison and Winselwan. Fig-

Table 2.2: **Relative outgassed atomic abundances (in %) summed over temperature of hydrogen, carbon, oxygen, nitrogen and sulfur for the three samples.** As in Table 2.1, abundances are in partial pressure normalized to the total pressure of all released gases measured and are reported as percentages. The uncertainties reported for Jbilet Winselwan are the 95% confidence intervals on the means. Comparison between the initial (pre-degassing) normalized atomic abundances for average CM chondrites and the outgassed normalized atomic abundances are shown, both reported as percentages (bottom two rows). These atomic abundances are normalized to the sum of the elements measured in the experiments, i.e., H, C, O, N, S. The uncertainties for the pre-degassing normalized atomic abundances are (1σ) standard deviations. The uncertainties for the outgassed quantities are expressed as the 95% confidence intervals of the means. The initial bulk atomic abundances of CM chondrites come from the literature (Nittler et al. 2004; Alexander et al. 2012).

Sample	Total H	Total C	Total O	Total N	Total S
Murchison	50.20	9.82	39.96	0.0	0.02
Jbilet Winselwan	44.95±35.69	13.39±17.86	41.62±17.97	0.0	0.04±0.14
Aguas Zarcas	47.83	12.04	40.09	0.0	0.04
Initial* Bulk CM Abundance	28.81±0.44	4.07±0.67	64.37±0.12	0.18±0.05	2.58±0.70
Outgassed CM Abundance	47.66±5.33	11.75±3.65	40.55±1.88	0.0	0.03±0.02

*Pre-degassing

ure 2.2 shows the relative abundance ratios for the three samples as a function of temperature, which can inform the chemistry of the initial atmospheres. The mean outgassed carbon-to-oxygen, hydrogen-to-carbon, sulfur-to-oxygen and hydrogen-to-oxygen ratios summed over temperature for the three chondrite samples are 0.29±0.08, 4.15±1.80, 0.0008±0.0006, and 1.18±0.18, respectively (uncertainties reported as the 95% confidence interval), with abundance ratios for the three chondrites within 2σ of each other.

The average C/O, H/C, S/O and H/O ratios for the initial bulk CM chondrite composition are 0.06±0.01, 7.09±1.18, 0.04±0.01, and 0.45±0.01, respectively (Nittler et al. 2004; Alexander et al. 2012). These initial bulk elemental abundances represent the volatile outgassing inventory for a planet that is outgassing predominantly CM chondrite-like material (Table 2.2). By comparing the outgassed and bulk CM chondrite

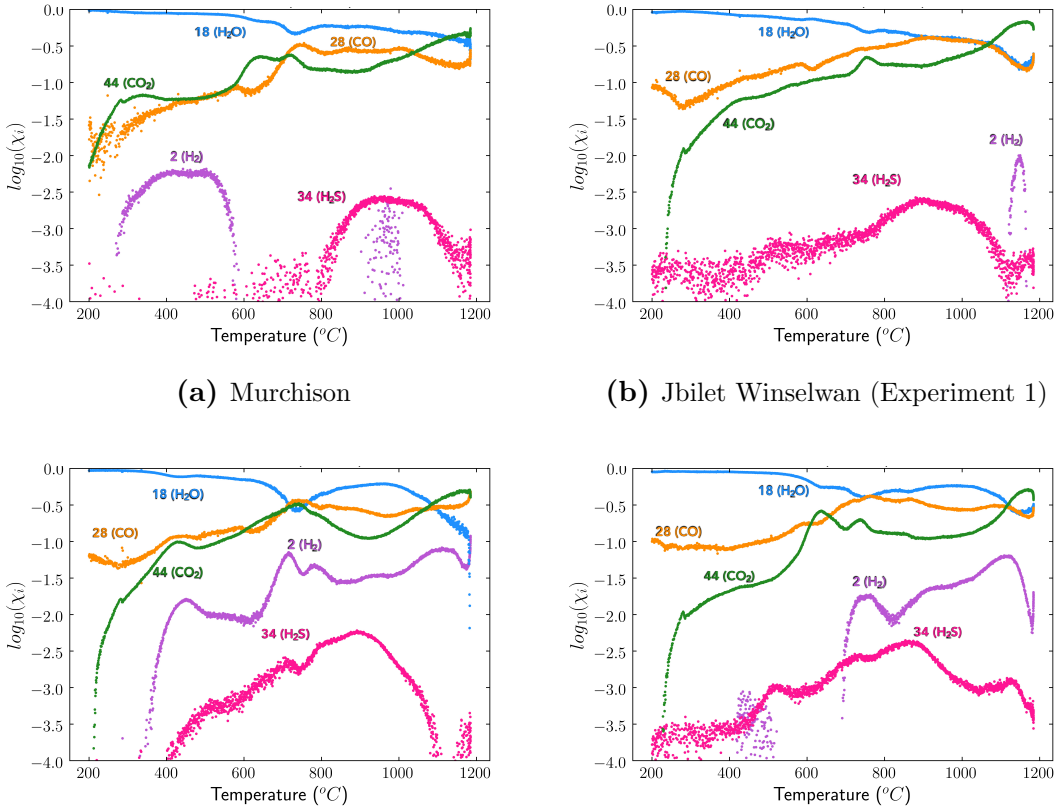

(a) Murchison

(b) Jbilet Winselwan (Experiment 1)

(c) Jbilet Winselwan (Experiment 2)

(d) Aguas Zarcas

Figure 2.1: **Mole fractions of the measured species outgassed as a function of temperature for each chondrite sample**. The results are for 3 mg samples of (a) Murchison, (b) and (c) Jbilet Winselwan, and (d) Aguas Zarcas. We analyzed two 3 mg samples of Jbilet Winselwan under identical conditions to test reproducibility and show the results in (b) and (c). H_2 has the largest variation between the two experiments with Jbilet Winselwan. Across the three samples, some species exhibit major variations in their relative abundances over specific temperature intervals. For instance, CO and CO_2's abundances increase around 650 - 750 °C. Although the mole fraction of H_2S varies considerably over the entire heating range, it peaks near ∼900-1000 °C and then decreases at higher temperatures for all three chondrites. For most samples, there is a prominent increase in H_2's abundance near ∼1100 °C.

abundance ratios, we find that, aside from the S/O ratios, the outgassed and bulk ratios are within an order of magnitude of each other. The C/O and H/O outgassed ratios are larger than the bulk ratios, which is likely due to the fact that many of the phases that host carbon and hydrogen (e.g., phyllosilicates, organics and carbonates) readily

break down upon heating whereas a significant portion of the oxygen is in phases that do not easily decompose (e.g., forsterite and CaO). On the other hand, the H/C and S/O ratios are smaller than the bulk ratios, with the largest difference between the outgassed and bulk S/O ratios. This may be due to the fact that models predict that S_2 and SO_2 should also outgas in this temperature range but we only measure H_2S due to the RGA's 10-species limit.

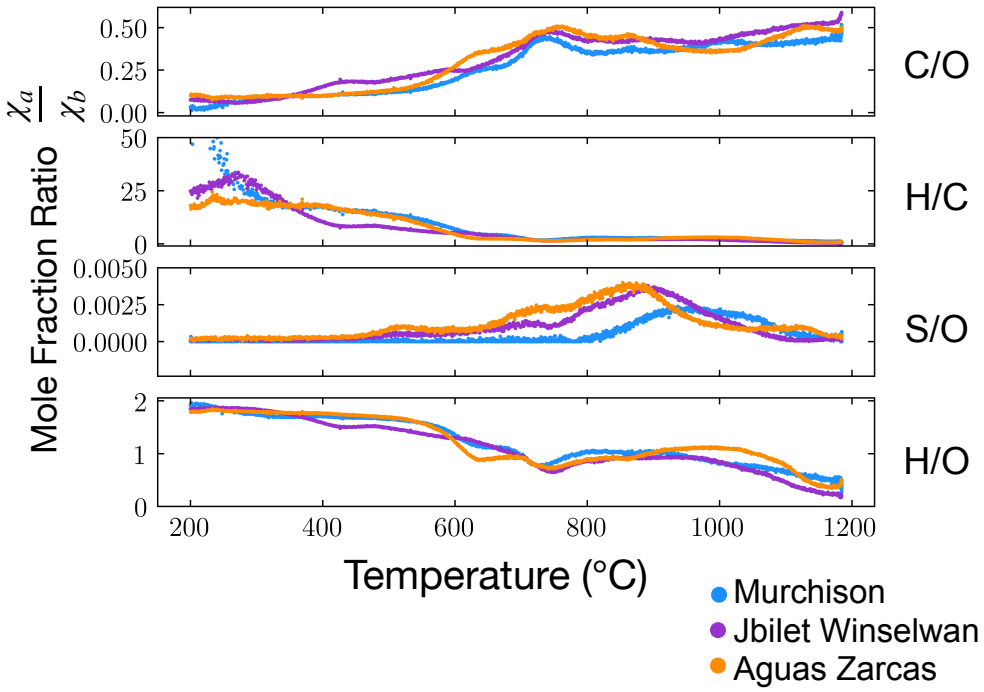

Figure 2.2: **Ratios of mole fractions of outgassed bulk elements hydrogen, carbon, oxygen, and sulfur as a function of temperature for the three chondrite samples.** From top to bottom the ratios are: carbon/oxygen, hydrogen/carbon, sulfur/oxygen and hydrogen/oxygen. Blue, purple and orange curves represent elements outgassed from Murchison, Winselwan, and Aguas Zarcas, respectively.

There are several major similarities between the results from our experiments

(Figure 2.3 (b, d)) and those from the equilibrium calculations (Figure 2.3 (a, c)). For instance, water is the dominant outgassed species over almost the entire temperature range for both experimental and theoretical methods, with the average mole fraction being 0.6 and 0.4 for the experiments and theoretical models, respectively. In addition, CO and CO_2 constitute significant fractions of the vapor phase over the temperature range. In particular, for the Murchison sample, the experimental and theoretical outgassing trends for CO_2 and CO generally match with CO_2 outgassing more at the lowest ($\sim$300 °C) and highest temperatures ($\sim$1100 °C), and CO outgassing more at intermediate temperatures ($\sim$800-1000 °C). In addition to the experimental results, we calculated 'equilibrium-adjusted' abundances using the equilibrium model to re-compute gas speciation based on the experimental abundances at intervals of 50 °C (dashed curves Figure 2.3 (b, d)). Generally, the 'equilibrium-adjusted' experimental H_2O and CO_2 abundances provide a better match to the equilibrium model results, and the CO abundance provides a better match at higher temperatures. On the other hand, the other significant outgassing species (H_2 and H_2S) did not exhibit an improved match compared to the experimental results, although the equilibrium-adjusted H_2 abundance is much larger compared to the experimental H_2. Although our experiments monitor signals at 12 amu (carbon), 14 amu (nitrogen), 16 amu (CH_4/O) and 40 amu (Ar), once we correct for ion fragments and atmosphere adsorption, we do not detect significant amounts of these species, also matching chemical equilibrium calculations (see Methods).

There are also significant differences between the experimental and theoretical results. For instance, although H_2S mole fractions reach similar maxima of $\sim$1E-3,

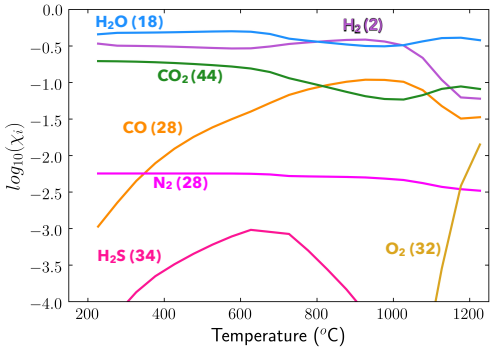

(a) Theoretical Equilibrium Results for Average CM Chondrite Composition

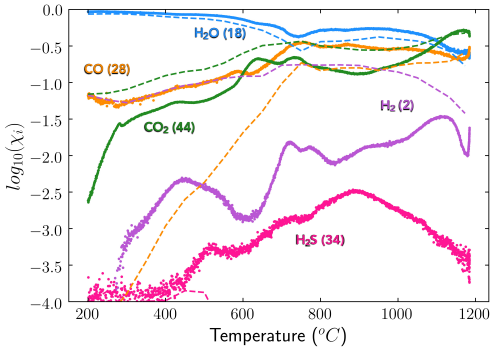

(b) Experimental Results for Average of 3 CM Chondrite Samples

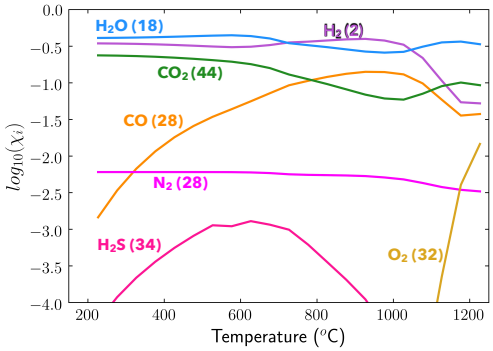

(c) Theoretical Equilibrium Results for Murchison

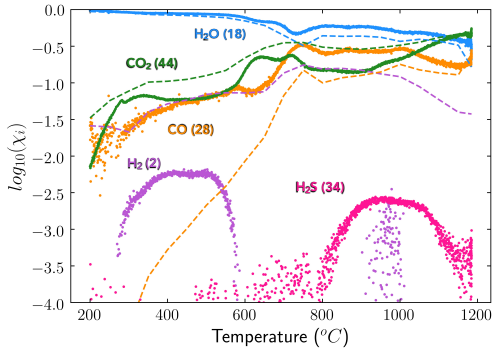

(d) Experimental Results for Murchison Sample

Figure 2.3: **Comparison between equilibrium calculations (left) and experimental results (right) under the same pressure and temperature conditions.** Figures (a) and (b) illustrate outgassing abundances calculated assuming chemical equilibrium for an average CM chondrite bulk composition at 1E-3 Pa (a) and experimental outgassing results for the average of the three CM chondrite samples measured at 1E-3 Pa (b). In (b), each species' curve is dominated by the sample that has the most abundant amount of that species at a given temperature. Figures (c) and (d) show the results for outgassing from a Murchison composition using chemical equilibrium calculations (c) and experimental outgassing results from the Murchison sample (d). The dashed curves in (b) and (d) show 'equilibrium-adjusted' experimental abundances in which the equilibrium model was used to recalculate gas speciation using the experimental abundances at intervals of 50 °C. The mass (in amu) of each species is in parentheses. See Figure 2.9 for other volatile species that theoretically degas with mole fractions above 1×10^{-4} according to chemical equilibrium calculations but are not measured in the experiments.

the peak is displaced from ~600 °C in the theoretical calculations to ~950 °C in the experiments. This offset may be due to the fact that, in carbonaceous chondrites, sulfur can occur as gypsum (a sulfate mineral, $CaSO_4H_2O$) which breaks down at 700 °C and the corresponding phase change for sulfur gas may be kinetically inhibited, causing it to outgas at higher temperatures (O'Brien & Nielsen 1959). Preliminary X-ray diffraction (XRD) analyses carried out in our lab indicate that gypsum may be breaking down during the experiments (see Methods section on solid phases). However, the equilibrium models do not show gypsum being in a solid phase, which may explain the mismatch in outgassing trends of H_2S. In addition, iron sulfide (FeS) and tochilinite ($2Fe_{0.9}S*1.67Fe(OH)_2$), which are known to be in carbonaceous chondrites, may decompose and contribute to the outgassed H_2S (Zhao et al. 2011; Gooding & Zolensky 1987). The 'equilibrium-adjusted' H_2S abundances are much lower than both the model and experimental results, further supporting H_2S production being kinetically inhibited. Another significant difference is the experiments' absence of N_2 gas which does not match equilibrium models that show outgassing over the entire temperature range. The primary reason the experimental N_2 abundance is negligible is due to the atmospheric adsorption correction we apply to account for the possibility of contaminated N_2 gas from Earth's atmosphere being adsorbed by the samples (see Methods). Without this correction, the measured N_2 outgassing varies from moderate levels consistent with theoretical models (i.e., average mole fractions of ~5E-2) to negligible amounts, depending on the sample being investigated.

Several other differences between experimental outgassing and equilibrium

model results lack complete explanations. For example, the second most abundant volatile species predicted to outgas over most temperatures in equilibrium models is H_2 with maxima mole fractions of ∼0.4, but our experimental results indicate an order of magnitude lower average H_2 mole fractions near ∼0.03. While the cause for much lower experimental H_2 abundance is uncertain, it may be due to the fact that our experiments do not allow sufficient time for some gas-gas reactions to take place that could raise the H_2 abundance, as equilibrium is reached between H_2O and H_2. The 'equilibrium-adjusted' H_2 abundances are larger than the experimental results, pointing to a likely disequilibrium for gas phase reactions in the experiments. By comparing gas-gas reaction rates to the experiment's vacuum pumping rate, we conclude that these species likely do not have sufficient time to reach chemical equilibrium (see Methods). In addition, the H_2 background signals are large relative to the samples' signals, so over-subtraction of the background signal could also explain the lower abundance. Finally, our experiments do not detect a significant amount of outgassed species with mass number 32 amu after correcting for the possibility of contaminated terrestrial atmospheric adsorption of O_2 (see Methods). In the chemical equilibrium calculations, O_2 should only begin outgassing significantly at the highest temperatures (∼1100 °C). As described further in Methods, an alternative data analysis technique using least-squares fitting produces non-zero yields of CH_4, which is not predicted to outgas based on equilibrium models (Figure 2.6, Table 2.5). It is possible that our original analysis (see Equations 4-15 in Methods) applies an overly conservative correction to CH_4's abundance, and further investigation is required to confirm if CH_4 is indeed outgassing

from the samples.

Oxygen fugacity (f_{O_2}) represents the chemical potential of oxygen in a system which affects its gas chemistry and may be equated to the partial pressure of oxygen in a gas phase under low pressure and near-ideal gas conditions such as present in these experiments. Our instrument set-up does not allow equilibrium to be achieved, especially at lower temperatures, because many gas species do not have sufficient time to interact since their mean collision time is either comparable to or longer than the vacuum system's evacuation rate. Therefore, it is not surprising that the experimental f_{O_2} curves from H_2O/H_2 and CO_2/CO do not agree in magnitude, except at the highest temperatures, revealing that the gas phase is likely not in equilibrium (see Figure 2.4).

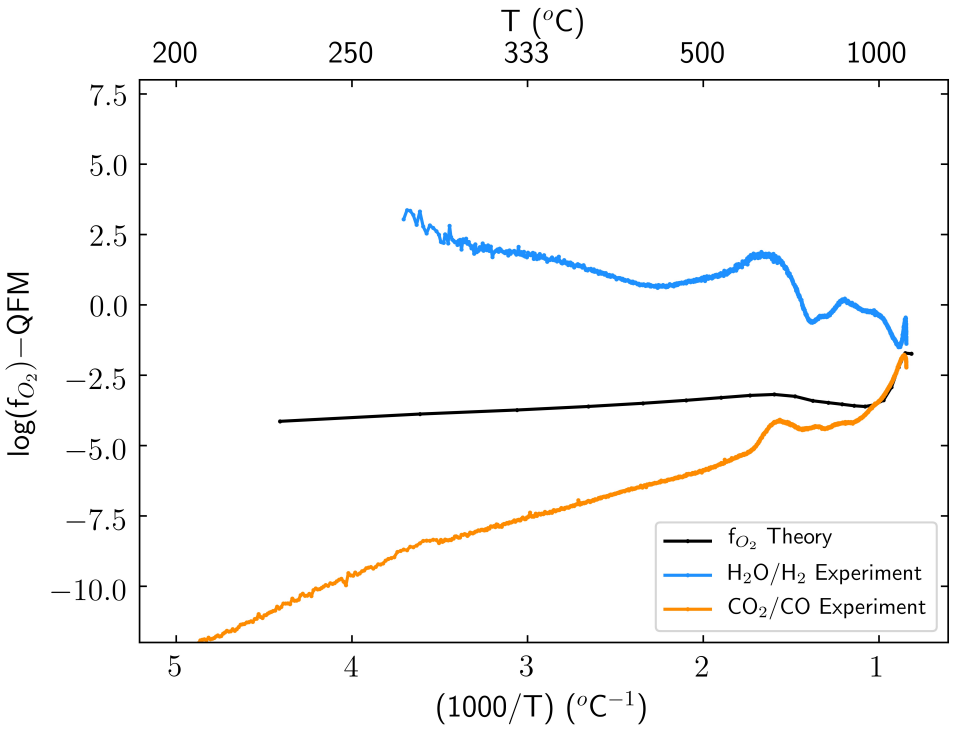

Figure 2.4: **Oxygen fugacities relative to the quartz-fayalite-magnetite (QFM) buffer from theory and experiments.** Oxygen fugacity of an average bulk CM chondrite composition as a function of temperature from chemical equilibrium calculations (black curve, labeled Theory) and the oxygen fugacity of the average of the three CM chondrites measured experimentally (blue and orange curves, labeled Experiment). Two abundance ratios were used to calculate f_{O_2}: H_2O/H_2 (blue curve) and CO_2/CO (orange curve). We cannot determine f_{O_2} directly from the O_2 abundance because after correcting for terrestrial atmospheric adsorption its abundance goes to zero (see Methods).

2.3 Discussion

The results from our outgassing experiments have several important implications for the initial atmospheric chemistry of low-mass exoplanets. While terrestrial planets experience a diversity of conditions during planet formation, these experiments represent an empirically-determined boundary condition of the less-theoretically-explored lower temperature/pressure paths that could be used to test outgassing models.

Our experimental conditions approximately simulate the initial heating phase during planet formation, revealing the initial volatile species that would outgas assuming the bulk composition of material being outgassed is CM chondrite-like. As such low-mass planets form their initial atmospheres via outgassing during accretion, H_2O-rich steam atmospheres form. These atmospheres will also likely contain significant amounts of CO and CO_2 and smaller amounts of H_2 and H_2S. Until now, several common assumptions used for low-mass exoplanet atmospheric modeling include ad hoc abundances such as H_2O-only or CO_2-only, solar abundances (dominated by H_2 and He), or atmospheric compositions of Solar System planets (Miller-Ricci et al. 2009; Fortney et al. 2013; Greene et al. 2016; Morley et al. 2017; Bower et al. 2019). Our outgassing experiments suggest initial atmospheres may differ significantly from many of the common assumptions in atmosphere models, and provide the basis for more refined future models of terrestrial planets' initial atmospheres (see "Comparison with Prior Studies" in Methods).

In proposing that our results be used as initial conditions for terrestrial exoplanet atmosphere models, we note that while our experiments cover a wide range of temperatures, they were conducted in a low-pressure environment. Schaefer & Fegley 2010 (Schaefer & Fegley 2010) suggest that varying pressure does not have a significant effect on the major gas composition of outgassed atmospheres from CM chondrite material. Chemical equilibrium or kinetics calculations can determine how these sets of initial compositions from outgassing experiments evolve as the pressure varies within a planet's atmosphere.

Theoretical models of terrestrial planet atmosphere formation usually lack experimental constraints. Based on the results from our experiments, the most direct way to improve such models of outgassing from CM chondritic-like building blocks would be to assume initial abundances at planetary surface boundaries averaging approximately 66% H_2O, 18% CO and 15% CO_2 over a temperature range similar to that used in this study. Depending on the capabilities of a particular model, temperature dependencies for species abundances could also be incorporated using our experimental results. Additional improvements could include the Langmuir coefficients for evaporation (and condensation) for the major outgassing species measured in our experiments to properly simulate chemical kinetics effects. Determining these coefficients often requires conducting Langmuir evaporation experiments (Sossi & Fegley 2018). In addition, reaction rates between the solid and gas phases relevant for chondrite outgassing would improve our understanding of when chemical equilibrium conditions are acceptable and when chemical kinetics effects are important. Subsequent experiments will determine whether other species predicted by chemical equilibrium models also outgas significantly. In addition, future experiments will measure volatiles from a wider variety of meteorites including ordinary and enstatite chondrites.

2.4 Extended Data Figures

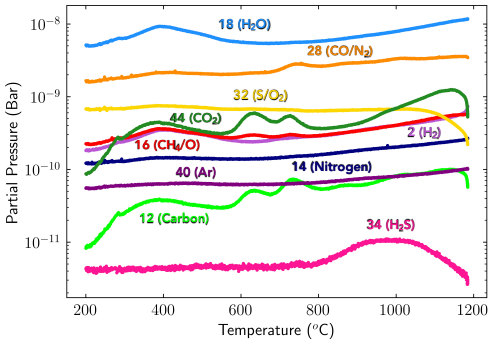

(a) Murchison Raw Measurement

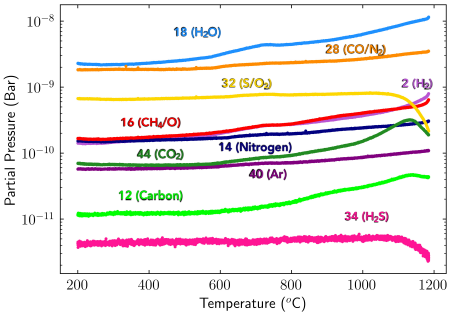

(b) Background Raw Measurement

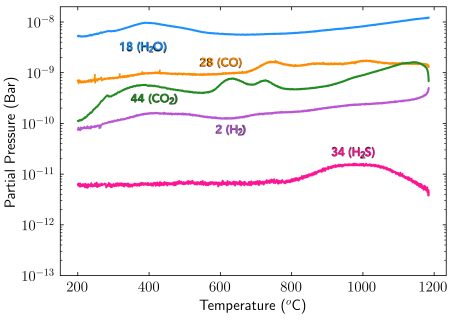

(c) Murchison Measurement Corrected for Ion Fragments and Atmospheric Adsorption

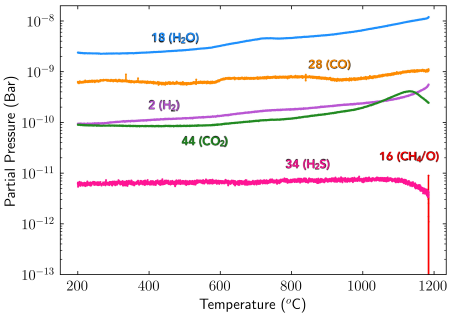

(d) Background Measurement Corrected for Ion Fragments and Atmospheric Adsorption

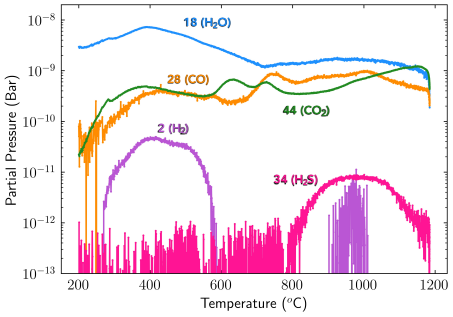

(e) Murchison Measurement Corrected for Ion Fragments and Atmospheric Adsorption and Background-Subtracted (i.e., data from (d) subtracted from data from (c)).

Figure 2.5: **Data Calibration Steps**. Each figure illustrates the partial pressures (bars) for the molecular species measured from 200 °C to 1200 °C. Each sample's data is calibrated by first correcting for ion fragments and atmospheric adsorption and then background subtracting.

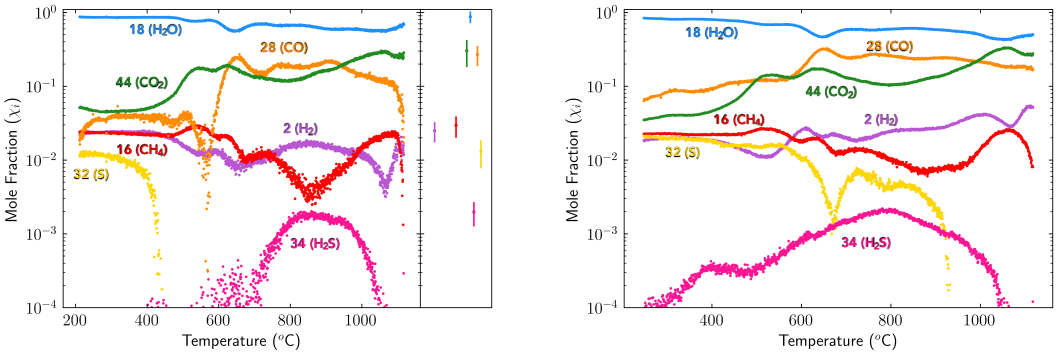

(a) Murchison

(b) Average of 3 CM Chondrites

Figure 2.6: **Results of analyzing ion fragments using a non-linear least squares regression**. The outgassing abundances in (a) are for the Murchison sample with the panel on the right side showing the average standard deviation determined from the Monte Carlo simulation for each of the species measured. The abundances in (b) are the average of the three CM chondrites.

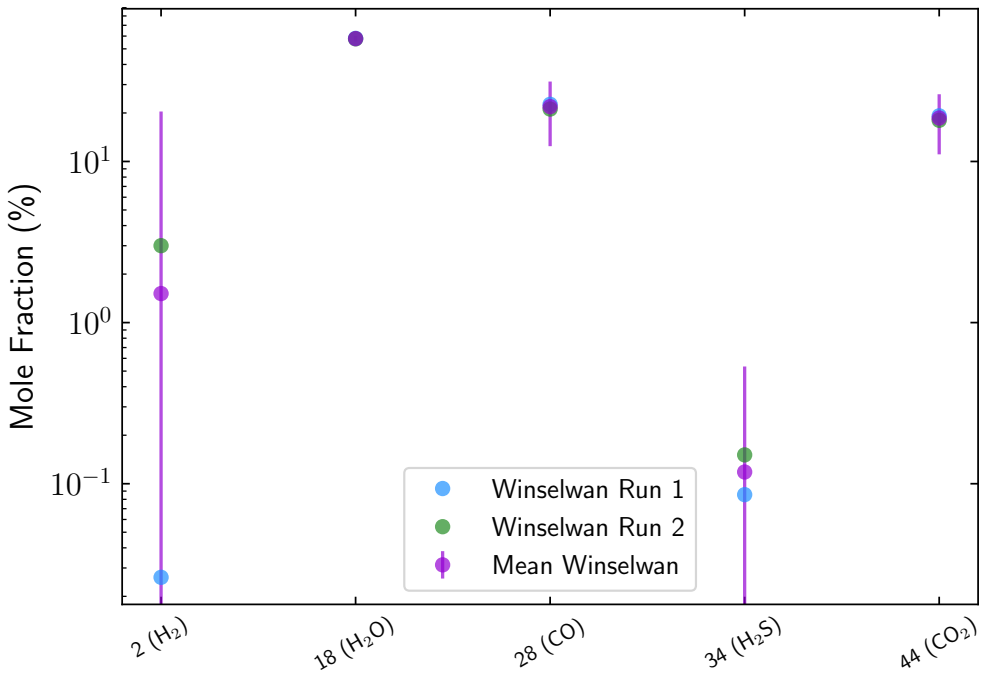

Figure 2.7: **Comparison between the yields of major volatiles released from Jbilet Winselwan samples during two identical experiments.** The mole fraction summed over temperature for each volatile species is normalized to the total mole fraction of released gases summed over temperature and expressed as a percentage. The uncertainty on the mean relative abundance for each volatile species is the 95% confidence interval of the mean. The volatile yields are fairly reproducible between the two experiments, especially for the most dominant outgassed species (H_2O, CO, CO_2).

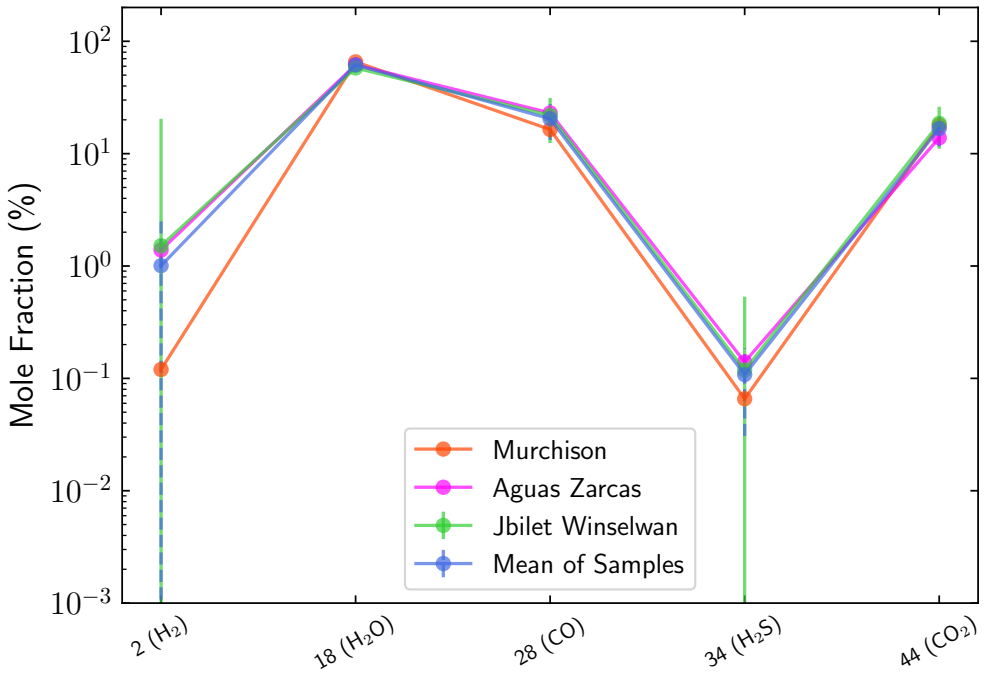

Figure 2.8: **Comparison between the yields of major volatiles released from the samples.** The mole fraction summed over temperature for each volatile species is normalized to the total mole fraction of released gases summed over temperature and expressed as a percentage. The data for Winselwan is the mean of the two individual experiments conducted with the uncertainty reported as the 95% confidence interval of the mean (see Methods and Figure 2.7). The mean relative abundance of all three samples for each volatile species is also shown with the uncertainty reported as the 95% confidence interval of the mean. All three samples have similar outgassing abundances for the most dominant outgassing species (H_2O, CO, and CO_2). While H_2 and H_2S have larger variations up to an order of magnitude, the relative abundances for each species across the three samples are within 2σ of each other.

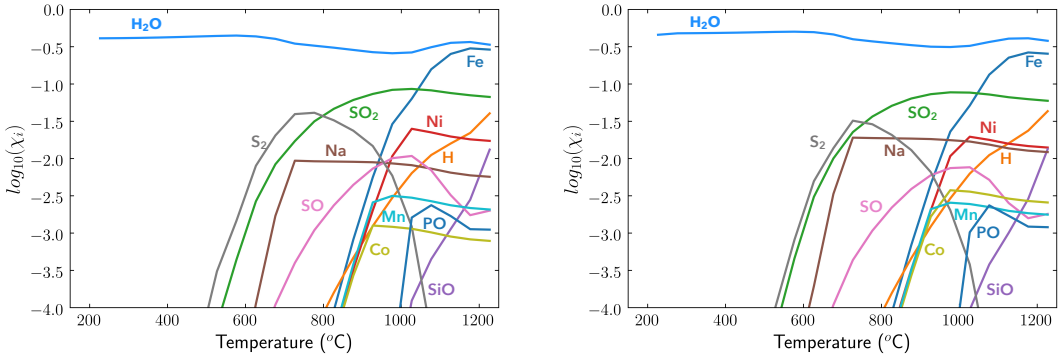

(a) Murchison (b) Average CM Chondrite Composition

Figure 2.9: **Additional Outgassing Species from Chemical Equilibrium Calculations** Outgassing abundances for additional species not measured in the experiments calculated assuming chemical equilibrium for Murchison (a) and an average CM chondrite bulk composition (b) at 1E-3 Pa. The outgassing of H_2O is also shown as a reference.

2.5 Methods

2.5.1 Sample Preparation & Experimental Procedure

CM chondrite samples were powdered with an agate mortar and pestle and sieved so that only material between 20 and 106 μm in diameter was analyzed to ensure homogeneous samples. Powdered samples were stored in a desiccator under vacuum to minimize terrestrial contamination. For each heating experiment, $\sim$3 mg of powdered sample was evenly distributed into a 6.5 $\times$ 4.0 mm^2 alumina crucible, as shown in Figure 2.10. This sample size was chosen because larger sample sizes saturate the RGA.

Prior to assaying each sample, we first heated an empty small crucible and the larger 50 $\times$ 20 $\times$ 20 mm^3 combustion boat in the tube furnace to allow impurities, particles in the tube and adsorbed volatiles to degas which otherwise could interfere with our measurements. The heating procedure to bake-out the tube and sample containers consisted of five steps: (1) heating from room temperature to 200 °C over 40 minutes, (2) holding at 200 °C for 30 minutes, (3) heating from 200 °C to 1200 °C over 5 hours, (4) holding at 1200 °C for 5 hours, and (5) cooling the system to room temperature over 5 hours. After one of the bake-outs, we calibrated the background signal by performing a similar heating procedure on empty sample containers except for step (4) in which the time at 1200 °C is reduced to 10 minutes.

The RGA mass spectrometer used in this study operates inside the vacuum chamber and ionizes gas molecules according to their molecular masses (up to 100 atomic mass units (amu)) and measures their partial pressures. Since an RGA is commonly used for detecting low-levels of contamination in vacuum systems, its sensitivity to trace

amounts of gas makes it ideal for carrying out this study (SRS 2009). The experimental procedure for each sample is identical to that used to determine the background signal. We chose the heating rate of 3.3 °C/min because it is similar to those in prior studies using mass spectrometers to monitor released gases from meteorite samples (e.g., Gooding & Muenow (1977), Okumura & Mimura (2011)). We also note that the combination of very low pressure and high vacuum pumping rate precludes many gas-gas reactions or volatile phase changes in the experimental system. At the high-temperature end of the experiments, some gas-gas reaction rates approach or exceed the vacuum pumping rate suggesting that some gas species, but not all, may approach equilibrium.

2.5.2 Data Calibration: Ion Fragmentation, Terrestrial Atmospheric Adsorption & Background Subtraction Corrections

The RGA's ionizer can cause different types of ions to be produced from a single species of gas molecule due to processes such as molecular fragmentation (SRS 2009). The mass spectrum of each molecule has contributions from all ion fragments formed from that molecule and they define the molecule's fragmentation pattern. In residual gas analysis, standard fragment patterns of common atoms and molecules are well established. Table 2.3 explains, for a given gas species whose mass number is analyzed during the experiments, the percentage each of its known ion fragments contributes to the intensity relative to the major peak due to that gas species itself. These fragment patterns were determined from the NIST Mass Spectrometry Data Center (NIST & Wallace 2018). To correct for ion fragments for each species, we subtract its partial pressure from the partial pressures of other species that contribute to its mass signal

weighted by the percentage of the other species's contribution (see Equations 4-15). For example, the partial pressure of H_2 is given by:

$$p_{H_2} = p_{2\text{amu}} - (0.02 * p_{H_2O}). \tag{2.1}$$

We also correct for the possibility of terrestrial atmospheric adsorption onto the samples. We assume that the signal at 40 amu is due entirely to atmospheric argon adsorbed onto the samples (see the section on degeneracies below). Given the composition of Earth's atmosphere (78% N_2, 21% O_2, 1% Ar), we determine the amount of atmospheric N_2 and O_2. After correcting for ion fragments, we subtract the atmospheric N_2 and O_2 contributions from the signals due to N_2 and 32 amu (see Equations 8, 12 and 14). We also subtract the ion fragments of atmospheric N_2 and O_2 from the signals at 14 and 16 amu (see Equations 6 and 9).

The step-wise heating procedure allows us to disentangle terrestrial weathering and contamination from the actual volatile composition of our samples (Grady & Wright 2003). In the heating procedure, we hold each sample at 200 °C for 30 minutes which helps eliminate any adsorbed water or nitrogen that is not intrinsic to the sample. Although we conduct each heating experiment under high-vacuum conditions ($\sim 10^{-4}$ Pa), slight contamination may still be possible. Therefore, to properly calibrate the background signal, we conducted an additional experiment following the same procedure used for the empty sample containers (see Figure 2.5). The partial pressures during this background measurement are corrected for ion fragments and terrestrial atmospheric adsorption and then serve as the background pressures which are subtracted

from the ion fragment-corrected and atmospheric adsorption-corrected partial pressures during sample heating to determine the fully calibrated (i.e., ion fragment-corrected, atmospheric adsorption-corrected and background-subtracted) partial pressures (i.e., for species i, p_i = $p_{i,\text{heating}}$ - $p_{i,\text{background}}$). The total background pressure averages ∼6E-4 Pa, and the dominant background species, H_2O, has an average partial pressure of ∼5E-4 Pa, both of which are ∼1.5 times lower than their corresponding sample values. The total pressure of the system at each temperature step is given by:

$$p_{\text{Total}} = \sum_i p_{i,\text{heating}} - \sum_i p_{i,\text{background}} \tag{2.2}$$

Figure 2.11 shows the variations in total pressure with temperature for the samples. To calculate the mole fraction (χ_i) of a gas species (atomic or molecular) at each temperature step, we divide its background-subtracted and ion fragment-corrected partial pressure by the total pressure, $\chi_i = p_i/p_{\text{Total}}$. For the elemental mole fractions of hydrogen, carbon, oxygen, nitrogen, and sulfur at each temperature step, we sum the mole fraction of each gas species containing the element of interest multiplied by the number of atoms of that element in the species, and divide by a normalization factor. For example, for hydrogen:

$$\chi_{\text{H}} = \frac{2\chi_{H_2O} + 4\chi_{CH_4} + 2\chi_{H_2} + 2\chi_{H_2S}}{\text{Norm}} \tag{2.3}$$

where Norm is the normalization factor that ensures that the elemental mole fractions sum to unity and is given by $\chi_H + \chi_C + \chi_O + \chi_N + \chi_S$. The reported relative

abundance of a given species i is its partial pressure summed over temperature and normalized to the total pressure of the released gases also summed over temperature ($P_{\text{i, Total}} = \sum_T p_i / \sum_T p_{\text{Total}}$), and is expressed as a percent (see Figure 2.8). The relative abundance of a given element j is its partial pressure, determined the same way as Equation 3 except using partial pressures instead of mole fractions, summed over temperature and normalized to the sum of the pressures of all elements measured in the experiments also summed over temperature ($P_{\text{j, Total}} = \sum_T p_j / \sum_T (\sum_j p_j)$).

2.5.3 Calculations to Determine Gas Species' Partial Pressures

Several of the mass numbers analyzed for this study correspond to multiple gas species (e.g., 28 amu corresponds to CO and N_2). Bulk composition measurements of the samples, measurements of the other masses, and melting/evaporation temperatures for the different species allow us to disentangle which species dominate the signal and, in some cases, distinguish between different gas species' signals that correspond to the same mass number. Equations 4-15 below show the calculations to determine the partial pressures of different volatile species by accounting for ionization fragmentation, disentangling some of the species with overlapping mass numbers and correcting for atmospheric adsorption:

$$p_{H_2} = p_{2\text{ amu}} - 0.02 p_{H_2O} \tag{2.4}$$

$$p_{H_2O} = 1.04 p_{18\text{ amu}} \tag{2.5}$$

$$p_{CH_4} = 1.25 p_{16\text{ amu}} - 0.10 p_{CO_2} - 0.015 p_{H_2O} - 4.96 p_{40\text{ amu}} \tag{2.6}$$

$$p_{N_2,\text{ pre-atmosphere correction}} = (p_{14\text{ amu}} - 0.21p_{CH_4})/0.14 \tag{2.7}$$

$$p_{N_2} = 1.14p_{N_2,\text{ pre-atmosphere correction}} - (83.96p_{40\text{ amu}}) \tag{2.8}$$

$$p_N = p_{14\text{ amu}} - 0.21p_{CH_4} - 0.14p_{N_2} \tag{2.9}$$

$$p_{CO} = 1.07(p_{28\text{ amu}} - p_{N_2,\text{ pre-atmosphere correction}}) - 0.10p_{CO_2} \tag{2.10}$$

$$p_C = p_{12\text{ amu}} - 0.09p_{CO_2} - 0.05p_{CO} - 0.04p_{CH_4} \tag{2.11}$$

$$p_S \text{ or } p_{O_2} = (1.22p_{32\text{ amu}}) - (22.53p_{40\text{ amu}}) \tag{2.12}$$

$$p_{H_2S} = 1.45p_{34\text{ amu}} \tag{2.13}$$

$$p_{Ar} = p_{40\text{ amu}} \text{ (All due to atmospheric adsorption)} \tag{2.14}$$

$$p_{CO_2} = 1.29p_{44\text{ amu}} \tag{2.15}$$

In Equation 6, we account for the fact that the signal at 16 amu can be due to ion fragments of CO_2 and H_2O. We also account for the fact that contaminated O_2 due to atmospheric adsorption has an ion fragment at 16 amu (see "16 and 32 amu" section in "Degeneracies" section). Although 16 amu can also be due to ion fragments of CO, we do not account for them because 16 amu only contributes 2% to CO. Equations 7-10 explain how we disentangle the signals due to CO and N_2 given that they have the same mass number (28 amu). In Equation 7, we first account for the fact that the signal at 14 amu can be due to ion fragments of CH_4. We assume that the remaining signal at 14 amu is due entirely to atomic nitrogen which is an ion fragment of N_2,

and we use it to determine the partial pressure of N_2. In Equation 8, we account for contaminated N_2 due to atmospheric adsorption by assuming all of the 40 amu signal is due to terrestrial atmospheric argon and using its signal and the known composition of Earth's atmosphere to determine the amount of contaminated N_2. In Equation 9, we determine the partial pressure of atomic nitrogen which is zero since we assume all of it was an ion fragment of N_2. In Equation 10, we determine the signal due to CO by subtracting the total amount of N_2 from the signal at 28 amu and also accounting for the fact that this signal can be an ion fragment of CO_2. Equation 11 determines the partial pressure of atomic carbon and accounts for the various ion fragments at 12 amu. The signal at 32 amu can be due to either O_2 or atomic sulfur. Equation 12 accounts for the contamination from atmospheric adsorbed O_2, and once this correction is applied the signal at 32 amu becomes negligible. Although the signal at 32 amu can be an ion fragment of H_2S, we do not account for it since we are not certain that this signal is due to sulfur or O_2. Equation 13 determines the partial pressure of H_2S, and Equation 14 assumes that the signal at 40 amu is entirely due to terrestrial atmospheric argon. Finally, Equation 15 determines the partial pressure of CO_2.

Equations 5, 6, 8, 10, 12, 13, and 15 determine the partial pressures of molecules subject to fragmentation. An additional factor that should be taken into account when correcting for ion fragments is adding fragments back to those species that are subject to molecular fragmentation. While this may cause a slight over-correction, it does not significantly affect the results, as the average difference between the relative abundances summed over temperature with or without adding fragments back in is $\sim$1%. The dif-

ferences between the relative abundances summed over temperature with or without adding fragments back in are also within the uncertainties (expressed as 95% confidence intervals of the means) for each species and atomic abundance. As examples, to determine H_2O and CH_4's partial pressures, we add back the contributions from their fragments:

$$p_{H_2O} = (1.0 p_{18\ \mathrm{amu}}) + (0.02 p_{18\ \mathrm{amu}}) + (0.02 p_{18\ \mathrm{mu}}) = 1.04 p_{18\ \mathrm{amu}} \tag{2.16}$$

$$\begin{aligned} p_{CH_4} &= ((1.0 p_{16\ \mathrm{amu}}) + (0.21 p_{16\ \mathrm{amu}}) + (0.04 p_{16\ \mathrm{mu}})) - (0.10 p_{CO_2}) - (0.02 p_{H_2O}) - (4.96 p_{40\ \mathrm{amu}}) \\ &= 1.25 p_{16\ \mathrm{amu}} - (0.10 p_{CO_2}) - (0.02 p_{H_2O}) - (4.96 p_{40\ \mathrm{amu}}) \end{aligned} \tag{2.17}$$

2.5.4 Reproducibility of Experimental Results

In order to test the reproducibility of our experiment and to confirm that it precisely measures the outgassed species from various samples, we analyzed samples of Jbilet Winselwan twice under identical conditions. Jbilet Winselwan's final reported relative abundances are given by the mean and the 95% confidence interval of the mean calculated from a t-distribution of the two trials (see Table 2.1 in main article). As Figure 2.8 illustrates, the relative abundances of the three most abundant outgassed species, H_2O, CO and CO_2, between the two experiments agree with each other within 6 % with 95% confidence intervals less than 35%. The other species' abundances be-

tween the two experiments have variations of up to ∼3 % and 95 % confidence intervals less than 16 %. As Tables 1 and 2 in the main article illustrate, the species with the largest uncertainties are CO_2, H_2O, and the total amount of H (95 % confidence intervals of ∼34 %, 34 %, and 36 %, respectively). These large confidence intervals are due to the the small sample size. All other species have confidence intervals less than 18 % with difference between the two measurements less than 3 %.

2.5.5 Calculating Oxygen Fugacity

Although our experiments simulate a non-equilibrium open system, we can compare our results to what is expected at equilibrium. For determining the oxygen fugacity of the system as shown in Figure 2.4, there are several ways to calculate f_{O_2} from the relative abundances of various gas species including ratios of H_2/H_2O and CO/CO_2. Since our experimental O_2 abundance is zero, we cannot use O_2 alone to compute f_{O_2}. Assuming the system is in equilibrium, to calculate f_{O_2} as a function of temperature from H_2 and H_2O we use Equations 18-20:

$$H_2O = H_2 + 0.5O_2 \tag{2.18}$$

$$\log_{10}(K_1) = \frac{-12794}{T} + 2.7768 \tag{2.19}$$

$$f_{O_2} = (K_1 \frac{\chi_{H_2O}}{\chi_{H_2}})^2 \tag{2.20}$$

Similarly, to calculate f_{O_2} from CO and CO_2 we use Equations 21-23:

$$CO_2 = CO + 0.5O_2 \tag{2.21}$$

$$\log_{10}(K_2) = \frac{-14787}{T} + 4.5472 \tag{2.22}$$

$$f_{O_2} = (K_2 \frac{\chi_{CO_2}}{\chi_{CO}})^2 \tag{2.23}$$

K_1 and K_2 are the equilibrium constants that are functions of temperature T (in Kelvin) and taken from the IVTANTHERMO database (see (Schaefer & Fegley 2017) for details). Figure 2.4 in the article shows f_{O_2} calculated from chemical equilibrium (black curve) and f_{O_2} determined using H_2/H_2O and CO/CO_2 from our experiments (blue and orange curves, respectively). The f_{O_2} are plotted relative to the quartz-fayalite-magnetite (QFM) mineral buffer (Fegley 2013). Under equilibrium conditions, we expect the f_{O_2} values calculated from H_2O/H_2 and CO_2/CO to match, but we do not find this with our experimental data. The fact that the H_2O/H_2 trend is larger than the theoretical f_{O_2} suggests that the abundance of H_2O compared to H_2 is larger than that predicted under chemical equilibrium conditions. This larger abundance may be due to kinetic barriers that result in hydrogen initially outgassing as H_2O, but our experiments do not allow sufficient time for reactions to take place that would transform it to H_2.

2.5.6 Comparison with Model Assumptions

A key distinction between our experimental results and equilibrium model calculations is that our experiments simulate *initial* (or instantaneous) outgassing compositions, not the long-term outgassing abundances once equilibrium has been achieved. Also, in our experiments the meteorite composition changes as the temperature increases and volatiles are removed whereas the equilibrium calculations assume a closed system in which the volatiles are not removed. Nevertheless, the preliminary outgassed abundances determined experimentally may have important implications for the subsequent evolution of outgassed atmospheres that eventually achieve chemical equilibrium, as initial outgassed species' abundances control what is available to subsequently evolve within an atmosphere. For example, our experiments find that H_2S outgasses at higher temperatures than predicted in equilibrium models, which means that if a planet does not reach 900-1000 °C, H_2S may not have a significant atmospheric abundance.

The experimental results for this work are the *instantaneous* outgassing compositions because those are the more appropriate ones to compare to thermochemical equilibrium models rather than the *cumulative* outgassing compositions. Both the instantaneous measurements and equilibrium model results represent contained assemblages, although the composition in the experiments is evolving. On the other hand, the *cumulative* outgassed abundances do not represent such an assemblage, since the gases are removed at each measurement and do not react with material outgassed at higher temperatures. However, the cumulative outgassed compositions are a useful way to determine the extent to which volatiles have been released, so we have calculated the

cumulative outgassing composition. Figure 2.13 illustrates the cumulative outgassing compositions as a function of temperature for each of the three chondrite samples as well as the average of the three samples. We see a leveling-off behavior at high temperatures for nearly all of the outgassing species across each of the three CM chondrite samples. Some of this leveling-off behavior is due to the fact that a volatile's outgassing is decreasing (e.g., H_2S), but there could still be other gas species being produced that we do not track in these experiments. Compared to the other volatiles measured, CO_2 and H_2's cumulative outgassing trends do not level off as significantly at the higher temperatures.

2.5.7 Least Squares Regression Technique for Ion Fragments and Species Degeneracies

Our chosen technique to correct for ion fragmentation and, when possible, break the degeneracies between volatile species that have the same mass number involves making logical assumptions regarding which gas species likely dominates a given mass signal and using a set of arithmetic corrections (see "Calculations to Determine Gas Species' Partial Pressures" section above). However, a non-linear least squares regression is an alternate method to account for ion fragments and disentangle gas species with overlapping mass numbers. This technique involves performing a least squares regression on the normalized mass spectrum library (Table 2.3, column 4) and constraining the outgassed abundances to be positive and less than appropriate upper bounds. For all of the species, the upper bounds are twice the maximum value of that species mass number. Figure 2.6 shows the fully-calibrated outgassing abundances calculated using

this method and Table 2.5 compares the average partial pressures for each gas species calculated using our original analysis to those from the least squares technique. In order to calculate the uncertainties on the fitted parameters from the least squares analysis, we ran a Monte Carlo simulation on a sparser data array. The least squares analysis results are consistent with the original results within 2σ for most species. While the results for the most dominant outgassing species (i.e., H_2O, CO, CO_2) are similar to our original analysis, the least squares result finds non-negligible amounts of methane and atomic sulfur. Outgassing of these species is not predicted from chemical equilibrium calculations, which suggests that this technique may not fully account for ion fragments compared to our original calculations or, in the case of sulfur, they are leftover fragments from species we are not currently measuring in our experiments (e.g., S_2, SO_2, etc.).

2.5.8 Degeneracies between Gas Species and Mass Numbers

For mass numbers that could correspond to multiple volatile species, we describe in the following subsections additional details on how we either determined which species dominates the signal or disentangled multiple species' signals.

16 and 32 amu: 16 amu is the molecular weight of CH_4 and the atomic weight of oxygen. As shown in Table 2.3, mass number 16 is affected by ionization fragmentation, being fragments of CO_2, CO, H_2O and O_2. Ion fragments at 16 amu contribute to 22% of O_2's signal (assuming the signal at 16 amu is due to atomic oxygen), 9.8% of CO_2's

signal, 2.2% of CO's signal, and 1.5% of H_2O's signal. We assume that the majority of the signal at 16 amu outgassing from the samples is due to CH_4 because prior meteorite ablation studies have detected small amounts CH_4 from carbonaceous chondrites and atomic oxygen is not expected to outgas significantly (Court & Sephton 2009). 32 amu is the atomic weight of sulfur and the molecular weight of O_2 and methanol (CH_3OH). If mass number 32 amu is due to atomic sulfur, then it can be an ion fragment of hydrogen sulfide (H_2S), contributing to 45% of H_2S's signal. According to theoretical calculations, atomic sulfur is not predicted to outgas significantly and O_2 is only predicted to begin outgassing around 1100 °C.

As indicated below, our data does not allow a definitive determination of which species dominate the signals at 16 and 32 amu. For the 32 amu signal, we correct for the possibility of atmospheric adsorption of O_2 onto the samples by assuming the 40 amu signal is entirely due to atmospheric argon and using the known ratio of O_2/Ar in Earth's atmosphere to subtract the atmospheric contribution to the signal at 32 amu (Equation 12). After correcting for atmospheric adsorption, we do not detect a significant outgassing signal at 32 amu for any of the samples. The signal at 32 amu is likely not due to methanol because it is not predicted to outgas significantly across the entire temperature range.

For the 16 amu signal, even after correcting for ion fragments of CO_2 and H_2O, the signal is still significant at lower temperatures (up to ~600 °C) for all three samples. However, since O_2 has an ion fragment at 16 amu, we also have to account for the possibility of atmospheric adsorption of O_2's ion fragment at 16 amu so we

subtract 22 % of the atmospheric adsorbed O_2 from the 16 amu signal. When we apply this correction, the signal at 16 amu becomes negligible across all temperatures for all samples. If the signal at 32 amu is predominantly due to sulfur not O_2, then the signal at 16 amu would be significant and likely due to CH_4. However, because we cannot definitively resolve which species dominate the signals at 32 and 16 amu, we must conservatively apply the atmospheric adsorption correction for both masses. In order to disentangle CO and N_2, as described in the next subsection, we assume the ion fragment of CO at 16 amu is negligible, which is reasonable because it only contributes to 2 % of CO's signal.

If we assume the signal at 16 amu is due entirely to atomic oxygen resulting from ion fragments of O_2, we can use it to disentangle the abundances of sulfur and O_2. To calculate O_2's signal from the 16 amu signal, we first correct for the fact that 16 amu can contribute to ion fragments of CO_2 and H_2O (we assume the ion fragment of CO at 16 amu is negligible), and then use the remaining signal to calculate the abundance of O_2, knowing that 16 amu contributes to 22% of O_2's mass spectrum (Equation 24). We then calculate the signal due to sulfur, by subtracting O_2's signal from the 32 amu signal and correcting for ion fragmentation of H_2S (Equation 25). Finally, we correct for atmospheric adsorption of O_2 (Equation 26). The resulting signal due to 16 amu is given by Equation 27. Once we disentangle the signals from O_2 and sulfur, we find that sulfur and O_2 abundances are negligible at all temperatures including higher temperatures where predictions indicate that O_2 should begin outgassing (Figure 2.12) In addition when the sulfur and O_2 components are separated, the abundance at 16 amu is also

negligible. Ultimately, further work is required to determine which species dominate the signals at 16 and 32 amu.

$$p_{O_2,\text{ pre-atmosphere correction}} = 1.22((1.25p_{16\text{ amu}} - 0.10p_{CO_2} - 0.02p_{H_2O})/0.22) \quad (2.24)$$

$$p_S = p_{32\text{ amu}} - p_{O_2,\text{ pre-atmosphere correction}} - 0.45p_{H_2S} \quad (2.25)$$

$$p_{O_2} = p_{O_2,\text{ pre-atmosphere correction}} - (22.53p_{40\text{amu}}) \quad (2.26)$$

$$p_{CH_4} = 1.25p_{16\text{ amu}} - 0.10p_{CO_2} - 0.02p_{H_2O} - (0.22p_{O_2}) \quad (2.27)$$

28 amu: This is the molecular weight of CO, N_2 and ethylene (C_2H_4). Mass number 28 amu can also be an ion fragment of CO_2, contributing to 10% of CO_2's signal (Table 2.3). To disentangle the signals due to CO and N_2, we assume the signal at 14 amu is predominantly due to ion fragments of N_2 which is valid because atomic nitrogen is not expected to outgas. We correct for the fact that 14 amu is also an ion fragment of CH_4, and then we use the resulting signal at 14 amu to calculate the signal due to N_2, knowing that 14 amu contributes to 14 % of N_2's mass spectrum (Equation 7). We then determine the signal due to CO by subtracting the N_2 signal from the 28 amu signal and correcting for ion fragmentation of CO_2 (Equation 10). We correct

for atmospheric adsorption of N_2 by assuming the signal at 40 amu is entirely due to atmospheric argon and using the known ratio of N_2/Ar in Earth's atmosphere to subtract the atmospheric contribution to N_2 (Equation 8). Even after disentangling the signal at 28 amu into the contributions from N_2 and CO and correcting for the effects of ionization fragmentation, the abundance of CO is still very high, being the second most abundant species (Figure 2.1 and Figure 2.8). After correcting for atmospheric adsorption, N_2's outgassed abundance is not significant for any of the three samples. Since CM chondrites have a higher bulk abundance of oxygen (432 mg/g) compared to hydrogen (14 mg/g) while prior theoretical and experimental studies do not predict significant amounts of C_2H_4 to outgas, the 28 amu signal is more likely to be CO than C_2H_4 (see 2.4). Further investigation is required to definitively rule out C_2H_4 contributing to the signal at 28 amu, so our experimental results should be considered an upper limit on the CO abundances. As Figure 2.3 illustrates, this result agrees fairly well with chemical equilibrium calculations. The fact that the oxygen fugacity calculated from the abundance ratios of CO_2 and CO is lower than f_{O_2} under chemical equilibrium at lower temperatures suggests that there is more CO than CO_2 in our experiments than would be expected if at equilibrium. Once our experiment reached higher temperatures (∼900 °C), the experimental f_{O_2} determined by CO_2/CO matches the theoretical chemical equilibrium value.

40 amu: This is the atomic weight of argon and the molecular weight of sodium hydroxide (NaOH), potassium hydride (KH), and methyl cyanide (CH_3CN). Mass number 40 should not contribute to the signals of any other gas species due to the ionization

fragmentation process. In terms of the average bulk composition of CM chondrites, oxygen has the highest abundance (432 mg/g) followed by carbon (22 mg/g), hydrogen (14 mg/g) and finally sodium (4.1 mg/g), nitrogen (1.52 mg/g) and potassium (0.4 mg/g) (Table 2.4). Although Argon has an even smaller bulk abundance than these species, it is relatively abundant in Earth's atmosphere ([Ar]/[O_2] for air is 0.05). Atmospheric ^{40}Ar is known to contaminate prior meteorite experiments (e.g., Huss et al. (1996)). In addition, NaOH, KH, and CH_3CN are not predicted to outgas significantly from CM chondrites at these temperatures. Therefore, we conclude that the 40 amu signal is due to atmospheric Ar. As described earlier, we use this signal to determine the atmospheric contributions of N_2 and O_2. Future investigation is required to determine if any of the 40 amu signal is due to outgassing from the samples rather than atmospheric adsorption of Ar.

2.5.9 Solid Phases

Twenty four solid phases are stable in the theoretical equilibrium calculations: $CaAl_2Si_2O_8$, Mg_2SiO_4, $MgCaSi_2O_6$, $MgSiO_3$, $MgTiO_3$, $FeCr_2O_4$, $FeTiO_3$, $FeSiO_3$, Fe_2SiO_4, $Ca_3(PO_4)_2$, Ni, Co, $Fe_{0.947}O$, Mn_2SiO_4, $MgAl_2O_4$, Ni_3S_2, FeS, $KAlSi_3O_8$, $NaAlSiO_4$, $Ca_5P_3O_{12}F$, Co_9S_8, $Na_8Al_6Si_6O_{24}C_{l2}$, Fe_3O_4, $NaAlSi_3O_8$. While many of these phases are only stable over a narrow temperature range, the phases that were stable across nearly the entire temperature range include Mg_2SiO_4, $MgCaSi_2O_6$, $FeCr_2O_4$, $FeTiO_3$, Fe_2SiO_4, $Ca_3(PO_4)_2$.

Preliminary X-ray diffraction (XRD) analyses were performed on the sample residues and unheated samples. For each XRD measurement, the ∼3 mg sample was

spread in a thin layer over a silicon sample holder and continuously rotated 360° for two hours while data was collected, covering angles 0 to 70°. Comparing the solid phases from the equilibrium calculations to what we detect in the samples from our preliminary XRD analysis, we find that almost all of these phases may be present in the unheated samples and the post-heated residues but, for the post-heated residues, most of the phases have reduced signals despite the unheated and post-heated sample masses being nearly the same. Notable exceptions include $Ca_3(PO_4)_2$ and Co which were not definitively detected in the unheated samples and post-heated residues, and $CaAl_2Si_2O_8$ and $Na_8Al_6Si_6O_{24}C_{l2}$ which were not detected in most of the post-heated residues. For example, troilite (FeS) is present in the unheated samples but has a much weaker signal in the post-heated residues, matching the equilibrium calculations that have FeS being a stable phase up until ∼775 °C. Our XRD analysis suggests that gypsum ($CaSO_4(H_2O)_2$) may be breaking down during the experiments. However, in the equilibrium calculations, gypsum is never stable, and this difference may be due to an issue with the data for gypsum that is used in the equilibrium models or uncertainties in the bulk composition used for the equilibrium calculations. Further XRD analyses are required to confirm these preliminary results.

2.5.10 Outgassed Gas Species' Masses

The average molar mass of the mixture across 200 to 1200 °C of volatile species i is determined by the equation: $\bar{M} = \sum_i M_i * \sum_T \chi_i$, where M_i is the molar mass of

species i. To calculate the mass fraction of a species, w_i:

$$w_i = 100 * ((\sum_T \chi_i) * M_i)/\bar{M}. \tag{2.28}$$

To determine the outgassed mass of a certain element or species (Mass_i), the mass fraction is multiplied by the total outgassed mass ($\text{Mass}_{\text{Total}}$) which is determined by measuring the mass change of the sample before and after heating:

$$\text{Mass}_i = w_i \times \text{Mass}_{\text{Total}}. \tag{2.29}$$

Each sample was weighed before and after heating to determine the mass loss of each volatile species as a result of outgassing. The total gas released during the experiments based on mass loss measurements is similar between Murchison and Winselwan but higher for Aguas Zarcas. For all three chondrites, the mass released is mostly in H_2O, CO, and CO_2. Comparing the initial bulk abundance of an element for CM chondrites to the outgassed abundance informs the degree to which the samples have outgassed relative to complete vaporization of the samples (Table 2.2 in main article). On average, the samples have higher outgassed abundances of hydrogen and carbon but lower outgassed abundances of oxygen, nitrogen and sulfur compared to the initial bulk abundances. These differences between the initial bulk abundances for an average CM chondrite composition and the outgassed abundances suggests that the samples have not outgassed fully relative to complete vaporization and could also reflect heterogeneities in the meteorite samples themselves.

2.5.11 Comparison with Prior Studies

Planetary outgassing has been modeled both for the Solar System's terrestrial planets and for some low-mass exoplanets. For instance, studies find that Earth's early degassing produced a steam atmosphere during planetary accretion and a reducing atmosphere of H_2 and/or CH_4 near the end of accretion (e.g., Zahnle et al. (1988); Lange & Ahrens (1982); Abe & Matsui (1985); Hasimoto et al. (2007)). The major factors controlling speciation during Earth's early degassing included the water content of accreting planetesimals as well as temperature and pressure conditions during the atmosphere's degassing history. For the Zahnle et al. 1988 model of Earth's steam atmosphere during accretion, water is the only atmospheric species considered, while the Hashimoto et al. 2007 model of Earth's reducing atmosphere assumed accretion of only a specific type of chondritic material with varying amounts of water (Zahnle et al. (1988); Hasimoto et al. (2007)). Outgassing models for a planet's magma ocean phase suggest that the degassed atmospheric composition depends on the concentration of volatiles in the accreted body and the pressure at which degassing occurs (Lammer et al. 2018; Gaillard & Scaillet 2014). Many of these studies assume chemical equilibrium conditions and lack experimental data to validate some of their assumptions. For example, Gaillard & Scaillet 2014 considered outgassed species composed of a limited set of elements (H, C, O, S, Fe) to investigate volcanic outgassing of basaltic material on planetary atmospheres. However, they do not include other potentially important elements (e.g., F, Na, Cl, K) nor do they apply experimental data to validate using a simplified set of elements. Finally, prior research used chemical equilibrium calculations assuming

meteorite abundances to determine planet atmospheric compositions (Schaefer & Fegley 2007, 2010; Lupu et al. 2014). These planetary outgassing models have been applied to low-mass exoplanet atmosphere studies to help interpret current observational data (e.g., (Mbarek & Kempton 2016; Dorn et al. 2018)).

As noted above, there is limited experimental data to inform these theoretical outgassing models and, in particular, none to fully inform meteorite outgassing work. Prior meteorite heating experiments have used a variety of instrumental techniques including mass spectrometry, infrared spectroscopy and shock devolatilization (e.g., Court & Sephton (2009); Gooding & Muenow (1977); Muenow et al. (1995); Lange & Ahrens (1982); Tyburczy et al. (1986); Gerasimov et al. (1998); Ikramuddin et al. (1977); Burgess et al. (1991); Springmann et al. (2019)). However, studies that heated meteorites were limited in several key ways due to restrictions in the number and type of samples used, the temperatures to which the samples where heated, and the number of gas species that were accurately measured. For example, some prior studies focused on the contribution from meteorites on impact-induced atmosphere formation which often involved shocking samples prior to analyzing their volatile contents, and therefore do not properly simulate conditions expected for outgassing from a planet (e.g., Court & Sephton (2009); Lange & Ahrens (1982); Tyburczy et al. (1986)). In addition, these experiments only measured a small subset of volatile species, namely H_2O and CO_2 (Court & Sephton (2009); Tyburczy et al. (1986)). It is important to note that the prior studies that focused on shock-induced devolatilization experiments did not continuously monitor the composition of degassed species and focused on higher pressures ($10^{-4} - 10^{4}$

bars) than those in our experiments ($\sim 10^{-8}$ bars). These prior works cannot be quantitatively compared to theoretical outgassing models because they either monitored the evolving composition of only a few gas species as a function of temperature or instead inferred loss of volatiles by comparing samples before and after heating. Other studies focused on trace metals (e.g., Co, Zn, In) and moderately volatile and volatile elements (e.g., Se, Ga, As), which are not major constituents of the atmospheres of temperate rocky planets (Springmann et al. (2019); Ikramuddin et al. (1977)). As a result, prior studies are unsuitable for validating outgassing models for low-mass planets. To fill this gap in the understanding of meteorite outgassing compositions, we designed an experimental procedure to analyze the abundances of a wide range of degassed components: H_2, C, N, CH_4/O, H_2O, CO, N_2, S/O_2, H_2S, Ar, CO_2, which informs the initial compositions of outgassed atmospheres assuming the outgassing material is CM chondrite-like.

Comparing our results to other prior meteorite heating experiments, we find that our detection of significant outgassing of H_2S from Murchison (beginning at 800 °C) is consistent with the stepped combustion experiments of Murchison from Burgess et al. 1991 that found the highest outgassing yield of sulfur occurring at 800 °C (Burgess et al. 1991). Court & Sephton 2009 rapidly heated CM2 chondrites to 1000 °C and using FTIR found that outgassed H_2O and CO_2 yields relative to the initial sample masses were ∼9 % and 5 %, respectively; they did not detect significant amounts of CO and CH_4. These H_2O and CO_2 yields are similar to those measured in our experiments, which reached higher temperatures over a much longer period of time: ∼9 % for H_2O

and ∼6 % for CO_2, where both of these values are determined by taking the outgassed mass of the volatile species divided by the initial sample mass (Court & Sephton 2009).

Mbarek & Kempton 2016 (Mbarek & Kempton 2016) used the theoretical outgassing composition of chondritic meteorites from Schaefer & Fegley 2010 (Schaefer & Fegley 2010) as their initial condition and then performed Gibbs free energy minimization to determine what condensate cloud species may form in super-Earth atmospheres. This work explores similar atmospheric temperatures to those measured in our experiments (∼350-1500 K) and finds that the C/O and H/O ratios have a strong influence on cloud chemistry in exoplanet atmospheres. They claim that if a planet's bulk composition is made of CM chondrite-like material, its outgassed atmosphere will have C/O and H/O ratios of 0.18 and 1.39, respectively (Mbarek & Kempton 2016). From our experimental outgassing abundances, we find similar C/O and H/O ratios, 0.29±0.08 and 1.18±0.18, respectively. Our experimental C/O ratio is between Mbarek & Kempton's values for CM, CI and CV chondrites, whereas our H/O ratio is closest to their values for CM and CI chondrites. They predict that the atmospheres of super-Earth exoplanets with bulk compositions similar to CM chondrites may form KCl and ZnS clouds, but slightly more oxidizing conditions (e.g., CV chondrites) may hinder the formation of cloud condensates (Mbarek & Kempton 2016).

In summary, our results provide a comprehensive experimental comparison to prior theoretical chemical equilibrium models (Schaefer & Fegley 2007, 2010) that aim to study the outgassing compositions of chondritic meteorites and their implications for terrestrial planets' early atmospheres. Additional experiments on a wider range of

chondritic meteorites, including ordinary and enstatite chondrites, will allow for a more complete comparison with prior theoretical work and will reveal more insight into the possible atmospheric composition of early Earth as well as various exoplanets.

2.6 Supplementary Information

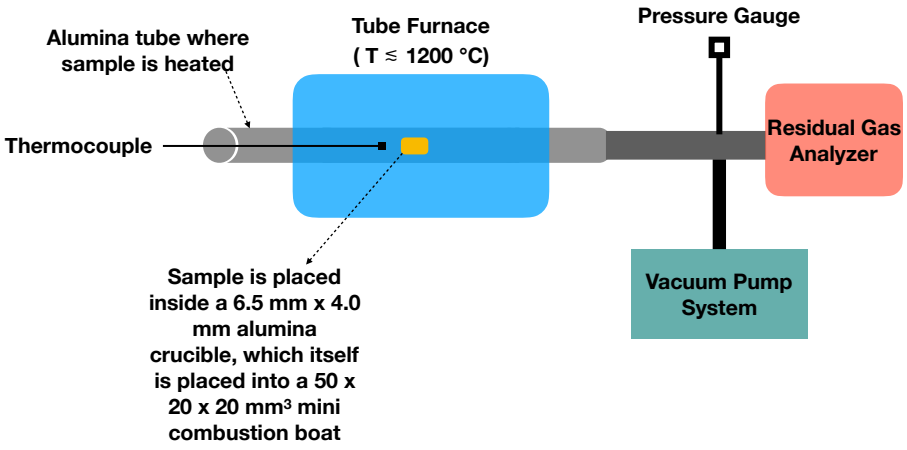

Figure 2.10: **Schematic of Instrument Set-Up.** Each powdered sample is placed inside a small alumina crucible which itself is placed inside a alumina mini combustion boat. The boat is inserted into an alumina tube to the center of the furnace that can reach temperatures up to 1200 °C. The furnace is connected to a turbomolecular pump which maintains the entire system at a high-level vacuum, and to a residual gas analyzer which measures the partial pressures of up to 10 species continuously throughout the experiment. A thermocouple inside the tube measures the temperature as a function of time. The thermocouple is placed within 50 mm of the sample containers and both are within the furnace's 13 cm hotspot to ensure accurate temperature measurements.

Data Availability: The data that support the findings of this study and corresponding plots in the paper are available from github.com/maggieapril3/CMChondritesOutgassingData or from the corresponding author upon request. Figures 1-4 and Extended Data Figures

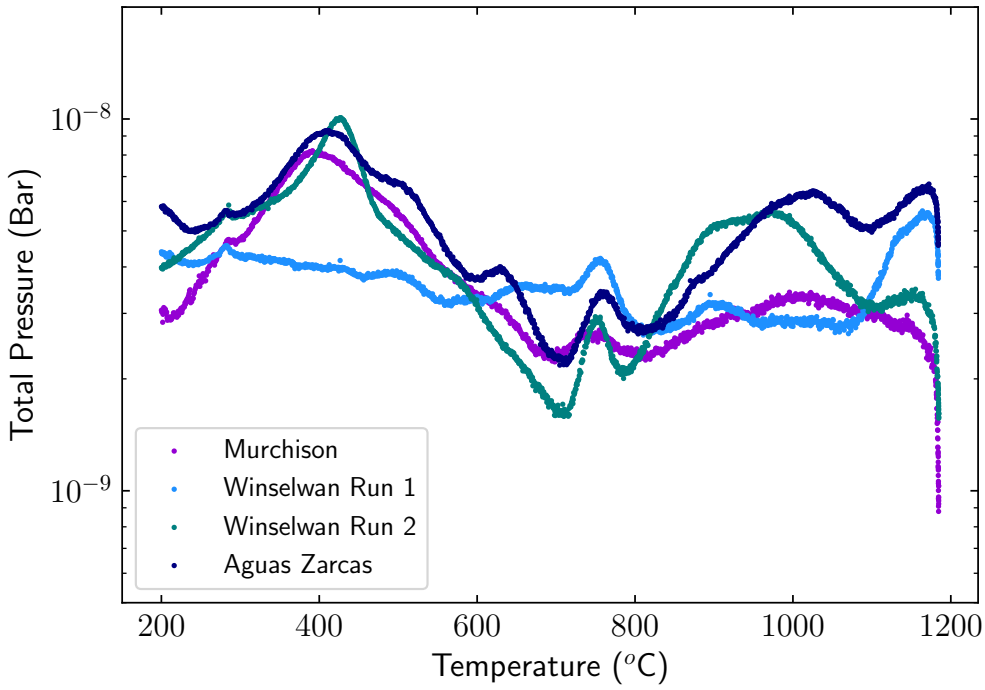

Figure 2.11: **Total pressure of measured volatiles released from the samples as a function of temperature.** Variations in total pressure with temperature suggest that the amount of outgassing varies throughout the experiment. The average difference between the maximum and minimum total pressure is 6E-9 bars. Most samples show an increase in total pressure near 400 °C.

1-5 and Supplementary Figures 2-4 have associated raw data that is available from https://github.com/maggieapril3/CMChondritesOutgassingData or from the corresponding author. The thermochemical equilibrium models used in Figures 3 and 4 are available from L.S. upon request.

Code Availability: The code used to calibrate and analyze the data used in this study is also available from https://github.com/maggieapril3/CMChondritesOutgassingData.

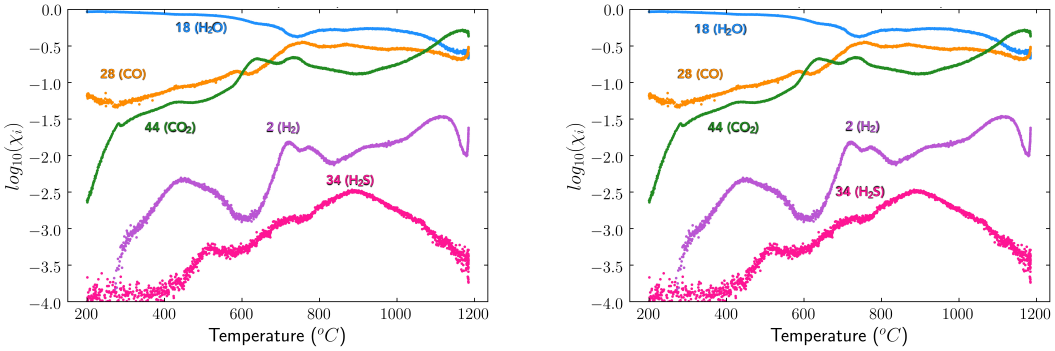

(a) Average of 3 CM Chondrite Samples with the Signal at 32 amu Not Separated into Sulfur and O_2 Components

(b) Average of 3 CM Chondrite Samples with the Signal at 32 amu Separated into Sulfur and O_2 Components

Figure 2.12: **Comparison between original results and results of separating the 32 amu signal into sulfur and O_2 components**. Figure (a) shows the outgassing abundances in which the signal at 32 amu is not separated into the sulfur and O_2 components (i.e., Figure 2.3 (b)). Figure (b) shows the results of separating the signal at 32 amu into its sulfur and O_2 abundances.

Table 2.3: **Table of the mass spectrum for each gas species in our experiments.** For the ten masses measured during the experiments, several could correspond to gas molecules that, when ionized by the RGA, produce fragments that contribute to the signal of other masses measured. For each of the gas species that correspond to one of the ten measured masses, we used the mass spectrum from National Institute of Standards and Technology (NIST)'s Mass Spectrometry Data Center to determine the possible ion fragments (NIST & Wallace 2018). We also include an additional ion fragment for water at 2 amu from MKS (MKS 2005). For each species in the table, we list the mass numbers of its known ion fragments and their signal intensities relative to the major peak due to the gas species itself (i.e., the signal percentage of the gas species is 100%). In the last column, we provide the normalized signal intensities (i.e., all of the signals sum to 100%). We only list ion fragments whose mass numbers correspond to those measured in our outgassing experiments. For atoms and species that either do not suffer from ion fragments or whose fragments correspond to masses that we do not measure, we assume all of its signal is concentrated at its mass number.

Gas Species	Mass Number (amu)	% of Signal Relative to Major Peak	Normalized % of Signal
H_2:	2	100	100
C:	12	100	100
N:	14	100	100
CH_4:	16	100	79.99
	14	20.7	16.56
	12	4.31	3.448
O:	16	100	100
H_2O:	18	100	96.62
	16	1.5	1.449
	2	2	1.932
CO:	28	100	93.11
	16	2.2	2.048
	12	5.2	4.842
N_2:	28	100	87.72
	14	14	12.28
S:	32	100	100
O_2:	32	100	81.97
	16	22	18.03
H_2S:	34	100	68.97
	32	45	31.03
Ar:	40	100	100
CO_2:	44	100	77.58
	28	10.2	7.913
	16	9.8	7.603
	12	8.9	6.905

Table 2.4: **Previously determined average bulk composition of CM chondrites and Murchison from literature** [a](Alexander et al. 2012), [b](Nittler et al. 2004), [c](Fuchs et al. 1973). The uncertainties are the 1σ standard deviations.

Element	Average CM Chondrite	Murchison
H	11.5±0.18[a] mg/g	10.7±0.002[a] mg/g
C	19.5±3.24[a] mg/g	20.8[a] mg/g
N	996.5±280[a] μg/g	1050[a] μg/g
O	412.0±0.75[a,b] mg/g	410[b] mg/g
S	33±9.0[b] mg/g	14[c] mg/g
K	400[b] μg/g	280[c] μg/g
Na	4.1[b] mg/g	4.2[c] mg/g

Table 2.5: **Comparison of primary algebraic data analysis and Monte Carlo non-linear least squares (MC) data analysis for Murchison.** The second and third columns show the average partial pressure (in bars) for each species. The fourth column shows the standard deviation of the average partial pressure for each species analyzed using the Monte Carlo technique. These partial pressures are corrected for ion fragments and atmospheric adsorption but have not been background subtracted.

Species	Primary Analysis	MC Analysis	Standard Deviation of MC Analysis
H_2	1.9E-10	3.4E-10	1.1E-10
C	0.0	1.3E-13	1.4E-25
N	0.0	0.0	0.0
CH_4	0.0	3.5E-10	9.7E-11
O	–	0.0	0.0
H_2O	7.6E-09	7.3E-09	1.9E-09
N_2	0.0	0.0	0.0
CO	1.2E-09	2.6E-09	6.3E-10
S	0.0	6.4E-10	1.0E-10
O_2	0.0	0.0	0.0
H_2S	8.5E-12	5.8E-12	2.2E-12
Ar	0.0	0.0	0.0
CO_2	6.9E-10	5.3E-10	2.9E-10

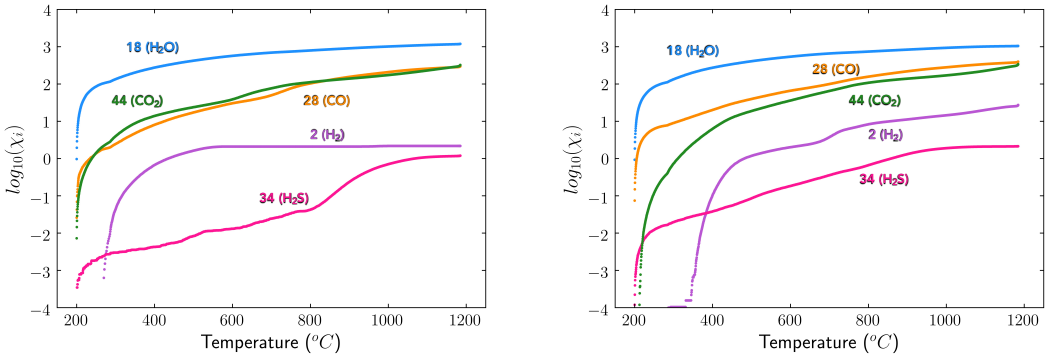

(a) Murchison

(b) Winselwan

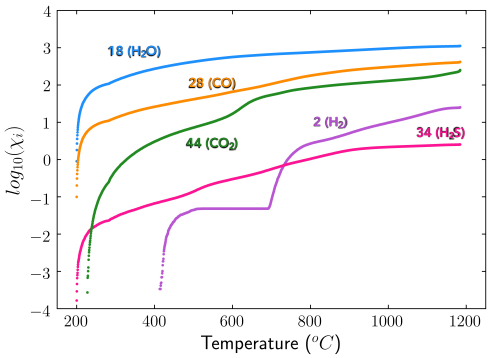

(c) Aguas Zarcas

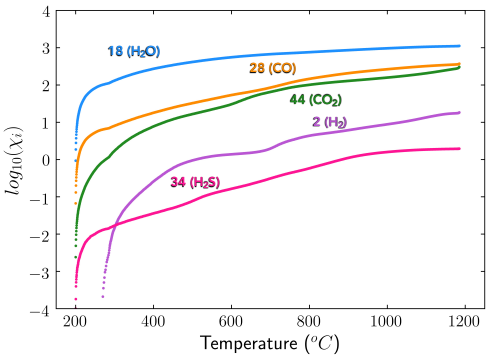

(d) Average of 3 CM Chondrites

Figure 2.13: **Cumulative Outgassing Abundances**. The cumulative outgassing trends for samples of (a) Murchison, (b) Jbilet Winselwan, (c) Aguas Zarcas, and (d) the average of the three CM chondrite samples.

Chapter 3

Outgassing composition of the Murchison meteorite: Implications for volatile depletion of planetesimals and interior-atmosphere connections

for terrestrial exoplanets

3.1 Introduction

We are entering an exciting new technological era in astronomy with NASA's recently launched James Webb Space Telescope (JWST) and upcoming large-aperture ground and space-based telescopes. These new observatories will allow us to begin characterizing terrestrial exoplanets and gain insights into their formation histories. For the foreseeable future, the main avenue for characterizing terrestrial exoplanets is through observations of their atmospheres. In addition, the primary technique for studying terrestrial planet formation in other stellar systems involves analyzing the chemistry in protoplanetary disks and, in particular, the inner regions of these disks. JWST observations are already planned to observe both the atmospheres of several known terrestrial exoplanets and the inner-regions of protoplanetary disks (e.g., Mansfield et al. (2021); Kreidberg et al. (2021); Salyk et al. (2021)). In order to optimize the use of this upcoming observational data, we need comprehensive theoretical tools to model the expected diversity of these planets' atmospheres and formation regions. When possible, it is vital that experimental data is used to inform these theoretical models. For example, laboratory data on molecular line lists is essential for spectroscopic studies of exoplanet atmospheres (e.g., Tennyson & Yurchenko (2018); Fortney et al. (2019)). With regards to terrestrial planet formation, bulk composition and early atmospheric properties, it is important to understand the building block materials of terrestrial planets. Solar Sys-

tem meteorites are the only direct analog samples to this primordial material unaltered by geologic processes and available for rigorous laboratory study.

Many terrestrial and other low-mass planets likely form their atmospheres via outgassing during and after accretion (Elkins-Tanton & Seager 2008). Even if accretion of nebular gas contributes to forming a terrestrial planet's early atmosphere, there are various situations under which the planet can lose these nebular gases early in its history, such as through small planetary mass, large impact events, and extreme-ultraviolet and X-ray flux from young host stars (e.g., Schlichting & Mukhopadhyay (2018); Lammer et al. (2018)). Planetary outgassing is a central process that controls terrestrial planet atmosphere formation. Therefore the composition of a terrestrial planet's early atmosphere prior to the magma ocean phase depends greatly on the composition of its interior building block materials that outgas to form such an atmosphere. In addition, volatile depletion of planetesimals via outgassing influences these bodies' final volatile inventories and those of the terrestrial planets into which they form. However, there is currently a limited understanding of the connection between a planet's interior composition and its early atmospheric properties that form during accretion. Traditional lines of thinking have claimed that the terrestrial planets in the Solar System formed out of material that is compositionally analogous to chondritic meteorites (i.e., chondrites) and achondritic meteorites (i.e., silicate achondrites and iron meteorites) (e.g., Lodders (2000); Lammer et al. (2018)). Recent work has shed some doubt on the idea that all of the Solar System's terrestrial planets, in particular Earth, can have their bulk compositions explained by combinations of known types of meteorites alone (e.g.,

Mezger et al. (2020); Burkhardt et al. (2021); Sossi et al. (2022)). Nevertheless, as meteorites are some of the only samples that preserve the composition of aggregate material in the protoplanetary disk during planet formation and are also available for direct laboratory study, it is essential to assay meteorites to inform the connection between terrestrial bodies (both planets and planetesimals), their volatile depletion patterns and their early atmospheres that form via outgassing during planetary accretion.

Chondrites are one of the three major types of meteorites, coming from undifferentiated planetesimals, meaning they did not experience significant heating to cause the body to melt and separate into a core and mantle. In general, chondrites can be divided into 15 groups: 8 carbonaceous (CI, CM, CO, CV, CK, CR, CH, CB), 3 ordinary (H, L, LL), 2 enstatite (EH, EL), and Rumuruti (R) and Kakangari-type (K) chondrites (Weisberg et al. 2006). The carbonaceous chondrites likely come from C-type asteroids which formed during the first few million years of the Solar System and are the most abundant type of asteroid in the main belt beyond 2.5 AU (Bell et al. 1989; Righter et al. 2006; Mezger et al. 2020). Among the different types of carbonaceous chondrites, CM chondrites are among the most volatile-rich and primitive materials in terms of their bulk composition (Lodders & Fegley 1998; Wasson & Kallemeyn 1988). Although CI-chondrites most closely match the composition of the solar photosphere for non-atmophile element ratios, they are very rare samples with limited material available for destructive experiments. CM chondrites are the second-best type of chondrite to use as there is more material available for study, they have the second closest bulk compositions to the solar photosphere, and they are among the most volatile-rich remnant

planet-forming materials. Since CM chondrites have similar bulk compositions to that of the solar photosphere, they represent a link between the composition of the material in the protoplanetary disk during planet formation and the stellar composition. CM chondrite-like material was also likely an important source of volatiles to the terrestrial planets during their formation (e.g., Lodders (2000); Marty (2012); Sakuraba et al. (2021)). Lastly, CM chondrites are an important material to use for understanding a preliminary connection to exoplanetary systems, since their bulk compositions are similar to that of the solar photosphere and, therefore, they may serve as representative volatile-rich planet-forming material around other Sun-like stars. As a result, CM chondrites are the focus of this study on the connection between interiors and early atmospheres for terrestrial planets and planetesimals both within and beyond our Solar System. In particular, we analyze the CM-chondrite Murchison. Like most CM chondrites, Murchison is of petrologic type 2 (i.e., CM2) meaning that it has experienced aqueous alteration but relatively less thermal alteration compared to other chondrite types like ordinary and enstatite chondrites (Fuchs et al. 1973; Weisberg et al. 2006). Murchison is predominantly composed of olivines, pyroxenes, and phyllosilicates along with metals, organics, sulfides, carbonates, oxides and Ca- and Al-rich glasses (Fuchs et al. 1973; Pizzarello & Shock 2010).

Theoretical work has been conducted on connecting terrestrial planet interiors to their initial atmospheric compositions. Some previous studies focused on Earth's early atmosphere, investigating outgassing during our planet's accretion (e.g., Abe & Matsui (1985); Matsui & Abe (1986); Zahnle et al. (1988, 2020); Lammer et al. (2018)),

while others investigated outgassing during a planet's magma ocean phase (e.g., Gaillard & Scaillet (2014); Herbort et al. (2020)). Several theoretical studies explored the outgassing compositions of primitive meteorites to inform terrestrial planets' and other rocky bodies' initial atmospheres (e.g., Schaefer & Fegley (2007, 2010); Herbort et al. (2020)). For example, a series of studies by Schaefer & Fegley used thermochemical equilibrium calculations to predict the outgassing compositions of a wide variety of chondrites, as a function of temperature and pressure, to inform the formation of terrestrial planets' early atmospheres during accretion (Schaefer & Fegley 2007, 2010). Although experimental data to constrain these models are limited, there have been many studies on heating of Murchison and other CM chondrites. As summarized in Tonui et al., prior studies have heated samples of Murchison and other carbonaceous chondrites under ambient conditions to inform thermal metamorphism on carbonaceous chondrite parent bodies (e.g., Clayton et al. (1997); Ikramuddin & Lipschutz (1975); Matza & Lipschutz (1977); Bart et al. (1980); Ngo & Lipschutz (1980)). For example, Tonui et al. heated several Murchison samples to temperatures between 400 and 1200 °C and then subsequently performed X-ray diffraction, electron beam and spectroscopic analyses on the sample residues to help interpret CM chondrites that did experience some amount of thermal alteration (Tonui et al. 2014). Some studies involved shock-induced devolatilization experiments to inform the contribution of chondrites to impact-induced atmosphere formation (e.g., Court & Sephton (2009)). A recent study by Braukmüller et al. (2018) measured the chemical compositions of a suite of carbonaceous chondrites and performed heating experiments on Murchison at ambient pressure under different

redox conditions to inform volatile depletion patterns in different planetary reservoirs (Braukmüller et al. 2018). A key limitation of these prior experimental studies for informing the outgassing models above is many of them focused on the effects of heating on the solid sample and did not study how the gas composition continuously varies as the samples are heated and volatiles are released.

To address some of the limitations of these prior experiments and to provide constraints for the theoretical models, a series of outgassing experiments was performed on three CM chondrites in which the abundances of various outgassing species were monitored (i.e., H_2O, CO, CO_2, H_2, H_2S) as a function of temperature to which the samples were heated (up to 1200 °C) under high-vacuum conditions ($\sim 10^{-4}$ Pa) (Thompson et al. 2021). These experiments simulated open-system outgassing conditions in which the composition of the meteorites changed as the temperature increased and volatiles were removed. Such open-system, low-pressure conditions are important for studying outgassing during the formation of planetesimals and early terrestrial planet atmospheres. However, this study was limited in its ability to measure all of the gas species that are predicted to outgas from CM chondrites according to chemical equilibrium models. In particular, the elements Fe, S, Ni, Co, P, and Mn are predicted to outgas in various elemental and molecular forms under chemical equilibrium conditions at temperatures ranging from ~600-1200 °C, but they were not monitored during the set of outgassing experiments of Thompson et al. (2021). Therefore, to fill this gap, we performed a series of heating experiments under two different pressure regimes and subsequent bulk element analyses on Murchison samples in order to experimentally de-

termine the outgassing trends of these heavier elements in CM chondrites. Combining the bulk element measurements of this study with the previous outgassing experiments provides a more complete understanding of Murchison's outgassing composition across a wide range of temperatures (∼400-1000 °C). These broad outgassing trends can be used to inform models of terrestrial planets' early atmospheres and volatile depletion of planetesimals along with upcoming observations of terrestrial exoplanet atmospheres.

In this paper, we first explain the set-up and procedure for the heating experiments and bulk element analysis (Section 3.2) and then present the results of the bulk elemental outgassing trends for the Murchison samples heated to a variety of temperatures under different pressure and redox conditions (Section 3.3). In Section 3.4, we discuss how to quantify the effects of the different experimental variables (e.g., pressure, redox state) and how these results compare to prior experimental and theoretical work on outgassing of CM chondrites. In Section 3.5, we explain the implications of these results for the formation and evolution of planetesimals and terrestrial planet atmospheres.

3.2 Methods

3.2.1 Heating Experiments

For this study, we analyzed powdered samples of the Murchison meteorite, a CM2 carbonaceous chondrite that fell in Australia in 1969 near Murchison, Victoria (Krinov 1970). The source of the Murchison samples is Mendy Ouzillou, SkyFall Meteorites, who obtained the specimens from a private collector. These meteorite fall samples

are minimally altered by terrestrial contamination as they were collected shortly after they fell and stored carefully prior to being acquired. Once we obtained the samples, we kept them in a desiccator prior to powdering to further minimize terrestrial alteration and hydration by the Earth's atmosphere. In addition, we further minimize weathering effects by using samples that have no fusion crust, the outermost layer that is altered during atmospheric entry. To prepare homogeneous samples for the heating experiments, a ∼2 cm piece of Murchison was powdered with an agate mortar and pestle and sieved to only include particle diameters between 20 and 106 μm, and then this bulk powder was separated into the samples used for the experiments. The powdered samples were kept in a vial and stored in a vacuum desiccator to minimize terrestrial contamination. Prior to each heating experiment, the vial was shook to further homogenize the powdered sample. A 6.5 mm×4.0 mm alumina crucible was used to hold each Murchison sample and was placed inside a larger 50 mm×20 mm×20 mm alumina combustion boat during each heating experiment. Two furnaces were used to perform the heating experiments. The first furnace is a Fisher Scientific Isotemp Programmable Forced-Draft Furnace that operates at atmospheric pressure (hereafter Furnace A), and the second is a Lindberg/Blue M 1700 °C Tube Furnace (hereafter Furnace B) connected to a Pfeiffer turbomolecular vacuum pump system that keeps the system in a high vacuum environment ($\sim 10^{-4}$ Pa). Furnace A is ventilated throughout all of the experiments and is only open to the atmosphere via a small ($\leq$1 inch) opening at the top of the furnace. For Furnace B, the pressure is monitored throughout each experiment using a pressure gauge, and we find that the pressure stays between $\sim 10^{-4}$ - 10^{-3} Pa ($\sim 10^{-9}$ - 10^{-8}

bar) throughout each experiment. Oxygen fugacity (fO_2) is a property that describes the chemical potential of oxygen in a system and affects the gas chemistry. Oxygen fugacity is a common way to describe the redox state of a planetary atmosphere or interior, which refers to how oxidized (i.e., O-rich) or reduced (i.e., O-poor) it is. Under low-pressure and near-ideal gas conditions, fO_2 can be equated to the partial pressure of oxygen in the gas phase. The experiments performed with Furnace A are operating in air and therefore simulate outgassing under a relatively oxidizing environment with fO_2=0.21 bar, whereas those performed with Furnace B simulate outgassing under more reducing conditions with fO_2 = 2.1E-10 - 2.1E-9 bar.

Prior to the heating experiments, all of the crucibles and the combustion boat were baked-out to degas adsorbed volatiles (Table 3.1). Each heating experiment used ∼4-5 mg of powdered Murchison sample, and before each experiment, we weighed the initial sample mass. As summarized in Table 3.1, we performed a series of experiments in which we heated Murchison samples up to 400, 600, 800 and 1000 °C (Figure 3.1). We performed two complete sets of heating experiments with Furnace A (i.e., eight Murchison samples were heated in total: two samples heated to 400 °C, two samples heated to 600 °C, two samples heated to 800 °C, and two samples heated to 1000 °C). We performed one set of heating experiments with Furnace B (i.e., four Murchison samples in total: one heated to 400 °C, one heated to 600 °C, one heated to 800 °C, and one heated to 1000 °C) (Table 3.1). After each experiment, we weighed the residue mass and calculated the amount of mass outgassed during the experiment. We stored all residue samples in the desiccator prior to the sample digestion process for the bulk

element analysis using inductively-coupled plasma mass spectrometry (ICP-MS).

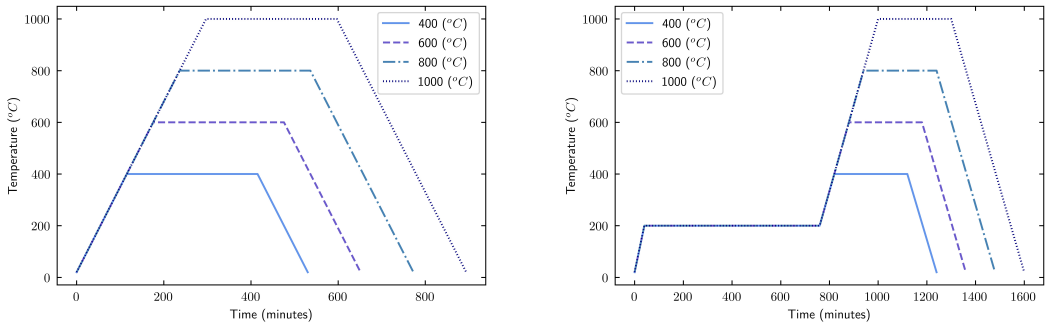

(a) Heating Schemes for Experiments at Atmospheric Pressure

(b) Heating Schemes for Experiments Under Vacuum

Figure 3.1: **The experimental heating procedures used for the two furnaces (temperature vs. time) to analyze the outgassing composition of Murchison.** (a) Heating schemes used for experiments performed with the furnace at atmospheric pressure (Furnace A). (b) Heating schemes used for experiments performed with the furnace operating in a high vacuum environment (Furnace B). Each set of experiments heated Murchison samples to 400, 600, 800 and 1000 °C.

3.2.2 Sample Digestion and ICP-MS Analysis

A total of 14 Murchison samples (eight samples heated with the furnace at atmospheric pressure, four samples heated with the furnace under vacuum, and two unheated Murchison samples), multiple rock standards, and a procedural blank were digested for ICP-MS analysis. For the Murchison samples heated at atmospheric pressure, the mass of the residual powder that was analyzed after the heating experiments was ∼4 mg for each sample, and for the Murchison samples heated under vacuum, the mass of the residual powder that was analyzed after the heating experiments was ∼2 mg for each sample (see Table 3.5). All samples were weighed into clean 7 ml Savillex perfluoroalkoxy (PFA) beakers. All reagents used were either triple-distilled or purchased at

ultra-pure trace metal grade and diluted with ultra-pure deionized (18 MΩ-cm) water. All acids are concentrated unless a molarity (M) or % dilution is specified.

Samples were digested with 1 ml HNO_3 and 0.5 ml HF and refluxed at 110 °C (i.e., heated in the PFA beakers with the lids on) for ∼36 hours. Next, the samples were evaporated to dryness and refluxed at 110 °C in 2 ml HCl and 0.5 ml HNO_3 for ∼24 hours. The samples were evaporated and refluxed for ∼24 hours in 2 ml ∼5M HCl with 50 μl of 2.5M HCl saturated with H_3BO_3 to mask fluoride complexes. We converted the dissolved samples from chloride to nitrate salts by sequentially evaporating, rehydrating, and refluxing for >2 hours with the following solutions: ∼1 ml 2M HCl, 2 ml 7M HNO_3, and 1 ml HNO_3. Throughout the digestion process, we visually inspected all of the beakers to ensure that there were no leftover undigested solid phases (e.g., fluoride precipitates, carbon solids). To prepare the final sample dilutions, the samples were dissolved in 5 ml of 5% HNO_3 with trace HF and fluxed for ∼1 hour and spiked with 100 μl of internal standard solution that contains In, Re, Rh, Bi at 1 ppm in 1% HNO_3. The final sample solutions were diluted by a factor of ∼1000 for analysis.

A Thermo Fisher Scientific Element XR (eXtended Range) magnetic sector high-resolution inductively-coupled plasma mass spectrometer (ICP-MS) at the Plasma Analytical Lab at UCSC analyzed the following isotopic intensities for each of the Murchison samples: ^{51}V, ^{61}Ni, ^{59}Co, ^{26}Mg, ^{57}Fe, ^{52}Cr, ^{31}P, ^{55}Mn, ^{66}Zn and ^{32}S. Instrumental settings, performance and acquisition parameters are outlined in Table 3.6. Tables 3.2- 3.4 and Table 3.7 show the measured ICP-MS intensities and analytical uncertainties (i.e., relative standard deviations (RSD), expressed as a %) for all samples,

rock standards and procedural blank. Despite the small sample masses, the ICP-MS signals are robust as evidenced by the fact that the samples' signal intensities exceed the intensities of the total procedural blank by at least an order of magnitude for the vast majority of the samples. In addition, the ICP-MS measurements for all the samples and the procedural blank had low analytical uncertainties (<6 %) (Table 3.4, Table 3.7).

Table 3.1: **Summary of the bake-out scheme prior to the heating experiments (top) and the steps for the heating experiments performed with Furnace A (middle) and B (bottom).** We performed two complete sets of heating experiments with Furnace A (i.e., eight Murchison samples were heated in total), and we performed one set of heating experiments with Furnace B (i.e., four Murchison samples heated).

Bake-Out of Crucibles and Combustion Boat:	
Furnace A:	1000 °C for 5 hrs.
Furnace B:	1400 °C for 5 hrs.
Furnace A Heating Steps:	
Step 1:	Insert Sample into Furnace
Step 2:	Heat from Room Temperature (T) to Desired T* at 3.3 °C/min
Step 3:	Hold at Desired T for 5 hrs.
Step 4:	Cool to Room T at 3.3 °C/min
Furnace B Heating Steps:	
Step 1:	Insert Sample Into Furnace
Step 2:	Heat from Room T to 200 °C over 40 mins.
Step 3:	Hold at 200 °C for 12 hrs.
Step 4:	Heat from 200 °C to Desired T at 3.3 °C/min.
Step 5:	Hold at Desired T for 5 hrs.
Step 6:	Cool to Room T at 3.3 °C/min.
	*Desired T: 400, 600, 800, or 1000 °C.

3.3 Results

Tables 3.2 and 3.3 show the signal intensities, in counts per second (cps), of Mg, P, S, V, Cr, Mn, Fe, Co, Ni, and Zn in the Murchison samples heated under atmospheric pressure and vacuum conditions, respectively, compared to those of the two unheated Murchison samples. Table 3.4 shows the analytical uncertainties (RSD, expressed as a %) for all of the Murchison samples. Figures 3.2(a) and 3.3(a) illustrate how the elements' intensities normalized to vanadium (V) (hereafter referred to as normalized intensities) change between the unheated samples and the residues heated to different temperatures under atmospheric pressure and vacuum conditions, respectively. We chose to normalize to V because it is a refractory element in carbonaceous chondrites and is the most cosmochemically refractory element measured in this study (Lodders 2003). As shown in Figure 3.2(a), we find that most elements, namely Ni, Co, Mg, Fe, Cr, P, Mn, and Zn, did not change significantly in normalized signal intensity between the unheated samples and the residues from each of the stepped-heating experiments using the furnace operating at atmospheric pressure. Sulfur varied the most over the course of the heating experiments at atmospheric pressure, with a large decrease in its intensity (by a factor of 2-3) between the residues that were heated to 600 °C to the residues heated to 800 °C. The residues heated to 1000 °C contained an order of magnitude lower signal intensity compared to those heated to 800 °C which suggests significant loss of sulfur during this heating experiment. Sulfur's decrease in intensity across the different samples suggests that significant outgassing occurred from the Murchison samples, especially during the heating experiments at 800 and 1000 °C.

The same general trends are observed when examining the intensities normalized to V and the average of the two unheated Murchison samples (Figure 3.2(b)). However, for the S measurement for the sample heated to 400 °C and all of the Zn measurements, their normalized intensities exceed the unheated values (i.e., ratio > 1). For the 400 °C S measurement, its percent difference relative to the unheated samples is ∼7 %, which is similar to the average analytical uncertainty (i.e., average relative standard deviation) for all the elements (∼4 %). However, the Zn enrichment is more significant, with percent differences relative to the unheated samples averaging ∼16 % for the heated samples. These enrichments are likely due to minor heterogeneities in the samples.

As illustrated in Table 3.8, to compare the normalized intensities of the residues from the two sets of heating experiments performed under atmospheric pressure along with the two unheated samples, we calculated the percent difference between each element's normalized signal intensity from the two residue samples heated to the same temperature (or in the unheated case, from the two unheated samples). We calculated the percent difference using the following formula:

$$\% \text{ Difference} = \frac{|C_1 - C_2|}{\frac{(C_1+C_2)}{2}} \times 100 \tag{3.1}$$

where C_1 and C_2 are an element's normalized intensities from the two residues heated to the same temperature using the furnace at atmospheric pressure (or in the unheated case, from the two unheated samples). For the unheated Murchison samples, the percent differences between the normalized intensities are all less than or equal to 2 % (1σ),

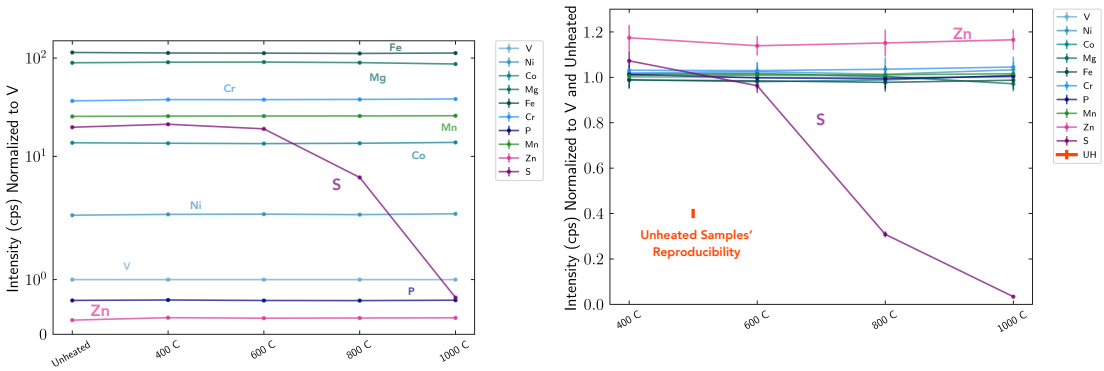

(a) Sample Intensities Normalized to V

(b) Sample Intensities Normalized to V and the Unheated Murchison Samples

Figure 3.2: **Average intensities from the unheated Murchison samples and the residues from the sets of stepped-heating experiments performed at atmospheric pressure (10^5 Pa/1 bar).** (a) Intensities normalized to V, (b) Intensities normalized to V and the average of the two unheated Murchison samples. The analytical uncertainties in (a) and (b) are the 1σ standard deviations for the normalized data propagated from the RSD uncertainties of Table 3.4. In (a) the uncertainties are smaller than the datapoints. In (b), the red vertical line represents the reproducibility between the V-normalized intensities of the two unheated Murchison samples, expressed as the maximum relative difference calculated using Equation 3.1. The x-axis refers to the temperature to which the residues were heated with "unheated" corresponding to the average of the two unheated Murchison samples and "400 C" corresponding to the average of the two residues heated to 400 °C, etc.

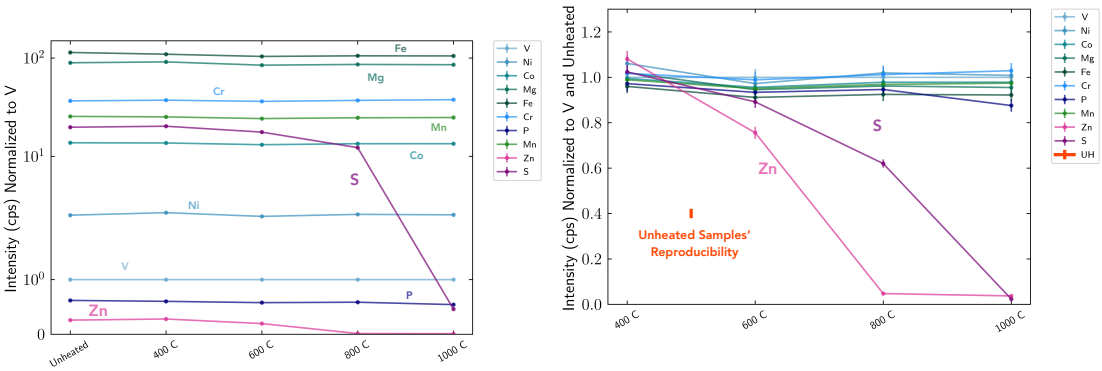

(a) Sample Intensities Normalized to V

(b) Sample Intensities Normalized to V and the Unheated Murchison Samples

Figure 3.3: **Average intensities from the unheated Murchison samples and the set of stepped-heating experiments performed in a high vacuum environment ($\sim$10^{-4}Pa/10^{-9} bar).** (a) Intensities normalized to V, (b) Intensities normalized to V and the average of the two unheated Murchison samples. The analytical uncertainties in (a) and (b) are the 1σ standard deviations for the normalized data propagated from the RSD uncertainties of Table 3.4. In (a) the uncertainties are smaller than the datapoints. In (b), the red vertical line represents the reproducibility between the V-normalized intensities of the two unheated Murchison samples, expressed as the maximum relative difference calculated using Equation 3.1. The x-axis refers to the temperature to which the residues were heated with "unheated" corresponding to the average of the two unheated Murchison samples and "400 C" corresponding to the residue heated to 400 °C, etc.

confirming that internal reproducibility is well within the average analytical uncertainty (Figures 3.2b and 3.3b). For the residues heated to 400 °C, Zn has the greatest percent difference of 33 %, but the other elements have percent differences less than 11 %. For the residues heated to 600 °C, Zn and S have the greatest percent differences of 20 and 14 % respectively, and all other elements have percent differences less than 10 %. For the normalized intensities of the residues heated to 800 °C, once again Zn and S have the greatest percent differences of 26 and 39 %, respectively. Finally, for the residues heated to 1000 °C, all of the elements have percent differences less than ∼15 % (Table 3.8).

As Figure 3.3(a) shows, for the set of heating experiments performed in a high-vacuum environment, the normalized intensities of Ni, Co, Mg, Cr, P, Fe, and Mn did not vary significantly across the samples. As shown in both Figure 3.3(a) and (b), sulfur's intensity varies over the set of heating experiments with it being an order of magnitude lower for the residue heated to 1000 °C compared to the unheated samples and other residues, just as with the samples heated to 1000 °C under atmospheric pressure. Therefore, during this set of stepped heating experiments, the sample heated to 1000 °C experienced significant outgassing of sulfur. Zinc's intensity also varies greatly in this set of heating experiments under vacuum, decreasing by over an order of magnitude for the residues heated to 800 and 1000 °C compared to the unheated samples and residues heated to lower temperatures, suggesting significant outgassing of Zn during these two heating experiments. The differences in the outgassing trends for S and Zn observed in these sets of heating experiments could be due to the pressure and

redox conditions, as discussed further in the next section. For example, the fact that Zn outgases significantly at the highest temperatures under vacuum conditions but not under atmospheric pressure suggests that lower pressure conditions promote degassing of Zn. In addition, this difference in Zn's outgassing behavior between the two sets of experiments could also be due to the different redox conditions, with the experiments performed under atmospheric pressure being more oxidizing compared to those under vacuum. A more quantitative investigation of the effects of these experimental variables is provided in the next section.

By examining the intensities normalized to both V and the average of the unheated Murchison samples for the samples heated under vacuum (Figure 3.3(b)), we can see that there is slightly more variation in the other elements' signals such as Ni and P. In this figure, P's intensity for the residue heated to 1000 °C is lower than that for the other residues heated to lower temperatures and the unheated samples, which may indicate slight outgassing of P at the highest temperatures. The cause of these variations in the other elements' intensities for the experiments performed under vacuum is uncertain. They could be due to heterogeneities in the samples possibly due to physical sorting during sample preparation (e.g., sorting of accessory phases like metal and magnetite causing some aliquots to have a greater abundance of Ni-hosting mineral phases compared to others (Menzies et al. 2005)) (see Section 3.5).

Table 3.2: **Intensities in counts per second (cps) for the two sets of Murchison samples heated under atmospheric pressure following the procedures outlined in Figure 3.1(a) determined by ICP-MS analysis.** The M-400 (1) and M-400 (2) columns show the intensities for the samples heated to 400 °C, and so on for the samples heated to 600, 800, and 1000 °C. The elements are listed in order of increasing atomic mass.

	M-400 (1)	M-400 (2)	M-600 (1)	M-600 (2)	M-800 (1)	M-800 (2)	M-1000 (1)	M-1000 (2)
Mg	17477811	25305512	18878687	19789443	19239591	22248901	20891728	28321135
P	127630	164853	137015	125366	142200	140562	153782	196848
S	4209065	5736516	4305460	3779425	1574352	1205515	153876	229145
V	193300	278072	211341	213560	216528	244859	236895	330248
Cr	7505883	10214594	8127006	7899891	8433478	9048714	9212195	12455276
Mn	5144041	6865671	5636696	5288440	5833572	6012278	6358103	8233937
Fe	22892406	29686727	24726993	22916881	25630126	25567575	27860425	35450579
Co	2723570	3637749	2927189	2795086	3070520	3176171	3362124	4465933
Ni	513856	687386	556754	539334	571538	602923	635414	832022
Zn	68192	70207	68230	56448	72720	63074	76797	91310

Table 3.3: **Intensities in counts per second (cps) for the set of Murchison samples heated under a high-vacuum environment ($\sim 10^{-4}$ Pa) following the procedures outlined in Figure 3.1(b) and the two unheated Murchison samples (M-UH) determined by ICP-MS analysis.** For the unheated Murchison samples, the average of the two samples is used in Figures 3.2 and 3.3. The elements are listed in order of increasing atomic mass.

	M-UH (1)	M-UH (2)	M-400	M-600	M-800	M-1000
Mg	20913327	24820001	17478014	34325817	26867055	30183350
P	145387	170738	115127	234460	182846	191397
S	4655929	5434405	3871570	7149632	3825466	162793
V	233150	277755	191307	405567	312092	353042
Cr	8520414	10208430	7130654	14697806	11573719	13314976
Mn	5945087	7071437	4820602	9819663	7701807	8762455
Fe	26597343	31608453	20921379	42110747	32880045	37088915
Co	3218042	3797360	2614786	5323911	4193445	4744623
Ni	591053	694435	510997	992714	800947	896097
Zn	60535	71074	53299	79024	3814	3375

Table 3.4: **ICP-MS analytical uncertainties (i.e., relative standard deviations (RSD)) for all Murchison samples analyzed.** Each value shows the RSD of the intensity (expressed as a %) measured by the ICP-MS. UH (1) and UH (2) refer to the two unheated samples of Murchison. Columns 400 (1), 600 (1), 800 (1), and 1000 (1) show the RSDs for the first set of samples heated under atmospheric pressure. Columns 400 (2), 600 (2), 800 (2), and 1000 (2) show the RSDs for the second set of samples heated under atmospheric pressure. Lastly, columns 400 (3), 600 (3), 800 (3), and 1000 (3) show the RSDs for the set of samples heated under vacuum.

	UH (1)	UH (2)	400 (1)	400 (2)	400 (3)	600 (1)	600 (2)	600 (3)	800 (1)	800 (2)	800 (3)	1000 (1)	1000 (2)	1000 (3)
Mg	1.2	0.8	1.5	1.6	0.9	0.3	0.7	0.8	1.1	0.4	0.5	0.4	0.5	0.5
P	1.0	1.4	0.4	1.2	1.4	0.5	0.7	1.6	2.0	0.5	1.1	1.4	1.0	0.5
S	0.7	1.0	1.7	1.3	1.2	0.8	1.0	0.7	1.8	1.0	0.3	1.0	1.4	0.5
V	0.3	2.2	1.5	1.5	1.0	0.6	0.9	0.8	2.5	0.2	1.0	1.0	1.4	0.5
Cr	1.8	1.1	1.4	0.6	1.5	0.8	1.1	1.1	3.3	0.3	1.0	1.0	2.1	0.5
Mn	0.3	0.9	1.6	0.8	0.8	0.9	1.0	0.7	1.9	0.5	0.1	0.2	1.6	0.6
Fe	0.5	1.4	1.6	0.2	0.2	0.7	1.2	0.3	1.7	0.8	0.9	1.3	1.4	0.3
Co	1.1	1.1	1.1	0.5	0.9	0.6	1.2	0.9	1.6	0.7	1.0	0.5	0.8	0.1
Ni	1.2	1.1	2.2	1.2	1.0	2.0	0.6	0.9	0.7	0.8	0.5	1.0	0.1	0.9
Zn	0.4	1.7	2.6	1.9	0.2	1.4	0.9	1.4	2.8	1.8	2.3	1.6	0.4	4.2

3.4 Discussion

3.4.1 Effects of Experimental Variables on the Degree of Vaporization

In our sets of heating experiments, we explicitly varied multiple experimental variables, namely the pressure and redox (fO_2) state. In the experiments performed under atmospheric conditions, the total pressure is 1 bar, consisting of 0.79 bar N_2 and 0.21 bar O_2, and therefore the fO_2 is 0.21 bar. The experiments performed under vacuum have a total pressure of $\sim 10^{-8}$-10^{-9} bar and a low fO_2 of ~2.1E-9 - 2.1E-10 bar. As degassing occurred in the vacuum chamber, the fO_2 may have changed. To understand the effect of pressure on the degree of elemental loss for the elements of interest (i.e., sulfur and zinc), we can use the Hertz-Knudsen-Langmuir (HKL) equation:

$$\frac{dn_i}{dt} = -A\frac{\alpha_e p_i - \alpha_c p_{i,s}}{\sqrt{2\pi R M_i T}} \tag{3.2}$$

where $\frac{dn_i}{dt}$ is the evaporation rate of species i (mol/s), A is the surface area (m^2), p_i is the equilibrium partial pressure of the gas species of element i (Pa), $p_{i,s}$ is its actual partial pressure at the surface (Pa), α_e and α_c are the dimensionless Langmuir coefficients for evaporation and condensation, M_i is its molar mass (kg/mol), R is the gas constant (J/mol K) and T is the temperature (K) (Chapman & Cowling 1970; Richter et al. 2002; Sossi et al. 2019). The value of element i's $p_{i,s}$ is dependent on the system's total pressure (P) due to the dependence of the binary diffusion coefficient (D) on total pressure as $D \propto \frac{1}{P}$ (Chapman & Cowling 1970; Bartlett 1967; Sossi et al. 2020b). The binary diffusion coefficient refers to a gas species in a binary gas mixture.

This dependence comes from the fact that at lower pressures, the mean free path of a gas is much longer and therefore there are fewer collisions, causing a faster diffusion rate of the gas away from the evaporating surface. As a result, at a given temperature, the evaporation rate of species i will increase with decreasing pressure (Chapman & Cowling 1970; Richter et al. 2011; Sossi et al. 2020b). The HKL equation demonstrates how the system's pressure influences the vaporization rate of Zn in our experiments, with Zn outgassing in the experiments performed under lower pressure (vacuum conditions) but not at higher (i.e., atmospheric) pressure.

In order to quantify the effects of fO_2 on the degree of elemental loss, we can consider the vaporization reactions for sulfur and zinc. Most sulfur in chondrites is present as sulfides, while zinc can occur in sulfides and silicates (Nozaki et al. 2006; King et al. 2021; Nishimura & Sandell 1964). The vaporization reactions for Zn in sulfides and their corresponding equilibrium constants (K_p) include:

$$2ZnS(s) \longrightarrow S_2(g) + 2Zn(g) \tag{3.3}$$

with

$$K_p = \frac{p_{S_2} p_{Zn}^2}{1} \tag{3.4}$$

or

$$ZnS(s) + O_2(g) \longrightarrow SO_2(g) + Zn(g) \tag{3.5}$$

and

$$K_p = \frac{p_{SO_2} p_{Zn}}{p_{O_2}} \tag{3.6}$$

These reactions and their associated equilibrium constants suggest that if most Zn resides in sulfides, then its partial pressure is proportional to fO_2. However, if Zn is in silicates and/or oxides in Murchison, as has been demonstrated by Sossi et al. 2019 to be the case for silicate melts where the stable melt component is ZnO, its evaporation reaction may look like (Sossi et al. 2019):

$$ZnO(s,l) \longrightarrow Zn(g) + \frac{1}{2}O_2(g) \tag{3.7}$$

with

$$K_p = \frac{p_{Zn} p_{O2}^{\frac{1}{2}}}{1} \tag{3.8}$$

It is important to note that in equations 3.4, 3.6, and 3.8, we are assuming pure phases for clarity and to demonstrate the proportionality relationships between partial pressure and fO_2. If Zn is predominantly in silicates or oxides, then this evaporation reaction suggests that Zn's partial pressure will be proportional to $fO_2^{-0.5}$. Therefore, fO_2 has an opposite effect on the vaporization of Zn depending on whether Zn resides mainly in sulfides or in silicates/oxides. Based on our findings that in the experiments with lower fO_2 we observe significant outgassing of Zn whereas in the experiments at higher fO_2 we do not observe any Zn outgassing, it would suggest that the main type of reaction taking place is with Zn evaporating from silicates or oxides (Eq. 3.7) rather than sulfides. However, we note that prior studies have shown that Zn can reside in silicates and sulfides in CM chondrites, which may indicate that pressure is the main

variable influencing Zn's outgassing trends. The HKL equation also shows the effects of surface area (A) and time interval (dt) over which evaporation occurs, which we discuss in the subsequent section on comparing our findings with prior experimental studies. We discuss these experimental variables and their effects on vaporization further in the subsequent sections.

3.4.2 Comparison with Prior Experimental Studies

Prior experimental studies on outgassing of carbonaceous chondrites, especially Murchison, that monitored various major and trace elements include Braukmüller et al. (2018); Matza & Lipschutz (1977); Mahan et al. (2018); Pringle et al. (2017); Burgess et al. (1991); Wulf et al. (1995); Springmann et al. (2019); Tonui et al. (2014). These studies analyzed the loss of sulfur, zinc and other labile elements during heating of Murchison due to the breakdown and transformation of various mineral phases (e.g., tochilinite and pyrrhotite to metal for sulfur). For example, Burgess et al. (1991) focused on sulfur released by stepped combustion experiments with Murchison and determined that Murchison releases the highest yield of sulfur at ~800 °C and smaller amounts at 1000 °C (Burgess et al. 1991). This result is broadly consistent with our results for Murchison samples heated under atmospheric pressure. A more recent study by Braukmüller et al. (2018) investigated volatile element depletion patterns of carbonaceous chondrites, including Murchison, by performing heating experiments up to 1000 °C in O_2 and argon gas streams. The broad outgassing trends between our experiments and those of Braukmüller et al. (2018) are similar; they detect loss of S during their samples heated under O_2 (high fO_2) and they detect loss of Zn from the samples heated

under Ar gas (lower fO_2). Their results support our findings that Zn outgasses at lower fO_2, suggesting that a main type of reaction taking place is with Zn evaporating from silicates or oxides. However, overall our experiments show more significant outgassing of S and Zn compared to their study. This difference may be due to the fact that the time interval (dt) of our heating experiments is longer compared to that of Braukmüller et al. (2018), which contributes to more evaporation of both S and Zn (Eq. 3.2). In addition, our vacuum experiments, for which we detect outgassing of both S and Zn, were performed at much lower pressures compared to those of Braukmüller et al. (2018), which also supports more significant outgassing in our experiments compared to their study.

Wulf et al. (1995) heated Murchison samples to ∼1350 °C under air and various oxygen fugacities and found that Zn volatilized more readily under reducing conditions compared to oxidizing conditions. As described in Section 3.4.1, assuming Zn resides primarily in silicates or oxides, this can be explained by examining the vaporization reaction of Eq. 3.7 and its equilibrium constant expression (Eq. 3.8), which demonstrates that Zn's partial pressure is proportional to $fO_2^{-0.5}$. Therefore, more reducing conditions lead to larger Zn partial pressures and a larger vaporization rate for Zn according to the HKL equation (Eq. 3.2). For our experiments, both total pressure and fO_2 decrease in tandem between our sets of experiments at atmospheric pressure and those under vacuum conditions. If Zn primarily resides in silicates or oxides in our samples as well, then both the fO_2 and total pressure decrease can contribute to the larger vaporization rate of Zn observed in our vacuum experiments (see Section 3.4.1). If however most of

the Zn resides in sulfides, then the total pressure is likely the main effect causing an increase in Zn's evaporation rate for the experiments under vacuum compared to those at atmospheric pressure (Eq. 3.2 and Section 3.4.1). Another study that demonstrates the effect of total pressure on Zn's outgassing rate is Matza & Lipschutz (1977). In this study, they heated Murchison samples in a low-pressure (∼2E-5 to 6E-4 bar) environment and found similar outgassing trends for Zn as with our study, showing that lower pressure conditions promote high vaporization rates for Zn (Figure 3.3, Eq. 3.2).

Mahan et al. (2018) recently analyzed volatile element abundances for several CM chondrite samples that are volatile depleted and have petrologic signs of heating (>700 °C). They found that these samples likely underwent open system heating and had depleted concentrations in Zn compared to less thermally-altered samples, consistent with our study and Matza & Lipschutz (1977). The findings of Mahan et al. (2018) support the importance of our open-system outgassing experiments for understanding volatile depletion of planetesimals. Another recent study by Springmann et al. (2019) heated Murchison samples to ∼900 °C under vacuum and found that they lost the most significant amount of sulfur between ∼300-400 °C with some continued loss up to 800 °C. The difference in sulfur's outgassing trends between this study and our experiments under vacuum could be due to the fact that the evaporating surface area in Springmann's experiments was larger than ours as they used larger sample containers (5 mm×7 mm boats) compared to ours (6.5 mm×4 mm). The HKL equation demonstrates that a larger surface area (A) contributes to a higher vaporization rate (Eq. 3.2), and therefore S likely degassed more readily and early in their experiments. Overall, these prior

experimental studies are broadly consistent with the findings of our study, mainly that sulfur (under both atmospheric pressure and vacuum) and zinc (under vacuum) outgas when samples are heated to temperatures above ~800 and ~600 °C, respectively.

3.4.3 Comparison with Our Outgassing Experiments and Thermochemical Equilibrium Models

Combining these bulk element outgassing trends determined by ICP-MS with the previous outgassing experiments of Thompson et al. (2021) that monitored the abundances of highly volatile species (e.g., H_2O, CO, CO_2, H_2S) degassing from a Murchison sample, we gain a more complete understanding of the outgassing compositions over a wide range of temperatures (~400-1000 °C). Using a furnace connected to a residual gas analyzer mass spectrometer and a vacuum system, these outgassing experiments monitored the abundances of up to 10 volatile species composed of hydrogen, carbon, oxygen, sulfur and nitrogen released from a 3 mg powdered Murchison sample as a function of temperature from 200-1200 °C heated at a rate of 3.3 °C/min under a high-vacuum environment (~ 10^{-4} Pa) (Thompson et al. 2021). In this study, they took multiple measures to minimize terrestrial contamination of adsorbed water and other volatile species including holding the sample at a low temperature prior to taking measurements and correcting the data for the background signal (see Thompson et al. (2021) for more details). This study measured significant outgassing of H_2O (~72%), CO (~13 %), CO_2 (~15 %), and smaller quantities of H_2 (~0.2 %) and H_2S (~0.05 %) from the Murchison sample (all percentages are relative to the total volatile species measured). Figure 3.4 (lower panel) shows the experimental outgassing composition,

expressed as mole fractions of various gas species, as a function of temperature to which the Murchison sample was heated. Comparing the outgassing trend of H_2S from Figure 3.4 (lower panel) with this study's bulk element measurements of sulfur outgassing from the stepped heating experiments performed under vacuum (Figure 3.4 top panel), we find that in both cases significant outgassing of sulfur begins at ∼800 °C. As Figure 3.4 illustrates, H_2S starts to outgas significantly at ∼800 °C and peaks in its outgassing abundance at ∼1000 °C. This is consistent with our bulk element studies which indicate some outgassing of sulfur during the experiment at 800 °C and very significant outgassing of sulfur at 1000 °C under vacuum conditions (Figure 3.3 and Figure 3.4). Therefore, based on these two independent results, sulfur outgases significantly from Murchison at temperatures from ∼800-1000 °C.

Theoretical work has also been conducted to determine the outgassing composition of carbonaceous chondrites under a variety of temperature and pressure conditions assuming thermochemical equilibrium. For example, a series of studies by Schaefer & Fegley modeled thermal outgassing for a wide variety of chondrites, including Murchison, using chemical equilibrium calculations to predict the atmospheric compositions of rocky bodies formed via outgassing of specific types of meteorites (Schaefer & Fegley 2007, 2010). These calculations use a Gibbs energy minimization code and include thermodynamic data for over 900 condensed and gaseous species composed of 20 major rock-forming and volatile elements (see Schaefer & Fegley (2007, 2010) and Supplementary Information for further details). A key distinction between the experiments and chemical equilibrium calculations is that the experiments simulate initial (or instanta-

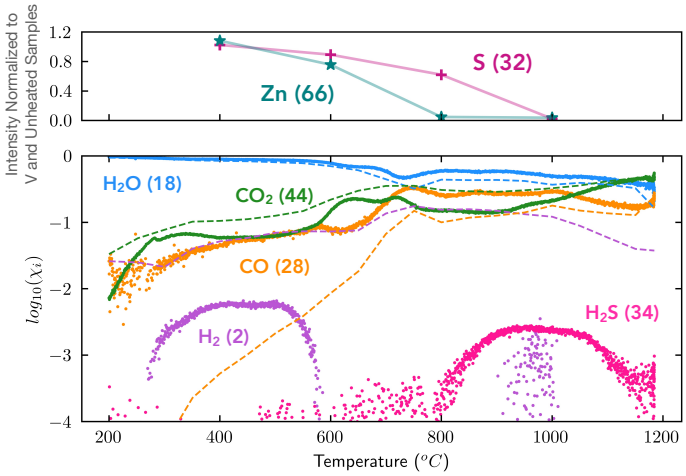

Figure 3.4: **Experimentally-measured outgassing composition of a 3 mg powdered Murchison sample from 200-1200 °C under a high-vacuum environment ($\sim 10^{-4}$ Pa at lower temperatures and $\sim 10^{-3}$ Pa at higher temperatures) (lower panel) compared with the outgassing trends of S and Zn under the same vacuum conditions from this study (upper panel).** In the lower panel, the outgassing composition is shown as mole fractions of different outgassed species on a log scale as a function of temperature. The outgassing composition of Murchison was determined using a residual gas analyzer mass spectrometer that monitored the abundances (i.e., mole fractions) of the highly volatile outgassing species H_2O, H_2, CO, CO_2 and H_2S (see Thompson et al. (2021) for further details). Each species is labeled and its mass number is in parentheses. The dashed curves show 'equilibrium-adjusted' experimental outgassing compositions which are the result of taking Thompson et al. (2021)'s experimental elemental outgassing results at intervals of 50 °C and inputting those into the chemical equilibrium model of Figure 3.5 (see Schaefer & Fegley (2007, 2010) for details on the equilibrium model) to recompute how the gas composition would speciate under equilibrium conditions. The upper panel shows the S and Zn outgassing trends from this study, expressed as these elements' intensities, normalized to V and the average of the two unheated Murchison samples, for the residues heated under vacuum.

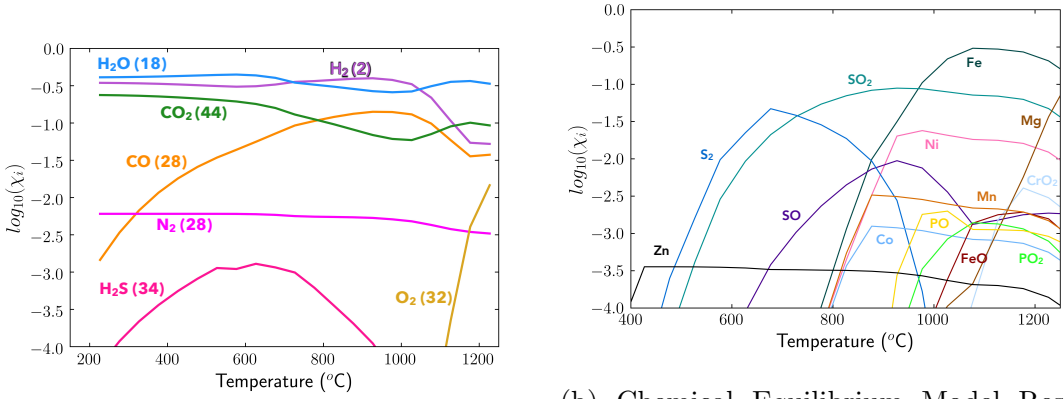

(a) Chemical Equilibrium Model Results for Species Measured in Figure 3.4

(b) Chemical Equilibrium Model Results for Additional Outgassing Species from Murchison

Figure 3.5: **Chemical equilibrium model results for the outgassing composition of Murchison from 200-1200 °C under a high-vacuum environment ($\sim 10^{-4}$ Pa).** (a) The calculated mole fractions of the gas species that were also measured in the outgassing experiments of Thompson et al. (2021) (Figure 3.4) assuming chemical equilibrium under the same temperature and pressure conditions as the laboratory experiments of Thompson et al. (2021) and the vacuum experiments in this study. (b) Calculated mole fractions of the additional gas species containing the elements measured in this bulk element study (e.g., S, Fe, Mg, Zn) according to chemical equilibrium calculations under the same temperature and high-vacuum pressure conditions.

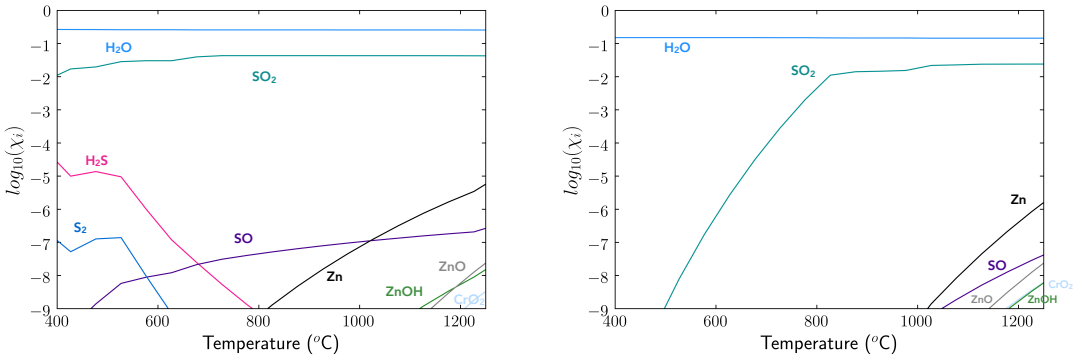

(a) 50 air

(b) 100 air

Figure 3.6: **Chemical equilibrium model results for the outgassing composition of Murchison from 400-1200 °C under atmospheric pressure.** Each figure shows outgassing of the species that contain the elements we measured in this bulk element study (i.e., S, Zn, Cr, etc.), and H_2O for reference. "50 air" (a) shows the results of the outgassing model for 100 g of Murchison, 50 g of air and the total gas pressure is fixed to 1 bar. "100 air" (b) shows the outgassing model results for 100 g of Murchison, 100 g of air and the total gas pressure is fixed to 1 bar.

neous) and evolving outgassing compositions whereas the equilibrium calculations simulate the long-term outgassing abundances once equilibrium has been achieved and the bulk composition does not evolve. In addition, the meteorite composition is changing throughout the experiments as the temperature increases and volatiles are removed (i.e., open system outgassing) while the equilibrium calculations assume a closed system in which volatiles are not removed. Equilibrium conditions may not be applicable in some planetary scenarios, so these experimental results can provide important constraints for such cases. Nevertheless, it is still informative to compare the equilibrium calculations and the experiments because the preliminary outgassing composition as simulated by the experiments may have important implications for the subsequent outgassing and atmospheric evolution that eventually achieves equilibrium.

Figure 3.5 shows the results of chemical equilibrium calculations for the outgassing composition of Murchison from 200-1200 °C under a high-vacuum environment, the same pressure and temperature conditions as in the experiments performed by Thompson et al. (2021). The combined pressures of the sulfur gases predicted to be stable in the equilibrium model (e.g., SO_2, S_2, SO, H_2S) result in significant sulfur outgassing at ~800 °C and continuing at higher temperatures (Figure 3.5). While this is broadly consistent with our results, our experiments show different outgassing trends for sulfur, with sulfur beginning to outgas at 800 °C and significantly outgassing at 1000 °C. Although the prior experimental outgassing study by Thompson et al. only monitored one sulfur species, H_2S, the difference between the experimental outgassing trend of H_2S and the equilibrium model's predictions for H_2S may help explain the difference between the findings of this study and the equilibrium model's predictions for sulfur outgassing in general. The major S-bearing phase in Murchison is tochilinite, a hydrated sulfide that is relatively abundant in CM chondrites and should decompose at ~300-400°C (Nozaki et al. 2006; King et al. 2021). Other studies have demonstrated that in chondrites tochilinite decomposes to troilite (FeS) which melts at ~850-1000 °C (Tomkins 2010). Troilite melting likely results in degassing of sulfur, which may explain why the experimental results show sulfur outgassing at higher temperatures compared to the equilibrium models. It is also possible that chemical kinetics effects contribute to sulfur outgassing at higher temperatures than chemical equilibrium models predict.

The equilibrium model also predicts other heavier elements and species to outgas significantly above 600 °C under vacuum conditions (total pressure ~1E-9 bars)

including Fe, Ni, Mg, Mn, Co, Zn, PO, PO_2, CrO_2, and FeO (Figure 3.5b). The fO_2 predicted by the equilibrium model, calculated using the H_2O/H_2 ratio, is significantly lower compared to that determined experimentally by Thompson et al. (2021). The fO_2 calculated under equilibrium conditions is approximately 4 $\log_{10}$ units below the quartz-fayalite-magnetite (QFM) mineral redox buffer at the lowest temperatures (∼300 °C) to about 1.7 $\log_{10}$ units below QFM at the highest temperatures (∼1200 °C). On the other hand, the fO_2 calculated using the experimental H_2O/H_2 from Thompson et al. (2021) is significantly higher, ranging from ∼5 $\log_{10}$ units above QFM at the lower temperatures to the QFM buffer at the highest temperatures (see Thompson et al. (2021) for more detailed discussion of the difference in these derived oxygen fugacities). While our results from the heating experiments performed under vacuum suggest significant outgassing of Zn above 600 °C, we do not detect any significant outgassing of the other elements (Figure 3.3). Of these heavier elements that outgas according to equilibrium models, Ni, Co, Mg, Fe, and Cr are moderately refractory whereas Mn and P are moderately volatile and Zn is volatile. Although Fe is predicted to outgas significantly at 1000 °C under equilibrium conditions, a prior study investigating chondrules in an ordinary chondrite, which has relatively similar bulk iron content as Murchison, suggested that under vacuum conditions negligible iron is expected to evaporate, consistent with our experimental results that find no significant loss of iron up to 1000 °C (Davis & Richter 2014; Alexander & Wang 2010). In addition, the fact that we do not detect significant outgassing of Ni, Co, Fe, P, Mg, Cr, and Mn up to 1000 °C is consistent with several prior experimental studies (Braukmüller et al. 2018; Wulf et al. 1995). Our equilibrium

calculations predict zinc vapor pressures that are several orders of magnitude higher for the 'vacuum' conditions than at atmospheric pressure. This leads to a larger numerator term for the HKL equation (Eq. 3.2) under vacuum conditions, which is consistent with our observations of significant outgassing of Zn in these experiments, unlike the experiments conducted at atmospheric pressure. Therefore, Zn is an important volatile species to include in models of outgassing from Murchison and other carbonaceous chondrites. It is important to note that the differences between experiments (including this study and the previous studies mentioned above) and the chemical equilibrium model results are due to a variety of factors, including fundamental differences in the experimental designs, kinetics effects, oxygen fugacity and pressure conditions, as discussed above (Section 3.4.1).

Since the equilibrium models assume enough time has passed for equilibration to take place, whereas in our experiments, Murchison samples are only held at each temperature for a finite amount of time (5 hours), it is possible that some of these moderately refractory and moderately volatile species did not have enough time to volatilize from their mineral host phases in our experiments. For example, a prior study found that in olivine, the diffusion of Cr occurs at a rate of $\sim 10^{-19}$ m^2/s (Ito & Ganguly 2006). Transporting significant amounts of Cr out of a <106 μm grain requires timescales of several thousand years, far exceeding the duration of our heating experiments. Ultimately, comparing the theoretical chemical equilibrium outgassing composition from Murchison to the experimental results of this study reveals that kinetics effects may inhibit outgassing of certain S-bearing species and that moderately refractory and mod-

erately volatile species do not outgas as significantly under the open system conditions of these experiments as the closed system models predict.

We can also compare results from the bulk elemental compositions of samples heated under atmospheric pressure to the calculated chemical equilibrium outgassing compositions from Murchison. Figure 3.6 shows the equilibrium outgassing composition of Murchison in air (0.79 bar N_2, 0.21 bar O_2). According to the chemical equilibrium model under atmospheric pressure, SO_2 is the only S-containing species that has a mole fraction above 10^{-3}. Other species such as S_2, H_2S, SO, Zn, ZnOH, ZnO, and CrO_2 have mole fractions less than 10^{-4}. Our experimental results are broadly consistent with the chemical equilibrium models as our bulk element studies for the samples heated under atmospheric pressure only show significant outgassing of sulfur.

We can also compare our bulk element measurements of S and Zn to the solids containing these elements that are predicted to be present in Murchison according to the chemical equilibrium models. With regards to Murchison outgassing under vacuum, the chemical equilibrium model finds that most S-containing solids are only stable until around 600 °C and are not stable at higher temperatures. As discussed above, our experiments suggest that under an open-system, mineral decomposition and potentially chemical kinetics effects could result in outgassing of S-species at higher temperatures ($\geq$800 °C) than predicted by chemical equilibrium models. For Murchison outgassing at atmospheric pressure, the chemical equilibrium models find the Zn-containing mineral $ZnCr_2O_4$ (zincochromite) to be stable from 400-1000 °C. While this is broadly consistent with our bulk element measurements that show no significant outgassing of Zn over this

temperature range at atmospheric pressure, most Zn in Murchison resides in silicates and sulfides not zincochromite (Nishimura & Sandell 1964). This is supported by the fact that Zn spinels like zincochromite have not been found in thermally metamorphosed carbonaceous chondrites.

3.5 Implications for Volatile Depletion of Planetesimals and Terrestrial Exoplanet Atmospheres

Focusing on the formation of terrestrial planets, the findings of this study have several implications for the formation and evolution of planetesimals. One of the central components of classic terrestrial planet formation models is the accretion of planetesimals from smaller dust and gas particles. Through collisional evolution of planetesimals, planetary embryos (i.e., intermediate objects between planetesimals and planets) form. Finally, once gas in the protoplanetary disk dissipates, instabilities in the embryos' orbits and mutual collisions result in forming the terrestrial planets that exist today (Morbidelli et al. 2012). It has been commonly claimed that a combination of different chondritic and achondritic meteorite types may explain the bulk compositions of the terrestrial planets. For example, several studies used oxygen isotope mixing models to determine the relative contributions of different chondrites in forming terrestrial bodies like Earth, Mars, and asteroid 4 Vesta (Lodders 2000; Delaney 1994; Boesenberg & Delaney 1997). Although the bulk compositions of Mars and Vesta can be reproduced by mixtures of different meteorite types, recent studies determined that Earth's bulk composition cannot be explained by combinations of the known meteorite types alone, and

rather a major component that is not represented in our meteorite collections is likely necessary (Righter et al. 2006; Mezger et al. 2020; Burkhardt et al. 2021). In particular, these studies often cite that the bulk silicate Earth is more depleted in moderately and highly volatile elements compared to chondrites (Mezger et al. 2020; Sossi et al. 2022).

The results of this study combined with the findings of Thompson et al. (2021) demonstrate that when CM-chondrite like planetary material is heated to 1000 °C, the initial outgassing composition will likely be composed of at least the following elements: H, C, O, S, and Zn. We find that these elements' outgassing trends depend on the temperature, pressure and redox conditions of the system. Carbonaceous chondrite-like material may have been incorporated into the terrestrial planets during their accretion (e.g., Lodders (2000); Marty (2012); Sakuraba et al. (2021)). Therefore, when planetesimals composed of CM-chondrite-like material are heated to such temperatures during the accretion of terrestrial planets, they will outgas and become depleted in some portion of these volatiles unless there are mechanisms that allow these bodies to retain the outgassed species. To understand the volatile depletions measured in our experimental residues of Murchison requires investigating Murchison's mineralogy and the phase changes that occur that result in outgassing of these different elements. Based on Murchison's mineralogy, the outgassing of light elements (e.g., C and H) at temperatures $< 800°C$ is likely due to the breakdown of H- and C-hosting phases like organics, carbonates and phyllosilicates that readily break down upon heating. One of the main mineralogical constituents of Murchison is olivine, for which its two solid solution endmembers (forsterite (Mg-rich) and fayalite (Fe-rich)) do not melt at atmospheric pres-

sure until ∼1900 °C and ∼1200 °C, respectively (Hurlbut & Klein 1985). The olivine in Murchison is mainly Mg-rich. Based on forsterite's melting temperatures, we do not expect significant decomposition of olivine to be taking place in our experiments, consistent with the stability of Mg throughout our heating experiments. However, we do detect slight variations in Fe's concentrations between the different samples. While the cause of these variations is uncertain, it may be due to inhomogeneities in the samples due to physical sorting during sample preparation (e.g., sorting of metal and magnetic grains in powders (Menzies et al. 2005)).

Of the elements for which we do not detect any significant outgassing over the entire temperature range (i.e., V, Ni, Co, Mg, Fe, Cr, P, and Mn), there are likely many mineral phases that host these elements (e.g., olivines, pyroxenes, metals, chromite, magnetite, and sulfides). Many of these mineral phases have much higher melting temperatures than those achieved during our experiments which likely explains why they remained stable during the experiments. On the very short timescales of our experiments compared to the evolutionary timescales of planetesimals, melting is likely necessary to release gaseous forms of these elements from their mineral phases, and the temperatures reached during our experiments are not high enough for melting to occur. However, on longer planetesimal timescales, $\sim 10^5 - 10^7$ years, diffusion through crystal lattices may play a role in outgassing of moderately volatile and moderately refractory elements (e.g., Chakraborty (1997)). As discussed in Section 3.4, sulfur outgases most significantly in our experiments which is likely due to the breakdown of tochilinite to troilite, which then decomposes and releases sulfur. The outgassing of zinc during the

heating experiments performed under vacuum conditions may be due to the breakdown or diffusion of Zn in silicates, oxides or sulfides (Savage et al. 2022; Nishimura & Sandell 1964; Wulf et al. 1995).

For undifferentiated CM-chondrite-like planetesimals, depending on whether there is an existing atmosphere or gaseous envelope around the planetesimals as they are accreting can influence whether the planetesimals are capable of retaining their degassed volatiles or if those species instead escape permanently. In addition to the pressure and temperature gradients inside the planetesimal, our study demonstrates that the total surface pressure and redox conditions influence the evaporation rate of materials (Eq. 3.2) and likely impact the temperatures at which certain elements degas. For example, for the samples of Murchison heated under atmospheric pressure and more oxidizing conditions compared to the vacuum experiments, sulfur degassed both at 800 °C and 1000 °C while zinc did not experience any detectable outgassing over the entire temperature range. On the other hand, for the samples heated under vacuum, sulfur significantly outgassed at 1000 °C with only minor outgassing at 800 °C, and zinc outgassed significantly above 600 °C. If these differences are indeed due in part to the different pressure conditions (as explained by the HKL equation, Eq. 3.2), then this suggests that the retention of an atmosphere (i.e., similar to a closed system) plays an important role in regulating planetesimal outgassing. In addition, slow transport of volatiles within a planetesimal may inhibit outgassing. For example, larger planetesimals have longer transport timescales and therefore may degas more slowly compared to smaller planetesimals.

Although other elements such as Fe, V, Ni, Mn, P, Co, Mg, Cr are predicted to outgas assuming chemical equilibrium conditions over the same temperature range of our experiments, we did not detect any significant outgassing of these elements, which is broadly consistent with other experimental works (e.g., Braukmüller et al. (2018); Wulf et al. (1995)). This difference may be due to the open system nature of our experiments compared to the closed system modeling framework and kinetics effects that inhibit these elements from outgassing experimentally at the temperatures predicted by chemical equilibrium models. Future studies should seek to determine if such elements do indeed outgas from CM chondrites under closed system conditions, as this will contribute to a comprehensive understanding of volatile loss from these volatile-rich planetesimal analog materials.

These experimentally-determined outgassing trends due to heating of Murchison samples have several important implications for the initial atmosphere-interior connection for terrestrial exoplanets. Despite the fact that the exact role that carbonaceous chondrite-like planetesimals played in forming the Solar System's terrestrial planets is uncertain, their primitive nature and volatile-rich composition provides an important end-member composition to consider for the formation of terrestrial exoplanets. Given that Murchison is a CM chondrite, its bulk composition is similar to that of the solar photosphere (second only to CI chondrites), representing a link between the composition of material in the protoplanetary disk during planet formation and the stellar composition (Lodders & Fegley 1998; Wasson & Kallemeyn 1988). In addition, CM chondrite-like material was likely an important source of volatiles to the terrestrial planets during their

accretion (e.g., Lodders (2000); Marty (2012); Sakuraba et al. (2021)). Therefore, CM chondrites may serve as a good compositional analog to volatile-rich building blocks in other planet-forming regions around Sun-like stars. Building upon the findings from Thompson et al. (2021) that Murchison's outgassing composition up to 1200 °C under vacuum conditions consisted primarily of H_2O, CO, CO_2, and smaller amounts of H_2 and H_2S, this study determines how heavier elements outgas as Murchison samples are heated to temperatures up to 1000 °C under two different pressure and redox regimes. During the formation of a terrestrial planetary body, if the bulk composition of material being outgassed from this body is like Murchison (CM-chondrite-like), then sulfur is expected to outgas at temperatures at and above ∼800 °C at atmospheric pressure, and both sulfur and zinc are expected to outgas at temperatures >800 °C under vacuum conditions.

Both sulfur and zinc have been theoretically investigated in terms of their possible presence in and relevance to terrestrial exoplanet atmospheres. For example, Hu et al. studied terrestrial exoplanet atmospheres with surface-derived H_2S and SO_2 and determined that, for oxidized atmospheres composed of N_2 and CO_2, a thick haze of sulfur aerosols may form if the sulfur emissions from the surface of the body are strong enough, and these aerosol features may be observable in reflected light with next generation space telescopes (Hu et al. 2013). Other studies have also investigated the feasibility of detecting sulfur species on terrestrial exoplanets and what the presence of such species can tell us about the geochemical cycles and surface properties of these planets (e.g., Kaltenegger & Sasselov (2010); Loftus et al. (2019)). Mbarek and Kemp-

ton used equilibrium chemistry to predict the cloud compositions that would form in super-Earth (exoplanets with radii between ∼1 and 1.8 $R_{\oplus}$) atmospheres assuming the atmospheres form by degassing of chondritic material. They found that, assuming the atmosphere formed via degassing of CM chondritic material, ZnS clouds may form on the super-Earth exoplanet HD 97658b (Dragomir et al. 2013) at ∼1100 °C, generally consistent with the findings of our study (Mbarek & Kempton 2016). In fact, previous transmission spectroscopy observations of HD 97658b suggest that the atmosphere may have a cloud or haze layer, although its atmospheric composition is still unknown (Knutson et al. 2014). Beyond theoretical studies, upcoming observations with JWST will search for evidence of volcanic outgassing on the hot rocky exoplanet LHS 3844b, which has already been observed to lack a thick atmosphere (Kreidberg et al. 2019), by searching for SO_2 with a sensitivity of 100 ppm in a 0.01 bar atmosphere (Kreidberg et al. 2021).

Ultimately, the results of this experimental study provide experimental constraints to models of volatile depletion of undifferentiated planetesimals and the early atmospheres of terrestrial planets. In particular, for studies that seek to understand volatile loss from planetesimals prior to differentiation and other evolutionary processes, our experimental results provide the approximate temperatures at which sulfur and zinc outgas from CM chondrite-like material under different pressure and redox regimes, and, combined with a previous set of outgassing experiments, the outgassing trends of highly volatile species like H_2O, CO and CO_2. For initial terrestrial exoplanet atmosphere models, these experimental results can provide constraints (e.g., surface boundary con-

ditions) for the elements released as a function of temperature assuming the composition of material being outgassed is like CM chondrites. Subsequent studies will analyze the outgassing compositions of a wide array of meteorite samples including ordinary and enstatite chondrites to infer the diversity of volatile depletion patterns and initial outgassing compositions from a diverse sample of remnant planetary building block materials.

3.6 Supplementary Information

3.6.1 Chemical Equilibrium Models

The chemical equilibrium models described in Section 3.4.3 and shown in Figures 3.5 and 3.6 use a Gibbs energy minimization code to calculate the outgassing composition from different chondritic materials as a function of temperature and pressure under chemical equilibrium. The models include thermodynamic data for over 900 condensed and gaseous species composed of 20 major rock-forming and volatile elements (Schaefer & Fegley 2007, 2010). Figure 3.6 shows the outgassing composition for the species composed of the elements that we measured in this bulk element study (and H_2O for reference) from Murchison in background air (i.e., 75 wt.% N_2, 23 wt.% O_2) with two different proportions of Murchison material to air. Figure 3.6(a) shows the results of the chemical equilibrium model for 100 g of Murchison and 50 g of air with the total gas pressure equaling 1 bar. Figure 3.6(b) shows the chemical equilibrium model results for 100 g of Murchison and 100 g of air, with the total gas pressure once again equaling 1 bar.

3.6.2 Data Calibration for Elemental Concentrations

While the main results of this study are the outgassing trends of Murchison samples heated to various temperatures under different pressure regimes, we also derived elemental concentrations by calibrating the ICP-MS data. As mentioned in Section 3.2.2, in addition to the Murchison samples and the procedural blank, we also digested five rock standards. The rock standards used for calibration include three basalts (Hawaiian Volcanic Observatory basalt (BHVO-2), Columbia River basalt (BCR-2), and Icelandic basalt (BIR-1)), a peridotite relatively enriched in rare earth and platinum group elements from Yukon Canada (WPR-1a), and a sulphide relatively enriched with gold and platinum group elements from Yukon Canada (WMS-1a). The masses of the rock standards digested ranged from ∼5-23 mg (see Table 3.5). Throughout the digestion process, solution concentrations were calculated by mass for all the samples, standards and blank.

To quantify the elemental concentrations in the Murchison samples, we first normalized all isotope intensities to In, and using the In-normalized measurements for the procedural blank, BCR-2, BHVO-2, WPS-1a, and WPR-1a along with their published concentrations from the Max Planck Institute's GeoReM database (Jochum et al. 2007), we created five-point calibration curves using a linear regression (most $r^2 > 0.95$) to relate elemental abundances to measured In-normalized isotope intensities (Figure 3.7). Using these calibration curves, we calculated the elemental concentrations in solution for the Murchison samples and the BIR-1 rock standard which was treated as an unknown standard. Finally, using our mass measurements, we calculated the concen-

trations (in ppm) of the following elements: V, Ni, Co, Mg, Fe, Cr, P, Mn, Zn and S for each of the samples.

3.6.3 Analysis of the Calibration to Derive Elemental Concentrations

To check the robustness of our calibration to determine elemental concentrations, we compared the calculated elemental concentrations for BIR-1 to its published concentrations from GeoReM (Table 3.11, Figure 3.8). Most calculated BIR-1 elemental concentrations match the published concentrations well with the percent error being less than ∼20 % (calculated according to Supplementary Equation 3.9). This % error is our metric for assessing the uncertainties on the measured elemental concentrations (Tables 3.9 and 3.10). The concentrations of P, S and Ni for BIR-1 are below the quantification limit, and this is likely due to the fact that BIR-1 has lower concentrations of P, S and Ni (131, 70 and 170 ppm, respectively) relative to the other standards used in the regression. In particular, BCR-2 and BHVO-2 have much higher concentrations of P (1568 and 1172 ppm, respectively) compared to BIR-1, and WMS-1a and WPR-1a have higher concentrations of S (17680 and 281700 ppm, respectively) and Ni (4390 and 30200 ppm, respectively) compared to BIR-1. These larger concentrations of P, S and Ni strongly control the regression (Figure 3.7, Jochum et al. (2007)). To further assess the uncertainties in our measurements, and in particular for P, S and Ni, we compared our results for the two unheated Murchison samples to the elemental concentrations of unheated Murchison samples measured by Braukmüller et al. (2018), hereafter B18. We found that the two datasets closely match within their uncertainties (expressed as 95% confidence intervals of the means) and the % errors are less than 20% for most

elements (Figure 3.9 and Table 3.12). Given that the P, S and Ni elemental concentrations for the unheated Murchison samples closely match those determined by B18 (% errors of 11, 20, and 2%, respectively), our calibration is robust for the carbonaceous chondrite compositions of interest here despite the non-detectable concentrations for these elements calculated for the BIR-1 standard. It is important to note that the focus of this study is on the outgassing trends of the elements measured rather than their exact concentrations, and therefore, the main results presented in this study are the normalized ICP-MS intensities. In the next section, we discuss the calculated elemental concentrations and their associated outgassing trends.

$$\%\text{Error} = \frac{|A_{\text{Published}} - A_{\text{Measured}}|}{A_{\text{Published}}} \times 100 \tag{3.9}$$

3.6.4 Elemental Concentrations and Outgassing Analysis

Figures 3.10 and 3.11 show the derived elemental concentrations for the Murchison samples heated at atmospheric pressure and under vacuum conditions, respectively. The broad outgassing trends are consistent with the findings presented in the main text: under atmospheric pressure, the main outgassing species is sulfur, and under vacuum, both sulfur and zinc outgas significantly. For the set of heating experiments performed under vacuum, the concentrations of V, Ni, Co, Mg, Cr, P, and Mn did not vary significantly across the samples; however, there is a slight systematic increase in these elements' concentrations from the unheated samples and the residues heated to 400 and 600 °C to the residues heated to higher temperatures. This increase is likely because the samples heated under vacuum had more time to outgas readily volatilized elements

(e.g., H, C, and O) (Table 3.1), and therefore they have higher relative concentrations of moderately volatile and refractory elements than those for the unheated samples and those heated under atmospheric pressure.

3.6.5 Alternative Data Calibrations

To determine the best calibration method for deriving elemental concentrations from our dataset, we tested multiple calibration methods, as summarized in Table 3.13. These different calibration methods involved using various subsets of the geological reference standards (and the total procedural blank) to create calibration curves and treating different standards as the "unknown" standard to determine the measurement uncertainties. We found that the broad outgassing trends discussed in the main text are consistent regardless of which data calibration method is used. Ultimately, we used the method outlined in the previous supplementary sections 3.6.2-3.6.4 because it resulted in the most robust calibrations for the largest set of elements. However, since the main the results of this study are the broad outgassing trends, we have reported the ICP-MS intensities as the key results in the main text.

3.6.6 Additional Elements Measured by ICP-MS

In addition to the ten elements that are the focus of this study, we also measured an additional four elements: Al, Ti, Ca, and Na. However, these elements are not discussed in the main text due to the fact that their data calibrations were not robust or they exhibited unexpected outgassing behavior, as discussed further below.

Calcium and Aluminum:

Using the data calibration method outlined in Section 3.6.3, the experimentally measured Ca and Al concentrations for BIR-1 closely match the published concentrations, with percent errors of 5 and <1 %, respectively. However, the unheated Murchison samples' concentrations of Ca and Al did not match those from Braukmüller et al. (2018) as closely, with higher percent errors of 29 and 40 %, respectively. In addition, with this calibration method, the concentrations of Al varied significantly for the different Murchison samples whereas the Ca concentrations were fairly constant for the samples heated under both atmospheric pressure and vacuum conditions. Although we tried different data calibration methods (as discussed above), we determined that the method outlined in Section 3.6.3 resulted in the most robust calibrations for the largest set of elements. With testing the different calibration methods (summarized in Table 3.13), we found that the Ca and Al concentrations varied significantly among the heated Murchison samples and in different ways depending on which calibration method was used, suggesting that the measurements for these two elements may not be robust. We checked the analytical uncertainties for the Ca and Al measurements for these samples and they are all less than 2% RSD, so an instrumental measurement issue is unlikely. It is possible that this variability may be due to inhomogeneities in the samples, such as differences in their relative abundances of carbonates (for Ca) and CAIs. In addition, stochastic contribution of alumina fragments from the alumina crucible either during the heating experiments or when removing the sample from the crucible for bulk element analysis is another possible explanation for the Al heterogeneity. Ultimately, since Ca and Al's concentrations are sensitive to the calibration method used, we did not include

them in the main analysis.

Titanium:

Although Ti's experimentally measured concentration for BIR-1 closely matches the published concentration, with a percent error of 4 %, it has non-detectable levels in all of the Murchison samples measured in this work, including the unheated samples. For some of the tested calibration methods, Ti's concentrations are quantifiable and they are constant across the unheated and heated samples. This behavior is expected because Ti is not expected to outgas at these temperatures. Since Ti's concentrations are sensitive to the calibration method used, we did not include it in the main analysis.

Sodium:

The calibration for Na is robust, with a percent error of 2 % between the experimentally measured BIR-1 concentration and its published concentration. However, the unheated Murchison samples are the only ones with quantifiable levels of Na, all of the heated samples had concentrations below the detection limit. Na is not expected to outgas at such low temperatures, which suggests a measurement issue. For some of the tested calibration methods, Na's concentrations are quantifiable for the heated samples and they are generally constant, which is consistent with the findings of Braukmüller et al. (2018). As with Ca, Al and Ti, since Na's concentrations are sensitive to the calibration method used, we did not include it in the main analysis.

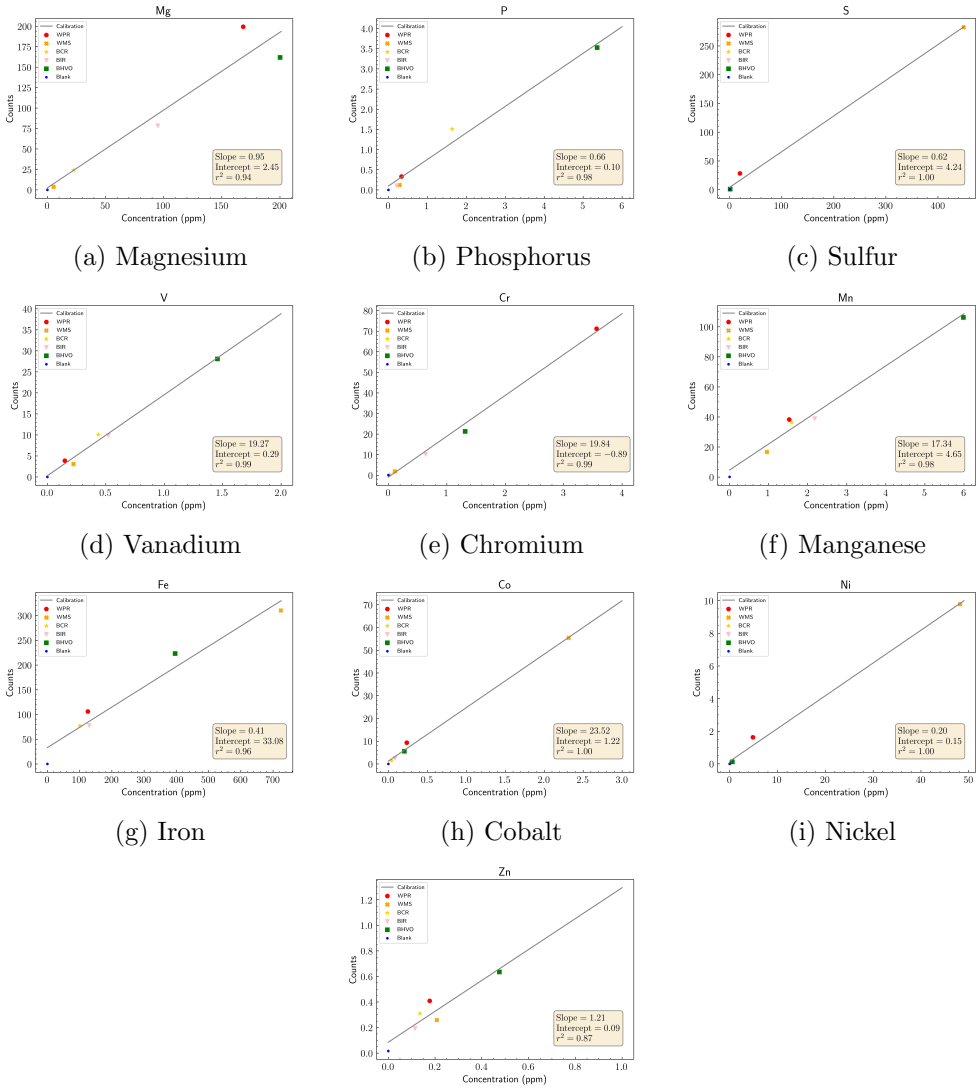

(a) Magnesium (b) Phosphorus (c) Sulfur

(d) Vanadium (e) Chromium (f) Manganese

(g) Iron (h) Cobalt (i) Nickel

(j) Zinc

Figure 3.7: **Calibration curves for determining sample concentrations.** We used the In-normalized measurements for the procedural blank (blue circle) and four geological reference standards, BCR-2 (yellow star), BHVO-2 (green square), WMS-1a (orange X), WPR-1a (red circle), along with their published concentrations (ppm) from GeoReM to create five-point calibration curves using a linear regression (gray line). The tan box shows the slope, intercept, and r^2 values for the linear regression line. We treated BIR-1 (pink triangle) as an "unknown" standard to test the robustness of our calibration (Figure 3.8).

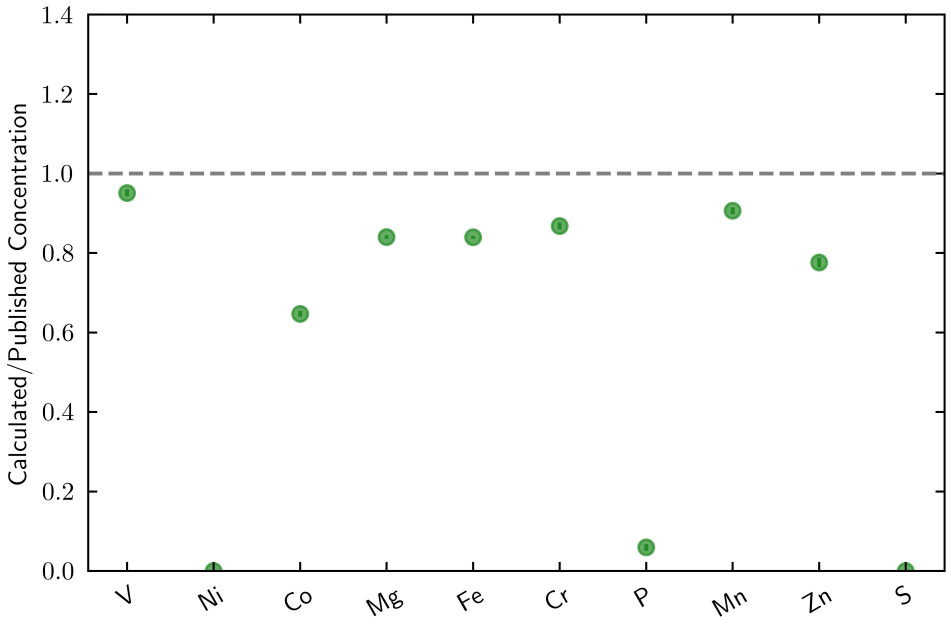

Figure 3.8: **Comparison of calculated BIR-1 elemental concentrations to the published concentrations from GeoReM.** The points show BIR-1's calculated concentrations (ppm) normalized to its published concentrations (ppm) from the GeoReM database (Jochum et al. 2007). The uncertainties of the published GeoReM concentrations are propagated and expressed as the 95% confidence intervals, all of which are within the datapoints. For most elements, the calculated concentrations reproduce the published concentrations within ∼20% error. Our calculated concentrations of S, Ni and P are near or below the quantification limit, which is why their ratios are at or near zero. However, the S, Ni and P concentrations for our unheated Murchison samples reproduce the unheated Murchison concentrations of Braukmüller et al. (2018) (B18) within 20% error (see Figure 3.9). Elements are arranged on the x-axis from left to right in order of decreasing 50% condensation temperature (Lodders 2003).

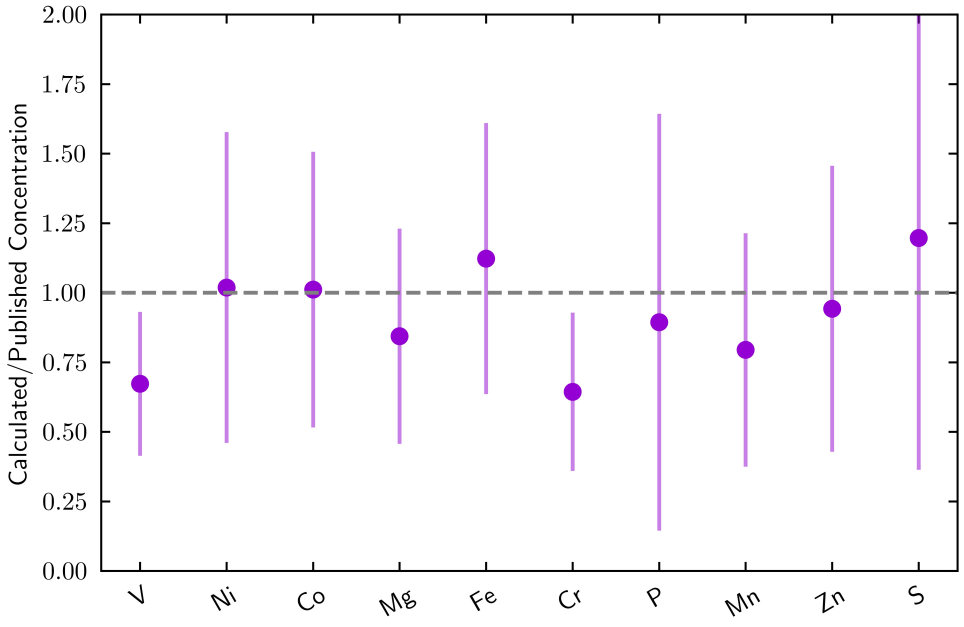

Figure 3.9: **Comparison of calculated elemental concentrations (in ppm) of the two unheated Murchison samples analyzed to the Murchison concentrations determined by Braukmüller et al. (2018) (B18).** The points show the average concentrations of the two unheated Murchison samples measured in this study normalized to the average elemental concentrations of the two Murchison samples measured by B18. The uncertainties are the propagated 95% confidence intervals of means from both our unheated Murchison samples and the two Murchison samples from B18. Elements are arranged on the x-axis from left to right in order of decreasing 50% condensation temperature (Lodders 2003).

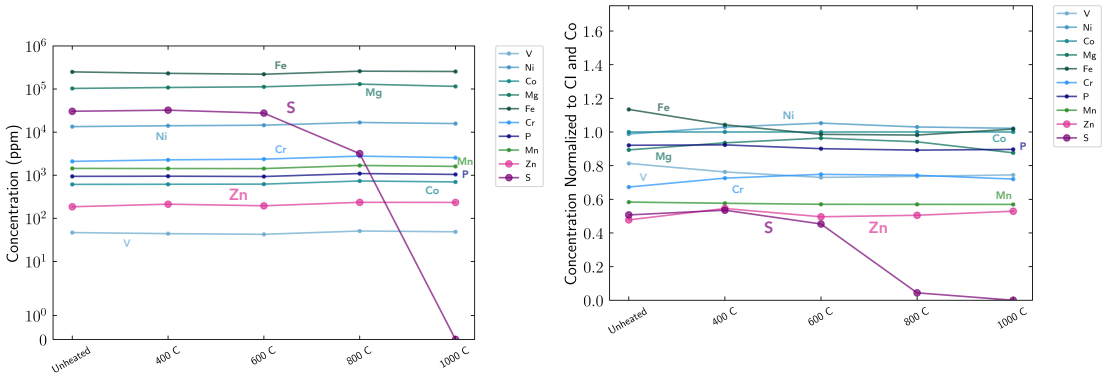

(a) Sample Concentrations

(b) Sample Concentrations Normalized to CI and Co

Figure 3.10: **Average elemental concentrations from the unheated Murchison samples and the residues from the sets of stepped-heating experiments performed at atmospheric pressure (10^5 Pa/1 bar).** (a) Elemental concentrations (ppm), (b) Elemental concentrations normalized to the CI chondrite Ivuna (Braukmüller et al. 2018) and Co. The x-axis refers to the temperature to which the residues were heated to with "unheated" corresponding to the average of the two unheated Murchison samples and "400 C" corresponding to the average of the two residues heated to 400 °C, etc.

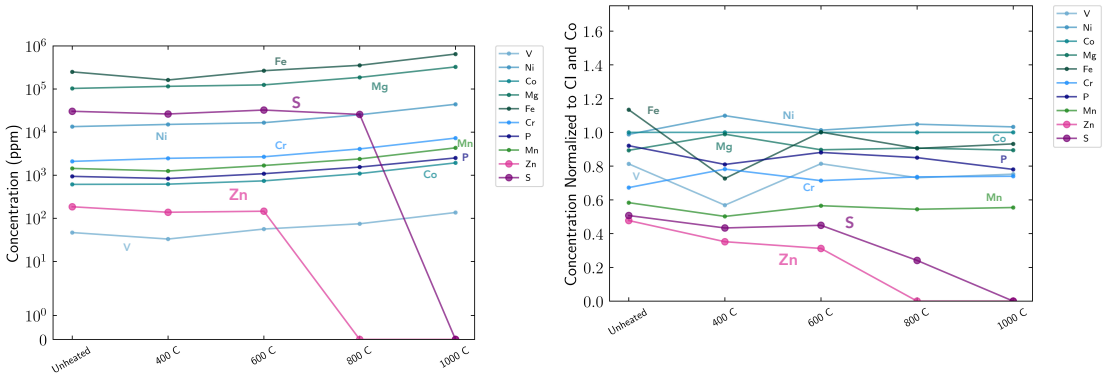

(a) Sample Concentrations

(b) Sample Concentrations Normalized to CI and Co

Figure 3.11: **Average elemental concentrations from the unheated Murchison samples and the set of stepped-heating experiments performed in a high vacuum environment (~10^{-4}Pa/10^{-9} bar).** (a) Elemental concentrations (ppm), (b) Elemental concentrations normalized to the CI chondrite Ivuna (Braukmüller et al. 2018) and Co. The x-axis refers to the temperature to which the residues were heated to with "unheated" corresponding to the average of the two unheated Murchison samples and "400 C" corresponding to the residue heated to 400 °C, etc.

Table 3.5: **Masses of the samples before and after the heating experiments and the masses digested for ICP-MS analysis**. For the mass of the samples heated to specific temperatures, the first column indicates the temperature to which the sample was heated. For example, for the first set of heating experiments performed under atmospheric pressure, 400 refers to the sample heated to 400 °C. All masses are shown in mg.

Sample	Pre-Heating Experiment	Post-Heating Experiment	Digested for ICP-MS
Unheated Sample 1	–	–	6.3
Unheated Sample 2	–	–	7.1
Atmospheric Furnace Set 1:			
400	5.0	4.8	4.5
600	5.1	4.7	4.7
800	5.0	4.3	3.9
1000	5.1	4.2	4.0
Atmospheric Furnace Set 2:			
400	5.0	4.9	4.5
600	5.0	4.9	3.0
800	5.1	4.5	2.8
1000	5.0	4.3	4.1
Vacuum Furnace Set:			
400	5.0	4.6	2.3
600	4.9	4.5	4.1
800	4.0	3.5	2.1
1000	4.1	3.4	1.3
Rock Standards:			
BHVO	–	–	22.9
BCR	–	–	5.2
WMS	–	–	7.9
WPR	–	–	5.5
BIR	–	–	8.1

Table 3.6: **Instrumental Settings, Performance and Acquisition Parameters for ICP-MS**. The instrument set-up for the ICP-MS consisted of a Peltier cooled (2 °C) cyclonic spray chamber. MR refers to medium resolution.

RF Power	1250 W
Cool gas	16 L/min
Resolution [m/δm]	MR: 4500
Scan Mode	Triple
Samples per peak	MR: 40
Mass window [%]	MR: 125
Search window [%]	MR: 50
Integration window [%]	MR: 60
Auxiliary gas	0.85 L/min
Sample gas	0.75 L/min
Additional gas	0.1-0.2 L/min
Sensitivity	$\sim 2.5 \times 10^6$ cps/ppb ^{115}In
Isotopes:	
MR: ^{26}Mg, ^{31}P, ^{32}S, ^{51}V, ^{52}Cr, ^{55}Mn, ^{57}Fe, ^{59}Co, ^{61}Ni, ^{66}Zn, ^{115}In	

Table 3.7: **ICP-MS intensities and analytical uncertainties for all rock standards analyzed along with the procedural blank measurement.** Each value shows the average intensity (in cps) measured by the ICP-MS and the value in parentheses is the analytical uncertainty for that average intensity measurement expressed as the relative standard deviation (RSD) in %.

	BHVO (RSD)	BCR (RSD)	WMS (RSD)	WPR (RSD)	BIR (RSD)	Blank (RSD)
Mg	57284699 (1.4)	10503787 (0.6)	1707192 (0.9)	74789537 (1.3)	30615112 (2.0)	6577 (0.6)
P	1248628 (0.8)	651906 (0.5)	57502 (1.3)	124385 (0.9)	40790 (2.3)	389 (3.1)
S	364975 (1.0)	277733 (0.9)	130967437 (1.2)	10634388 (0.7)	65843 (1.3)	112314 (1.2)
V	9941015 (1.4)	4345172 (0.7)	1424586 (0.5)	1444651 (0.6)	3846187 (2.5)	307 (5.2)
Cr	7540015 (0.8)	148856 (1.4)	879136 (0.3)	26704694 (1.1)	3950376 (1.9)	13759 (1.5)
Mn	37612944 (1.2)	15680845 (0.8)	7755534 (1.1)	14357370 (0.6)	15203774 (1.6)	44071 (2.5)
Fe	79024263 (1.8)	33409537 (0.6)	143915654 (0.7)	39755405 (0.7)	30348365 (2.2)	7411 (2.7)
Co	1970218 (0.1)	635432 (0.1)	25692133 (0.7)	3503588 (1.2)	982011 (2.8)	785 (3.7)
Ni	43617 (0.5)	1927 (1.6)	4536852 (0.6)	610492 (0.8)	28271 (2.7)	132 (5.9)
Zn	224810 (0.2)	133676 (1.6)	119871 (0.8)	153349 (0.3)	75277 (2.4)	6949 (1.3)
In	354007 (0.6)	431697 (1.0)	463602 (0.6)	375091 (0.2)	390792 (2.4)	422644 (2.0)

Table 3.8: **Percent differences (%) between the V-normalized intensities of the two sets of Murchison samples heated under atmospheric pressure.** UH refers to the percent difference between the two unheated Murchison samples. 400, 600, 800 and 1000 refer to the percent differences between the two Murchison samples heated to those respective temperatures under atmospheric pressure.

Sample	Mg	P	S	V	Cr	Mn	Fe	Co	Ni	Zn
UH	0.4	1.4	2.0	-	0.6	0.2	0.2	1.0	1.4	1.5
400	0.6	10.8	5.4	-	5.5	7.5	10.4	7.4	7.3	33.1
600	3.7	9.9	14.1	-	3.9	7.4	8.6	5.7	4.2	19.9
800	2.2	13.4	38.5	-	5.3	9.3	12.5	8.9	6.9	26.4
1000	2.8	8.5	6.6	-	3.1	7.4	9.1	4.8	6.3	15.9

Table 3.9: **Elemental concentrations in ppm for the two sets of Murchison samples heated under atmospheric pressure following the procedures outlined in Figure 3.1(a) determined by ICP-MS analysis.** For each element, the uncertainty is expressed as the % error between the calculated elemental concentration for BIR-1 and the published concentration following Equation 3.9 in Supplementary Information. The elements are listed in order of increasing atomic mass. *For S, Ni and P, because their calculated concentrations for BIR-1 are at or below the quantification limit, we instead use the % error between the calculated elemental concentrations for the unheated Murchison samples and those determined by Braukmüller et al. (2018) (B18).

	M-400 (1)	M-400 (2)	M-600 (1)	M-600 (2)	M-800 (1)	M-800 (2)	M-1000 (1)	M-1000 (2)	% Error
Mg	104387	112745	98523	126856	113010	147496	112459	117802	16
P	970	927	907	958	1056	1129	1048	1037	11*
S	32022	32613	28155	27015	5861	478	0	0	20*
V	42	46	40	45	45	56	46	51	5
Cr	2257	2286	2137	2584	2501	3044	2500	2604	13
Mn	1434	1424	1374	1476	1592	1777	1596	1602	9
Fe	236698	225558	222327	218185	256602	262205	257479	253171	16
Co	618	615	580	663	684	786	688	708	35
Ni	14071	14011	13318	15636	15370	18138	15692	15880	2*
Zn	251	174	213	177	256	214	247	221	22

Table 3.10: **Elemental concentrations in ppm for the set of Murchison samples heated under a high-vacuum environment ($\sim 10^{-4}$ Pa) following the procedures outlined in Figure 3.1(b) and the two unheated Murchison samples (M-UH) determined by ICP-MS analysis.** For each element, the uncertainty is expressed as the % error between the calculated elemental concentration for BIR-1 and the published concentration following Equation 3.9 in Supplementary Information. For the unheated Murchison samples, the average of the two samples is used in Figures 3.9-3.11. The elements are listed in order of increasing atomic mass. *For S, Ni and P, because their calculated concentrations for BIR-1 are at or below the quantification limit, we instead use the % error between the calculated elemental concentrations for the unheated Murchison samples and those determined by Braukmüller et al. (2018) (B18).

	M-UH (1)	M-UH (2)	M-400	M-600	M-800	M-1000	% Error
Mg	106717	99459	115442	124714	186106	325570	16
P	977	904	837	1085	1544	2515	11*
S	31712	29176	26331	32519	25746	0	20*
V	48	45	33	56	75	136	5
Cr	2159	2028	2463	2678	4075	7264	13
Mn	1483	1393	1252	1680	2386	4314	9
Fe	257249	242506	162004	266060	354693	647735	16
Co	636	590	620	739	1090	1933	35
Ni	13939	12869	15084	16565	25297	44189	2*
Zn	192	179	138	146	0	0	22

Table 3.11: **Concentrations of the BIR-1 standard measured by ICP-MS compared to the published values from GeoReM (Jochum et al. 2007).** Each value in the first two columns shows the concentration (in ppm). The third column shows the uncertainty of the published BIR-1 uncertainties from GeoReM reported as the 95% confidence intervals of the means. The last column shows the uncertainty between our measured BIR-1 concentrations and those from GeoReM, expressed as the % error between the calculated elemental concentration for BIR-1 and the published concentration following Equation 3.9 in Supplementary Information.

	BIR Measured	BIR Published	BIR Published Uncertainty	% Error
Mg	49087	58429	314	16
P	–	131	19	–
S	–	70	0	–
V	305	321	3	5
Cr	341	393	4	13
Mn	1215	1341	12	9
Fe	66931	79735	350	16
Co	34	52	1	35
Ni	–	169	2	–
Zn	55	70	1	22

Table 3.12: **Comparison of the elemental concentrations (in ppm) of our two unheated Murchison samples and those of the two unheated Murchison samples from Braukmüller et al. (2018) (B18).** The second and third columns correspond to the elemental concentrations determined for our two unheated Murchison samples, with the fourth column showing their uncertainties. The fifth and sixth columns correspond to the elemental concentrations for two Murchison samples measured in B18, with the seventh column giving their uncertainties. The concentrations are reported in ppm and the uncertainties are the calculated 95% confidence intervals of the means.

Element	Unheated 1	Unheated 2	Uncertainty	Published Unheated 1	Published Unheated 2	Uncertainty
Mg	106717	99459	46113	121196	123113	12179
P	977	904	465	996	1108	712
S	31712	29176	16113	24536	26347	11505
V	48	45	17	69	70	10
Cr	2159	2028	833	3202	3300	623
Mn	1483	1393	572	1761	1860	629
Fe	257249	242506	93666	218752	226411	48658
Co	636	590	290	600	612	76
Ni	13939	12869	6799	12944	13376	2745
Zn	192	179	85	192	201	57

Table 3.13: **Summary of data calibration methods tested.** The calibration methods can be divided into two types: 1) the left column shows the different calibration methods tested using data that has been In-normalized and blank-subtracted (i.e., the In-normalized data was subtracted from the total procedural blank's (TPB) In-normalized data); 2) the right column shows the different calibration methods tested using data that has been In-normalized and the TPB was used as a point in the calibration curves. The major outgassing trends are consistent regardless of which calibration method is used. The method highlighted by * is the method that we used to derive elemental concentrations because it resulted in the most robust calibrations for the largest set of elements.

Calibration Schemes Using In-Normalized, Blank-Subtracted Data	**Calibration Schemes Using In-Normalized Data and Including the Total Procedural Blank (TPB) in the Calibration Curves**
BHVO as the unknown standard, use BIR, WPR, WMS and BCR to create calibration curves	BHVO as the unknown standard, use BIR, WPR, WMS, BCR and TPB to create calibration curves
BIR as the unknown standard, use WPR, WMS, BCR, and BHVO to create calibration curves	BIR as the unknown standard, use WPR, WMS, BCR, BHVO and TPB to create calibration curves*
BCR as the unknown standard, use BIR, WPR, WMS, and BHVO to create the calibration curves	BHVO as the unknown standard, remove WMS from the analysis, use BIR, WPR, BCR and TPB to create calibration curves
BHVO as the unknown standard and remove WMS from the analysis, use BIR, WPR and BCR to create calibration curves	BIR as the unknown standard, remove WMS and WPR from the analysis, use BCR, BHVO and TPB to create calibration curves
BHVO as the unknown standard and remove WPR from the analysis, use BIR, WMS, and BCR to create calibration curves	BIR as the unknown standard, remove WMS from the analysis, use WPR, BCR, BHVO and TPB to create calibration curves
BIR as the unknown standard and remove BHVO from the analysis, use WMS, WPR, and BCR to create calibration curves	BCR as the unknown standard, remove WMS from the analysis, use BIR, WPR, BCR and TPB to create calibration curves

Chapter 4

The Case and Context for Atmospheric Methane as an Exoplanet Biosignature

4.1 Introduction

The next phase of exoplanet science will focus on characterizing exoplanet atmospheres, including those of potentially habitable planets. For example, the James Webb Space Telescope (JWST) will be capable of characterizing the atmospheres of transiting, terrestrial planets around low mass stars, such as the TRAPPIST-1 system (Gillon et al. 2017; Morley et al. 2017). A new class of ground-based telescopes (e.g., Gilmozzi & Spyromilio (2007)) may be able to detect atmospheric constituents such as oxygen, water, and carbon dioxide on nearby rocky exoplanets via high resolu-

tion spectroscopy (López-Morales et al. 2019a). In subsequent decades, the Astro2020 Decadal Survey report has prioritized a large infrared/optical/ultraviolet telescope built to search for signs of life–biosignatures–on ∼25 habitable zone planets (Harrison et al. 2021). Life may modify its planetary environment in multiple ways, including producing waste gases that alter a planet's atmospheric composition. As a result, an understanding of detectable biogenic waste gases and their non-biological false positives is needed.

Terrestrial planets, which are the focus of this study, require significant methane surface fluxes to sustain high atmospheric abundances. On Earth, life sustains large methane surface fluxes, and so methane has long been regarded as a potential biosignature gas for terrestrial exoplanets. Previous studies have considered abiotic methane production (Schindler & Kasting 2000; Guzmán-Marmolejo et al. 2013; Kasting 2005; Marais et al. 2004; Etiope & Lollar 2013; Wogan et al. 2020), methane biosignatures in the context of chemical disequilibrium (Lovelock 1975; Simoncini et al. 2013; Krissansen-Totton et al. 2018b; Schwieterman et al. 2018), and prospects for remote detection of methane in terrestrial atmospheres (Schindler & Kasting 2000; Marais et al. 2004; Arney et al. 2018; Schwieterman et al. 2018; Mikal-Evans 2021). During the Archean eon (4 to 2.5 Ga), Earth's atmosphere likely had high methane abundances (∼10^2-10^4 times modern) due to life (i.e., methanogenesis) (Catling et al. 2001; Kasting 2005; Catling & Zahnle 2020). Methane is thus not a hypothetical biosignature because we know of an inhabited terrestrial planet with detectable levels of biogenic methane – the Archean Earth. However, methane is sometimes dismissed as irredeemably ambiguous due to its ubiquity in planetary environments and potential for non-biological production (e.g.,

Kasting (2005), Marais et al. (2004)). Additional work is clearly needed to understand methane biosignatures and its false positives within different planetary contexts.

While other studies have reviewed the biosignature gases oxygen (Meadows et al. 2018), phosphine (Sousa-Silva et al. 2020), and isoprene (Zhan et al. 2021), in the near-term, these gases will likely be difficult to detect or will only be detectable in extended H_2-dominated atmospheres on planets with large biogenic fluxes. In contrast, for Earth-like biogenic fluxes, methane is one of the few biosignatures that may be readily detectable with JWST (e.g., Gialluca et al. (2021); Wunderlich et al. (2019); Wunderlich et al. (2020)). For example, biological methane on an early Earth-like Trappist-1e could be detectable with 5-10 transits with JWST (Krissansen-Totton et al. 2018a; Mikal-Evans 2021), and would remain detectable even with an optically thick aerosol layer at 10-100 mbar, assuming plausible instrument noise and negligible stellar contamination (Mikal-Evans 2021).

Given the imminent feasibility of observing methane with JWST, it is imperative to determine the planetary conditions where methane is a compelling biosignature. Despite the patchwork of past studies on methane biosignatures, a recent and dedicated investigation into the conditions needed for atmospheric methane to be a good exoplanet biosignature is lacking. This study provides an updated assessment of the necessary planetary context for methane biosignatures. First, we present the case for methane as a biosignature, including its short photochemical lifetime and relationship with chemical disequilibrium and CO anti-biosignatures. We then explore the possibility of abiotic methane fluxes as large as those caused by known biogenic sources, in

part using new modeling tools. We also discuss the purported presence of methane on Mars and simulate atmospheric methane on temperate Titan-like exoplanets. Based on these results, we propose a framework for identifying methane biosignatures and discuss detectability prospects with next-generation missions.

4.1.1 Biological Methane Production on Earth

The vast majority of methane in Earth's atmosphere today, and throughout most of its history, is biogenic. At present, Earth's ∼30 Tmol/year global methane emissions are predominantly produced directly by life (including anthropogenic sources), and most of the rest is thermogenic methane that derives from previous life, such as fossil fuel burning or metamorphic reactions of organic matter (Jackson et al. 2020). Genuinely abiotic methane emissions, while uncertain, are comparatively tiny (Jackson et al. 2020).

Biological methane production, or methanogenesis, is a simple metabolism performed by anaerobic microbes (i.e., those not requiring oxygen for growth). Methanogenic microbes can be divided into three groups: hydrogenotrophic (Reaction 4.1), acetoclastic (Reaction 4.2), and methylotrophic methanogens.

$$CO_2 + 4H_2 \longrightarrow CH_4 + 2H_2O \tag{4.1}$$

$$CH_3COOH \longrightarrow CH_4 + CO_2 \tag{4.2}$$

Hydrogenotrophic methanogens typically oxidize H_2 and reduce CO_2 to CH_4 and con-

tribute ∼1/3 of current biogenic methane emissions. Acetoclastic methanogens use acetate, contributing ∼2/3 of current biogenic methane emissions, and lastly, methylotrophic methanogens use methylated compounds but do not contribute significantly to global biogenic methane emissions (Lyu et al. 2018). Methane can also be produced indirectly by life as a byproduct of degrading organic matter from dead organisms, called "thermogenic methane."

If life elsewhere is common, methanogenesis may be widespread due to the likely ubiquity of the CO_2+H_2 redox couple in terrestrial planet atmospheres and the potential metabolic payoff from exploiting such commonly outgassed substrates. Methanogenesis is an ancient metabolism on Earth with phylogenetic analyses implying that methanogenesis originated between 4.11 and 3.78 (Ga) and reconstructions of the last universal common ancestor suggesting methanogens were one of the earliest life-forms to evolve on Earth (Wolfe & Fournier 2018; Battistuzzi et al. 2004; Weiss et al. 2016).

There are several reasons to expect methane-cycling biospheres to produce large CH_4 fluxes. During the Archean, xenon isotopes - which ostensibly reflect abundances of escaping, hydrogen-bearing species in the upper atmosphere - likely imply large methane abundances (>0.5%) (Zahnle et al. 2019; Catling & Zahnle 2020). This Xe isotope fractionation can potentially be explained by another hydrogen-bearing species (e.g., >1% H_2 or >1% H_2O), but such explanations are tentatively disfavored: Kadoya & Catling place an upper limit of H_2 in the Archean atmosphere of 1% and other paleo-pressure and surface temperature estimates likely preclude >1% H_2O above

the tropopause (Kadoya & Catling 2019; Catling & Zahnle 2020). Moreover, multiple ecosystem models for the Archean Earth estimate large biogenic CH_4 fluxes and abundant atmospheric CH_4 (Kharecha et al. 2005; Ozaki et al. 2017; Schwieterman et al. 2019; Sauterey et al. 2020). Motivated by observations of inefficient methane generation in a ferruginous, sulfate-poor lake ostensibly representative of Precambrian conditions, biogeochemical models of low Precambrian methane have been proposed (Laakso & Schrag 2019). However, Lenton (2020) found that such model behavior is dictated by arbitrary forcings and is not compatible with the rock record. In any case, hydrogenotrophic methanogenesis in the Archean water column could maintain substantial CH_4 fluxes regardless of organic burial efficiency in sediments (Kharecha et al. 2005; Sauterey et al. 2020; Laakso & Schrag 2019).

4.2 Results

4.2.1 The Case for Methane as a Biosignature

Methane has been highlighted as a potential biosignature gas because it has a short photochemical lifetime (less than ∼1 Myr) on habitable-zone, rocky planets orbiting solar-type stars. A short photochemical lifetime requires substantial replenishment fluxes to sustain large atmospheric abundances. Methane is removed from an atmosphere photochemically in two ways, depending on the concentration of CO_2 relative to CH_4 and the presence of other oxidants (Zahnle et al. 2020). In the case where CO_2 is significantly more abundant, CH_4 is destroyed by oxidants and is converted to CO_2 (and see SI Section 4.5.3 for additional reactions):

$$CH_4 + h\nu \longrightarrow CH_3 + H(\uparrow space) \tag{4.3}$$

or

$$CH_4 + OH \longrightarrow CH_3 + H_2O \tag{4.4}$$

and, subsequently,

$$CH_3 + O \longrightarrow H_2CO + H(\uparrow space) \tag{4.5}$$

The C in H_2CO is further oxidized to CO_2. The H produced can then be lost to space, thereby irreversibly destroying CH_4. Note that OH and O are byproducts of H_2O and CO_2 photolysis; an O_2-rich atmosphere is not required for rapid CH_4 destruction, although it does decrease the CH_4 lifetime.

For the case where CH_4 is more abundant than CO_2, CH_4 polymerizes to aerosols, which fall to the ground and remove the atmospheric CH_4 (see SI Section 4.5.3 for sequence of reactions). If temperatures are high enough in the lower atmosphere, these aerosols could break down and release CH_4 back into the atmosphere. In addition, surface deposition and subsequent thermal decomposition in the subsurface could release methane back into the atmosphere. However, some portion of the hydrogen produced by methane photolysis is lost to space, and so, without H_2 replenishment, the C:H ratio of condensate material will rise such that the methane is irreversibly lost.

The short atmospheric lifetime of terrestrial planet methane can be quantified. Using the photochemical model PhotochemPy adapted from the Atmos code (Arney et al. 2016) and created by N. Wogan (see Section 4.6.1 in SI), we explore the stability

of atmospheric CH_4 for an Archean Earth-like planet (i.e., N_2-CO_2-CH_4) orbiting a 2.7 Ga Sun-like star. Every calculation conserves redox. Consistent with previous studies (Prinn et al. 2001; Simoncini et al. 2013; Kasting & Brown 1996; Guzmán-Marmolejo et al. 2013), we find that for atmospheric CH_4 mixing ratios greater than $\sim 10^{-3}$ to be stable against photochemistry requires replenishing CH_4 surface fluxes that are larger than Earth's current biological flux (Figure 4.6). If a planet is orbiting a different stellar-type host star it will be necessary to recalculate the threshold for biological methane surface fluxes. For example, planets orbiting M-stars tend to have lower near-UV radiation compared to Sun-like stars which reduces the OH produced by H_2O photolysis, permitting higher atmospheric CH_4 concentrations (Segura et al. 2005). Ultimately, however, a terrestrial planet atmosphere that is rich in CH_4 cannot persist unless there is a significant replenishment source flux, making it an intriguing candidate for further investigation.

Methane Biosignatures and Chemical Disequilibrium

The methane biosignature case is strengthened if its presence in the atmosphere is accompanied by that of a strongly oxidizing companion gas such as CO_2 or O_2/O_3. This is because it is difficult to explain abundant methane if a terrestrial planet's atmospheric redox state is sufficiently oxidized such that the thermodynamically stable form of carbon is not CH_4. Methane in O_2-rich atmospheres requires large replenishment fluxes because CH_4 and O_2 are kinetically unstable and out of thermodynamic equilibrium (Olson et al. 2016; Krissansen-Totton et al. 2016). The kinetic lifetime of methane in O_2-rich atmospheres is $\sim$10 years (Prinn et al. 2001) due to the following

net reaction, which is the end result of reactions 4.3-4.5 above after the H_2CO has been further oxidized to CO_2:

$$CH_4 + O_2 \longrightarrow CO_2 + H_2O \tag{4.6}$$

Another important thermodynamic disequilibrium is that between CH_4 and CO_2, which was present on the Archean Earth prior to the rise of O_2. Specifically, CH_4, CO_2, N_2, and liquid H_2O coexisted out of equilibrium on the early Earth due to the replenishment of CH_4 by life (Krissansen-Totton et al. 2018b). In a weakly reduced Archean atmosphere, CH_4's lifetime would have been short (up to ∼2,000-20,000 years) compared to geologic timescales (Pavlov et al. 2001; Kasting & Brown 1998). This short kinetic lifetime of methane does not depend on this thermodynamic disequilibrium with CO_2; methane has a short photochemical lifetime in high mean molecular weight atmospheres regardless of whether or not CO_2 is present in abundance. However, the thermodynamic disequilibrium is of fundamental importance for the discussion of abiotic methane that follows. Crucially, CH_4 and CO_2 are at opposite ends of the redox spectrum for carbon, separated by 8 electrons. This has implications for how both species can be produced via abiotic planetary interior processes which we explore subsequently, c.f. the discussion of CO below. On the basis of both this thermodynamic disequilibrium and methane's short photochemical lifetime, Krissansen-Totton et al. 2018b Krissansen-Totton et al. (2018b) argued that detecting both abundant CH_4 and CO_2 in a habitable zone rocky exoplanet may be a biosignature and, if CH_4's mixing ratio is greater than ∼0.001, the methane is probably biogenic because it is challenging

for abiotic sources to sustain large methane fluxes in anoxic atmospheres, similar to the findings of Schindler & Kasting (2000).

CO Anti-biosignatures and their Relationship to CH_4 Biosignatures

In the above scenario, the absence of significant atmospheric CO may strengthen the case for biogenic CH_4 since (i) microbial life readily consumes CO, a source of free energy, and (ii) many abiotic processes that produce CH_4 also result in abundant CO (Sholes et al. (2019), Krissansen-Totton et al. (2018b) and see below on magmatic outgassing). Life on Earth metabolizes CO because oxidizing it with water yields free energy, and because CO metabolism serves as a starting point for carbon fixation (Zahnle et al. 2011; Ragsdale 2004). Multiple lines of evidence suggest that CO consumption could be a ubiquitous metabolic strategy given its ancient origin on Earth (Ragsdale 2004; Ferry & House 2006; Daniel J. Lessner 2006; Weiss et al. 2016), and because the required enzymes possess a variety of simple Ni-Fe, Mo or Cu active sites, suggesting that they have evolved independently multiple times (Ragsdale 2004; Techtmann et al. 2009; Jeoung & Dobbek 2007). However, the mere presence or absence of CO may not be an unambiguous discriminator between a CH_4-producing biosphere and an uninhabited world. An inhabited planet may have CH_4, CO_2 and some CO in its atmosphere if life is unable to efficiently consume all of the CO (Wogan et al. 2020; Schwieterman et al. 2019; Sauterey et al. 2020). In this case, however, the CO/CH_4 atmospheric ratio in terrestrial planets' high mean molecular weight atmospheres could potentially be used as a diagnostic tool to distinguish anoxic, inhabited planets from lifeless worlds because the CO/CH_4 atmospheric ratio reflects the fractional atmospheric free energy that has

been exploited.

Schwieterman et al. 2019, Sauterey et al. 2020, and Kharecha et al. 2005 found that the atmospheric CO/CH_4 ratio for abiotic worlds is predicted to be ∼two orders of magnitude larger than that for inhabited worlds that have anoxic biospheres over a wide range of volcanic H_2 fluxes (Schwieterman et al. (2019); Sauterey et al. (2020); Kharecha et al. (2005), Figure 4.1). Note that we only consider the ecosystems from Kharecha et al. (2005) and Sauterey et al. (2020) where both methanogenesis and CO consumption (acetogenesis+acetotrophy) have evolved; if these conditions are not met, then larger CO/CH_4 ratios are possible, but note the arguments for rapid emergence of CO-consumption outlined above. While the atmospheric CO/CH_4 ratio is likely an observable parameter that can be used to distinguish lifeless from inhabited, anoxic worlds, additional modeling is required to explore the possible range of CH_4, CO_2 and CO abundances for a wide variety of biospheres and uninhabited worlds around different host star types.

4.2.2 Abiotic Sources of Methane

While the vast majority of Earth's atmospheric methane is produced biotically Jackson et al. (2020), there are various small abiotic sources of methane that could potentially be enhanced on other planets. Understanding plausible abiotic methane fluxes is necessary for discriminating methane biosignature false-positive scenarios from true signs of metabolism. These abiotic sources can be broadly divided into the following categories (Figure 4.2): (1) Volcanism and high-temperature magmatic processes; (2) Low-temperature water-rock and metamorphic reactions; (3) Impact events.

Volcanism/High-Temperature Magmatic Outgassing

Volcanoes on Earth today do not outgas significant methane. Most subaerial volcanoes produce less than $\sim 10^6$ Tmol CH_4/yr (Ryan et al. 2006; Etiope & Lollar 2013), and given the ∼1500 active volcanoes on Earth today, the estimated global CH_4 flux is $<10^{-3}$ Tmol/year, much less than the current biogenic flux of 30 Tmol/year. Similarly, Schindler & Kasting 2000 estimated the CH_4 flux from submarine volcanism to be $\sim 10^{-2}$ Tmol/year (Schindler & Kasting 2000). Although mud volcanoes, geological structures that transport clay rocks and sediment from Earth's interior to the surface, can emit large amounts of methane and CO_2 (Huff & Owen 2013), the methane is largely thermogenic, ultimately deriving from organic matter produced by life (Etiope et al. 2009). In principle, a terrestrial planet could abiotically emit methane through mud volcanoes given an abiotic source for the organic matter, such as hydrocarbon deposition from an organic haze. But that organic matter would need to be continuously replenished, and it is challenging for abiotic sources to provide the necessary replenishment (e.g., Arney et al. (2016, 2018)), especially under conditions sufficiently oxidizing to maintain a CO_2-rich atmosphere.

Wogan et al. 2020 Wogan et al. (2020) investigated whether magmatic outgassing could produce genuinely abiotic CH_4 fluxes on terrestrial planets with diverse compositions and surface conditions. They determined that volcanoes are unlikely to produce CH_4 fluxes comparable to Earth's biological flux because water has a high solubility in magma which limits how much hydrogen (and therefore CH_4) can outgas. Also, CH_4 formation is thermodynamically favorable at temperatures lower than typi-

cal magma temperatures on Earth and at magma oxygen fugacities much more reduced than that expected for most terrestrial planets (Wogan et al. 2020).

Could planets with significantly more reduced mantles and crusts produce high CH_4 fluxes via magmatic outgassing? Mercury's silicate interior has a low oxygen fugacity of approximately 5 $\log_{10}$ units below the Iron-Wüstite (IW) redox buffer, and its crust is enriched in graphite, a crystalline form of carbon (Namur et al. 2016; Peplowski et al. 2016). While Mercury's small size and proximity to the Sun preclude the retention of an atmosphere, if there are large terrestrial exoplanets with similarly reducing interiors, then it is important to determine if magmatic outgassing could produce CH_4-rich atmospheres.

Following the melting and volatile partitioning methods used in Ortenzi et al. (2020), we applied a batch melting model, which assumes a partial melt is in equilibrium with the source rock before it rises to the surface, to determine the partitioning of volatiles from the rock to the melt (see Section 4.6.2 in SI). We assume the partitioning of carbon between the melt and solid phases is controlled by oxygen fugacity-dependent graphite saturation. For the top ~10 km of crust (pressures from ~0-0.5 GPa and solidus temperatures from ~1400-1445 K), we ran a Monte Carlo simulation to explore a range of source rock CO_2 and H_2O concentrations, melt fractions, and planetary melt production volumes with oxygen fugacities from IW-11 to IW+5. We find that for very reduced melts at or below IW-2, essentially all of the carbon (>99%) will precipitate as graphite during partial melting, so there is negligible carbon available for gaseous phases (Figure 4.3, Figure 4.7), consistent with observations of Mercury's graphite-enriched

crust Guimond et al. (2021). Rocky exoplanets with ultra-reduced magma compositions are unlikely to outgas significant quantities of CH_4 due to graphite saturation, although more experiments are needed to confirm reduced magmas' outgassing compositions.

In the rare cases where volcanoes could produce biogenic levels of CH_4 assuming magma production rates larger (>10 times) than those on Earth today, they would also outgas significant amounts of carbon monoxide (CO) gas (Wogan et al. 2020). As described above, the atmospheric CO/CH_4 ratio could be used to distinguish between abiotic (outgassed) and biotic scenarios (Wogan et al. 2020; Schwieterman et al. 2019). Ultimately, high-temperature magmatic outgassing, such as through volcanism, is unlikely to produce atmospheric CH_4 fluxes similar to those produced by biology on Earth.

Low-Temperature Water-Rock Reactions and Metamorphic Reactions

The reliability of methane as a biosignature on habitable planets depends upon the tendency of low-temperature (below solidus) systems to generate methane via abiotic reactions. Under oxidizing planetary conditions conducive to CO_2 degassing, low-temperature CH_4 production is ultimately limited by the supply of reducing power in the form of ferrous iron (Fe^{2+}) in newly produced crust. One of the most frequently discussed processes for methane production is serpentinization, through which iron-bearing minerals are altered by hydration to produce H_2 via the oxidation of Fe^{2+} by water (Etiope & Lollar 2013; McCollom & Bach 2009; McCollom & Seewald 2001):

$$3FeO + H_2O \longrightarrow Fe_3O_4 + H_2 \tag{4.7}$$

Subsequently, H_2 can react with oxidized forms of carbon to produce CH_4 by Fischer-Tropsch-type (FTT) reactions:

$$4H_2 + CO_2 \longrightarrow CH_4 + 2H_2O \tag{4.8}$$

Metamorphic reactions may also produce CH_4 via iron oxidation. For example, Fe-bearing carbonates can decompose when metamorphosed and react with water to form CH_4 (McCollom 2013):

$$3FeCO_3 + H_2O \longrightarrow Fe_3O_4 + CO_2 + CO + CH_4 + \text{Hydrocarbons} \tag{4.9}$$

Experimental methane and hydrocarbon yields via such reactions are typically very low compared to that of CO_2 (McCollom 2003).

Experimental, observational, and theoretical approaches have been taken to determine the efficiency of hydrothermal and metamorphic processes and their corresponding abiotic CH_4 production fluxes on Earth and how they may apply in other planetary environments. Various geological settings are potentially conducive to CH_4 generation, including mid-ocean ridges, subduction zones, and continental settings. For example, Keir (2010) and Cannat et al. (2010) investigated the concentrations of CH_4 produced by serpentinization at mid-ocean ridges and both found global abiotic CH_4 fluxes to be about three orders of magnitude smaller than the global biogenic CH_4 flux. Combining observational and theoretical approaches, Catling & Kasting 2017 esti-

mated abiotic hydrothermal CH_4 fluxes from both axial and off-axis vents ranging from 0.015 to 0.03 Tmol/year (Catling & Kasting 2017b). In addition, Guzmán-Marmolejo et al. 2013 and Kasting 2005 determined abiotic CH_4 fluxes from hydrothermal systems ranging from 0.1-0.4 Tmol/year at present, and Kasting 2005 found that this flux may potentially have been larger during the Hadean, ∼1.5 Tmol/year, but this is still over an order of magnitude smaller than the current biogenic flux (Guzmán-Marmolejo et al. 2013; Kasting 2005). Brovarone et al. 2017 and Fiebig et al. 2007 estimated abiotic hydrothermal CH_4 fluxes at subduction zones, finding modern fluxes of $\sim 10^{-2}$ Tmol/year similar to the above estimates (Brovarone et al. 2017; Fiebig et al. 2007). In continental settings, abiotic methane has been reported in low-temperature environments such as orogenic massifs and intrusions, seeps, crystalline shields, and ophiolites, with serpentinization of (iron-bearing) peridotites being the major source of methane in these settings (Figure 4.2) (Etiope 2017). However, the amount of abiotic methane generated in continental settings is several orders of magnitude smaller than the biogenic flux (Fiebig et al. 2009; Etiope 2017; Kietäväinen et al. 2017; de Melo Portella et al. 2019; Klein et al. 2019).

Experimental studies on abiotic CH_4 production via water-rock and metamorphic reactions have also been conducted. The availability of H_2, the amount of excess aqueous carbonates, and the presence of mineral catalysts can greatly affect the amount of CH_4 generated experimentally (e.g., Jones et al. (2010) and Oze et al. (2012)). While Oze et al. (2012) and Neubeck et al. (2011) found that CH_4 production by serpentinization is enhanced by the presence of mineral catalysts (e.g., chromite, magnetite and

awaruite), McCollom (2013) caution that these experimental studies did not quantify their organic contamination. (McCollom 2016) used isotopic labeling to differentiate CH_4 produced by serpentinization from background sources. They found abiotic CH_4 formation via serpentinization to be extremely limited, with most of the experimentally-generated CH_4 deriving from background sources. While iron oxidation and FTT-type reactions (or their metamorphic equivalents) are the most commonly discussed mechanisms for large abiotic fluxes on terrestrial planets, other possible mechanisms for reducing carbon include direct carbonate methanation and hydration of graphite-carbonate-bearing rocks, but they are also unlikely to generate false positive scenarios (Section 4.5.2 SI).

The critical limitation of hydrothermal CH_4 production is the supply of Fe^{2+} and the efficiency with which iron can be oxidized to generate CH_4. The availability of iron and the efficiency of its oxidation on a planetary scale depends on a range of geological and geochemical processes that operate across disparate spatial and temporal scales. Tectonic regime, mineral catalysis, volatile inventories, surface climate, and crustal composition and permeability/porosity all potentially modulate the efficiency and extent of crustal hydration. To investigate this process's limitations, Krissansen-Totton et al. (2018b) estimated the maximum CH_4 flux generated via serpentinization by exploring plausible ranges of parameters including crustal production rate, the fraction of FeO in fresh crust, the maximum fractional conversion of FeO to H_2 via serpentinization, and the maximum fractional conversion of H_2 to CH_4 via FTT reactions. Producing a probability distribution for the maximum abiotic CH_4 flux, they found that Earth-like

biological CH_4 fluxes are at least an order of magnitude larger than plausible abiotic fluxes from serpentinization, consistent with the findings of the studies discussed above (Krissansen-Totton et al. (2018b), Figure 4.4).

Ultimately, abiotic CH_4 generation via low-temperature water-rock or metamorphic reactions is unlikely to produce atmospheric CH_4 fluxes comparable to modern biotic fluxes in combination with atmospheric CO_2 (Tables 4.2, 4.3, 4.4, 4.5, 4.6, Figure 4.4). In fact, all CH_4 flux extrapolations from low-temperature system studies discussed above are consistent with the maximum abiotic flux estimates in Krissansen-Totton et al. (2018b). Nevertheless, the possible parameter space for crustal methane production is vast, and work remains to be done to determine if unfamiliar environmental conditions may exist on other planets that could produce a false-positive signal. For example, Fe-enriched olivine may be more common compositions for the mantles of other rocky planets compared to the Mg-rich olivine characteristic of Earth's mantle. McCollom et al. (2022) determined that serpentinization of Fe-rich olivine can generate significantly more H_2 compared to that of Mg-rich olivine (by a factor of ∼two to 10) (McCollom et al. 2022). Another source of uncertainty is what catalysts might be available in natural settings. At temperatures $\leq$ 600 K, in gas mixtures with CO_2 and H_2, CH_4 is thermodynamically preferred, but the reaction is kinetically inhibited and will only proceed if catalyzed. Future investigations could seek to develop coupled geochemical evolution models of a planet's mantle and crust that can self-consistently predict CH_4, CO_2, and CO fluxes from high-temperature magmatic processes and low-temperature hydrothermal and metamorphic systems, such that the contextual clues of

abiotic methane can be explored for different compositional assumptions.

Impacts

The Solar System terrestrial planets likely experienced a late-accreting veneer from impacts of comets and asteroids prior to 3.8 Ga (Chyba 1990). Impact events are plausible abiotic sources that can generate methane in two ways: (1) after a cometary impactor hits a planet, it vaporizes, and in the cooling impactor, some of the molecules delivered by the impactor may react to form CH_4 (Kress & McKay 2004); and (2) large asteroid impactors could deliver a reducing power (i.e., iron) and vaporize a planet's surface ocean, causing a steam atmosphere to form, and CH_4 may form in such a cooling steam atmosphere (Zahnle et al. 2020). To generate significant methane, impact events require either a large, constant flux of impactors (case 1), or a transient post-impact atmosphere from a giant impact event (case 2).

For case (1), Kress & McKay (2004) and Kasting (2005) modeled CH_4 formation from volatile-rich impactors. Kress & McKay (2004) found that a 1-km comet can generate 0.6 Tmol of atmospheric CH_4 per impact event, and Kasting (2005) estimated that the global CH_4 impact flux during the Hadean was $\sim$1.25 Tmol/year. However, it is unknown whether condensing dust from cometary impactors has effective catalytic properties to enable CH_4 generation. Recent theoretical and experimental work investigated the outgassing compositions of chondritic materials that may represent cometary impactors and found that there is small to negligible amounts of outgassed CH_4 from some of the most volatile-rich chondrites (i.e., CM chondrites) (Schaefer & Fegley 2010; Thompson et al. 2021).

For case (2), Zahnle et al. (2020) showed that a transient reducing atmosphere (rich in CH_4, H_2 and NH_3) could have been generated on the early Earth by large asteroid impacts during the late-accreting veneer. Such giant impacts would produce methane since they delivered metallic iron, a significant reducing power, to the surface (Zahnle et al. 2020). The iron could react with Earth's existing H_2O to produce H_2 and FeO, which would subsequently react with atmospheric CO_2 or CO to produce CH_4. The amount of methane that could form depends on the amount of carbon available prior to the impact, how much iron the impactor delivers, how much of that iron reacts with the atmosphere, and the presence of catalysts that can reduce the quench temperature so methane is thermodynamically stable (Zahnle et al. 2020). A possible false-positive scenario is one in which a giant impact event could produce a transient atmosphere with abundant CH_4 and CO_2 but low CO. However, calculations of transient impact-generated atmospheres of (Zahnle et al. 2020) suggest that such false positive scenarios are unlikely to be long-lived for significant portions of geologic time and would be accompanied by H_2-dominated atmospheres (e.g., their Figure 7, 8 and 12).

4.2.3 Methane Beyond Earth: Mars and Temperate Exo-Titans

Methane exists in other locations besides Earth throughout the Solar System, including in the atmospheres of the outer planets and in comets (Guzmán-Marmolejo & Segura 2015). While super-Earths and sub-Neptune planets do not exist in our Solar System, they are common among other planetary systems, and future studies could determine the surface pressures necessary for these planets to sustain methane via thermochemical recombination, without the need for a significant surface flux (Section 4.5.5

SI). For example, if atmospheric H_2 is abundant, then CH_4 will efficiently recombine after photolysis which dramatically increases the CH_4 lifetime (Section 4.5.3 SI). As the focus of this study is on terrestrial planets, this section discusses atmospheric methane sources in other terrestrial worlds, in particular Mars and temperate Titan-like exoplanets (exo-Titans).

Mars

The presence of methane on Mars is debated, with claims of detections at the ∼10-60 ppbv level that are highly variable in time and space by ESA's Mars Express, NASA's Curiosity rover, and ground-based observations (e.g., Formisano et al. (2004), Mumma et al. (2009), Zahnle et al. (2011), Webster et al. (2015)). However, the most recent and most sensitive measurements by the ESA-Roscosmos ExoMars Trace Gas Orbiter did not detect any significant methane over all observed latitudes and reported an upper limit of ∼20 ppt methane for altitudes above a few kms, several orders of magnitude lower than all previous purported CH_4 detections (Thomas et al. 2021). Regardless, methane detections of a few ppb to 10s of ppb are much lower than the terrestrial exoplanet thresholds for biogenic CH_4 considered in this study. There are a variety of plausible abiotic explanations for methane on Mars including water-rock reactions, the release of clathrates, and degradation of organic matter.

Temperate Exo-Titans

Methane exists (at ∼1-5%) in the N_2-rich atmosphere of Saturn's largest moon Titan (Lindal et al. 1983). Photochemical models predict that the current CH_4 in Ti-

tan's atmosphere would be destroyed in ∼30 Myr unless there is a mechanism that resupplies CH_4 to the atmosphere (Yung et al. 1984; Wilson & Atreya 2004). Possible mechanisms for Titan's CH_4 resupply include its subsurface ocean, CH_4 clathrate hydrates in the crust, liquid hydrocarbons in the subsurface, or outgassing from the interior (Hörst 2017). While life has been suggested as a possible explanation (McKay & Smith 2005), the absence of conventionally habitable surface conditions makes geochemical processes more attractive explanations.

Whatever the source of Titan's methane, temperate Titan-like exoplanets are unlikely to produce a CH_4+CO_2 biosignature false positive. We estimate the atmospheric CH_4 lifetime for an Earth-sized exoplanet with a Titan-like volatile inventory that migrates to the habitable zone where all surface ice melts (see SI Section 6D for scenario where ice remains). Given initial CH_4 and CO_2 reservoirs relative to H_2O based on Titan's volatile inventory (Tobie et al. 2012), we neglect oxidation via OH to be conservative and calculate the loss of CH_4 via diffusion-limited hydrogen escape (Catling & Kasting 2017a). We assume that the atmospheric mixing ratio of CH_4 is 10%, which is conservative given the respective solubilities of CH_4 and CO_2 and plausible background N_2 inventories (see SI Section 4.6.4). We find that for planets with water mass fractions that are <1.0 wt% of the planet's mass, the atmospheric CH_4 lifetime is short at habitable zone separations (less than ∼10 Myrs) (Figure 4.5). If the water mass fraction is ∼10 wt% of the planet's mass, then atmospheric CH_4 may last for longer periods of time (∼100 Myrs), but even so the duration is much shorter than typical stellar ages. In any case, it will likely be possible to identify planets with such large water inventories

via their low densities. Whether hydrogen's removal timescale could be dramatically lengthened via low loss rates or other large hydrogen reservoirs (whilst maintaining a CO_2-rich atmosphere) is a promising topic for future computational studies.

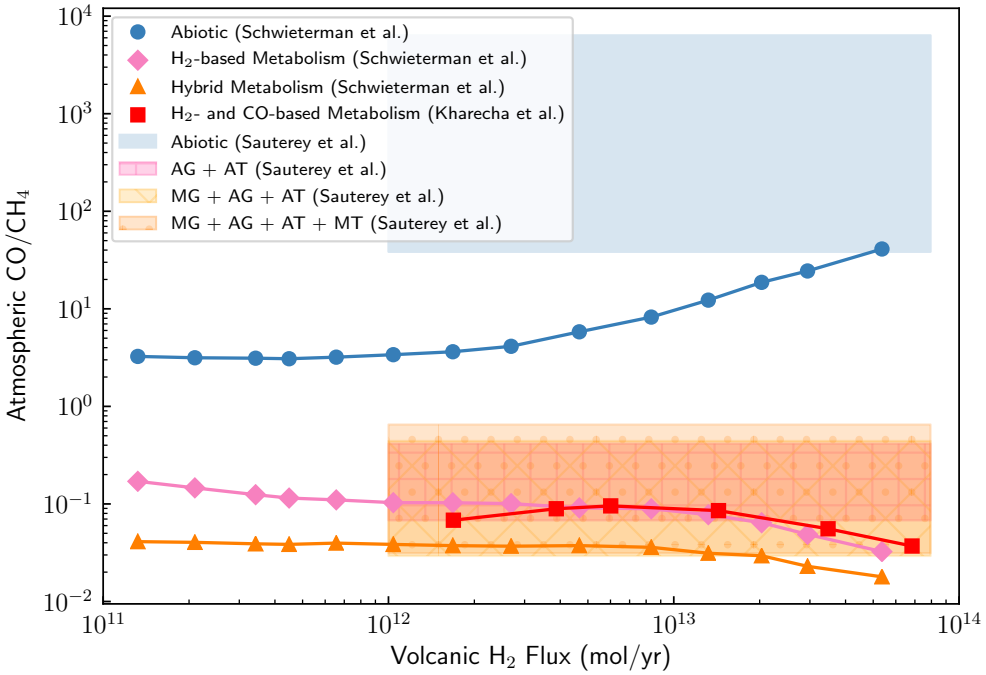

Figure 4.1: **Atmospheric CO to CH_4 ratio may help distinguish biogenic and abiotic methane.** Ratio of atmospheric CO to CH_4 for abiotic worlds and those with biospheres as a function of volcanic H_2 flux. The curves show the calculated atmospheric CO/CH_4 as a function of volcanic H_2 flux for abiotic worlds (blue circles), H_2-based biospheres (includes H_2-consuming anoxygenic photosynthesis, CO-consuming acetogenesis, organic matter fermentation and acetotrophic methanogenesis) (pink diamonds), H_2-based and Fe-based photosynthesis biospheres (i.e., "hybrid," orange triangles) from Schwieterman et al. (2019), and the methanogen-acetogen ecosystem and anoxygenic phototroph-acetogen ecosystem from Kharecha et al. (2005) (i.e., their cases 2 and 3) (red squares). The horizontal shaded regions correspond to the distributions of atmospheric CO/CH_4 for abiotic worlds (blue) and those with methanogenic biospheres (pink, yellow and orange) as a function of volcanic H_2 flux calculated by Sauterey et al. (2020). The atmospheric CO/CH_4 for abiotic worlds is predicted to be several orders of magnitude greater than that for inhabited worlds. Schwieterman et al. (2019), Kharecha et al. (2005) and Sauterey et al. (2020) found that low CO/CH_4 atmospheric ratios ($\sim$0.1) are a strong sign of methane-cycling biospheres for reducing planets orbiting Sun-like stars like Archean Earth, suggesting that atmospheric CO/CH_4 is a good observable diagnostic tool to distinguish abiotic planets from those with anoxic biospheres. The light pink '+'-hatched region corresponds to an ecosystem with CO-based autotrophic acetogens (AG) and methanogenic acetotrophs (AT); the light orange 'X'-hatched region corresponds to an ecosystem with H_2-based methanogens (MG), AG, and AT; the orange '.'-hatched region corresponds to the most complex ecosystem consisting of MG, AG, AT and anaerobic methanotrophy (MT) (Sauterey et al. 2020). All calculations assume a CO_2-CH_4-N_2 bulk atmosphere.

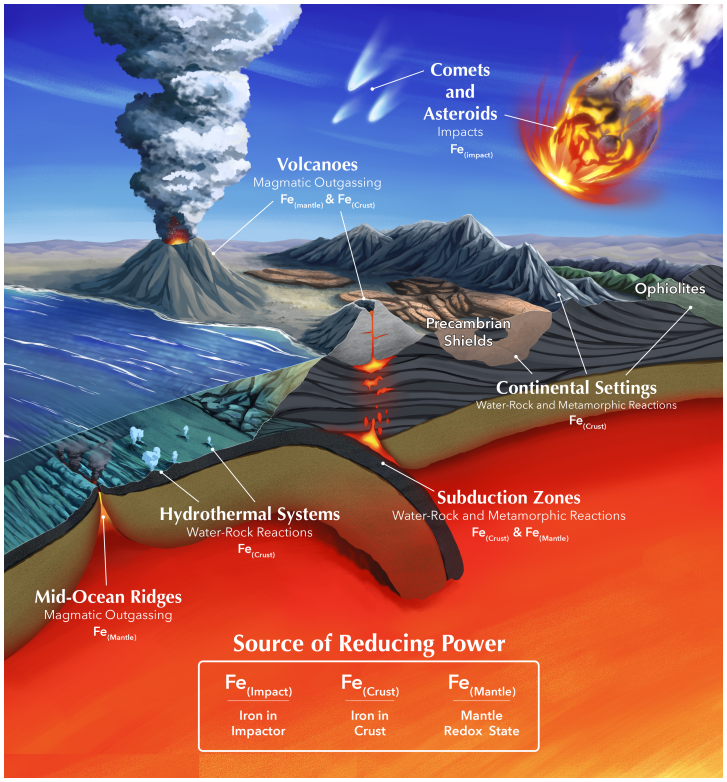

Figure 4.2: **Summary of known abiotic sources of methane on Earth (© 2022 Elena Hartley (elabarts.com)).** In general, the abiotic sources of methane can be divided into three categories: high-temperature magmatic outgassing (volcanism); low-temperature water-rock and metamorphic reactions; and impacts. Currently, subaerial (submarine) volcanoes on Earth only generate $\leq 10^{-3}$ ($\sim 10^{-2}$) Tmol/year of methane (see main text). Low-temperature water-rock reactions that generate methane occur at mid-ocean ridges, deep-sea hydrothermal vents, subduction zones, and continental settings. Methane can also be generated by metamorphic reactions, particularly in subduction zones and continental settings such as ophiolites, orogenic massifs, and Precambrian shields. Both water-rock and metamorphic reactions can generate variable quantities of methane depending on the geochemical conditions, but, on Earth, methane fluxes are orders of magnitude smaller than biological sources. Finally, impacts or other exogeneous sources can generate methane. The impact flux was larger during earlier periods in Earth's history, and such large impact fluxes are necessary to generate significant methane. A critical factor that influences the amount of methane that can be generated via all of these processes is the source of reducing power; in comparatively oxidizing surface environments with abundant CO_2, a reductant is needed to reduce carbon to CH_4. For magmatic outgassing, the reducing power ultimately comes from the mantle, with more reduced mantles outgassing more methane relative to CO_2 and CO. For low-temperature water-rock and metamorphic reactions, the key source of reducing power is ferrous iron (Fe^{2+}) in the crust, and in some cases the redox state of the mantle can also influence methane generation. For impact events, the metallic or ferrous iron that is delivered by the impactor serves as the source of reducing power

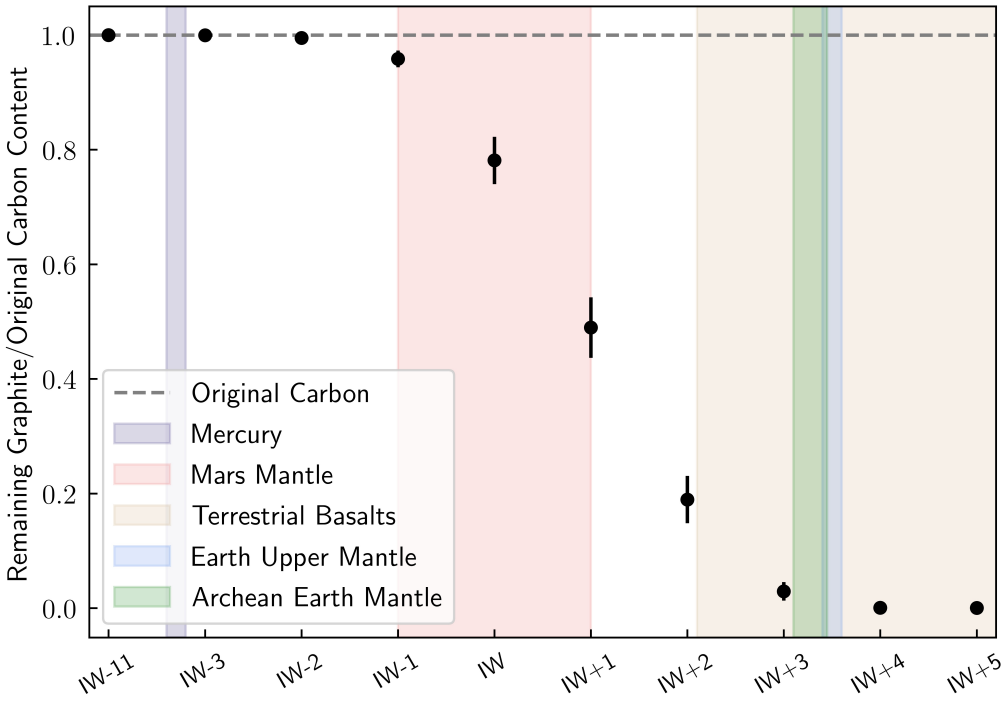

Figure 4.3: **Most carbon partitions into graphite under reducing conditions and so cannot degas as CH_4.** The ratio of the amount of remaining graphite to the original carbon content as a function of oxygen fugacity. We used a batch-melting model to determine how volatiles would partition between the rock and melt over a ~10 km deep column of newly produced crust with pressures from ~0-0.5 GPa and temperatures from 1400-1445 K (Section 4.6.2 in SI). For each oxygen fugacity, we ran a Monte Carlo simulation varying the input parameters including CO_2 and H_2O mass fractions in the mantle source rock, the fraction of source material that is melted during emplacement, and the planetary melt production rate. The average ratio of remaining graphite to initial carbon content from the Monte Carlo simulation is shown with the uncertainty reported as the 95% confidence interval. The horizontal dashed line (y = 1) illustrates the original amount of carbon, and ratios that fall on this line have all of the original carbon stable as graphite. The shaded vertical regions show the estimated oxygen fugacities of Mercury's lavas (Namur et al. 2016), the Martian mantle (Hirschmann & Withers 2008), terrestrial basalts (Doyle et al. 2019), Earth's upper mantle (Cottrell & Kelley 2011), and Archean Earth's mantle (Kadoya et al. 2020) for reference.

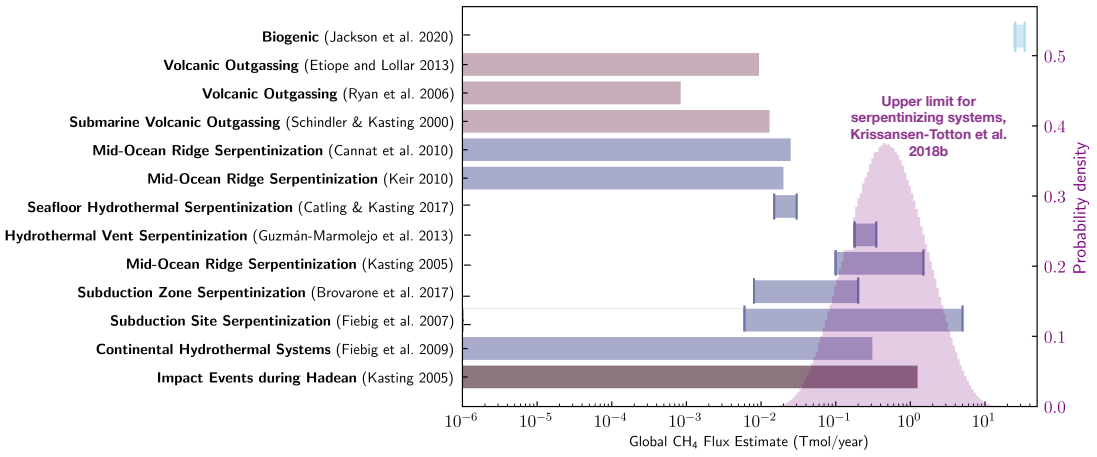

Figure 4.4: **Summary of known abiotic CH_4 sources with their estimated global CH_4 flux values compared to Earth's current biogenic CH_4 flux.** As in Table S1, for each abiotic source considered, we present those sources for which we can estimate global CH_4 flux values from a given reference. In the cases where there are multiple global CH_4 flux estimates for a given reference of an abiotic source, we show the maximum and minimum CH_4 flux estimates by the vertical lines. The transparent purple probability distribution for the maximum abiotic CH_4 flux from serpentinization is from Krissansen-Totton et al. (2018b), and the right-hand y-axis shows the probability density of this distribution. None of the abiotic sources considered have estimated global CH_4 fluxes that are similar to or exceed Earth's modern biogenic CH_4 flux. In fact, most of the abiotic sources have predicted global CH_4 fluxes that are at least an order of magnitude less than Earth's biogenic CH_4 flux. We do not show the flux estimates that exceed the iron supply because such extremely large fluxes are based on experimental results for which there are issues with organic contamination (see main text).

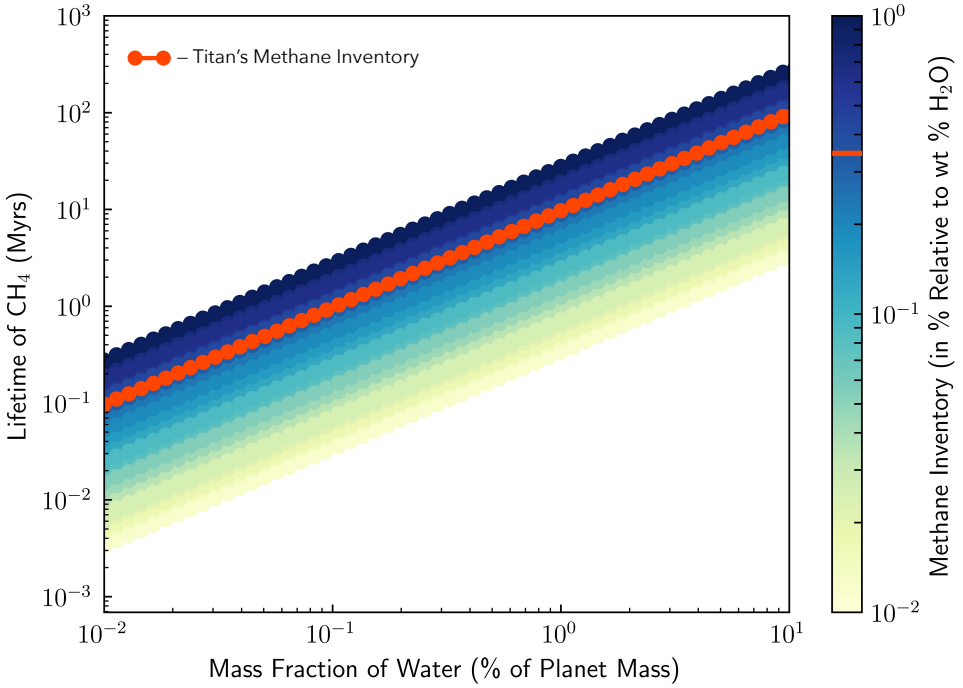

Figure 4.5: **The photochemical lifetime of methane biosignature false positives produced by melting volatile-rich Titan-analogs is short.** Estimated lifetime of atmospheric methane as a function of planet's water mass and initial methane volatile inventory. Assuming methane's escape rate is diffusion-limited and that its steady-state mixing ratio is 10%, we varied the initial methane volatile inventory (drawing values from a uniform distribution from 0.01% to 1.0% relative to weight % water, represented by the color bar) and the mass fraction of the planet's water (exploring values from 0.01% to 10% of the mass of the planet, assuming an Earth-mass planet) and calculated the estimated lifetime for methane in the atmosphere (see SI Section 4.6.4). The red curve represents Titan's methane inventory (∼0.35 %, Tobie et al. (2012)). For planets with Titan-like methane inventories and water mass fractions that are 1% (10%) of the planet's mass, the lifetime of atmospheric methane will be ∼10 Myrs (∼100 Myrs).

4.3 Discussion

4.3.1 Towards Procedures to Identify Methane Biosignatures

Any procedure for observationally identifying methane biosignatures must take into account the broader planetary and astrophysical context and will be dictated by the capabilities of the available instruments. Major steps might include: (1) Detecting a terrestrial planet within the habitable zone of its host star and characterizing its bulk properties (e.g., mass, radius, orbital properties); (2) Measuring its atmospheric composition, namely the abundances of CH_4, CO_2, CO, H_2O, H_2 and confirming that the atmosphere is anoxic; (3) Identifying possible false positives and combining this information with observational data on the planet's broader context to determine the likelihood of abiotic vs. biotic sources of methane (Figure 4.8). It is important that the host star is well-characterized (i.e., UV radiation and stellar activity) to understand the planet's photochemical environment. Identifying the presence of liquid water on the surface of a planet would suggest a particularly compelling target since it is a likely requirement for life.

Constraining the atmospheric abundances of CH_4, CO_2 and CO and confirming that the atmosphere is not H_2-dominated is essential for determining if the planet's atmosphere is indicative of the presence of a biosphere. Terrestrial planets with high mean-molecular-weight atmospheres are better candidates to search for methane biosignatures because in such atmospheres, the CH_4 lifetime will be very short without a significant replenishment source. In addition, confirming that the planet's atmosphere is anoxic is necessary to distinguish a false positive case for an anoxic planet with

abundant atmospheric CH_4, CO_2 and CO from an oxic planet with an oxygen-based biosphere that has atmospheric CH_4, CO_2, CO and O_2 (Schwieterman et al. 2019). With these abundances constrained, a photochemical model can infer the surface fluxes of the atmospheric constituents. Indications that these surface fluxes may be consistent with a biosphere include large implied CH_4 fluxes coexisting with atmospheric CO_2 but comparatively low CO abundances.

Even if the surface fluxes are consistent with a biosphere, it is necessary to identify all possible false positives including magmatic outgassing from a reduced mantle (Figure 4.3), water-rock and metamorphic reactions (Figure 4.4), large impact fluxes, and large volatile inventories (Figure 4.5). The viability of detecting methane biosignatures depends on our knowledge of abiotic methane sources and their production rates. One of the most outstanding uncertainties is a complete understanding of plausible abiotic methane production on a planetary scale via water-rock and metamorphic reactions. If a planet has an atmospheric composition consistent with a methanogenic biosphere but false positives cannot be entirely ruled out, it will be necessary to search for corroborating evidence such as additional biosignature gases (e.g., methyl chloride (Segura et al. 2005), organosulfur compounds (Domagal-Goldman et al. 2011)), signs of atmospheric seasonality and reflectance signatures from pigmented surface organisms (Olson et al. 2018; Schwieterman et al. 2015) (Figure 4.8). Ultimately, definitively detecting the presence of methane biosignatures on a terrestrial exoplanet will require taking into account the entire planetary and astrophysical context, characterizing the planet's atmospheric composition, investigating all potential false positive scenarios,

and likely searching for supporting evidence.

4.3.2 Detectability Prospects

Prospects for detecting biogenic levels of methane in terrestrial exoplanet atmospheres in the near future with JWST are promising (e.g., Krissansen-Totton et al. (2018a); Wunderlich et al. (2019); Gialluca et al. (2021); Mikal-Evans (2021)). However, it may be challenging to obtain sufficient observational data on the planetary context to confirm the presence of methane biosignatures and rule out false positives. Although JWST may be able to detect CO_2, it may only provide crude constraints on CO abundances (Krissansen-Totton et al. 2018a; Mikal-Evans 2021). Krissansen-Totton et al. (2018a) determined that JWST could place upper bounds on CO abundances in ∼10 transits and constrain the CO/CH_4 ratio with more transits for an Archean Earth-like Trappist-1e (Krissansen-Totton et al. 2018a). Mikal-Evans (2021) confirm that JWST will likely be able to crudely constrain the CO/CH_4 ratio and note that CO constraints will be possible with high-resolution spectroscopy measurements with Extremely Large Telescopes (ELTs). If biospheres are dominated by oxygenic photosynthesis, they may produce large CO fluxes through biomass burning (Schwieterman et al. 2019). Therefore, to distinguish an anoxic, lifeless world with abundant atmospheric CH_4, CO_2 and CO from an oxic, inhabited planet with CH_4, CO_2, CO and O_2 requires observations that can detect or rule out the presence of atmospheric O_2/O_3 which will be challenging with JWST (Schwieterman et al. 2019). In addition, JWST will not be able to detect water vapor with transit observations due to water cloud condensation nor constrain surface properties, so it will not be able to fully assess habitability (Komacek et al.

2020; Fauchez et al. 2019). Nevertheless, if JWST detects significant CH_4 and CO_2 and places some constraints on the CO/CH_4 ratio in a terrestrial exoplanet's atmosphere, such a discovery would certainly motivate observations with future instruments.

Looking ahead, ground-based ELTs will help characterize terrestrial exoplanets and their biosignatures (López-Morales et al. 2019b). Wunderlich et al. (2020) determined that for a cloud-free, low-CO_2 Trappist-1e atmosphere, a mere 10 ppm CH_4 is likely detectable with high resolution transit spectroscopy with the European ELT in less than ∼30 transits, and CO detections may be possible with ∼40 transits (Wunderlich et al. 2020). In addition, the Astro2020 Decadal Survey recommended a ∼6 m infrared/optical/ultraviolet space telescope to characterize the atmospheres of dozens of habitable-zone terrestrial exoplanets, including detecting methane (Harrison et al. 2021; Team 2019). Identifying methane biosignatures will not only require detecting and constraining the atmospheric abundances of CH_4, CO_2 and CO, but also using a combination of observational tools to comprehensively characterize the broader planetary context.

4.4 Conclusions

With the upcoming technological advancements in exoplanet observations enabling the characterization of potentially habitable exoplanets, it is important to consider possible biosignature gases and the sources of false-positive detections. This is particularly urgent for methane since biogenic methane is likely detectable for some terrestrial exoplanets with JWST. The case for methane as a biosignature stems from

the fact that photochemistry of terrestrial planet atmospheres implies that large CH_4 surface fluxes are required to sustain high levels of atmospheric methane. Although a variety of abiotic mechanisms could, under diverse planetary environments, replenish atmospheric methane, we find that it is challenging for such sources to produce abiotic CH_4 fluxes comparable to Earth's biogenic flux without also generating observable contextual clues that would signify a false positive. For example, we investigated whether planets with very reduced mantles and crusts can generate large methane fluxes via magmatic outgassing and assessed the existing literature on low-temperature water-rock and metamorphic reactions, and, where possible, determined their maximum global abiotic methane fluxes. In every case, abiotic processes cannot easily produce atmospheres rich in both CH_4 and CO_2 with negligible CO due to the strong redox disequilibrium between CO_2 and CH_4 and the fact that CO is expected to be readily consumed by life. We also explored whether habitable-zone exoplanets that have large volatile inventories like Titan could have long lifetimes of atmospheric methane. We found that, for Earth-mass planets with water mass fractions that are less than $\sim$1 % of the planet's mass, the lifetime of atmospheric methane is less than $\sim$10 Myrs, and observational tools can likely distinguish planets with larger water mass fractions from those with terrestrial densities.

Clearly, the mere detection of methane in an exoplanet's atmosphere is not sufficient evidence to indicate the presence of life given the variety of abiotic methane-production mechanisms. Instead, the entire planetary and astrophysical context must be taken into account to interpret atmospheric methane. Figure 4.8 illustrates a tentative

procedure for identifying methane biosignatures in the atmospheres of habitable terrestrial exoplanets. Ultimately, methane is more likely to be biogenic on a habitable zone planet when (1) planet bulk density is terrestrial (no large surface volatile reservoirs), the atmosphere has a high mean molecular weight and is anoxic, and the host star is old; (2) the atmospheric CH_4 abundance is high, with implied surface replenishment fluxes exceeding what could plausibly be produced by known abiotic processes ($\sim$10 Tmol/yr); and (3) when atmospheric methane is accompanied by CO_2 but comparatively little CO (or $CO/CH_4<1$).

Materials and Methods:

We use the photochemical model PhotochemPy in Figure 4.6 (see SI Section 4.6.1). The calculations for determining how carbon partitions between different phases under various redox conditions for Figure 4.3 follow the methods in Ortenzi et al. (2020) and are discussed further in SI Section 4.6.2. The global abiotic CH_4 flux estimates in Figure 4.4 are described in detail in SI Section 4.6.3. For Figure 4.5, we estimate the atmospheric CH_4 lifetime for an Earth-mass terrestrial planet with different water mass fractions and Titan-like volatile inventories by assuming the escape flux of hydrogen is diffusion-limited (SI Section 4.6.4). The codes used for our analysis are available on GitHub (SI Section 4.6).

4.5 Supplementary Information

4.5.1 Atmospheres with Abundant CH_4 and CO_2 in Chemical Equilibrium– Discussion of Woitke et al. 2021

Could there be a biosignature false-positive scenario in which abundant CH_4 and CO_2 (without CO) coexist in thermochemical equilibrium in a rocky planet's atmosphere? Woitke et al. 2021 Woitke et al. (2021) show that at temperatures below ∼600 K, CO_2, CH_4, N_2, and H_2O could coexist in chemical equilibrium if aqueous species are neglected. However, Woitke et al. 2021 Woitke et al. (2021) did not consider photochemistry and its effects on the stability of these atmospheres. Photochemistry is essential when assessing the plausibility of proposed terrestrial planet atmospheres.

To illustrate how a large CH_4 surface flux would be required to sustain high levels of atmospheric CH_4, a series of photochemical models were run simulating terrestrial planet atmospheres. We used PhotochemPy, a photochemical model adapted from the Atmos code (Arney et al. 2016) and created by N. Wogan (`https://github.com/Nicholaswogan/PhotochemPy`), that uses a set of inputs (e.g., stellar flux, atmospheric temperature structure, chemical species and reactions) and then integrates the atmosphere forward in time until it reaches a photochemical steady state (see SI Section 6A). A series of models were generated assuming a planet with an initial atmospheric composition that is Archean Earth-like (i.e., N_2-CO_2-CH_4), orbiting a 2.7 Ga Sun-like star and explored a range of CO_2 and CH_4 surface mixing ratios from 0.1 to 0.5 and from 10^{-5} to 0.1, respectively.

Figure **??** illustrates that abundant atmospheric CH_4 in atmospheres contain-

ing CO_2, N_2, and H_2O, requires CH_4 surface fluxes similar to or greater than modern Earth's biogenic flux to balance photochemical destruction. Therefore, such an atmosphere will not be stable without a significant CH_4 replenishment source that likely exceeds Earth's modern biogenic flux. For example, in order to sustain high atmospheric CH_4 mixing ratios of ∼0.1 along with significant amounts of CO_2, the required CH_4 surface fluxes are on the order of $\sim 3.7 \times 10^{12}$ molecules/cm^2/s (∼1000 Tmol/year), corresponding to the yellow regions of Figure **??**. Such a large CH_4 replenishment flux would be about 30 times larger than Earth's current biogenic flux (30 Tmol/year). Considering the global redox budget, such abundant atmospheric CH_4 requires that either the flux of reductants from Earth's interior is at least three orders of magnitude higher than Earth's modern hydrogen outgassing rate or that the H_2 escape rate is much less than the diffusion limit (Catling & Kasting 2017b). In addition, the equilibrium calculations of Woitke et al. (2021) did not consider the formation of dissolved ammonium (NH_4^+) and bicarbonate (HCO_3^-), which are shown to be the equilibrium products of CO_2, CH_4, and N_2 in the presence of liquid water in Krissansen-Totton et al. (2018b). The thermochemical calculations of Woitke et al. (2021) could instead have relevance for deep sub-Neptune atmospheres.

4.5.2 Additional Water-Rock and Metamorphic Reactions and Key Unknowns

While iron oxidation and FTT-type reactions (or their metamorphic equivalents) are the most commonly discussed mechanisms for large abiotic fluxes on terrestrial planets (Figure 4.2, it is worth considering other possible mechanisms for reducing car-

bon. Direct carbonate methanation can produce CH_4 given an exogeneous supply of H_2 (Etiope & Lollar 2013; Giardini et al. 1968; Reller et al. 1987; Yoshida et al. 1999), as follows:

$$CaCO_3 + 4H_2 \longrightarrow CH_4 + Ca(OH)_2 + H_2O \tag{4.10}$$

$$MgCO_3 + 4H_2 \longrightarrow CH_4 + Mg(OH)_2 + H_2O \tag{4.11}$$

Here, the production of H_2 is likely to be limited by iron oxidation via water rock reactions, unless conditions are sufficiently reducing that H_2 rather than H_2O is the dominant H-bearing product from magmatic outgassing. In this scenario, however, simultaneously large fluxes and atmospheric concentrations of CO_2 are unlikely (Figure **??**).

Hydration of graphite-carbonate bearing rocks can similarly generate CH_4 without the need for iron oxidation (Holloway 1984), in the following reaction:

$$Mg_3Si_4O_{10}(OH)_2(\text{talc}) + 3CaCO_3(\text{calcite}) + 6C(\text{graphite}) + 5H_2O \longrightarrow \tag{4.12}$$

$$3CaMg(CO_3)_2(\text{dolomite}) + 4SiO_2(\text{quartz}) + 3CH_4 \tag{4.13}$$

However, in the absence of biological organic matter, crustal compositions rich in

graphite, require strongly reducing conditions (Figure 4.3). These are unlikely to coexist with high magmatic CO_2 fluxes, which require oxidizing conditions, without large magmatic fluxes of CO (Figure **??**).

Some of the other fundamental unknowns with regards to water-rock and metamorphic reactions include the efficiency and extent of hydration reactions under different tectonic regimes, the importance of carbonate hydration in the presence of graphite in generating CH_4, the extent to which H_2 can directly react with carbonates to produce CH_4 under reducing melt conditions, and the extent to which heterogeneous surface environments could simultaneously produce high CH_4 and CO_2 fluxes.

4.5.3 Photochemical Destruction and Recombination Pathways for Methane

Methane is removed from an atmosphere photochemically in two ways, depending on the concentration of CO_2 relative to CH_4 and the presence of other oxidants (Zahnle et al. 2020). In the first case where CO_2 is more abundant, then CH_4 is destroyed by oxidants and ultimately is converted to CO_2, such as through the following reactions:

$$CH_4 + h\nu \longrightarrow CH_3 + H(\uparrow space) \tag{4.14}$$

or

$$CH_4 + OH \longrightarrow CH_3 + H_2O \tag{4.15}$$

or

$$CH_4 + O^1D \longrightarrow OH + CH_3 \tag{4.16}$$

and, subsequently, either

$$CH_3 + O \longrightarrow H_2CO + H(\uparrow space) \tag{4.17}$$

or

$$CH_3 + O_2 \longrightarrow H_2CO + OH \tag{4.18}$$

The C in H_2CO is further oxidized to CO_2. The H produced can then be lost to space, thereby irreversibly destroying the CH_4. Note that OH, O^1D, O and O_2 are byproducts of H_2O and CO_2 photolysis; an atmosphere rich in molecular oxygen is not required for rapid CH_4 destruction (although it does decrease the CH_4 lifetime). The pathway involving OH and O_2 is the dominant destruction pathway in Earth's modern atmosphere, and all of these pathways were likely important for the Archean atmosphere (Zahnle et al. 2020).

For the second case where CH_4 is more abundant than CO_2, CH_4 polymerizes to aerosols, which fall to the ground and remove the atmospheric CH_4. The chemistry producing aerosols is complex, but this sequence of reactions (Equations 4.19-4.24) demonstrates the general process:

$$CH_4 + h\nu \longrightarrow^1 CH_2 + H_2(\uparrow space) \tag{4.19}$$

$$^1CH_2 + N_2 \longrightarrow ^3 CH_2 + N_2 \tag{4.20}$$

$$^3CH_2 + ^3 CH_2 \longrightarrow C_2H_2 + H_2(\uparrow space) \tag{4.21}$$

$$C_2H_2 + h\nu \longrightarrow C_2H + H(\uparrow space) \tag{4.22}$$

$$C_2H_2 + C_2H \longrightarrow C_4H_2 + H(\uparrow space) \tag{4.23}$$

$$C_4H_2 + C_2H \longrightarrow \text{bigger hydrocarbons} \tag{4.24}$$

These hydrocarbons condense into aerosols that fall to the ground and thus remove CH_4 from the atmosphere. These aerosols could break down and release CH_4 back into the atmosphere or they could get buried and subducted into the planet. However, some portion of the hydrogen produced by methane photolysis will be lost to space, and so, without H_2 replenishment, the C:H ratio of condensate material will rise such that the methane is irreversibly lost.

Ultimately, the lifetime of atmospheric CH_4 is determined by the efficiency of the pathways outlined above. Atmospheric composition is an important determinant of that efficiency. For example, if H_2 is abundant, then CH_4 will efficiently recombine after photolysis via:

$$CH_3 + H + M \longrightarrow CH_4 + M \tag{4.25}$$

where M is an unspecified collision partner that carries away excess energy, which dramatically increases the CH_4 lifetime.

4.5.4 Gas Giant Planets

The giant planets in the Solar System contain abundant methane in their H_2-rich atmospheres due to accreting and processing primordial material from the solar nebula (Wong et al. 2004; Fletcher et al. 2009). Methane in the atmospheres of giant planets can be replenished indefinitely because, although methane gets photodissociated in the upper atmosphere, hydrogen is never depleted via escape, and carbon and hydrogen can recombine deeper in the atmosphere where temperatures and pressures are high enough for methane production to be thermodynamically favorable and kinetically viable (Moses et al. 2005). Conversely, temperate terrestrial planets with high mean molecular weight atmospheres and surfaces do not have deep enough atmospheres to replenish methane without an additional source (abiotic or biotic). In terrestrial atmospheres without a replenishment source, methane is photodissociated and hydrogen is lost to space on short timescales (e.g., $\sim$10's of thousands of years for $\sim$1 bar atmospheres). However, if a H_2-rich atmosphere on a terrestrial planet exists, then the CH_4 lifetime would be long due to stabilizing reaction pathways like those that operate in giant planet atmospheres.

4.5.5 Super-Earths and Sub-Neptune Planets

Although the focus of this study is on methane biosignatures on terrestrial planets, it is important to consider methane in the atmospheres of super-Earths (planets with radii between 1 and ∼1.8 $R_\oplus$) and sub-Neptunes (radii larger than ∼1.8 $R_\oplus$ and less than ∼3.5 $R_\oplus$) (Fulton et al. 2017). These planets are expected to span a diverse range in bulk compositions from rocky to gaseous, and therefore their atmospheres are also expected to have various compositions, from thick, H_2/He-rich primary atmospheres to thin secondary atmospheres comparable to that of terrestrial planets. Methane in sub-Neptune atmospheres would be unremarkable due to the possibility of thermodynamic recombination at depth. However, future studies could seek to determine the atmospheric pressure necessary for a planet to sustain methane via thermodynamic recombination against photodissociation. Observational methods to distinguish super-Earths from sub-Neptunes are also relevant for excluding deep atmosphere replenishment as a source of methane (Yu et al. 2021).

When searching for methane in the atmospheres of super-Earths and sub-Neptunes, as is the case for terrestrial planets, it is also important to understand the effects of the host star. For example, M dwarfs tend to be more active longer into their life cycles and have stronger far-UV and weaker near-UV emissions compared to solar-type stars, making it essential to determine how such host stars may impact such an exoplanet's atmosphere (e.g., photochemistry). Future work should aim to couple geochemical and photochemical models to better understand how cooler host stars can affect a planet's atmosphere.

4.6 Materials and Methods

All codes used in this study are publicly available at https://github.com/maggieapril3/MethaneBiosignature.

4.6.1 Photochemical Model: PhotochemPy

We use the PhotochemPy photochemical model in Figure **??** to illustrate the methane fluxes required to sustain atmospheric methane in various atmospheres. PhotochemPy is a descendant of the Photochem model contained in the Atmos modeling suite, which was originally developed by Jim Kasting and Kevin Zahnle (Kasting et al. 1983) and has since been developed by many of their students and colleagues. Appendix B in Catling & Kasting (2017c) contains an in-depth description of the main equations solved in the Photochem model. The physics and chemistry in PhotochemPy are very similar to the physics and chemistry in the version of Atmos used in Arney et al. (2016). The main exception is that we have updated several reactions, and water photolysis cross sections following Ranjan et al. (2020). However, PhotochemPy deserves a distinct name because it is a modern Fortran rewrite of the original Fortran 77 code. Additionally, PhotochemPy uses Numpy F2PY (Peterson 2009) to generate a Python wrapper to the compiled Fortran library (https://github.com/Nicholaswogan/PhotochemPy).

4.6.2 Carbon Partitioning and Magmatic Outgassing Calculations

For Figure 4.3 and Figure **??**, to calculate how carbon partitions between different phases under various redox conditions for ∼10 km of crust (pressures from ∼0-0.5

GPa and solidus temperatures from ∼1400-1445 K), we follow the melting and volatile partitioning methods outlined in Ortenzi et al. (2020). We first compute batch melting with standard partition coefficients for CO_2 and H_2O which returns how concentrated CO_2 and H_2O are in the melt for a given melt fraction, F:

$$X_{CO_2}^{\text{melt}} = (1-(1-F))^{1/0.002}(m_{\text{mantle},CO_2}/m_{\text{mantle}})/F \tag{4.26}$$

$$X_{H_2O}^{\text{melt}} = (1-(1-F))^{1/0.01}(m_{\text{mantle},H_2O}/m_{\text{mantle}})/F \tag{4.27}$$

where m_{mantle} is the mantle mass (in kg, which for Earth is 4×10^{24} kg) and m_{mantle,CO_2} and m_{mantle,H_2O} are the masses of CO_2 and H_2O in the mantle, respectively (in kg). However, if the source material is reducing, the melt will never get this carbon rich due to graphite saturation. Therefore, we compute the carbon melt concentration assuming graphite saturation. We assume the carbon is stored in the mantle as graphite and dissolves into the melt as carbonate ions ($CO_3{}^{2-}$). The amount of carbonates dissolved in the melt are calculated from equilibrium constants K_1 and K_2:

$$X_{CO_3{}^{2-}}^{\text{melt}} = \frac{K_1K_2f_{O_2}}{1+K_1K_2f_{O_2}} \tag{4.28}$$

$$log_{10}K_1 = 40.07639 - 2.53932\times10^{-2}T + 5.27096\times10^{-6}T^2 + 0.0267\frac{(P-1)}{T} \tag{4.29}$$

$$log_{10}K_2 = -6.24763 - \frac{282.56}{T} - 0.119242\frac{(P-1000)}{T} \tag{4.30}$$

for temperature (T, in K) and pressure (P, in bars) and f_{O_2}, which is the oxygen fugacity calculated based on the Iron-Wüstite redox buffer:

$$f_{O_2} = 10^{-27215/T+6.57+0.0552(P-1)/T} \tag{4.31}$$

Then, we calculate the CO_2 melt abundance:

$$X^{\text{melt}}_{CO_2} = [\frac{M_{CO_2}}{\text{fwm}} X^{\text{melt}}_{{CO_3}^{2-}}]/[1-(1-\frac{M_{CO_2}}{\text{fwm}})X^{\text{melt}}_{{CO_3}^{2-}}] \tag{4.32}$$

where M_{CO_2} is CO_2's molar mass and fwm is the formula weight of the melt (36.594) (Ortenzi et al. 2020). We take the minimum of the graphite-saturated CO_2 melt concentration (Equation 4.32) and the constant partition coefficient concentration (Equation 4.26) and use that $X^{\text{melt}}_{CO_2}$ value to calculate the flux of CO_2 in the melt:

$$F^{\text{melt}}_{CO_2} = X^{\text{melt}}_{CO_2} m_{\text{melt}} F \tag{4.33}$$

where m_{melt} is the planetary melt production rate (in g/s, where Earth's nominal melt production rate is 3.2×10^9 g/s). To compare the original carbon content to the amount that remains as graphite, we compute:

$$\text{Original Carbon} = \frac{m_{\text{mantle},CO_2}}{m_{\text{mantle}}} m_{\text{melt}} \tag{4.34}$$

$$\text{Remaining Graphite} = \text{Original Carbon} - F_{CO_2}^{\text{melt}} \tag{4.35}$$

For the Monte Carlo simulation, we vary the input parameters and sample distributions according to Table 4.1.

To calculate the species that would be released by magmatic outgassing and their corresponding outgassing fluxes, we use the outgassing speciation model described in Wogan et al. (2020). As magma ascends to the surface, the overburden pressure decreases and the dissolved volatiles in the magma may reach saturation. At that point, volatiles exsolve from the magma and form gas bubbles, which can be released to the atmosphere. In addition, chemical reactions take place within the bubbles which can alter their chemical compositions. This model estimates the composition of these gas bubbles just prior to their release to the atmosphere by solving a system of equations including the Iacono-Marziano solubility relationships for H_2O and CO_2, gas-phase equilibrium relationships and mass conservation of hydrogen and carbon (Wogan et al. 2020). The model assumes that the oxygen fugacity of the gas is set by the oxygen fugacity of the magma and requires the following inputs: initial concentrations of H_2O and CO_2 in the melt prior to outgassing, temperature and pressure of outgassing, and redox state of the melt. Please refer to Wogan et al. (2020) for further details.

Swain et al. (2021) recently claimed the detection of a thin, reducing atmosphere around the rocky exoplanet GJ 1132 b that is H_2-dominated and rich in CH_4 ($\sim$0.5%). They simulated mantle outgassing and argued that an ultra-reduced magma could reproduce the observed atmosphere, with the best fitting model parameters giving

an extremely reduced oxygen fugacity of $logf_{O_2} = IW - 11$ (Swain et al. 2021). Such reduced conditions could conceivably arise if significant amounts of hydrogen from a planet's primary atmosphere dissolve into the magma ocean and were sequestered into the interior, thereby providing a reservoir of volatiles that can later be outgassed to form a secondary atmosphere (Swain et al. 2021; Kite et al. 2019). However, the outgassing model of Swain et al. (2021) omits carbon partitioning between solid, liquid and gas phases under ultra-reducing redox conditions.

We find that for an ultra-reduced melt of $logf_{O_2} = IW - 11$, essentially all of the carbon (>99%) will remain saturated as graphite during partial melting, so there is negligible carbon available for gaseous phases (Figure 4.3). To confirm this, we used the above outgassing speciation model which solves for the gas-gas and gas-melt equilibrium in a C-O-H system, to predict the gases that would be released from the melt by magmatic outgassing. From this model, we determine that the CH_4, CO_2, and CO outgassing fluxes would be negligible (<1E-10 Tmol/year) at such a reduced oxygen fugacity (Figure **??**). It is important to note that these calculations do not include carbon in the form of iron carbonyls and methyl (CH_3) groups bonded to Si^{4+} in the melt as some studies have suggested will be present under reducing conditions (Wetzel et al. 2013; Mysen et al. 2011). However, it is not expected that these additional carbon-bearing species will significantly alter our findings as these studies also found carbon stable in the melt under reducing conditions. Therefore our findings suggest that the outgassing mechanism proposed for GJ 1132 b is improbable. Additionally, an independent study that analyzed the same Hubble Space Telescope (HST) transit data

found no methane signature and instead claim a featureless spectrum for GJ 1132 b (Mugnai et al. 2021), and the findings of Swain et al. (2021) conflict with Lyman-alpha observations of the system (Waalkes et al. 2019).

4.6.3 Calculations of Global CH_4 Flux Estimates from Abiotic Sources

The global CH_4 flux estimates for different abiotic sources in Tables 4.2, 4.3, 4.4, 4.5, 4.6 (and illustrated in the schematic Figure 4.2) and Figure 4.4 are calculated as follows:

Higher Temperature:

- **Etiope & Lollar 2013:** To determine an estimated global abiotic CH_4 flux from surface volcanism, we take their CH_4 flux estimates for individual volcanoes and multiply these values by the number of active volcanoes on Earth today ($\sim$1500) (Etiope & Lollar 2013).

- **Ryan et al. 2006:** To determine an estimated global abiotic CH_4 flux from surface volcanism, we followed the same procedure as described above for Etiope & Lollar 2013, except with Ryan et al.'s estimates for individual volcanic outgassing CH_4 fluxes (Ryan et al. 2006).

- **Schindler & Kasting 2000:** They estimated the current global CH_4 flux from submarine volcanism to be $\sim 10^{-2}$ Tmol/year by taking an observed ratio of CH_4/CO_2 in mid-ocean ridge hydrothermal vent fluids and an estimated total outgassed carbon flux at the mid-ocean ridges.

Lower Temperature:

Observational and Theoretical Studies:

- **Cannat et al. 2010:** They derive a global serpentinization-related methane flux at slow spreading mid-ocean ridges of 2.5×10^{-2} Tmol/year (Cannat et al. 2010).

- **Keir 2010:** Keir calculates a global methane flux of 2×10^{-2} Tmol/year from mid-ocean ridges, similar to the findings of Cannat et al. 2010 (Keir 2010).

- **Jones et al. 2010:** Their serpentinization experiments for mid-ocean ridges and forearcs determined CH_4 production rates ranging from 1×10^{-5} to 0.05 μmol/kg/hr (Jones et al. 2010). Taking these rates and extrapolating to the mass of the entire oceanic crust, we find that the corresponding global abiotic CH_4 estimates exceed the Earth's iron supply. However McCollom (2013) caution that Jones et al. did not determine their background levels of CH_4 so it is possible that a portion of the methane generated in their experiments came from sources of contamination. Therefore, the findings of Jones et al. cannot be extrapolated to a global abiotic flux.

- **Catling & Kasting 2017:** Using a combination of different observational studies, they determined abiotic CH_4 flux estimates for hot, axial vents and off-axis vent fields of 0.015 and 0.03 Tmol/year, respectively (Catling & Kasting 2017b). For hot, axial vents, they estimated the abiotic CH_4 flux by using observed CH_4 and CO_2 concentrations from East Pacific Rise fluids. For the off-axis vent fields, they used an estimated H_2 flux and the CH_4/H_2 ratio in ultramafic vent fields to determine an abiotic CH_4 flux estimate (Catling & Kasting 2017b).

- **Guzmán-Marmolejo et al. 2013:** They estimated the amount of CH_4 generated by serpentinization in hydrothermal vent systems. For $1M_\oplus$ and 5 $M_\oplus$ planets, they determined abiotic CH_4 fluxes of 0.18 Tmol/year and 0.35 Tmol/year, respectively (Guzmán-Marmolejo et al. 2013). These estimates account for the supply rate of available FeO in the crust which is determined in part by the crustal production rate. For the 5 $M_\oplus$ planet, the crustal production rate is scaled from Earth using a power law. They also take into account the limitations of CO_2 in hydrothermal systems based on different observational studies.

- **Kasting 2005:** Kasting 2005 estimated the global abiotic CH_4 flux from off-axis mid-ocean ridges by extrapolating from observed methane concentrations in hydrothermal fluids. They found that, at present, the abiotic hydrothermal CH_4 flux is $\sim$0.1 Tmol/year, but during the Hadean the flux may have been larger, $\sim$1.5 Tmol/year (Kasting 2005). They note that if seafloor creation during the Hadean was much faster, the abiotic CH_4 flux could have increased by a factor of 5-10. However, given that seafloor production rates during that period are uncertain, we only include their Hadean estimate of 1.5 Tmol/year in Figure 4.4 and Tables 4.2, 4.3, 4.4, 4.5, 4.6. These estimates are about an order of magnitude larger than those of Catling & Kasting 2017 because Kasting 2005 assumed a larger water circulation rate compared to that of Catling & Kasting 2017 (Catling & Kasting 2017b). In addition, the Kasting 2005 Hadean abiotic flux estimate is larger than Guzman-Marmolejo et al.'s estimates because Guzman-Marmolejo took into account the iron supply and CO_2 limitations in hydrothermal systems

(Guzmán-Marmolejo et al. 2013; Kasting 2005).

- **Brovarone et al. 2017:** This study determined several different global CH_4 flux estimates for different sites where serpentinization takes place including subduction zone fluids, forearc mantle wedges above subduction zones, and sub-seafloor conditions (Brovarone et al. 2017).

- **Fiebig et al. 2007:** They investigated subduction-related hydrothermal sites in the Mediterranean and computed both an uppermost flux estimate for abiogenic CH_4 during the Archean (2.5-5 Tmol/year) and a present-day flux (6×10^{-3} Tmol/year) (Fiebig et al. 2007).

- **Fiebig et al. 2009:** This study estimated the abiogenic CH_4 flux from continental hydrothermal systems to be 0.31 Tmol/year (Fiebig et al. 2009).

- **Portella et al. 2019:** Their study of serpentinization of chromitites in ophiolites found that chromitites can contain CH_4 gas concentrations up to 0.31 $\mu g/g_{rock}$ (de Melo Portella et al. 2019). Extrapolating this concentration by Earth's global melt production rate gives a negligible CH_4 flux compared to the biogenic flux. However, due to uncertainties in how these gas concentrations vary in time and between different sites and whether such processes could take place on a global scale, we do not include a global abiotic flux extrapolation for this source.

- **Klein et al. 2019:** They studied methane formation in olivine-hosted secondary fluid inclusions to inform serpentinization in subduction zones, mid-ocean ridges and ophiolites. They determined that the Chimaera serpentinization system has

released 0.076 to 0.5 km^3 CH_4 during the past 2000 years which is equivalent to 2×10^6-11×10^6 mol/year of CH_4. They also estimated that the lower oceanic crust contains a total of ∼300 Tmol of CH_4 gas (Klein et al. 2019). Taking this amount of methane gas in the lower oceanic crust and dividing it by the lifetime of Earth's oceanic crust results in a negligible global abiotic CH_4 flux. However, due to various uncertainties in extrapolating these findings to a global scale, we do not include a global abiotic flux extrapolation for this source.

Experiments:

- **McCollom 2013:** The hydrocarbon formation experiments discussed in McCollom 2013 measure the amount of dissolved CH_4 gas in serpentinized olivine at 300 ^oC as a function of time (see their Figure 7). Taking their experimental methane production rate of 0.05 μmol/kg/hr and scaling it to the entire mass of oceanic crust on Earth ($\sim 6 \times 10^{21}$ kg) results in a global flux estimate that exceeds Earth's iron supply (McCollom 2013). Such an estimate requires the whole crust to be at a high temperature which is unrealistic for a habitable zone terrestrial planet. Therefore, it is not possible to extrapolate their experimental findings to a global abiotic flux rate.

- **Oze et al. 2012:** They performed experiments to investigate the influence of mineral catalysts on serpentinization and found that the CH_4 production rate varied from ∼0.09 to 0.15 μmol/kg/hr. If we take their experimental CH_4 production rates and extrapolate to the mass of the oceanic crust, we find a global CH_4 flux estimate that exceeds Earth's iron supply. As with Jones et al. (Jones et al. 2010),

McCollom 2013 (McCollom 2013) note that Oze et al. did not quantify their background levels of CH_4, so it is not possible to properly extrapolate a global abiotic CH_4 flux from their experiments.

- **Neubeck et al. 2011:** Their serpentinization experiments on forsteritic olivine determined CH_4 accumulation rates ranging from 2.7×10^{-11} to 7.3×10^{-11} mol/m^2/s. However, McCollom 2013 (McCollom 2013) noted that Neubeck et al. did not quantify their background CH_4 levels, so it is not possible to extract an abiotic global flux estimate from this study.

- **McCollom 2016:** They performed serpentinization experiments with olivine and measured a range of dissolved CH_4 concentrations from 5.5 to 270 μmol/kg$_{\text{olivine}}$. They used isotopic labeling to differentiate CH_4 produced by serpentinization from background sources, and found that in almost all experiments, the majority of CH_4 produced actually derived from background sources rather than from reduction of dissolved inorganic carbon. Using the isotopic labeling, for the experiments performed at or above 300 ^{o}C, the amount of CH_4 generated via reduction of inorganic carbon was 16-50 μmol/kg$_{\text{olivine}}$ (McCollom 2016). Taking these concentrations, dividing by the duration of the experiments and extrapolating to the mass of the oceanic crust, we find that the corresponding global abiotic CH_4 estimates exceed the Earth's iron supply. As with McCollom 2013, these experiments suggest that high temperatures are necessary to generate CH_4. Such temperatures are higher than typical temperatures for habitable zone terrestrial planets. Therefore, we cannot properly extrapolate these experimental findings to a global abiotic CH_4

flux on temperate terrestrial planets.

Impacts:

- **Kasting 2005:** Kasting estimated the global CH_4 flux due to impact events during the Hadean to be 1.24 Tmol/year (Kasting 2005).
- **Kress & McKay 2004:** They determined that 0.6 Tmol of CH_4 is generated by a 1-km cometary impactor (Kress & McKay 2004).
- **Zahnle et al. 2020:** For a highly-reduced Pluto-sized dwarf planet impactor, they determined that it would generate ∼2300 moles CH_4/cm^2 (Zahnle et al. 2020).
- **Court & Sephton 2009:** Experimentally studied ablation of carbonaceous chondritic materials and found that they release <100 ppm of CH_4 at temperatures up to 1000^{o}C (Court & Sephton 2009).

4.6.4 Calculations of Atmospheric Methane Lifetime for Volatile-Rich Bodies

In Figure 4.5, we estimate the atmospheric lifetime of methane for an Earth-mass terrestrial planet with different water mass fractions and Titan-like initial volatile inventories. Using model calculations based on Cassini data for Titan's interior composition from Tobie et al. (2012), we assume Titan's volatile content consists of 0.35 % CH_4 and ∼4-6 % CO_2 relative to weight % H_2O (Tobie et al. 2012). We conservatively assume that the escape flux of hydrogen is diffusion-limited and calculate the atmospheric lifetime of CH_4. First we calculate the mass of methane:

$$m_{CH_4} = (0.35/100) m_{H_2O} \tag{4.36}$$

where m_{H_2O} is the water mass fraction of the planet (in kg). Then we calculate the diffusion-limited escape flux of H_2.

$$\Phi = C f_T(H_2) \tag{4.37}$$

Φ is the escape flux of H_2 from Earth at the diffusion limit (in molecules/cm^2/s). Assuming the atmosphere is 10% CH_4, the fraction of hydrogen ($f_T(H_2)$) is 0.2 (i.e., $0.1 \times 2 = 0.2$ with two H_2 molecules per CH_4 molecule) and C for Earth's atmosphere is 2.5×10^{13} cm^{-2}s^{-1}. The atmospheric lifetime of CH_4 (in years) is given by:

$$T_{CH_4} = (\frac{m_{CH_4}}{M_{CH_4}} \mathrm{NA})/(\Phi \times \mathrm{SA} \times 3.154 \times 10^7) \tag{4.38}$$

where M_{CH_4} is the molar mass of CH_4 in mol/kg, NA is the Avogadro constant and SA is the surface area of the Earth (in cm^2). Table 4.7 demonstrates how the lifetime of atmospheric CH_4 increases with increasing planetary mass fraction of water. For Figure 4.5, we ran a Monte Carlo simulation and varied the CH_4 inventory, sampling a uniform distribution from 10^{-4} to 10^{-2} relative to weight % water, for water mass fractions from 10^{-2} to 10 weight % of the planet's mass (assuming an Earth-mass planet).

To check that our estimated CH_4 atmospheric mixing ratio of 10% is reasonable, we calculate the solubilities of CH_4 and CO_2 for the atmosphere-ocean system reservoir using Henry's Law partitioning. For CH_4:

$$(C \times m_{H_2O} \times M_{CH_4}) + m_{\rm atm} = m_{CH_4} \tag{4.39}$$

where m_{H_2O} and m_{CH_4} are the masses of H_2O and CH_4, respectively. M_{CH_4} is CH_4's molar mass (kg/mol) and $m_{\rm atm}$ is the mass of the atmosphere, given by:

$$m_{\rm atm} = PA/g \tag{4.40}$$

where P is pressure in bars, A is the surface area of the planet in m^2, and g is surface gravity (9.8 m/s^2). $[CH_4]$ is the concentration of dissolved CH_4 (mol/kg), which is given by Henry's Law:

$$[CH_4] = kP \tag{4.41}$$

where k is Henry's Law constant (0.0014 mol/kg/bar for CH_4). Solving for pressure, we find that for an Earth-mass planet with 1% of its mass consisting of water, the pressure of methane is ∼32 bars. Following the same formalism above for CO_2, which has a Henry's Law constant of 0.04 mol/kg/bar, its pressure is ∼22 bars. Therefore, our choice of CH_4's atmospheric mixing ratio of 10% is conservative given the volatile inventories, which also allow for plausible inventories of N_2 gas.

We also consider whether volatile-rich, habitable zone planets could produce a long-lived CH_4+CO_2 biosignature false positive if not all water is melted. The storage and slow release of CH_4 and CO_2 from clathrates (ices that trap gases) on a Titan-like planet could conceivably mimic a biosphere. If surface conditions are habitable,

however, then storage of large volumes of CH_4 in pure clathrates is not possible because CH_4 clathrates are less dense than liquid water at all pressures (Tobie et al. 2006). Any CH_4 clathrates stored in high pressure ices would therefore rise to the surface and rapidly dissociate. It is true that methane clathrates are a CH_4 reservoir on Earth, but this is only because they are trapped by the weight of sediments above them, and are thus in a quasi-stable state (and will be potentially perturbed by slight surface warming). The weight of sediments could not trap the $\sim 10^{22}$ mol of CH_4 required to sustain biogenic-like fluxes of CH_4 for Gyr timescales.

If surface conditions are sub-freezing, CH_4 clathrates can inhibit subsurface ocean formation at all depths, and tectonically driven ice resurfacing may continuously bring fresh clathrates to the surface, maintaining CH_4 fluxes larger than Earth's biological flux (Levi et al. 2014). The region of parameter space for which atmospheric CH_4 can be maintained is likely small, however, since clathrates are unstable against surface warming: liquid water from warming will destabilize CH_4 clathrates, causing CH4 release into the atmosphere and even more greenhouse warming (Levi et al. 2014). Initial surface temperatures must therefore be low to prevent this runaway melting. For many planets, clathrate false positives may be ruled out by estimating minimum surface temperatures from observed atmospheric gases and plausible albedos. However, additional modeling work is required to characterize clathrate-atmosphere interactions across diverse planetary conditions.

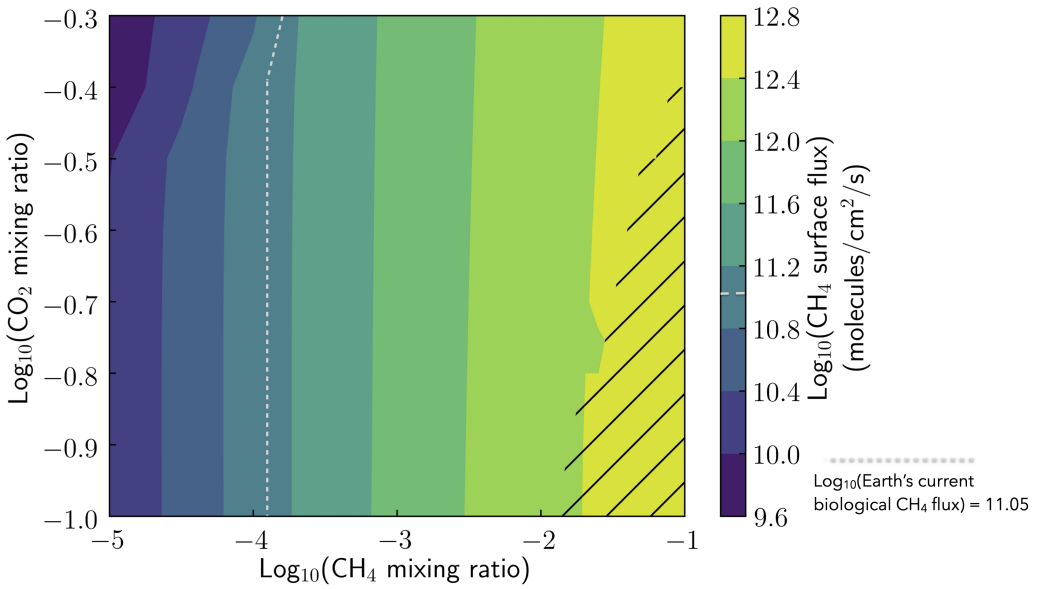

Figure 4.6: **Methane surface flux required to sustain CH_4- and CO_2-rich atmospheres in photochemical steady state.** Using PhotochemPy, we ran a series of models with an initial atmospheric composition that is Archean Earth-like (orbiting the Sun at 2.7 Ga) exploring a range of CH_4 and CO_2 surface mixing ratios from 10^{-5} to 0.1 and 0.1 to 0.5, respectively. The contour colors correspond to the CH_4 surface flux required to sustain the atmospheric mixing ratios. While the model accounts for haze formation, we found that at higher CH_4 mixing ratios, the model had trouble converging to a steady-state solution. For those cases corresponding to the hatched region of the figure, we ran models that used the same Archean Earth-like initial atmospheric composition but removed the haze component in order to ensure model convergence. Ultimately, for abundant atmospheric CH_4 (i.e., surface mixing ratios above $\sim 10^{-3}$) to be stable against photochemistry in terrestrial planet atmospheres requires a significant replenishment source that results in large CH_4 surface fluxes that are likely much larger than Earth's current biological flux.

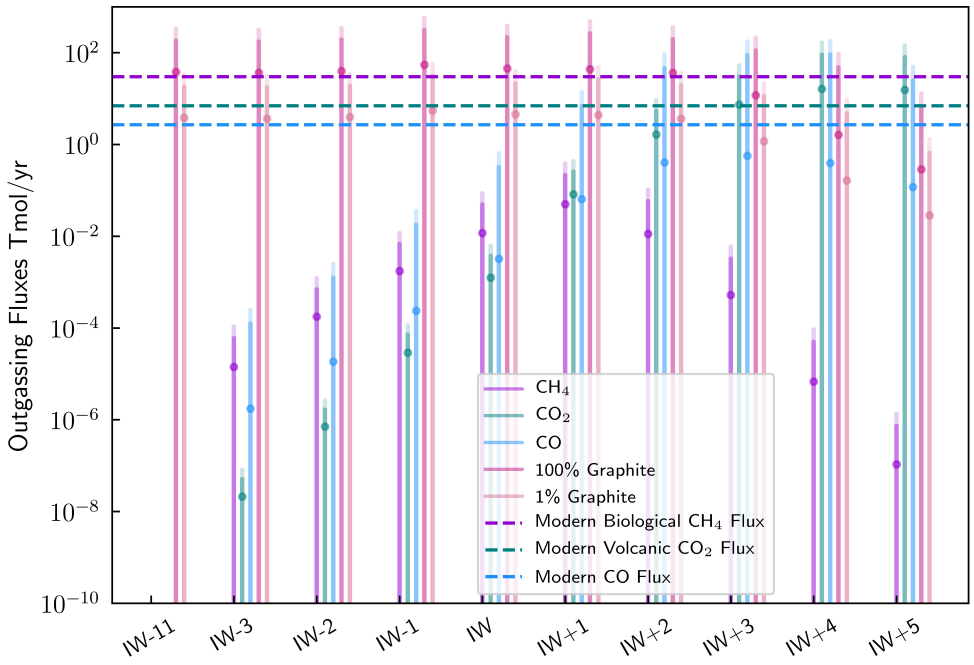

Figure 4.7: **Simultaneous outgassing of CH_4 and CO_2 with negligible CO is highly unlikely unless large quantities of graphite are efficiently converted to CH_4 via metamorphism.** Outgassing fluxes as a function of oxygen fugacity. We used the same batch-melting model as described in Figure 4.3 and solved for speciation of gases produced by magmatic outgassing. The results are the average outgassing fluxes (in Tmol/year) of CH_4, CO_2 and CO from the Monte Carlo simulation with uncertainties reported as the 95% confidence intervals. The graphite results assume that either 100% or 1% of the remaining graphite can be converted into outgassed CH_4. The horizontal dashed lines show current outgassing fluxes on Earth for reference (e.g., biological CH_4 flux). For a planet with a very reduced melt composition, outgassing of any carbon species (i.e., CH_4, CO_2, and CO) will be negligible. In addition, for all oxygen fugacities considered from extremely reduced ($IW - 11$) to highly oxidized ($IW + 5$), the magmatic outgassing fluxes of CH_4 are still orders of magnitude lower than Earth's modern biological CH_4 flux of 30 Tmol/year.

Input Parameter	Low	High	Sampling Method
Mantle Mass (M_{mantle}) (kg)	$0.1(4 \times 10^{24})$	$10(4 \times 10^{24})$	log_{10} Uniform Distribution
Mantle CO_2 Mass (M_{mantle,CO_2}) (kg)	$1 \times 10^{-5}(4 \times 10^{24})$	$1 \times 10^{-2}(4 \times 10^{24})$	log_{10} Uniform Distribution
Mantle H_2O Mass (M_{mantle,H_2O}) (kg)	$1 \times 10^{-5}(4 \times 10^{24})$	$1 \times 10^{-1}(4 \times 10^{24})$	log_{10} Uniform Distribution
Melt Fraction (F)	0.1	0.5	Uniform Distribution
Planetary Melt Production (M_{melt}) (g/s)	$0.1(3.2 \times 10^{9})$	$10(3.2 \times 10^{9})$	log_{10} Uniform Distribution

Table 4.1: Monte Carlo sampling distributions for carbon partitioning and gas speciation calculations.

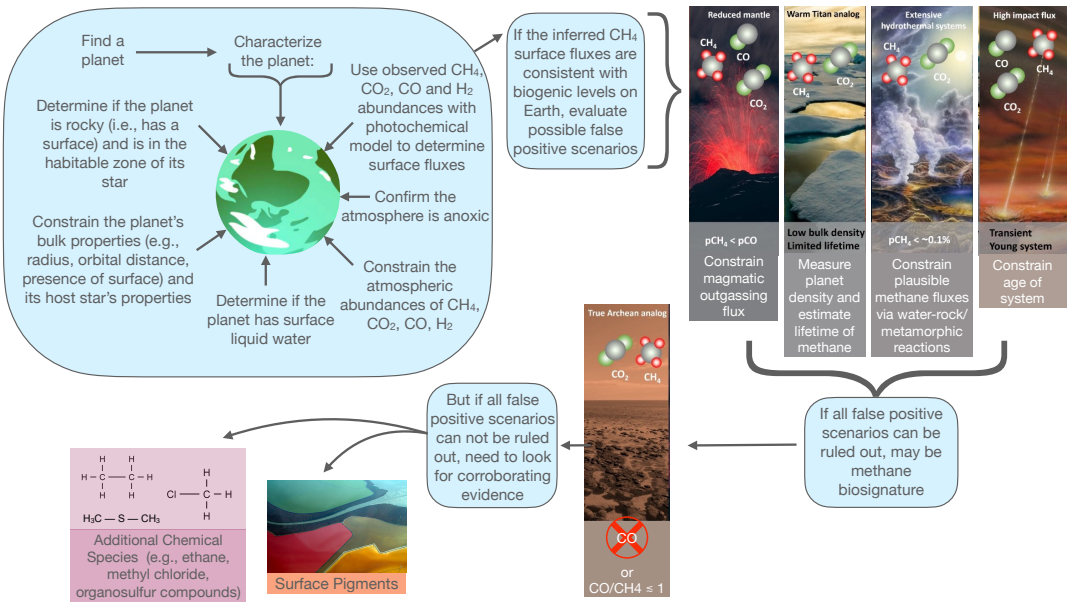

Figure 4.8: **Possible procedure to search for methane biosignatures on terrestrial exoplanets that takes into account the planetary context.** Once an exoplanet has been detected, it is important to characterize its bulk properties (e.g., mass, radius, orbital properties, presence of a surface, host star properties). In addition, constraining its atmospheric composition, particularly the abundances CH_4, CO_2, CO, H_2, H_2O and confirming that the atmosphere is anoxic, is essential for determining the presence of a methanogenic biosphere. Using this data with a photochemical model can determine the surface fluxes of the different atmospheric constituents that are necessary to sustain the observed atmospheric abundances. If the inferred CH_4 surface fluxes are consistent with plausible biogenic levels, then all possible false positive scenarios must be evaluated. If all false positives can be definitively ruled out then a methane biosignature has been identified at a high level of confidence that must be statistically determined. However, if all false positives cannot be ruled out, then it is necessary to look for corroborating evidence like additional gas species (e.g., methyl chloride, and organosulfur compounds) and the presence of surface pigments. Credits (images): Don Dixon, Wikimedia Commons; Donald Hobern; kuhnmi; NASA/JPL-Caltech/Lizbeth B. De La Torre; Doc Searls.

Abiotic Source	Reference	CH_4 Flux	Global CH_4 Flux Estimate
Higher Temperature			
Volcanic	Etiope & Lollar 2013 Etiope & Lollar (2013)	100 tons/yr (Mt. Etna, most Icelandic volcanoes)	9.4E-3 Tmol/year
Volcanic	Ryan et al. 2006 Ryan et al. (2006)	9 tons/yr	8.4E-4 Tmol/yr
Submarine Volcanism	Schindler & Kasting (2000)	–	1.3E-2 Tmol/year
Lower Temperature			
Serpentinization at slow-spreading mid-ocean ridges	Cannat et al. 2010 Cannat et al. (2010)	3.9E7 mol/yr (Rainbow Hydrothermal Field); 0.04-0.3E7 mol/km/yr (Ridge domains with frequent ultramafic outcrops)	2.5E-2 Tmol/yr
Serpentinization in vent fluids from mid-ocean ridges	Keir 2010 Keir (2010)	0.1-4 mmol/kg	2E-2 Tmol/yr

Table 4.2: Summary of abiotic CH_4 sources and their estimated global CH_4 flux values (Part 1). *Indicates that the experimental measurements may have over-estimated the amount of methane generated due to the presence of background sources.

Abiotic Source	Reference	CH_4 Flux	Global CH_4 Flux Estimate
Lower Temperature (Cont.)			
Serpentinization at seafloor hydrothermal systems	Catling & Kasting (2017b)	–	0.015 - 0.03 Tmol/year
Serpentinization at hydrothermal vent systems	Guzmán-Marmolejo et al. (2013)	–	0.18 Tmol/year (for 1 M_{Earth}), 0.35 Tmol/year (for 5 M_{Earth})
Serpentinization at off-axis mid-ocean ridges	Kasting (2005)	–	0.1 Tmol/year (at present), 1.5 Tmol/year (during Hadean)
Serpentinization and carbonate reduction at subduction zones	Brovarone et al. (2017)	–	9E-2 Tmol/yr (subduction zone fluids); 8E-3-0.2 Tmol/yr (forearc mantle wedges above subduction zones); 1E-2-0.1 Tmol/yr (sub-seafloor)
Serpentinization at subduction-related sites (and estimates for Archean Eon)	Fiebig et al. (2007)	–	2.5-5 Tmol/yr (during Archean), 6E-3 Tmol/yr (at present)

Table 4.3: Summary of abiotic CH_4 sources and their estimated global CH_4 flux values (Part 2). *Indicates that the experimental measurements may have over-estimated the amount of methane generated due to the presence of background sources.

Abiotic Source	Reference	CH_4 Flux	Global CH_4 Flux Estimate
Lower Temperature (Cont.)			
Reduction of CO_2 in continental hydrothermal systems	Fiebig et al. (2009)	–	0.31 Tmol/year
Serpentinization of chromitites in ophiolites	de Melo Portella et al. (2019)	0.31 μg/g (rock) in chromitites	–
Serpentinization in subduction zones, mid-ocean ridges and ophiolites	Klein et al. (2019)	2E6-11E6 mol/yr (Chimaera system)	–
Experiments of hydrocarbon formation in deep subsurface	McCollom (2013)	0.05 μmol/kg/hr	CH_4 Flux > Fe supply

Table 4.4: Summary of abiotic CH_4 sources and their estimated global CH_4 flux values (Part 3). *Indicates that the experimental measurements may have over-estimated the amount of methane generated due to the presence of background sources.

Abiotic Source	Reference	CH_4 Flux	Global CH_4 Flux Estimate
Lower Temperature (Cont.)			
Serpentinization experiments for mid-ocean ridges and fore-arcs	Jones et al. (2010)	1E-5 - 0.06 μmol/kg/hr	CH_4 Flux > Fe supply*
Serpentinization experiments investigating mineral catalysts	Oze et al. (2012)	0.15 μmol/kg/hr	CH_4 Flux > Fe supply*
Serpentinization experiments on forsteritic olivine	Neubeck et al. (2011)	2.7E-11-7.3E-11 mol/m^2/s	0.64-1.2 Tmol/yr*
Serpentinization experiments on olivine	McCollom (2016)	$\sim$7.7E-3-1.3E-2 μmol/$kg_{olivine}$/hr	CH_4 Flux > Fe supply

Table 4.5: Summary of abiotic CH_4 sources and their estimated global CH_4 flux values (Part 4). *Indicates that the experimental measurements may have over-estimated the amount of methane generated due to the presence of background sources.

Abiotic Source	Reference	CH_4 Flux	Global CH_4 Flux Estimate
Impacts			
Impact events during the Hadean	Kasting (2005)	–	1.24 Tmol/year
Cometary impact events	Kress & Kress & McKay (2004)	0.6 Tmol (generated by 1-km comet impactor)	–
Impact events for early Earth	Zahnle et al. (2020)	2300 moles/cm^2 (generated by a highly-reduced Pluto-sized dwarf planet impactor)	Not applicable - transient event lasting ∼10,000 years
Meteorite ablation experiments	Court & Sephton (2009)	<100 ppm from gasification of carbonaceous asteroid	–

Table 4.6: Summary of abiotic CH_4 sources and their estimated global CH_4 flux values (Part 5). *Indicates that the experimental measurements may have over-estimated the amount of methane generated due to the presence of background sources.

Mass Fraction of Water (wt% of planet mass)	0.1	1.0	10	50
Lifetime of CH_4 (Myr)	1	10	100	500

Table 4.7: Estimated lifetime of atmospheric CH_4 for Earth-mass terrestrial planets with Titan-like initial volatile inventory and different size water mass fractions.

Chapter 5

Summary and Future Directions

5.1 Summary

This thesis examined both the outgassing origins and near-term observable biosignatures for rocky exoplanet atmospheres through a combination of laboratory experiments and theoretical modeling tools. Chapters 2 and 3 analyzed the origins of rocky exoplanet atmospheres and their primordial compositions using outgassing experiments and subsequent analyses of chondritic meteorites (Thompson et al. (2021), Thompson et al. 2023). Using a combination of theoretical models, Chapter 4 evaluated the planetary context for atmospheric methane as a near-term biosignature gas (Thompson et al. 2022).

Chapter 2 presented a set of experiments conducted in a high-vacuum environment that simultaneously heated and monitored the abundances of volatile species evolved from various chondrite samples as a function of temperature. Using mass spectrometry, these experiments determined that heating of CM chondrites to 1200 °C

consistently produced H_2O-rich atmospheres with substantial amounts of CO and CO_2 and smaller quantities of H_2 and H_2S. These experiments provided the first set of meteorite outgassing abundances to compare to thermochemical equilibrium calculations that predict the outgassing compositions of meteorites. Similarities between the experimental and chemical equilibrium results included that water was the dominant outgassing species and CO and CO_2 also outgassed significantly. However, this study also uncovered key differences, such as the fact that H_2 had a much lower outgassing abundance in the experiments than predicted by theory as well as differences in peak temperatures at which H_2S outgassed, highlighting the importance of disequilibrium and kinetics effects. This study demonstrated the importance of experimentally measuring the outgassing compositions of planetary materials and how such results can differ from equilibrium models. As published in *Nature Astronomy*, these experiments provided ground-truth constraints on the chemical compositions used in theoretical models of rocky exoplanets' early atmospheres by supplying abundances of principal gas species as a function of temperature (Thompson et al. 2021).

To gain a more complete understanding of the outgassing composition of carbonaceous chondrites, Chapter 3 presented a bulk element analysis using inductively-coupled plasma mass spectrometry (ICP-MS) of samples of the Murchison meteorite heated to 1000 °C under atmospheric pressure and vacuum conditions. This study explored the effects of temperature, pressure and redox state on Murchison's outgassing composition. By measuring the outgassing trends of a suite of major elements (e.g., Fe, Mg, Zn, S) as a function of temperature and pressure, it determined that sulfur out-

gassed significantly under both pressure conditions and zinc outgassed under vacuum. Together with the first set of experiments presented in Chapter 2, Chapter 3 provided important insights into the volatile depletion patterns of primitive meteorites and the initial outgassing compositions of rocky exoplanets.

Chapter 4 undertook a comprehensive analysis of the necessary planetary conditions for atmospheric methane to be a compelling biosignature gas, together with potential false positive scenarios that arise from its abiotic sources. Potential abiotic sources of methane include high-temperature magmatic processes (e.g., volcanism), low-temperature water-rock and metamorphic reactions, and impact events. Using a combination of multiphase thermodynamic and atmospheric chemistry models, including photochemistry, volatile speciation, and atmospheric escape, this study investigated these various abiotic sources and determined if, under different conditions, they could be enhanced on other planets to result in false positives for biological activity. For example, applying a melting model showed that rocky exoplanets with very reduced magma compositions are unlikely to outgas significant amounts of CH_4 due to graphite saturation. Through this modeling work, it was determined that known abiotic processes cannot easily generate atmospheres rich in CH_4 and CO_2 with limited CO due to the strong redox disequilibrium between CH_4 and CO_2. As published in *PNAS*, Chapter 4 provided the first tentative framework for assessing methane biosignatures, concluding that methane is more likely to be biogenic for terrestrial planets with (1) a high mean molecular weight and anoxic atmosphere, (2) an atmospheric CH_4 abundance that implies surface fluxes exceeding what could be generated by known abiotic processes, and

(3) atmospheric CO_2 with comparatively little CO (Thompson et al. 2022).

5.2 Future Directions

There are many avenues to extend the work presented in this thesis, several of which will be undertaken in the coming years.

5.2.1 Experimental Constraints on Volatile Partitioning in Magma Exoplanets

Given the chemical range observed in stars, the plausible diversity of rocky exoplanets is vast, including wide ranges in bulk compositions, temperatures, atmospheric constituents, and surface properties (Putirka & Rarick 2019; Adibekyan et al. 2021). Due to their observational advantages of having short orbital periods and bright day-side fluxes in infrared light, some of the most characterizable rocky exoplanets of the coming decades are magma planets, which have extensive lava or magma oceans at their surfaces (Henning et al. 2018). Understanding these magma worlds may unlock a new pathway for studying the early Earth during the Hadean Eon and the origin of life on both our planet and others.

In preparation for upcoming observations of magma exoplanets, suitable theoretical tools, informed by experimental data, are necessary to model the diversity of these planets and their atmospheres and to ensure that observations are properly interpreted. As described in Chapter 2, rocky exoplanets likely form their atmospheres via outgassing during and after accretion, indicating that the atmospheres are strongly

linked to their interiors (Elkins-Tanton & Seager 2008). Given the vast parameter space of possible rocky exoplanet interior compositions, to establish this connection between planetary interiors and atmospheres it is important to start with diverse materials unlike the present-day Earth but that exist in the Solar System, such as meteorites and synthetic analogs representative of the mantle during earlier periods in Earth's history. Unfortunately, there is limited experimental data on the compositions and properties of these materials at the high temperature conditions relevant for magma exoplanets. This experimental data is necessary for models to properly predict the atmospheric compositions that would form via outgassing on these magma exoplanets.

The chemical composition of magma exoplanet interiors and surfaces are fundamental properties for understanding their outgassed atmospheres, the main observable features of these worlds for the coming decades. For planets with extensive magma on their surfaces, some portion of the volatile elements (e.g., H, C, O, N, S) can partition and dissolve into the melt. The degree to which volatiles can enter the magma is dependent on the planet's interior composition and in turn can strongly influence the planet's atmospheric composition, internal structure and potential to eventually evolve to temperate conditions conducive to life (Gaillard et al. 2021). Extensive work has been done in the Earth and planetary science communities to understand volatile partitioning and solubility in silicate melts and other materials that exist on modern Earth to inform planetary differentiation, magma oceans, and the chemistry of planetary mantles (e.g., Solomatova et al. (2020); Grewal et al. (2020); Sossi et al. (2020a); Bower et al. (2022)). However, there is currently only a limited understanding of how volatiles parti-

tion between the interior, surficial and atmospheric reservoirs for diverse planetary bulk compositions unlike the present-day Earth, such as that of Earth's primitive mantle or meteorite compositions which are likely more representative of diverse rocky exoplanet compositions (Chao et al. 2021).

Volatile solubility measurements for modern Earth-like compositions cannot be extrapolated to exoplanets if they have different volatile inventories or redox environments compared to Earth. This lack of data for compositionally diverse melts is mainly because conducting experiments with these compositions is challenging. In particular, to measure volatile solubilities in melts, the samples must be quenched into clean glasses to preserve their melt compositions and structure for subsequent analysis. Diverse materials with primitive compositions are challenging to quench into clean glasses, as crystals quickly form and modify the volatile content unless the quench time is extremely short. However, modern instrumental techniques, like aerodynamic laser levitation heating systems, resolve this issue with extremely rapid quenching ($\sim$800 °C/s) of melts to form clean glasses of a diverse range of materials. For example, recent work by Sossi et al. provided the first experimental constraints on the solubility of water in peridotite (ultramafic igneous rock) liquids, representative of Earth's current mantle, over a range of atmospheric redox conditions (Sossi et al. 2023). In addition, experiments on peridotite at higher pressures indicate that its H2 solubilities are unlike what would be expected based on extrapolations from basaltic liquids (Brugman et al. 2022), highlighting the limitations in experimental data.

An important way to fill this significant gap in experimental data is to measure

the solubilities of volatiles (i.e., carbon and hydrogen) in exoplanet melt analog materials over a range of atmospheric temperatures and redox states. Carbon and hydrogen are important life-forming elements, but their solubility behavior in compositionally diverse melts and at temperatures relevant to magma worlds is not well constrained. Solubilities relate the dissolved mole fraction of a given species (e.g., X_{H_2O}) in the silicate melt, with its fugacity (e.g., f_{H_2O}) in the gas, with a generalized law:

$$X(H_2O) = \alpha f(H_2O)^{\beta} \tag{5.1}$$

The α coefficient is a function of temperature and melt composition, whereas β depends on the speciation of the dissolved volatile. Water is known to dissolve in terrestrial silicate melts as H_2O at high f_{H_2O} ($\beta = 1$), but as f_{H_2O} decreases, it dissolves as OH^- ($\beta = 0.5$; Stolper (1982); Newcombe et al. (2017)). The dissolution mechanism of H_2O is modulated by the availability of suitable sites in the silicate network that can accommodate it, and hence its composition. Therefore, future work should seek to determine α and β for volatiles in a range of exoplanet-relevant silicate melt compositions and temperatures. To do so, melts with bulk compositions like those of the silicate portions of various meteorites, including enstatite and ordinary chondrites, aubrites and angrites, should be synthesized. These meteorites have reducing (i.e., oxygen-limited) compositions that are representative of material in the inner solar system during terrestrial planet formation (Lodders 2000). In addition, current exoplanet mass and radius measurements along with host star abundance data suggest that some rocky exoplanets are likely chemically reduced and compositionally distinct relative to Earth (Putirka &

Rarick 2019; Howard et al. 2013). The oxygen fugacity (f_{O_2}) determines the relative abundances of gas species:

$$H_2O = H_2 + \frac{1}{2}O_2 \tag{5.2}$$

Hence, the atmospheric gases in exoplanets may not be H_2O- and CO_2-rich like on Earth, but H_2- and CO-dominated. Solubilities of reduced species, particularly H_2, are significant in terrestrial basalt compositions (Hirschmann et al. 2012). Indeed, the abundance of exoplanets with 2-3 Earth radii (sub-Neptunes) has been proposed to result from H_2 dissolution into silicate melt, thereby preventing further growth (Kite et al. 2019). Determining the solubilities of reduced species is key to testing these models. As Sossi et al. 2022 determined, Earth's building-block materials are not completely represented by the meteorites available in our collections, and instead Earth, and possibly Earth-like exoplanets, likely formed by stochastic accretion of many different bodies of variable compositions (Sossi et al. 2022). Therefore, it is essential to study the behavior of volatiles in melts with a wide range of bulk compositions.

An aerodynamic laser levitation and Fourier Transform infrared spectrometer (FTIR) system can both simulate exoplanet analog materials at the high-temperature conditions expected for magma worlds and monitor the fugacities of various outgassed species (e.g., f_{H_2}, f_{H_2O}, f_{CO_2}). Using the mechanics of evaporation (e.g., Hertz-Knudsen-Langmuir equation) the physical state of the vapor evolved from exoplanet analog samples can be computed. Such measurements would provide fundamental constraints on the atmospheric composition formed via outgassing of diverse magma ocean

analog materials. Once these melts have been quenched into glasses, various instruments, such as electron probe micro-analyzers, Raman and FTIR spectrometers, can determine the major element composition and concentration of volatiles in the melt (e.g., X_{H_2}, X_{H_2O}, X_{CO_2}). As proposed above, more experiments are needed to deliver new, ground-truth measurements of volatile parititioning and speciation across the interior and atmospheric reservoirs for compositionally diverse rocky exoplanet magma analogs.

5.2.2 Modeling the Compositional Diversity of Rocky Exoplanets

Volatile partitioning and solubility data alone are not sufficient to predict the composition, structure, and evolution of rocky exoplanet atmospheres. These data need to be placed within the framework of a thermochemical model to predict atmospheric compositions for upcoming ground- and space-based observations of these worlds. It will be important to incorporate new experimental volatile solubility measurements into coupled interior-atmosphere climate models to determine plausible end-member atmospheric compositions for the known rocky exoplanets that are observable with upcoming telescopes. In addition, such models should simulate how planets with different initial surface and atmospheric compositions evolve with time and to determine if some of these planets could possess habitable surface conditions.

An example of such a valuable tool would be a 1-dimensional interior-atmosphere model that predicts a planet's atmospheric composition, structure, and visible and infrared spectra depending on its magma ocean redox state and the redox-dependent partitioning of volatiles between the melt and the atmosphere. The types of exper-

iments described above will provide fundamental information on carbon and hydrogen's solubilities over a range of redox conditions and temperatures representative of the magma ocean-atmosphere interface, which should be incorporated into interior-atmosphere models to inform how volatiles partition for various planetary bulk compositions. For a planet's surface temperature, pressure and interior composition, a model can assume thermochemical equilibrium to determine its magma ocean redox state, which is an appropriate assumption since magma ocean viscosities are low (0.1 Pa.s, Liebske et al. (2005)) leading to high Rayleigh numbers (Ra), such that it is well mixed over convective length scales and rapidly reaches equilibrium with the atmosphere.

Models should use experimentally-measured solubilities to determine the speciation and partitioning of volatiles between a planet's magma ocean and atmosphere. In the atmosphere, radiative-convective equilibrium can be assumed, and models can utilize a variety of publicly-available radiative transfer packages, such as petitRADTRANS, that calculate transmission and emission spectra of planetary atmospheres (Mollière et al. 2019). Models should also be capable of evolving a planet as its magma ocean solidifies, such as the planetary evolution model of Krissansen-Totton (Krissansen-Totton et al. 2021; Krissansen-Totton & Fortney 2022). It is important to include the effects of atmospheric escape and photochemistry in future models as they can greatly influence how the speciation of gases in the atmosphere evolve.

These coupled interior-atmosphere climate models should be used to determine plausible atmospheric compositions and simulated spectra for sets of known, potentially magma exoplanets (e.g., LHS 3844 b, K2-141 b, TRAPPIST-1 b) assuming a range of

bulk compositions, redox states, and surface temperatures and pressures. Such models can also assess important atmospheric properties, including what cloud species are likely to form at different regions in the atmosphere and if a greenhouse effect is to be expected. Planetary evolution models should investigate how rocky exoplanets' atmospheric and surface conditions could evolve with time and their potential to evolve to a habitable state. For example, these tools can be used to analyze the planetary context for various chemical disequilibrium biosignatures (e.g., the presence of both CH_4 and CO_2/O_2) and the abiotic processes that could produce chemical disequilibrium in a planet's atmosphere to rule out biosignature false positives (Krissansen-Totton et al. 2016).

Models that incorporate experimentally-determined volatile solubilities will an important complement to existing models that assume either ad-hoc atmospheric compositions, compositions based on planetary evolution models, or metal-enriched H_2-dominated atmospheres (Morley et al. 2017; Krissansen-Totton & Fortney 2022; Miller-Ricci et al. 2009). Models that include such ground-truth experimental data may reveal the extent to which volatile solubilities in Earth-like, primitive melts are comparable to those in meteoritic and synthetic exoplanet analog melts, which would indicate that magma ocean evolution may be unified for all terrestrial planets and is shaped mostly by the planet's redox state. In the coming years, it is important to make imminently testable predictions for the atmospheric compositions of terrestrial exoplanets with diverse compositions to help interpret JWST and other upcoming space- and ground-based observations of magma exoplanets. In addition, these theoretical tools will inform the

design of next generation space-based missions such as the Habitable Worlds Observatory, NASA's next proposed flagship mission, by providing a framework for assessing how a planet evolves to a habitable state and identifying what atmospheric compositions are indicative of habitability.

Bibliography

Abe, Y., & Matsui, T. 1985, Journal of Geophysical Research, 90, C545

Adibekyan, V., Dorn, C., Sousa, S. G., et al. 2021, Science, 374, 330

Ahrens, T. J., O'Keefe, J. D., & Lange, M. A. 1989, Origin and Evolution of Planetary and Satellite Atmospheres, ed. S. K. Atreya, J. B. Pollack, & M. S. Matthews (University of Arizona Press)

Alexander, C. M. O., Bowden, R., Fogel, M. L., et al. 2012, Science, 337, 721

Alexander, C. M. O., & Wang, J. 2010, Meteoritics and Planetary Science, 36, 419

Andrews, S. M. 2020, Annual Review of Astronomy and Astrophysics, 58, 483

Arney, G., Domagal-Goldman, S. D., & Meadows, V. S. 2018, Astrobiology, 18, 311

Arney, G., Domagal-Goldman, S. D., Meadows, V. S., et al. 2016, Astrobiology, 16, 873

Bart, G., Ikramuddin, M., & Lipschutz, M. E. 1980, Geochimica et Cosmochimica Acta, 44, 719

Bartlett, R. W. 1967, Journal of The Electrochemical Society, 114, 547

Battistuzzi, F. U., Feijao, A., & Hedges, S. B. 2004, BMC Ecology and Evolution, 4, 14

Bell, J. F., Davis, D. R., Hartmann, W. K., & Gaffey, M. J. 1989, in Asteroids II, ed. R. P. Binzel, T. Gehrels, & M. S. Matthews, 921–945

Boesenberg, J. S., & Delaney, J. S. 1997, Geochimica et Cosmochimica Acta, 61, 3205

Bower, D. J., Hakim, K., Sossi, P. A., & Sanan, P. 2022, The Planetary Science Journal, 3, 28

Bower, D. J., Kitzmann, D., Wolf, A. S., et al. 2019, Astronomy Astrophysics, 631, 18

Braukmüller, N., Wombacher, F., Hezel, D. C., Escoube, R., & Münker, C. 2018, Geochimica et Cosmochimica Acta, 239, 17

Brovarone, A. V., Martinez, I., Elmaleh, A., et al. 2017, Nature Communications, 8, 13

Brugman, K., Shahar, A., Badro, J., & Cody, G. 2022, in Goldschmidt Conference No. 10267

Burgess, R., Wright, I. P., & Pillinger, C. T. 1991, Meteoritics, 26, 55

Burkhardt, C., Spitzer, F., Morbidelli, A., et al. 2021, Science Advances, 7, 11

Cannat, M., Fontaine, F., & Escartin, J. 2010, in Diversity of Hydrothermal Systems on Slow Spreading Ocean Ridges, ed. P. A. Rona, C. W. Devey, J. Dyment, & B. J. Murton, Vol. 188 (American Geophysical Union), 241–264

Catling, D. C., & Kasting, J. F. 2017a, in Atmospheric Evolution on Inhabited and Lifeless Worlds (Cambridge University Press), 129–168

Catling, D. C., & Kasting, J. F. 2017b, Atmospheric Evolution on Inhabited and Lifeless Worlds (Cambridge University Press)

—. 2017c, Atmospheric Evolution on Inhabited and Lifeless Worlds (Cambridge University Press)

Catling, D. C., & Zahnle, K. J. 2020, Science Advances, 6, 17

Catling, D. C., Zahnle, K. J., & McKay, C. P. 2001, Science, 293, 839

Chakraborty, S. 1997, Journal of Geophysical Research: Solid Earth, 102, 12317

Chambers, J. 2023, The Astrophysical Journal, 944, 23

Chambers, J. E. 2010, Icarus, 208, 505

Chao, K.-H., deGraffenried, R., Lach, M., et al. 2021, Geochemistry, 81, 32

Chapman, S., & Cowling, T. G. 1970, The Mathematical Theory of Non-Uniform Gases, 3rd edn., ed. C. U. Press

Chyba, C. F. 1990, Nature, 343, 129

Clayton, R. N., Mayeda, T. K., Hiroi, T., Zolensky, M., & Lipschutz, M. E. 1997, Meteoritics and Planetary Science, 32, A30

Clery, D. 2023, Science, 379, 2

Connelly, J. N., Bizzarro, M., Krot, A. N., et al. 2012, Science, 338, 651

Cormier, V. F., Bergman, M. I., & Olson, P. L. 2022, Earth's Core: Geophysics of a Planet's Deepest Interior, ed. V. F. Cormier, M. I. Bergman, & P. L. Olson (Elsevier), 247–280

Cottrell, E., & Kelley, K. A. 2011, Earth and Planetary Science Letters, 305, 270

Court, R. W., & Sephton, M. A. 2009, Geochimica et Cosmochimica Acta, 73, 3512

Dang, L., Cowan, N. B., Kreidberg, L., et al. 2021, JWST Proposal. Cycle 1, 5

Daniel J. Lessner, Lingyun Li, Q. L. T. R. V. P. A. M. R. K. H. J. J. M. B. L. K. J. G. F. 2006, Proceedings of the National Academy of Sciences, 103, 17921

Davis, A. M., & Richter, F. M. 2014, Treatise on Geochemistry, 1, 335

de Melo Portella, Y., Zaccarini, F., & Etiope, G. 2019, Minerals, 9, 15

Delaney, J. S. 1994, Meteoritics, 29, 459

Domagal-Goldman, S. D., Meadows, V. S., Claire, M. W., & Kasting, J. F. 2011, Astrobiology, 11, 419

Dorn, C., Noack, L., & Rozel, A. B. 2018, Astronomy Astrophysics, 614, 20

Doyle, A. E., Young, E. D., Klein, B., Zuckerman, B., & Schlichting, H. E. 2019, Science, 366, 356

Dragomir, D., Matthews, J. M., Eastman, J. D., et al. 2013, The Astrophysical Journal, 772, 6

Dressing, C. D., & Charbonneau, D. 2015, The Astrophysical Journal, 807, 23

Elkins-Tanton, L. T. 2012, Annual Review of Earth and Planetary Sciences, 40, 113

Elkins-Tanton, L. T., & Seager, S. 2008, The Astrophysical Journal, 685, 1237

Etiope, G. 2017, Procedia Earth and Planetary Science, 17, 9

Etiope, G., Feyzullayev, A., & Baciu, C. L. 2009, Marine and Petroleum Geology, 26, 333

Etiope, G., & Lollar, B. S. 2013, Reviews of Geophysics, 51, 276

Fauchez, T. J., Turbet, M., Villanueva, G. L., et al. 2019, The Astrophysical Journal, 887, 194

Fegley, B. 2013, Practical Chemical Thermodynamics for Geoscientists (Academic Press (Elsevier)), 482

Ferry, J. G., & House, C. H. 2006, Molecular Biology and Evolution, 23, 1286

Fiebig, J., Woodland, A. B., D'Alessandro, W., & Püttmann, W. 2009, Geology, 37, 495

Fiebig, J., Woodland, A. B., Spangenberg, J., & Oschmann, W. 2007, Geochimica et

Cosmochimica Acta, 71, 3028

Fletcher, L. N., Orton, G. S., Teanby, N. A., Irwin, P. G. J., & Bjoraker, G. L. 2009, Icarus, 199, 351

Foreman-Mackey, D., Hogg, D. W., & Morton, T. D. 2014, The Astrophysical Journal, 795, 12

Formisano, V., Atreya, S., Encrenaz, T., Ignatiev, N., & Giuranna, M. 2004, Science, 306, 1758

Fortney, J. J., Mordasini, C., Nettelmann, N., et al. 2013, The Astrophysical Journal, 775, 13

Fortney, J. J., Robinson, T. D., Domagal-Goldman, S., et al. 2019, Astro2020 Science White Paper, 10

Fuchs, L. H., Olsen, E., & Jensen, K. J. 1973, Smithsonian Contributions to the Earth Sciences, 1

Fulton, B. J., Petigura, E. A., Howard, A. W., et al. 2017, The Astronomical Journal, 154, 109

Gaillard, F., & Scaillet, B. 2014, Earth and Planetary Science Letters, 403, 307

Gaillard, F., Bouhifd, M. A., Füri, E., et al. 2021, Space Science Reviews, 217

Gerasimov, M. V., Ivanov, B. A., Yakovlev, O. I., & Dikov, Y. P. 1998, Earth, Moon and Planets, 80

Gialluca, M. T., Robinson, T. D., Rugheimer, S., & Wunderlich, F. 2021, Publications of the Astronomical Society of the Pacific, 133, 054401

Giardini, A. A., Salotti, C. A., & Lakner, J. F. 1968, Science, 159, 317

Gillon, M., Triaud, A. H. M. J., Demory, B.-O., et al. 2017, Nature, 542, 456

Gilmozzi, R., & Spyromilio, J. 2007, The Messenger, 127, 9

Gooding, J. L., & Muenow, D. W. 1977, Meteoritics, 12, 401

Gooding, J. L., & Zolensky, M. E. 1987, Lunar and Planetary Science Conference, 18, 343

Grady, M. M., & Wright, I. P. 2003, Space Science Reviews, 106, 231

Greene, T. P., Line, M. R., Montero, C., et al. 2016, The Astrophysical Journal, 817, 22

Grewal, D. S., Dasgupta, R., & Farnell, A. 2020, Geochimica et Cosmochimica Acta, 280, 281

Guimond, C. M., Noack, L., Ortenzi, G., & Sohl, F. 2021, Physics of the Earth and Planetary Interiors, 320, 15

Guzmán-Marmolejo, A., & Segura, A. 2015, Boletín De La Sociedad Geológica Mexicana, 67, 377

Guzmán-Marmolejo, A., Segura, A., & Escobar-Briones, E. 2013, Astrobiology, 13, 550

Halliday, A. N., & Kleine, T. 2006, Meteorites and the Early Solar System II, ed. D. S. Lauretta & H. Y. M. Jr. (University of Arizona Press), 19–52

Harrison, F. A., Kennicutt, R. C., Dalcanton, J., et al. 2021, National Academies of Science, Engineering and Medicine, Washington, DC

Hasimoto, G. L., Abe, Y., & Sugita, S. 2007, Journal of Geophysical Research, 112, 12

Henning, W. G., Renaud, J. P., Saxena, P., et al. 2018, White Paper for National Academy of Sciences 2018 Exoplanet Science Strategy Solicitation, 6

Herbort, O., Woitke, P., Helling, C., & Zerkle, A. 2020, Astronomy & Astrophysics, 636, 1

Hirschmann, M. M., & Withers, A. C. 2008, Earth and Planetary Science Letters, 270, 147

Hirschmann, M. M., Withers, A. C., Ardia, P., & Foley, N. T. 2012, Earth and Planetary Science Letters, 345-348, 38

Hoehler, T. M., Bains, W., Davila, A., Parenteau, M. N., & Pohorille, A. 2020, Planetary Astrobiology, ed. V. S. Meadows, G. N. Arney, B. E. Schmidt, & D. J. D. Marais (University of Arizona Press)

Holloway, J. R. 1984, Geology, 12, 455

Hörst, S. M. 2017, Journal of Geophysical Research: Planets, 122, 432

Howard, A. W., Sanchis-Ojeda, R., Marcy, G. W., et al. 2013, Nature, 503, 381

Hu, R., Peterson, L., & Wolf, E. T. 2020, The Astrophysical Journal, 888, 15

Hu, R., Seager, S., & Bains, W. 2013, The Astrophysical Journal, 769, 14

Hu, R., Brandeker, A., Damiano, M., et al. 2021, JWST Proposal. Cycle 1, 6

Huff, W. D., & Owen, L. A. 2013, Treatise on Geomorphology, 5, 148

Hurlbut, C. S., & Klein, C. 1985, Manual of Mineralogy, 20th edn.

Huss, G. R., Lewis, R. S., & Hemkin, S. 1996, Geochimica et Cosmochimica Acta, 60, 3311

Ikramuddin, M., Binz, C. M., & Lipschutz, M. E. 1977, Geochimica et Cosmochimica Acta, 41, 393

Ikramuddin, M., & Lipschutz, M. E. 1975, Geochimica et Cosmochimica Acta, 39, 363

Ito, M., & Ganguly, J. 2006, Geochimica et Cosmochimica Acta, 70, 799

Jackson, R. B., Saunois, M., Bousquet, P., et al. 2020, Environmental Research Letters, 15, 7

Javoy, M. 1995, Geophysical Research Letters, 22, 2219

Javoy, M., Kaminski, E., Guyot, F., et al. 2010, Earth and Planetary Science Letters, 293, 259

Jeoung, J.-H., & Dobbek, H. 2007, Science, 318, 1461

Jochum, K. P., Nohl, U., Herwig, K., et al. 2007, Geostandards and Geoanalytical Research, 29, 333

Jones, C. L., Rosenbauer, R., Goldsmith, J. I., & Oze, C. 2010, Geophysical Research Letters, 37, L14306

Kadoya, S., & Catling, D. C. 2019, Geochim. Cosmochim. Acta, 262, 207

Kadoya, S., Catling, D. C., Nicklas, R. W., Puchtel, I. S., & Anbar, A. D. 2020, Nature Communications, 11, 9

Kaltenegger, L., & Sasselov, D. 2010, The Astrophysical Journal, 708, 1162

Kasting, J. F. 2005, Precambrian Research, 137, 119

Kasting, J. F., & Brown, L. L. 1996, Origins of life and evolution of the biosphere, 26, 2

—. 1998, The Molecular Origins of Life: Assembling Pieces of the Puzzle, ed. A. Brack (Cambridge University Press), 35–56

Kasting, J. F., Zahnle, K. J., & Walker, J. C. G. 1983, Precambrian Research, 20, 121

Keir, R. S. 2010, Geophysical Research Letters, 37, L24609

Kharecha, P., Kasting, J., & Siefert, J. 2005, Geobiology, 3, 53

Kietäväinen, R., Ahonen, L., Niinikoski, P., Nykänen, H., & Kukkonen, I. T. 2017, Geochimica et Cosmochimica Acta, 202, 124

King, A. J., Schofield, P. F., & Russell, S. S. 2021, Geochimica et Cosmochimica Acta, 298, 167

Kite, E. S., Jr., B. F., Schaefer, L., & Ford, E. B. 2019, The Astrophysical Journal, 887, L33

Klein, F., Grozeva, N. G., & Seewald, J. S. 2019, Proceedings of the National Academy of Sciences, 116, 17666

Kleine, T., Budde, G., Burkhardt, C., et al. 2020, Space Science Reviews, 216, 27

Knutson, H. A., Dragomir, D., Kreidberg, L., et al. 2014, The Astrophysical Journal, 794, 155

Komacek, T. D., Fauchez, T. J., Wolf, E. T., & Abbot, D. S. 2020, The Astrophysical Journal, 888, L20

Kopparapu, R. K., Wolf, E. T., & Meadows, V. S. 2020, Planetary Astrobiology, ed. V. S. Meadows, G. N. Arney, B. E. Schmidt, & D. J. D. Marais (University of Arizona Press)

Kreidberg, L., Hu, R., Kite, E. S., et al. 2021, JWST Proposal. Cycle 1

Kreidberg, L., Koll, D. D. B., Morley, C., et al. 2019, Nature, 573, 87

Kreidberg, L., Agol, E., Bolmont, E., et al. 2021, Hot Take on a Cool World: Does Trappist-1c Have an Atmosphere?, JWST Proposal. Cycle 1

Kress, M. E., & McKay, C. P. 2004, Icarus, 168, 475

Krinov, E. L. 1969, The Meteoritical Bulletin (Meteoritics), 5, 2

—. 1970, Meteoritics, 5, 85

Krissansen-Totton, J., Bergsman, D. S., & Catling, D. C. 2016, Astrobiology, 16, 39

Krissansen-Totton, J., & Fortney, J. J. 2022, The Astrophysical Journal, 933, 32

Krissansen-Totton, J., Fortney, J. J., Nimmo, F., & Wogan, N. 2021, AGU Advances, 2, 20

Krissansen-Totton, J., Garland, R., Irwin, P., & Catling, D. C. 2018a, The Astronomical Journal, 156, 13

Krissansen-Totton, J., Olson, S., & Catling, D. C. 2018b, Science Advances, 4, 14

Krissansen-Totton, J., Thompson, M., Galloway, M. L., & Fortney, J. J. 2022, Nature Astronomy, 6, 189

Laakso, T. A., & Schrag, D. P. 2019, Earth and Planetary Science Letters, 522, 48

Lammer, H., Zerkle, A. L., Gebauer, S., et al. 2018, The Astronomy and Astrophysics Review, 26, 72

Lange, M. A., & Ahrens, T. J. 1982, Icarus, 51, 96

Lapôtre, M. G. A., O'Rourke, J. G., Schaefer, L. K., et al. 2020, Nature Reviews Earth and Environment, 1, 170

Lenton, T. M. 2020, Interface Focus, 10, 15

Levi, A., Sasselov, D., & Podolak, M. 2014, The Astrophysical Journal, 792, 125

Liebske, C., Schmickler, B., Terasaki, H., et al. 2005, Earth and Planetary Science Letters, 240, 589

Lim, O., Doyon, R., Cowan, N. B., et al. 2022, JWST Proposal. Cycle 1, 18

Lindal, G. F., Wood, G. E., Hotz, H. B., et al. 1983, Icarus, 53, 348

Lodders, K. 2000, Space Science Reviews, 92, 341

—. 2003, The Astrophysical Journal, 591, 1220

Lodders, K., & Fegley, B. 1998, The Planetary Scientist's Companion

Loftus, K., Wordsworth, R. D., & Morley, C. V. 2019, The Astrophysical Journal, 887, 15

López-Morales, M., Ben-Ami, S., Gonzalez-Abad, G., et al. 2019a, The Astronomical Journal, 158, 15

López-Morales, M., Currie, T., Teske, J., et al. 2019b, Bulletin of the American Astronomical Society, 51, 162

Lovelock, J. E. 1975, Proceedings of the Royal Society of London, 189, 167

Luger, R., & Barnes, R. 2015, Astrobiology, 15, 24

Lupu, R. E., Zahnle, K., Marley, M. S., et al. 2014, The Astrophysical Journal, 784, 19

Lyu, Z., Shao, N., Akinyemi, T., & Whitman, W. B. 2018, Current Biology, 28, 727

Mahan, B., Moynier, F., Beck, P., Pringle, E. A., & Siebert, J. 2018, Geochimica et Cosmochimica Acta, 220, 19

Mansfield, M., Bean, J. L., Kempton, E. M. R., et al. 2021, Constraining the Atmosphere of the Terrestrial Exoplanet Gl486b, JWST Proposal. Cycle 1

Marais, D. J. D., Harwit, M. O., Jucks, K. W., et al. 2004, Astrobiology, 2, 153

Marty, B. 2012, Earth and Planetary Science Letters, 313-314, 56

Matsui, T., & Abe, Y. 1986, Nature, 322, 526

Matza, S. D., & Lipschutz, M. E. 1977, Lunar and Planetary Science Conference Pro-

ceedings, 8, 161

Mbarek, R., & Kempton, E. M.-R. 2016, The Astrophysical Journal, 827, 10

McCollom, T. M. 2003, Geochimica et Cosmochimica Acta, 67, 311

—. 2013, Reviews in Mineralogy and Geochemistry, 75, 467

—. 2016, Proceedings of the National Academy of Sciences, 113, 13965

McCollom, T. M., & Bach, W. 2009, Geochimica et Cosmochimica Acta, 73, 856

McCollom, T. M., Klein, F., & Ramba, M. 2022, Icarus, 372, 114754

McCollom, T. M., & Seewald, J. S. 2001, Geochimica et Cosmochimica Acta, 65, 3769

McKay, C. P., & Smith, H. D. 2005, Icarus, 178, 274

McSween, H. Y., & Huss, G. R. 2010, Cosmochemistry

Meadows, V. S., Reinhard, C. T., Arney, G. N., et al. 2018, Astrobiology, 18, 33

Menzies, O. N., Bland, P. A., Berry, F. J., & Cressey, G. 2005, Meteoritics and Planetary Science, 40, 1023

Mezger, K., Schönbächler, M., & Bouvier, A. 2020, Space Science Reviews, 216, 24

Mikal-Evans, T. 2021, Detecting the proposed CH4-CO2 biosignature pair with the James Webb Space Telescope: TRAPPIST-1e and the effect of cloud/haze, Accepted in MNRAS, arXiv:2111.09685

Miller-Ricci, E., Seager, S., & Sasselov, D. 2009, The Astrophysical Journal, 690, 1056

MKS. 2005, RGA Application Bulletin 208 Spectra Reference, 03rd edn., MKS,

Mollière, P., Wardenier, J. P., van Boekel, R., et al. 2019, Astronomy and Astrophysics, 627, 17

Morbidelli, A., Lunine, J., O'Brien, D., Raymond, S., & Walsh, K. 2012, Annual Review

of Earth and Planetary Sciences, 40, 251

Morley, C. V., Kreidberg, L., Rustamkulov, Z., Robinson, T., & Fortney, J. J. 2017, The Astrophysical Journal, 850, 121

Moses, J. I., Fouchet, T., Bézard, B., et al. 2005, Journal of Geophysical Research, 110, 45

Muenow, D. W., Keil, K., & McCoy, T. J. 1995, Meteoritics, 30, 639

Mugnai, L. V., Modirrousta-Galian, D., Edwards, B., et al. 2021, The Astronomical Journal, 161, 284

Mulders, G. D., Pascucci, I., Apai, D., & Ciesla, F. J. 2018, The Astronomical Journal, 156, 20

Mumma, M. J., Villanueva, G. L., Novak, R. E., et al. 2009, Science, 323, 1041

Mysen, B. O., Kumamoto, K., Cody, G. D., & Fogel, M. L. 2011, Geochimica et Cosmochimica Acta, 75, 6183

Nagashima, K., Kita, N. T., & Luu, T.-H. 2018, Chondrules: Records of Protoplanetary Disk Processes, ed. S. S. Russell, H. C. Connolly, & A. N. Krot (Cambridge University Press)

Namur, O., Charlier, B., Holtz, F., Cartier, C., & McCammon, C. 2016, Earth and Planetary Science Letters, 448, 102

Neubeck, A., Duc, N. T., Bastviken, D., Crill, P., & Holm, N. G. 2011, Geochemical Transactions, 12, 10

Newcombe, M. E., Brett, A., Beckett, J. R., et al. 2017, Geochimica et Cosmochimica Acta, 200, 330

Ngo, H. T., & Lipschutz, M. E. 1980, Geochimica et Cosmochimica Acta, 44, 731

Nishimura, M., & Sandell, E. B. 1964, Geochimica et Cosmochimica Acta, 28, 1055

NIST, M. S. D. C., & Wallace, W. E. 2018, NIST Chemistry WebBook, ed. P. J. Linstrom & W. G. Mallard No. 69 (NIST Standard Reference Database)

Nittler, L. R., McCoy, T. J., Clark, P. E., et al. 2004, Antarctic Meteorite Research, 17, 231

Nozaki, W., Nakamura, T., & Noguchi, T. 2006, Meteoritics and Planetary Science, 41, 1095

O'Brien, W. J., & Nielsen, J. P. 1959, Journal of Dental Research, 38, 541

Okumura, F., & Mimura, K. 2011, Geochimica et Cosmochimica Acta, 75, 7063

Olson, S. L., Reinhard, C. T., & Lyons, T. W. 2016, Proceedings of the National Academy of Sciences, 113, 11447

Olson, S. L., Schwieterman, E. W., Reinhard, C. T., et al. 2018, The Astrophysical Journal, 858, L14

Ortenzi, G., Noack, L., Sohl, F., et al. 2020, Scientific Reports, 10, 14

Ozaki, K., Tajika, E., Hong, P. K., Nakagawa, Y., & Reinhard, C. T. 2017, Nature Geoscience, 11, 55

Oze, C., Jones, L. C., Goldsmith, J. I., & Rosenbauer, R. J. 2012, Proceedings of the National Academy of Sciences, 109, 9750

Pavlov, A. A., Brown, L. L., & Kasting, J. F. 2001, Journal of Geophysical Research, 106, 23267

Peplowski, P. N., Klima, R. L., Lawrence, D. J., et al. 2016, Nature Geoscience, 9, 273

Peterson, P. 2009, International Journal of Computational Science and Engineering, 4

Petigura, E. A., Howard, A. W., & Marcy, G. W. 2013a, Proceedings of the National Academy of Sciences, 110, 19273

Petigura, E. A., Marcy, G. W., & Howard, A. W. 2013b, The Astrophysical Journal, 770, 21

Piani, L., Marrocchi, Y., Rigaudier, T., et al. 2020, Science, 369, 1110

Pizzarello, S., & Shock, E. 2010, Cold Spring Harbor Perspectives in Biology, 2, a002105

Planavsky, N. J., Asael, D., Hofmann, A., et al. 2014, Nature Geoscience, 7, 4

Pringle, E. A., Moynier, F., Beck, P., Paniello, R., & Hezel, D. C. 2017, Earth and Planetary Science Letters, 468, 62

Prinn, R. G., Huang, J., Weiss, R. F., et al. 2001, Science, 292, 1882

Putirka, K. D., & Rarick, J. C. 2019, American Mineralogist, 104, 817

Ragsdale, S. W. 2004, Critical Reviews in Biochemistry and Molecular Biology, 39, 165

Ranjan, S., Schwieterman, E. W., Harman, C., et al. 2020, The Astrophysical Journal, 896, 21

Reinhard, C. T., Planavsky, N. J., Olson, S. L., & Erwin, D. H. 2016, Proceedings of the National Academy of Sciences, 113, 8933

Reller, A., Padeste, C., & Hug, P. 1987, Nature, 329, 527

Richter, F. M., Davis, A. M., Ebel, D. S., & Hashimoto, A. 2002, Geochimica et Cosmochimica Acta, 66, 521

Richter, F. M., Mendybaev, R. A., Christensen, J. N., Ebel, D., & Gaffney, A. 2011, Meteoritics and Planetary Science, 46, 1152

Righter, K., Drake, M. J., & Scott, E. R. D. 2006, Compositional Relationships Between Meteorites and Terrestrial Planets, ed. D. S. Lauretta & H. Y. McSween, 803

Ruzicka, A., Grossman, J., Bouvier, A., Herd, C. D. K., & Agee, C. B. 2015, Meteoritics and Planetary Science, 50

Ryan, S., Dlugokencky, E. J., Tans, P. P., & Trudeau, M. E. 2006, Geophysical Research Letters, 33, L12301

Sakuraba, H., Kurokawa, H., Genda, H., & Ohta, K. 2021, Scientific Reports, 11, 14

Salyk, C., Pontoppidan, K. M., Andrews, S. M., et al. 2021, A DSHARP-MIRI Treasury survey of Chemistry in Planet-forming Regions, JWST Proposal. Cycle 1

Sauterey, B., Charnay, B., Affholder, A., Mazevet, S., & Ferrière, R. 2020, Nature Communications, 11, 12

Savage, P. S., Moynier, F., & Boyet, M. 2022, Icarus, 386, 7

Schaefer, L., & Elkins-Tanton, L. T. 2018, Philosophical Transactions of the Royal Society of London. Series A, Mathematical and Physical Sciences, 376, 17

Schaefer, L., & Fegley, B. 2007, Icarus, 186, 462

—. 2010, Icarus, 208, 438

—. 2017, The Astrophysical Journal, 843, 18

Schindler, T. L., & Kasting, J. F. 2000, Icarus, 145, 262

Schlichting, H. E., & Mukhopadhyay, S. 2018, Space Science Reviews, 214

Schrödinger, E. 1944, What Is Life? The Physical Aspect of the Living Cell

Schwieterman, E. W., Cockell, C. S., & Meadows, V. S. 2015, Astrobiology, 15, 341

Schwieterman, E. W., Reinhard, C. T., Olson, S. L., et al. 2019, The Astrophysical

Journal, 874, 10

Schwieterman, E. W., Kiang, N. Y., Parenteau, M. N., et al. 2018, Astrobiology, 18, 663

Scott, E. R. D., & Krot, A. N. 2014, Treatise on Geochemistry, 1, 65

Segura, A., Kasting, J. F., Meadows, V., et al. 2005, Astrobiology, 5, 706

Sharp, Z. D. 2017, Chemical Geology, 448, 137

Sholes, S. F., Krissansen-Totton, J., & Catling, D. C. 2019, Astrobiology, 19, 655

Simoncini, E., Virgo, N., & Kleidon, A. 2013, Earth System Dynamics, 4, 317

Solomatova, N., Caracas, R., & Cohen, R. 2020, Carbon in Earth's Interior, ed. C. E. Manning, J.-F. Lin, & W. L. Mao (Wiley)

Sossi, P. A., Burnham, A. D., Badro, J., et al. 2020a, Science Advances, 6, 8

Sossi, P. A., & Fegley, B. 2018, Reviews in Mineralogy Geochemistry, 84, 393

Sossi, P. A., Klemme, S., O'Neill, H. S. C., Berndt, J., & Moynier, F. 2019, Geochimica et Cosmochimica Acta, 260, 204

Sossi, P. A., Moynier, F., Treilles, R., et al. 2020b, Geochimica et Cosmochimica Acta, 288, 316

Sossi, P. A., Stotz, I. L., Seth A. Jacobson, A. M., & O'Neill, H. S. C. 2022, Nature Astronomy, 6, 951

Sossi, P. A., Tollan, P. M. E., Badro, J., & Bower, D. J. 2023, Earth and Planetary Science Letters, 601, 13

Soto, G., Madrigal, P., Lucke, O., Garvie, L., & Ziegler, K. 2019,

Sousa-Silva, C., Seager, S., Ranjan, S., et al. 2020, Astrobiology, 20, 235

Springmann, A., Lauretta, D. S., Klaue, B., et al. 2019, Icarus, 324, 104

SRS. 2009, Operating Manual and Programming Reference: Models RGA100, RGA200, and RGA300 Residual Gas Analyzer, 1st edn., Stanford Research Systems,

Stark, C. C., Belikov, R., Bolcar, M. R., et al. 2019, Journal of Astronomical Telescopes, Instruments, and Systems, 5, 20

Stolper, E. 1982, Geochimica et Cosmochimica Acta, 46, 2609

Swain, M. R., Estrela, R., Roudier, G. M., et al. 2021, The Astronomical Journal, 161, 213

Team, T. L. 2019, The LUVOIR Mission Concept Study Final Report, Tech. rep.,

Techtmann, S. M., Colman, A. S., & Robb, F. T. 2009, Environmental Microbiology, 11, 1027

Tennyson, J., & Yurchenko, S. N. 2018, Atoms, 6

Thomas, N., Svedhem, H., Forget, F., et al. 2021, in 43rd COSPAR Scientific Assembly. Held 28 January - 4 February, Vol. 43, 149

Thompson, M. A., Krissansen-Totton, J., Wogan, N., Telus, M., & Fortney, J. J. 2022, Proceedings of the National Academy of Sciences, 119, 10

Thompson, M. A., Telus, M., Schaefer, L., et al. 2021, Nature Astronomy, 5, 575

Tobie, G., Gautier, D., & Hersant, F. 2012, The Astrophysical Journal, 752, 125

Tobie, G., Lunine, J. I., & Sotin, C. 2006, Nature, 440, 61

Tomkins, A. G. 2010, Meteoritics and Planetary Science, 44, 1133

Tonui, E., Zolensky, M., Hiroi, T., et al. 2014, Geochimica et Cosmochimica Acta, 126, 284

Tyburczy, J. A., Frisch, B., & Ahrens, T. J. 1986, Earth and Planetary Science Letters, 80, 201

Waalkes, W. C., Berta-Thompson, Z., Bourrier, V., et al. 2019, The Astronomical Journal, 158

Wasson, J. T., & Kallemeyn, G. W. 1988, Philosophical Transactions of the Royal Society of London. Series A, Mathematical and Physical Sciences, 325, 535

Webster, C. R., Mahaffy, P. R., Atreya, S. K., et al. 2015, Science, 347, 415

Weisberg, M. K., McCoy, T. J., & Krot, A. N. 2006, Meteorites and the Early Solar System II, ed. D. S. Lauretta & H. Y. M. Jr. (University of Arizona Press), 19–52

Weiss, M. C., Sousa, F. L., Mrnjavac, N., et al. 2016, Nature Microbiology, 1, 8

Wetzel, D. T., Rutherford, M. J., Jacobsen, S. D., Hauri, E. H., & Saal, A. E. 2013, Proceedings of the National Academy of Sciences, 110, 8010

Wilson, E. H., & Atreya, S. K. 2004, Journal of Geophysical Research: Planets, 109, E06002

Wogan, N., Krissansen-Totton, J., & Catling, D. C. 2020, The Planetary Science Journal, 1, 58

Woitke, P., Herbort, O., Helling, C., et al. 2021, Astronomy and Astrophysics, 646, 10

Wolfe, J. M., & Fournier, G. P. 2018, Nature Ecology and Evolution, 2, 897

Wong, M. H., Mahaffy, P. R., Atreya, S. K., Niemann, H. B., & Owen, T. C. 2004, Icarus, 171, 153

Wordsworth, R., & Kreidberg, L. 2022, Annual Review of Astronomy and Astrophysics, 60, 159

Wordsworth, R., & Pierrehumbert, R. 2014, The Astrophysical Journal, 785, 4

Wu, J., Desch, S. J., Schaefer, L., et al. 2018, Journal of Geophysical Research: Planets, 123, 2691

Wulf, A., Palme, H., & Jochum, K. 1995, Planetary and Space Science, 43, 451, small Bodies in the Solar System - Origin, Evolution, and Significance for the Formation of Planets

Wunderlich, F., Godolt, M., Grenfell, J. L., et al. 2019, Astronomy and Astrophysics, 624, A49

Wunderlich, F., Scheucher, M., Godolt, M., et al. 2020, ApJ, 901, 126

Yoshida, N., Hattori, T., Komai, E., & Wada, T. 1999, Catalysis Letters, 58, 119

Yu, X., Moses, J. I., Fortney, J. J., & Zhang, X. 2021, The Astrophysical Journal, 914, 18

Yung, Y. L., Allen, M., & Pinto, J. P. 1984, The Astrophysical Journal Supplement Series, 55, 465

Zahnle, K., Freedman, R. S., & Catling, D. C. 2011, Icarus, 212, 493

Zahnle, K. J., Gacesa, M., & Catling, D. C. 2019, Geochimica et Cosmochimica Acta, 244, 56

Zahnle, K. J., Kasting, J. F., & Pollack, J. B. 1988, Icarus, 74, 62

Zahnle, K. J., Lupu, R., Catling, D. C., & Wogan, N. 2020, The Planetary Science Journal, 1, 11

Zhan, Z., Seager, S., Petkowski, J. J., et al. 2021, Astrobiology, 21, 62

Zhao, S., Jiang, J., & Zheng, J. 2011, Journal of Chongqing University